DIPLOMARBEIT
Master Thesis

Insight into the structural behavior of concrete hinges by means of Finite Element simulations

ausgeführt zum Zwecke der Erlangung des akademischen Grades
eines Diplom-Ingenieurs

unter der Leitung von

Associate Prof. Dipl.-Ing. Dr. techn. Bernhard Pichler
und
Univ.-Ass. Dipl.-Ing. Thomas Schlappal
E202
Institut für Mechanik der Werkstoffe und Strukturen

eingereicht an der Technischen Universität Wien
Fakultät für Bauingenieurwesen

von

Johannes Kalliauer
[redacted]

Wien, im April 2016 .....

Danksagung

Ein ganz besonderer Dank gebührt Herrn Associate Prof. Dipl.-Ing. Dr.techn. Bernhard Pichler und Herrn Univ.Ass. Dipl.-Ing. Thomas Schlappal, nicht nur für die hervorragende Betreuung, sondern vor allem auch für die schöne Zeit und das gute Arbeitsklima. Sie boten mir ideale Arbeitsbedingungen, indem sie mir jederzeit mit Rat und Tat zur Seite standen und mir bei der Erstellung der Arbeit wesentlich geholfen haben.

Ich möchte mich bei den Geldgebern (FFG, ÖBB und Asfinag) als auch bei dem gesamten Projektteam der Smart Minerals GmbH, der Vill Ziviltechniker GmbH, sowie beim Institut für Mechanik der Werkstoffe und Strukturen der TU Wien, bedanken, welche durch ihre wertvollen Anmerkungen bei Besprechungen die Arbeit wesentlich gefördert haben.

Bei dem Support von Atena/Sara bedanke ich mich herzlich für die wertvolle Unterstützung, bei Herrn Dr.-Ing. Dobromil Pryl, Herrn Ing. Jan Červenka Ph.D, Herrn Dr. Radomir Puckl und Herrn Prof. Dr. Novak Drahomir.

Mein herzlicher Dank gebührt meinen Eltern Elisabeth und Dipl.-Ing. Dr.techn. Alfred Kalliauer, die es mir erlaubten, mich sorglos und ohne behindernde Ablenkungen meinem größten Hobby, dem Studium, zu widmen.

Vorwort

Die Erstellung der vorliegenden Masterarbeit erfolgte im Rahmen zweier Forschungsprojekte. Die konkrete Auseinandersetzung mit Betongelenken und die Analyse von Experimenten ist dem Verkehrsinfrastrukturforschungsprojekt „Betongelenke“ zu verdanken, das durch

- die Österreichischen Forschungsförderungsgesellschaft (FFG)[1]
- die ÖBB Infrastruktur Aktiengesellschaft (ÖBB Infra AG) und
- die Autobahnen- und Schnellstraßen-Finanzierungs-Aktiengesellschaft (ASFINAG)

beauftragt wurde und durch das Projektteam bestehend aus

- Smart Minerals GmbH,
- Vill Ziviltechniker GmbH, und
- TU Wien, Institut für Mechanik der Werkstoffe und Strukturen,

bearbeitet wird. Die beschriebenen Mehrskalenstrukturanalysen sind insbesondere durch das FWF-Projekt[2] „Bridging the Gap by Means of Multiscale Structural Analyses“ motiviert, im Rahmen dessen der Mehrwert aufgezeigt wird, der sich dadurch ergibt, moderne Mehrskalenmodelle für Beton in Struktursimulationen von Stahlbetontragwerken einfließen zu lassen.

Der Text der vorliegenden Masterarbeit (exklusive der Anhänge) bildet einen weit vorangeschrittenen Entwurf für ein Manuskript, das im Lauf des Frühjahres 2016 in weiter verbesserter und leicht ergänzter Fassung zur Begutachtung und möglichen Publikation bei der Zeitschrift „Structural Concrete – Journal of the fib (Fédération internationale du béton)“, mit den Autoren Johannes Kalliauer[3] , Thomas Schlappal[3], Markus Vill[4], und Bernard Pichler[3] eingereicht werden soll.

Die Anhänge beinhalten die Ergebnisse einer der vorliegenden Masterarbeit vorangegangenen Projektarbeit, im Rahmen derer *ergänzende* numerische Sensitivitätsanalysen vorgenommen wurden. Sie wurden daher der vorliegenden Arbeit angefügt.

---

[1] ProjektNr: *845681*

[2] ProjektNr: *P 281 31-N32*

[3] Institut für Mechanik der Werkstoffe und Strukturen, Technischen Universität Wien, Karlsplatz 13/202, 1040 Wien, Österreich

[4] Vill Ziviltechniker GmbH, Hermanngasse 18, 1070 Wien, Österreich

Erweiterte Kurzfassung

Betongelenke erleben aktuell eine Renaissance, weil sich die zahlreichen Ausführungsbeispiele, die insbesondere in den 50er und 60er Jahren des 20. Jahrhunderts realisiert wurden, in den vergangenen Jahrzehnten in der Ingenieurpraxis als sehr rotationsfähige, nichtsdestotrotz aber auch sehr tragkräftige und dauerhafte Konstruktionselemente bewährt haben. Dieser Befund motiviert Bauingenieure, das Strukturverhalten von Betongelenken mit den aktuell zur Verfügung stehenden experimentellen und theoretischen Methoden zu untersuchen.

Die vorliegende Arbeit baut auf vorangegangenen Experimenten auf. Letztere sind in einem weit vorangeschrittenen Entwurf für ein Manuskript zusammengefasst [24], das demnächst zur Begutachtung und möglichen Publikation bei der Zeitschrift „Experimental Mechanics“ eingereicht werden soll. Darin sind Materialtests beschrieben, die am verwendeten Beton durchgeführt wurden, um die Würfeldruckfestigkeit und einen Steifigkeitsmodul zu bestimmen. Weiters wurden Strukturtests an Betongelenken in Form von zentrischen und exzentrischen Druckversuchen dokumentiert. Die dabei gemessenen Zusammenhänge zwischen äußerer Belastung der Betongelenke und Verformung in Form von Stauchungen und Verdrehungen des Gelenkshalses bilden die Grundlage für die vorliegende Arbeit.

Die vorliegende Arbeit zielt darauf ab, das experimentell beobachtete Verhalten von bewährten Betongelenken mit Hilfe von nichtlinearen dreidimensionalen Finite Elemente (FE) Simulationen zu reproduzieren. Dazu wird das kommerzielle FE Programm ATENA science (Version 5.1) verwendet, das für die Strukturanalyse von Stahlbetonkonstruktionen entwickelt worden ist. Weil das elasto-plastische Materialverhalten duktiler Bewährungsstähle kaum Streuungen unterliegt, kann es sehr zuverlässig simuliert werden. Beton ist hingegen ein sehr variabler Rezeptwerkstoff, dessen Materialeigenschaften von der gewählten Rezeptur abhängen. Weil Beton zudem ein chemisch aktiver und poröser Werkstoff ist, ist die Entwicklung seiner mechanischen Materialeigenschaften auch von den Umgebungsbedingungen wie Temperatur und Luftfeuchtigkeit abhängig. Die Entschlüsselung der Zusammenhänge zwischen Materialeigenschaften von Beton und seiner Materialrezeptur sowie der Umgebungsbedingungen sind eine aktuelle Herausforderung der wissenschaftlichen Forschung. Daher beinhalten derzeit verfügbare Materialmodelle für Beton zahlreiche und vielfach rein phänomenologische Materialparameter. Es ist gängige Praxis, diese Materialparameter innerhalb üblicher Schranken so zu wählen, dass entsprechende Struktursimulationen experimentell oder baupraktisch beobachtetes Verhalten wiedergeben. Diese Vorgangsweise birgt die Gefahr, dass die

Ermittlung geeigneter Materialparameter zu einer mathematischen Optimierungsaufgabe degeneriert, bei der physikalische Aspekte des Materialverhaltens unbeachtet bleiben. Die Aussagekraft von Struktursimulationen, die aus einer derartigen Vorgangsweise resultieren, ist in Hinblick auf das mechanische Verhalten der untersuchten Baukonstruktion sehr stark limitiert. Daher ist es wünschenswert, geeignete Materialparameter unter Verwendung physikalischer Argumente zu identifizieren. Dieser Herausforderung widmet sich die vorliegende Arbeit.

Die ersten Struktursimulationen erfolgen mit Standardeinstellungen, die sich durch Vorgabe der gemessenen Materialeigenschaften (Steifigkeit und Festigkeit) ergeben. Die damit erhaltenen numerischen Berechnungsergebnisse überschätzen die experimentell ermittelte Struktursteifigkeit und die Traglast der Betongelenke wesentlich.

Zur Verbesserung der Struktursimulationen wird im Rahmen einer Sensitivitätsanalyse untersucht, ob chemisches und trocknungsinduziertes Schrumpfen von Beton zu einer Vorschädigung des Materials geführt haben kann. Dazu werden in einer Abfolge mehrerer FE Simulationen verschieden große Schrumpfdehnungsintensitäten als Eigendehnungen in Rechnung gestellt. Diese Analysen verdeutlichen, dass schrumpfungsinduzierte Vorschädigung von Beton sowohl die Struktursteifigkeit als auch die Traglast von Betongelenken abmindert. Während die gemessene Struktursteifigkeit durch geeignete Wahl der Schrumpfdehnungsintensität quantitativ zufriedenstellend wiedergegeben werden kann, bleibt die experimentell erreichte Traglast überschätzt.

Zur weiteren Verbesserung der Struktursimulationen wird beachtet, dass sich im ungerissenen Teil des Gelenkshalses – bei Beanspruchung des Betongelenks durch eine Drucknormalkraft und ein Biegemoment – ein triaxialer Druckspannungszustand ergibt, wobei die entsprechenden Druckhauptnormalspannungen ein charakteristisches Verhältnis von $1 : 0.5 : 0.\dot{3}$ aufweisen. Der isotrope (hydrostatische) Anteil dieses Spannungszustands ist bemerkenswert hoch und bedingt eine ganz wesentliche Festigkeitssteigerung des Betons, mit deren Hilfe die hohe Belastbarkeit von Betongelenken erklärt werden kann. Diese durch allseitigen Druck bedingte Festigkeitssteigerung wird allerdings auf Basis der Standardeinstellungen des verwendeten FE Programms überschätzt. Dafür lassen sich folgende Gründe angeben.

1. Triaxiale Festigkeitstests werden üblicherweise in Öldruckzellen durchgeführt und stellen nach wie vor eine sehr große Herausforderung dar. Fotos von zerstörten Betonprobekörpern zeigen tonnenförmige Restverformungen, die auf wesentliche Schubspannungen in der Kontaktfläche zwischen Probekörper und Lastplatte rückschließen lassen. Von derartigen, experimentell unerwünschten, aber unvermeidbaren Schubspannungen ist bekannt, dass sie die Festigkeit von Betonprobekörpern weiter steigern. Daher liegt die Vermutung nahe, dass die in der verfügbaren Literatur

beschriebenen triaxialen Festigkeiten von Beton die tatsächliche Belastbarkeit des Materials überschätzen. Nichtsdestotrotz werden die überschätzen Festigkeiten verwendet, um Festigkeitsmodelle von Beton zu kalibrieren.

2. Die somit auch von den Betonmodellen überschätzen triaxialen Festigkeiten sind für Standardanwendungen der Softwareprogramme irrelevant. Bei der üblichen Simulation von Stahlbetonstützen, -trägern, -platten, -scheiben und -schalen liegen nämlich entweder einaxiale oder biaxiale Spannungszustände vor. Das heißt, dass kommerziell angebotene Berechnungsprogramme praktisch nie im Bereich der triaxialen Spannungszustände getestet werden.

Daher wird in der vorliegenden Arbeit in die Materialparameter eingegriffen, um die simulierte triaxiale Festigkeit von Beton abzumindern. Dabei wird allerdings Sorge getragen, dass die einaxiale Druckfestigkeit von Beton unverändert bleibt. Das ist erreichbar, indem eine *fiktive* (d.h. für die tatsächliche Simulation unmaßgebliche) Zugfestigkeit vergrößert wird. Auch in diesem Zusammenhang wird wieder eine Sensitivitätsanalyse vorgenommen. Dazu werden in einer Abfolge mehrerer FE Simulationen verschieden große Festigkeitsreduktionen in Rechnung gestellt. Diese Analysen verdeutlichen, dass die Reduktion der triaxialen Festigkeit von Beton die anfängliche Strukturseifigkeit erwartungsgemäß nicht beeinflusst, aber die simulierten Traglasten von Betongelenken sinken. Die gemessene Traglast kann durch geeignete Wahl der Festigkeitsreduktion quantitativ zufriedenstellend wiedergegeben werden.

Schließlich wird der Mehrwert von Mehrskalenstrukturanalysen aufgezeigt, bei denen moderne Mehrskalen-Betonmodelle als Grundlage für die numerische Simulation von Stahlbetonstrukturen verwendet werden. Die Motivation dafür ist, dass die Berücksichtigung von behinderten Schrumpfdehnungen von Beton die *Struktur*steifigkeit und -festigkeit von Betongelenken zwar reduziert, der Einblick in die *Material*schädigung von Beton aber stark limitiert bleibt. Es stellt sich die Frage nach der Korrelation von materiellem Steifigkeits- und Festigkeitsverlust von Beton durch behinderte Schrumpfdehnungen. Zu diesem Zweck wird ein unlängst entwickeltes Mehrskalenmodell zur Beschreibung der Zugfestigkeit und der Zugentfestigung von Beton angewendet [13]. Als Schädigungsvariable dient dabei der physikalisch interpretierbare Rissdichteparameter nach Budiansky und O'Connel [4]. Zuerst wird der Zusammenhang zwischen Schädigungsvariable und Materialsteifigkeit betrachtet, um den Rissdichteparameter zu identifizieren. Davon ausgehend wird die Abminderung der Zugfestigkeit von Beton quantifiziert. Schließlich wird noch beachtet, dass schrumpfungsinduziere Rissbildung zu Energiedissipation führt, was die verbleibende Bruchenergie reduziert. Sie wird ebenfalls quantifiziert. Im Anschluss wird gezeigt, dass es gleichwertig ist, entweder Schrumpfdehnungen in Form von Eigendehnungen vorzuschreiben oder im Rahmen einer alternativen Vorgangsweise

reduzierte Eingabewerte für den Elastizitätsmodul, die Zugfestigkeit und die Bruchenergie vorzuschreiben.

Anhand der vorgenommenen Struktursimulationen lassen sich folgende Schlussfolgerungen ziehen.

- Belastet man Betongelenke verschiebungsgesteuert bis zur Traglast und darüber hinaus, ist ein für baupraktische Zwecke sehr gutmütiges Verhalten zu erwarten. Beim Erreichen der Traglast werden Betongelenke nämlich sehr nachgiebig, was zu signifikant anwachsenden Relativdrehwinkeln führt, wohingegen die Belastbarkeit nur unwesentlich absinkt.

- Eine wesentliche Ursache für dieses Verhalten ist das gutmütige Druckversagen von Beton an der Oberfläche im innersten Bereich des Gelenkshalses. Die Gelenkshalswurzel ist nämlich eine der Luft ausgesetzte *freie Oberfläche* des Betongelenks. Daher liegt dort ein *ebener* Spannungszustand vor. Die oberflächliche Betonschichte wird daher auf *biaxialen* Druck beansprucht. Die biaxiale Druckfestigkeit ist aber nur unwesentlich größer als die einaxiale Druckfestigkeit und somit wesentlich kleiner als die triaxiale Festigkeit von Beton. Daher wird die oberflächliche Betonschichte bereits auf Gebrauchslastniveau ihre Festigkeit erreichen. Obwohl bei weiterer Belastungssteigerung die Dehnungen der Oberflächenschichte wesentlich zunehmen, platzt die Oberflächenschichte aber ganz offensichtlich nicht ab. Nur dadurch ist es möglich, dass sich *hinter* der Oberflächenschichte (im Volumen des Betongelenks) ein triaxialer Druckspannungszustand aufbaut, der hohe Materialfestigkeiten zur Folge hat. Würde die Oberflächenschichte nämlich abplatzen, dann würde die dahinter liegende Schichte, die anfänglich im Volumen des Betongelenks positioniert war, zur neuen Oberfläche werden. Aufgrund der beschriebenen Oberflächenrandbedingung würde diese Schichte nicht mehr triaxial sondern nur mehr biaxial auf Druck beansprucht sein, die Festigkeit würde wesentlich absinken, und somit wäre auch die neue Oberflächenschichte überlastet, was dazu führen würde, dass auch sie abplatzt. Damit würde sich ein katastrophaler Dominoeffekt ergeben, nämlich das progressive Ausbreiten der Abplatzungsfront von der Gelenkshalswurzel in Richtung der Betongelenksmitte.

- Diese Schlussfolgerung legt nahe, bei zukünftigen Betongelenken über eine konstruktive Lösung zum Abplatzungsschutz der auf Druck beanspruchten Gelenkshalswurzel nachzudenken.

Abstract

Concrete hinges experience a renaissance, because the past decades have provided practical evidence that they are durable structural elements, but the functionality of concrete hinges remains to a considerable extent an enigma. This provides the motivation to gain further insight into the structural behavior of concrete hinges, based on nowadays-available experimental and theoretical methods. The present master thesis focuses on the numerical re-analysis of recently performed centric and eccentric compression tests on concrete hinges, based on nonlinear Finite Element (FE) simulations carried out with concrete model "CC3DNonLinCementitious2" and the software ATENA science 5.1. FE simulations based on default material parameters, related to the measured Young's modulus and to the measured cube compressive strength of concrete, significantly overestimate the experimentally observed structural stiffness and ultimate load carrying capacity of concrete hinges. Consideration of concrete shrinkage and of a more moderate strengthening of concrete under triaxial compression allows for a qualitatively and quantitatively satisfactory reproduction of experimental measurements. In addition, a recently developed multiscale model for tensile strength and softening of concrete is used to quantify damage of concrete resulting from shrinkage strains restrained by the two connected reinforcement cages. The FE simulations underline that concrete hinges exhibit a structural behavior which is very beneficial for structural applications. Close to the ultimate load carrying capacity, rotation angles increase significantly, while the strength of the structure is almost constant. This results from the rather ductile behavior of concrete forming the surface at the innermost region of the neck, where a biaxial compressive stress state prevails. Only because this concrete surface layer remains in place (no spalling), a triaxial compressive stress state can build up behind the surface layer, i. e. inside the volume of the neck. The resulting confinement pressure increases the strength of concrete considerably, and this explains the unexpected large load carrying capacity of concrete hinges.

Contents

List of symbols and abbreviations

List of Greek symbols and abbreviations

	direction of plastic flow ($= 0 \ldots$ purely deviatoric plastic strains)
ΔG_f	*fracture energy, dissipated due to shrinkage-induced cracking*
ϵ_c^p	*plastic strain* at uniaxial compressive strength
λ_t	*ratio of tensile strength of Menétrey-Willam failure surface to the tensile strength of Rankine criterion*
ν	*Poisson's ratio*
ν_c	*Poisson's ratio* of sane concrete
σ_y	von Mises *yield stress* of steel
ω	*dimensionless crack density* parameter [13]
ω_s	*dimensionless crack density* parameter, due to shrinkage-induced cracking

List of Latin upper case symbols and abbreviations

E	*Young's modulus*
E_c	*Young's modulus* of sane concrete
$E_{c,dam}$	*Young's modulus* of damaged concrete
$Fixed$	*control of crack rotation* ($Fixed = 1 \ldots$ no crack rotation)
G_f	*fracture energy*
K_{Ic}	*fracture toughness*
M	bending *moment*
N	axial *normal force*

List of Latin lower case symbols and abbreviations

a	*neck width*
a_g	maximum *aggregate size*
b_R	*size of front-side notch*
c	*hardening/softening parameter*
c_1, c_2	*constants* intervening in the crack opening law by Hordijk [14]
c_{ini}	*initial value of* c
e	*eccentricity* of the axial force
e_σ	*eccentricity* of the Menétrey-Willam failure surface in the deviatoric plane
f_c	uniaxial *compressive strength*
f_{c0}	initial *elastic limit* under uniaxial compression
f'_c	evolving elastic limit of concrete under uniaxial compression used for the Menétrey-Willam failure surface
f_{ck}	characteristic *compressive cylinder strength* of concrete at 28 days
$f_{c,cube}$	mean value of *cube compressive strength*
$f_{ck,cube}$	characteristic value of *cube compressive strength*
f_t	uniaxial *tensile strength*
f'_t	uniaxial *tensile strength* used for the Menétrey-Willam failure surface
$f_{t,dam}$	damaged *tensile strength*
m	*dimensionless eccentricity* $m = e/a$
m_a	*mass of aggregates*
m_c	*mass of cement*
m_w	*mass of water*
r_c	*compressive strength reduction*, due to cracks with normal orthogonal to the loading direction
w	*crack opening* displacement
w_c	*value of* w at the complete release of stress
w_s	*value of* w due to shrinkage-induced cracking
w_d	*critical compression displacement*

Chapter 1

Introduction

Concrete hinges are un-reinforced or marginally reinforced necks in beam-like or column-like reinforced concrete structures. Typically, a few pairs of crossed steel rebars run across a concrete hinge, and the cross-over point is at the center of the neck. Therefore, the bending stiffness of the neck is significantly smaller than the one of the full beam or column cross-section. This results in a desired concentration of bending deformations at the concrete hinge. In addition, it is part of the structural concept, that concrete hinges exhibit bending-induced tensile cracking even under regular service loads. Cracking further reduces the bending stiffness of the neck, and this further promotes the ability of a concrete hinge to develop desired relative rotation angles. The large rotation ability of concrete hinges is evidenced by several test series see, e. g. [11, 17, 24, 26].

Concrete hinges were invented before world war II by Eugène Freyssinet, and they enjoyed great popularity after the war. In the 1960s, Leonhardt [17] developed pioneering design guidelines for concrete hinges, see also the reformulation of these guidelines in the nomenclature of modern European design standards by Marx [18]. Anyway, decades-long durability of concrete hinges remained questionable at the end of the 1960s. Therefore, the civil engineering community decided to gain practical experience from quasi-continuous monitoring of existing structures. Now, more than five decades later, there is plenty of practical evidence that concrete hinges indeed provide the expected long-term durability associated with reliable services and small costs for maintenance and repair. Therefore, concrete hinges experience a renaissance in practical engineering, particularly so in integral bridge construction, see, e. g. [23, 27, 21].

Nowadays, several powerful software products for the numerical simulation of reinforced concrete structures are commercially available. This provides motivation for the present basic-research contribution, where we re-analyze a recently performed testing se-

ries on reinforced concrete hinges [24] using the nonlinear Finite Element program ATENA science [7]. Our goal is to further deepen the available insight into the structural behavior of concrete hinges, whereby particular attention is paid to the questions regarding (i) the triaxiality of compressive stress states in the neck region, (ii) the initial extensional and bending stiffness of the neck, (iii) the structural behavior of concrete hinges under eccentric compression right up to the load carrying capacity, (iv) the damaging effect of concrete shrinkage both on the stiffness and on the tensile strength of concrete, and (v) the functionality of front-side notches.

Nonlinear Finite Element simulations and the interpretation of their results are the main original contributions. At first, numerical simulations of concrete hinges will be based on measured mechanical properties of concrete and on default inputs of ATENA science. Corresponding two-dimensional plane strain simulations will be used to quantify the triaxiality of compressive stress states in the neck region. Results from three-dimensional simulations, in turn, will be compared with measurements from structural testing. Subsequently, the Finite Element model will be further improved, whereby special attention will be paid to shrinkage of concrete and to the strengthening of the material resulting from the confinement pressure of triaxial compressive stress states. In order to quantify the damaging effects of partly restrained shrinkage strains both on the stiffness and on the tensile strength of concrete, a recently developed multiscale material model for tensile failure of concrete [13] will be adopted. The corresponding dimensionless damage variable will be used to relate the damaged stiffness to the damaged tensile strength of concrete, leading to multiscale structural analysis of concrete hinges. Finally, the functionality and usefulness of front-side notches will be studied based on simulated stress distributions in a concrete hinge without front-side notches.

The present master thesis is structured as follows. The recently performed experiments on concrete hinges, are briefly summarized in Chapter 2. They represent target values for nonlinear Finite Element simulations documented in Chapter 3, containing (i) nonlinear Finite Element simulations based on measured mechanical properties of concrete and on default inputs of ATENA science, (ii) the improvement of the model regarding shrinkage and the triaxial compressive strength of concrete, as well as (iii) a micromechanical approach, to damage induced by shrinkage. This leads to a discussion, including the usefulness of front-side notches, see Chapter 4. Conclusions are drawn in Chapter 5.

Chapter 2

Experimental data from testing of concrete hinges, taken from [24]

In the sequel, we revisit experimental results from [24], which serve as desired target values for Finite Element analyses. This includes information on the used materials (Section 2.1), on the geometric dimensions of the tested concrete hinges (Section 2.2), on the test setup (Section 2.3), as well as test results from centric compression up to 200 kN (Section 2.4), from eccentric compression with eccentricity $e = 20\,\text{mm}$ and loading up to 200 kN (Section 2.5), as well as compression with eccentricity $e = 25\,\text{mm}$ and loading up to the load carrying capacity (Section 2.6). Notably, compression is considered with a positive sign throughout the entire work.

2.1 Materials: concrete and steel rebars

The three tested concrete hinges consisted of steel-reinforced concrete. Concrete C35/45 F45 GK16 B5 was produced with a commercial CEM II/A-L 42.5N cement, Viennese tab water, and calcitic aggregates with a maximum size of 16 mm. The initial water-to-cement mass ratio m_w/m_c amounted to

$$m_w/m_c = 0.48\,. \tag{2.1}$$

The initial aggregate-to-cement mass ratio m_a/m_c was equal to

$$m_a/m_c = 3.97\,. \tag{2.2}$$

Cube compressive strength $f_{c,cube}$ and Young's modulus E were determined 28 days after production, following Austrian standards for testing of concrete [25]; resulting in [24]

$$f_{c,cube} = 56.25\,\text{MPa}\,, \qquad E = 34.75\,\text{GPa}\,. \tag{2.3}$$

As for the steel rebars, steel quality BSt 550 was chosen. It exhibits an expected value of the von Mises yield stress σ_y amounting to

$$\sigma_y = 605\,\text{MPa}\,. \tag{2.4}$$

2.2 Geometric dimensions of the tested concrete hinges and arrangement of steel reinforcements

The three tested concrete hinges complied with the design guidelines of Leonhardt [17]. They exhibited an overall width of 25 cm, a height of 35 cm, and a depth of 40 cm, see Fig. 2.1. Side notches were 8.75 cm deep, and front notches 5 cm (Fig. 2.1), such that the cross-section of the neck amounted to $7.5 \times 30\,\text{cm}^2$. The top and bottom 2 centimeter of the concrete hinges were made of steel plates, ensuring effective distribution of concentrated external line loads. The top and bottom reinforcement cages were connected by three pairs of crossed steel rebars, with cross-over points right at the center of the neck, see Fig. 2.1.

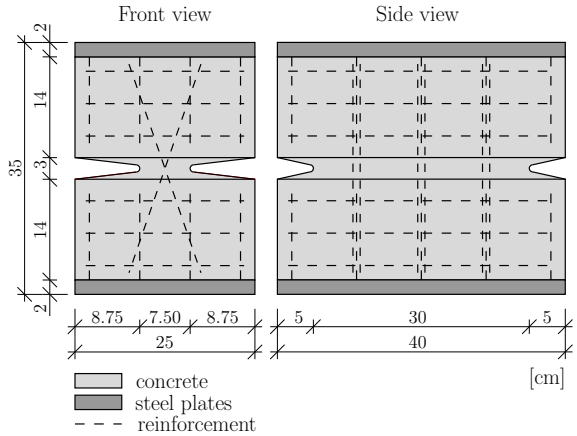

Figure 2.1: Geometric dimensions of the tested concrete hinges and arrangement of steel reinforcements; after [24]

2.3 Test setup and displacement measurement equipment

During testing, the three nominally identically concrete hinges were subjected to line loads distributed along the entire concrete hinge in thickness direction (Fig. 2.2). As for displacement quantification, Linear Variable Displacement Transducers were mounted to the side surfaces of the concrete hinges. They measured changes of the notch mouth opening displacements of the lateral notches.

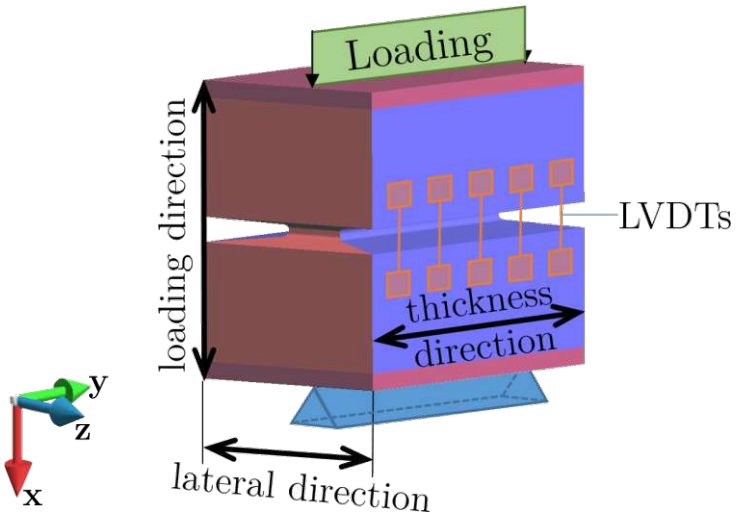

Figure 2.2: Definition of coordinate system: x denotes the loading direction, y the thickness direction, and z the lateral direction; schematic illustration of loading and support conditions as well as of displacement sensors (LVDT) positions

2.4 Centric compression up to 200 kN

In order to characterize the undamaged extensional stiffness of the neck region, centric compression tests were carried out. Three nominally identical concrete hinges were subjected, one after the other, with a loading speed of 5 kN/s, to 200 kN. The three 40 second compression tests delivered very similar results, underlining satisfactory test repeatability (Fig. 2.3). The measured force-shortening relationships are virtually linear, and the shortening of the neck at 200 kN amounted to some 35 μm (Fig. 2.3).

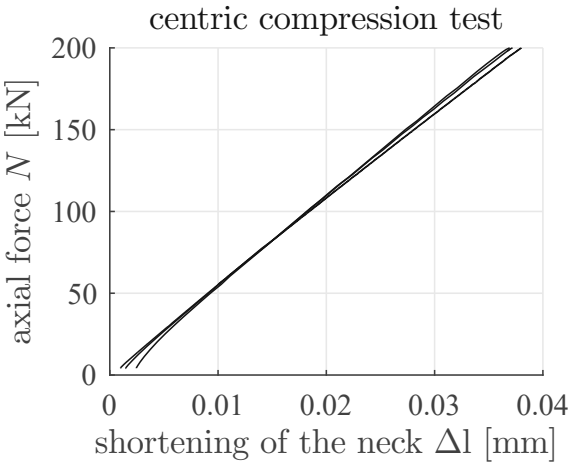

Figure 2.3: Shortening of the neck region of three nominally identical concrete hinges (Fig. 2.1 and 2.2), measured in centric compression tests; loading was increased with a force rate of 5 kN/s; experimental data after [24]

2.5 Eccentric compression up to 200 kN ($e = 20\,$mm)

In order to characterize the undamaged bending stiffness of the neck region, eccentric compression tests were carried out with a loading speed of 5 kN/s. The eccentricity

$$e = 20\,\text{mm} \tag{2.5}$$

was chosen such that no significant bending-induced tensile cracking is to be expected when increasing the loading up to 200 kN. Eccentric compression, namely, is a combined compression–bending test, with a bending moment M which is at any time t proportional to the applied normal force N

$$M(t) = N(t) \cdot e\,. \tag{2.6}$$

The 40 second tests on three nominally identical concrete hinges delivered very similar results, underlining satisfactory test repeatability (Fig. 2.4). The measured force-rotation relationships are virtually linear, and the rotation angle of the neck at 200 kN amounted to some 0.75 mrad (Fig. 2.4).

2.6 Eccentric compression up to the load carrying capacity ($e = 25\,$mm)

In order to characterize the structural behavior up to the load carrying capacity of the three nominally identical concrete hinges (Fig. 2.1 and 2.2), eccentric compression tests were carried out. The eccentricity

$$e = 25\,\text{mm} \tag{2.7}$$

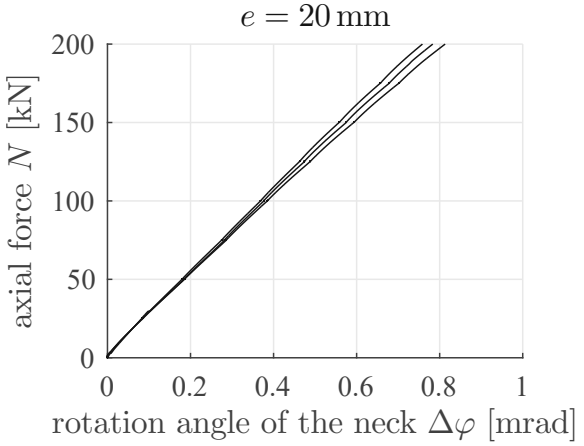

Figure 2.4: Rotation angles of three nominally identical concrete hinges (Fig. 2.1 and 2.2), measured in eccentric compression tests with eccentricity $e = 20\,\mathrm{mm}$; loading was increased with a force rate of $5\,\mathrm{kN/s}$; experimental data after [24]

was chosen to be equal to one third of the neck width

$$a = 75\,\mathrm{mm}\,, \tag{2.8}$$

representing the largest eccentricity which may be analyzed based on the design guidelines of Leonhardt [17]. Loading was controlled manually. After an initially linear behavior, rotation angles increased superlinearly with increasing loading. Once rotation angles reached some 15 mrad, the structural behavior was apparently ductile with significantly increasing rotation angles, while the loading could not be increased significantly any more (Fig. 2.5). The load carrying capacity was equal to some 700 kN, and this is related to a nominal bending moment amounting to some 17.5 kNm, see Eqs. (2.6) and (2.7).

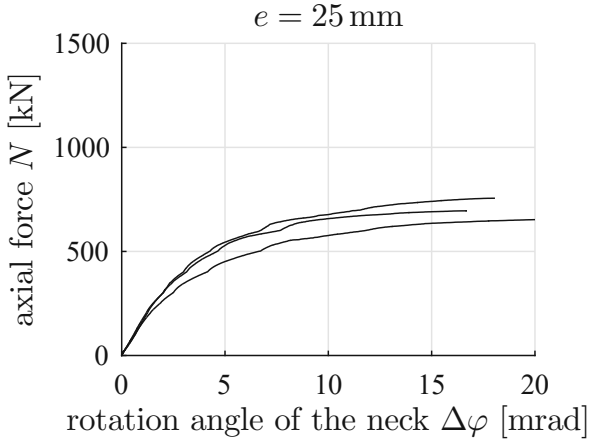

Figure 2.5: Rotation angles of three nominally identical concrete hinges (Fig. 2.1 and 2.2), measured in eccentric compression tests with eccentricity $e = 25\,\mathrm{mm}$; loading was increased manually; experimental data after [24]

Chapter 3

Finite Element Simulations of the tested concrete hinges

Geometric linear Finite Element (FE) Simulations are performed with ATENA science (version 5.1), with the aim to gain insight into the structural behavior of concrete hinges based on quantification of stress states *inside* their volume, which are typically inaccessible in experimental testing. In order to reproduce the experimental observations described in Chapter 2, the FE simulations are based on *expected values* of all material properties, i. e. the simulation option "Safety Format: mean" is chosen.

As for modeling of concrete, the nonlinear material model "CC3DNonLinCementitious2" is used, because it allows for performing both two-dimensional *and* three-dimensional simulations. "CC3DNonLinCementitious2" models the inelastic material behavior of concrete based on two failure surfaces: a Rankine surface for the description of tension induced failure, and a Menétrey-Willam failure surface [5, 6, 7, 19] for compression-induced failure. The mathematical formulation of the latter is based on hydrostatic stress ξ, deviatoric stress ρ, as well as Lode angle θ, and it reads as follows

$$F_{3P}^{p}\left(\xi,\rho,\theta\right)=\frac{3}{2}\cdot\frac{\rho^{2}}{{f_{c}'}^{2}}+\frac{m}{f_{c}'}\cdot\quad\rho\cdot\frac{r(\theta)}{\sqrt{6}}+\frac{\xi}{\sqrt{3}}\Bigg)\Bigg(-c=0\,, \tag{3.1}$$

where m/f_c' is defined as

$$\frac{m}{f_{c}'}=\frac{3\cdot e_{\sigma}}{e_{\sigma}+1}\cdot\frac{1-\left(\frac{f_{t}'}{f_{c}'}\right)^{2}}{f_{t}'}\,, \tag{3.2}$$

and where $r(\theta)$ is defined as

$$r(\theta)=\frac{4\cdot\left(1-e_{\sigma}^{2}\right)\cdot\cos\left(\theta\right)^{2}+\left(2\cdot e_{\sigma}-1\right)^{2}}{2\cdot\left(1-e_{\sigma}^{2}\right)\cdot\cos\left(\theta\right)+\left(2\cdot e_{\sigma}-1\right)\cdot\sqrt{\Bigg(4\cdot\left(1-e_{\sigma}^{2}\right)\cdot\left(\cos\left(\theta\right)\right)^{2}+5\cdot{e_{\sigma}}^{2}-4\cdot e_{\sigma}}}\,. \tag{3.3}$$

In Eq. (3.1), c denotes the hardening/softening parameter [7], with initial value

$$c_{ini} = 1\,. \tag{3.4}$$

In Eqs. (3.2) and (3.3), e_σ denotes the so-called eccentricity of the failure surface in deviatoric planes; and its default value amounts to

$$e_\sigma = 0.52\,. \tag{3.5}$$

In Eqs. (3.1) and (3.2), f_c' denotes the evolving elastic limit stress of concrete under uniaxial compression. The corresponding initial value, denoted as f_{c0}, represents a required input value for the material model. Because of strain hardening, f_c' will increase until the uniaxial compressive strength f_c is reached. The latter is another required input value for the material model. Also in Eqs. (3.1) and (3.2), f_t' denotes the uniaxial tensile strength predicted by the Menétrey-Willam failure surface. Because of the combination with the Rankine criterion, f_t' is a *fictitious* tensile strength value, without real mechanical relevance in tension.

3.1 Default input values related to the measured stiffness and strength of concrete

While the only measured mechanical properties of concrete are the cube compressive strength $f_{c,cube}$ and the Young's modulus E, see Eqs. (2.3), the chosen material model requires more than ten numerical input values, see Table 3.1. Notably, ATENA science provides recommended default values for all input quantities which were not directly measured. Several of these default values depend on the compressive strength, which is generally a known quantity in concrete engineering. For instance, the relation between the cube compressive strength $f_{c,cube}$ and the uniaxial compressive strength f_c reads as

$$\begin{aligned} f_{ck,cube} &= f_{c,cube} - 8\,\mathrm{MPa}\,, \\ f_{ck} &= 0.85 \cdot f_{ck,cube}\,, \\ f_c &= f_{ck} + 8\,\mathrm{MPa}\,, \end{aligned} \tag{3.6}$$

where index k denodes *characteristic* strength values, i. e. intentionally decreased strength values for semiprobabilistic design calculations. The relation between the uniaxial compressive and tensile strength values is adopted from the Model Code [12] and Eurocode 2 [2]. For concrete with $f_{ck} \leq 50\,\mathrm{MPa}$, as in the present case, it reads as

$$f_t = 0.30 \cdot f_{ck}^{2/3}\,, \tag{3.7}$$

where both strength values need to be inserted in MPa. The ratio between the actual uniaxial tensile strength f_t, intervening in the Rankine criterion, and the *fictitious* tensile strength of the Menétrey-Willam failure surface reads as

$$\lambda_t = \frac{f_t'}{f_t} \tag{3.8}$$

where $\lambda_t = 2$ is the corresponding default input value, see Table 3.1 for all default input values obtained with the cube compressive strength $f_{c,cube}$ and the Young's modulus E from Eqs. (2.3).

Table 3.1: Default input values of concrete model "CC3DNonLinCementitious2" of ATENA science, related to cube compressive strength $f_{c,cube}$ and to Young's modulus E from Eqs. (2.3) as well as to the maximum aggregate size amounting to $a_g = 0.016\,\mathrm{m}$

description	name	value, unit
Young's modulus	E	34750 MPa
Poisson's ratio	ν	0.2
uniaxial tensile strength	f_t	3.57 MPa
uniaxial compressive strength	f_c	49 MPa
fracture energy	G_f	147 J/m^2
critical compression displacement	w_d	0.5 mm
eccentricity of the Menétrey-Willam failure surface	e_σ	0.52
direction of plastic flow ($= 0 \ldots$ purely deviatoric plastic strains)		0
elastic limit under uniaxial compression	f_{c0}	7.49 MPa
plastic strain at uniaxial compressive strength	ϵ_c^p	$1.24 \cdot 10^{-3}$
control of crack rotation ($Fixed = 1 \ldots$ no crack rotation)	$Fixed$	1
compressive strength reduction from cracks with normal orthogonal to the loading direction	r_c	0.8
maximum aggregate size	a_g	0.016 m
ratio of tensile strength of Menétrey-Willam failure surface to the tensile strength of Rankine criterion	λ_t	2

3.2 Quantification of stress triaxiality in the neck region based on 2D plane strain simulations

2D plane strain simulations are relevant for the midplane of the concrete hinges, with plane-normal pointing in thickness direction. The width of the neck ($a = 7.5\,\text{cm}$), namely, is by a multiplicative factor of 4 smaller than the dimension of the neck in thickness direction (30 cm). In other words, the real strain state in the midplane must be close to a plane strain state.

The used FE mesh consists of 26400 quadrilateral Finite Elements with bilinear displacement interpolation, 26885 nodes, and 53770 degrees of freedom, see Fig. 3.1. This FE mesh was the result of a study regarding mesh dependency [15]. While coarser meshes resulted in FE results depending on the discretization fineness, finer meshes delivered objective results, i. e. the used mesh represents a close-to-optimal trade-off between simulation effort and reliability of numerical results.

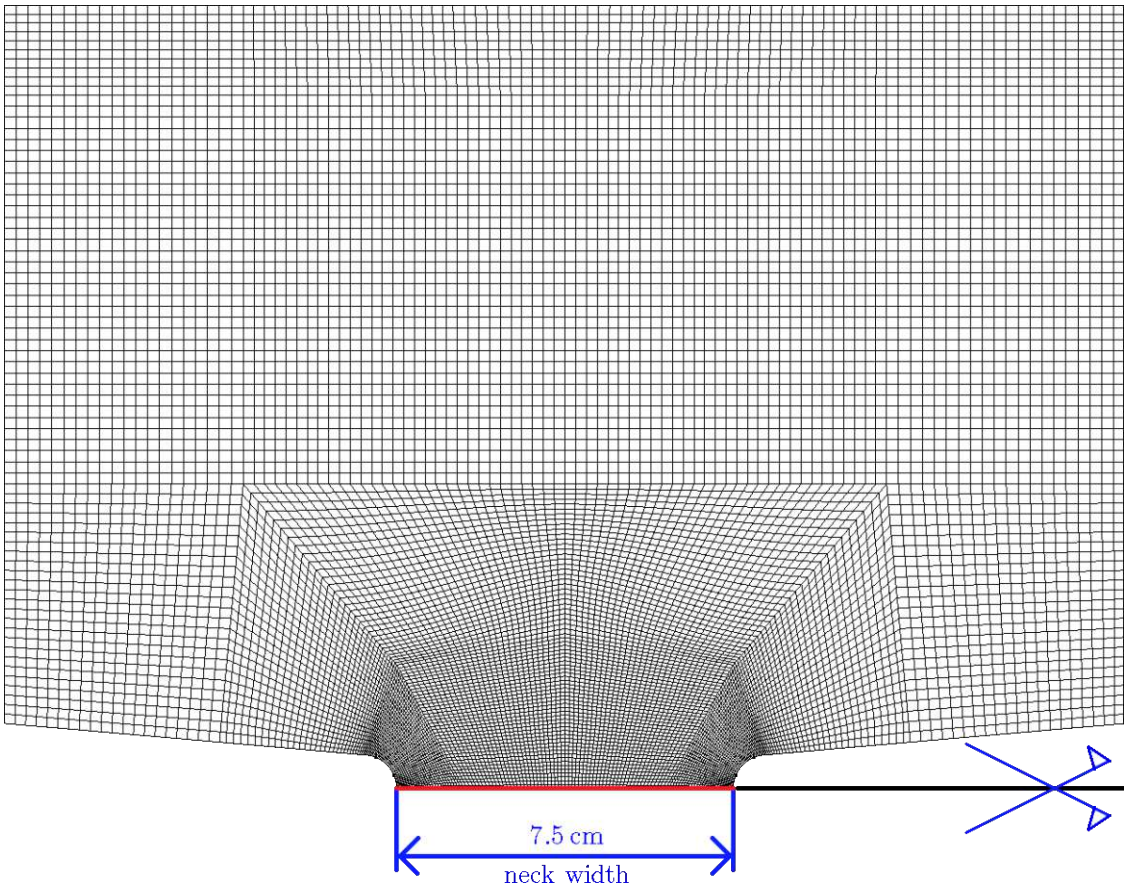

Figure 3.1: Upper half of two-dimensional Finite Element mesh consisting of 26400 quadrilateral Finite Elements with bilinear displacement interpolation, 26885 nodes, and 53770 degrees of freedom; used for plane strain simulations of eccentric compression tests

As for the re-analysis of the tests used to quantify the load carrying capacities of the concrete hinges, eccentric compression with eccentricity $e = 25\,\text{mm}$ is simulated, based on input values listed in Table 3.1. Loading is increased in load increments of $0.5\,\text{kN/cm}$, such that after 70 successive load steps a simulated load of $35\,\text{kN/cm}$ is reached. Stress distributions are evaluated along the 7.5 cm wide neck, see the red line in Fig. 3.1. Principal stress states prevail along this line, given that the line coincides with the intersection of two planes of symmetry of the concrete hinge, see Figs. 3.2, 3.3, and 3.4 for the distribution of principal stresses acting in loading direction, in lateral direction, and in thickness direction, respectively. The simulation steps are well converged, as quantified by the following convergence errors: the *Residual Error* amounts to $1.4 \cdot 10^{-3}$ (default threshold: $1 \cdot 10^{-2}$), the *Absolute Residual Error* amounts to $5.5 \cdot 10^{-4}$ (default threshold: $1 \cdot 10^{-2}$), the *Displacement Error* amounts to $3 \cdot 10^{-4}$ (default threshold: $1 \cdot 10^{-2}$) the *Energy Error* amounts to $2.6 \cdot 10^{-7}$ (default threshold: $1 \cdot 10^{-4}$).

Considerable compressive stresses are limited to one half of the neck width (Figs. 3.2, 3.3, and 3.4). This is consistent with Leonhardt's design guidelines [17], which assume that tension-induced cracking will happen along half of the neck width, provided that the eccentricity-to-neck width ratio e/a amounts to $1/3$, as in the simulated case with $e = 25\,\text{mm}$ and $a = 75\,\text{mm}$. The compressive stresses, in turn, show nonlinear distributions, i. e. they increase with increasing distance from the center of the concrete hinge, but close to the lateral surface, they decease again. Normal stresses in lateral direction even decrease down to zero at the lateral surface of the neck (Fig. 3.4), because of the corresponding free-surface boundary condition. Still, at larger load intensities, the stress distributions in loading direction is somewhat reminiscent of a triangular distribution (Fig. 3.2), such as considered by the design guidelines of Leonhardt [17]. The largest compressive normal stresses, obtained with the external load intensity of $35\,\text{kN/cm}$, amount to 224 MPa, 104 MPa, and 64 MPa in loading direction, in thickness direction, and in lateral direction, respectively (Fig. 3.2, 3.3, and 3.4). In other words, concrete hinges exhibit pronouncedly triaxial compressive stress states with principal stress ratios amounting approximately to $1 : 0.5 : 0.\dot{3}$. This implies that the isotropic ("hydrostatic") part of the stress state amounts to some 60 % of the compressive normal stress in loading direction. This confinement results in a significant strengthening of concrete, and this explains why concrete hinges are very durable structures, even through stress levels under regular service conditions are larger than tolerated stress levels in bridges or high-rise buildings.

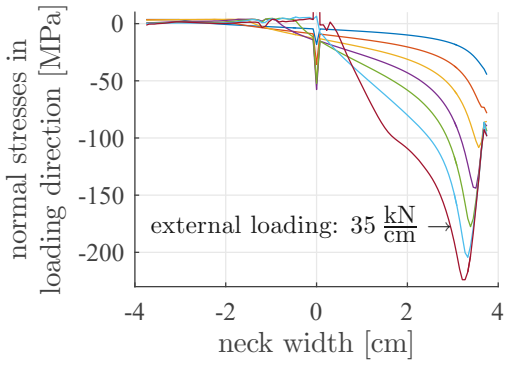

Figure 3.2: Normal stresses in loading direction across the neck width of the concrete hinge, as quantified by two dimensional plane strain FE simulations with mesh according to Fig. 3.1 and ATENA science input quantities listed in Table 3.1, the seven graphs refer to external load intensities increased in steps of 5 kN/cm

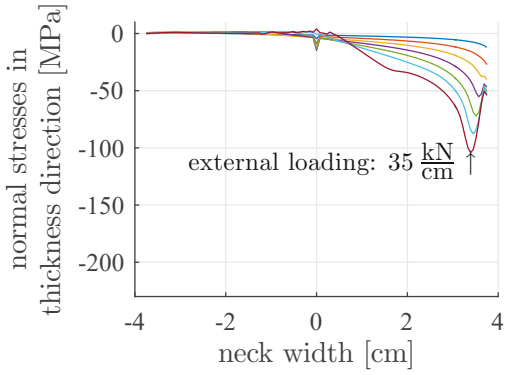

Figure 3.3: Normal stresses in thickness direction across the neck width of the concrete hinge, as quantified by two dimensional plane strain FE simulations with mesh according to Fig. 3.1 and ATENA science input quantities listed in Table 3.1, the seven graphs refer to external load intensities increased in steps of 5 kN/cm

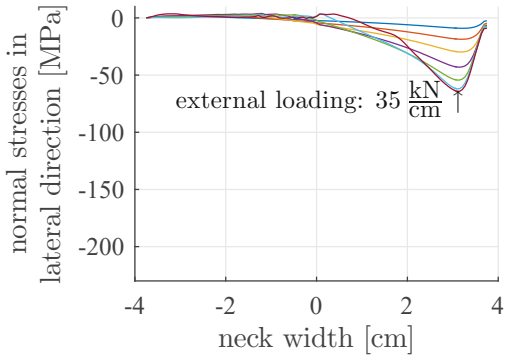

Figure 3.4: Normal stresses in lateral direction across the neck width of the concrete hinge, as quantified by two dimensional plane strain FE simulations with mesh according to Fig. 3.1 and ATENA science input quantities listed in Table 3.1, the seven graphs refer to external load intensities increased in steps of 5 kN/cm

3.3 3D FE simulations of centric and eccentric compression tests

In order to gain further improved insight into the behavior of the tested concrete hinges, three-dimensional FE simulations are carried out. Considering the double symmetry of the problem, it is sufficient to discrete one fourth of the structure (Fig. 3.5). The used FE mesh consists of 27776 four-noded hexahedra elements using trilinear displacement interpolation, 31730 nodes, and 95190 degrees of freedom (Fig. 3.5). Again, this mesh was the result of a study regarding discretization errors, i. e. it represents a close-to-optimal trade-off between simulations effort and reliability of simulation results.

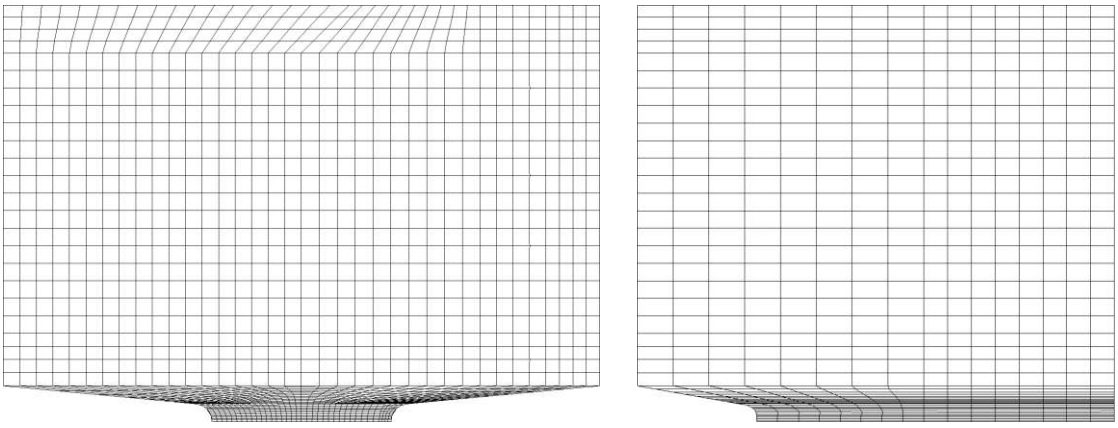

Figure 3.5: Three-dimensional Finite Element mesh discretizing one fourth of the studied concrete hinges; the mesh consists of 27776 hexahedra Finite Elements with trilinear displacement interpolation, 31730 nodes, and 95190 degrees of freedom

The simulation of the centric compression test described in Section 2.4 delivers numerical results which are qualitatively similar to experimental observations, i. e. the shortening of the neck region increases virtually linearly with increasing loading (Fig. 3.6). The extensional stiffness of the undamaged concrete hinge, however, is quantitatively overestimated by some 40 %.

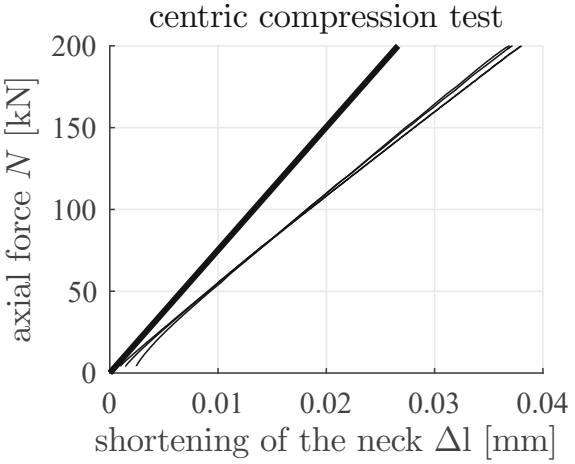

Figure 3.6: Comparison of (i) numerical results of 3D FE simulation obtained with the mesh shown in Fig. 3.5 as well as with input parameters listed in Eqs. (2.3) and Table 3.1 (thick line) with (ii) measurements from centric compression tests (thin lines)

The simulation of the eccentric compression test with an eccentricity of $e = 20\,\text{mm}$ and loading up to 200 kN (Section 2.5) also reproduces experimental observations in a qualitatively similar fashion (Fig. 3.7). The rotation angle of the concrete hinge increases virtually linearly with increasing loading. Still, the bending stiffness of the undamaged concrete hinge is overestimated by some 40 %.

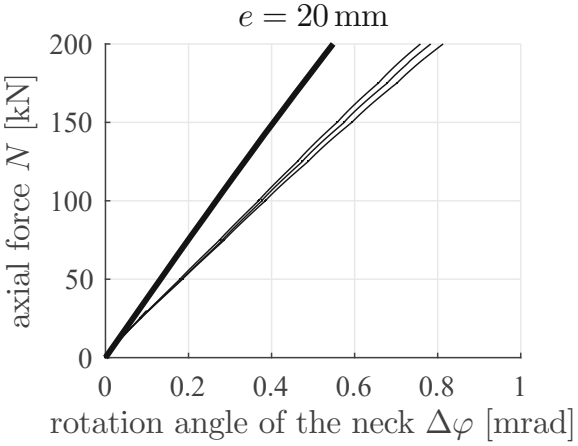

Figure 3.7: Comparison of (i) numerical results of 3D FE simulation obtained with the mesh shown in Fig. 3.5 as well as with input parameters listed in Eqs. (2.3) and Table 3.1 (thick line) with (ii) measurements from eccentric compression tests with $e = 20\,\text{mm}$ (thin lines)

The simulation of the eccentric compression test with eccentricity $e = 25\,\text{mm}$ and loading up to the load carrying capacity (Section 2.6) reproduces experimental observations again in a qualitatively satisfactory fashion. The rotation angle first increases linearly

and later superlinearly with increasing loading (Fig. 3.8). However, the simulated initial bending stiffness and the simulated load carrying capacity overestimates corresponding experimental observations by some 40 and 100 %, respectively.

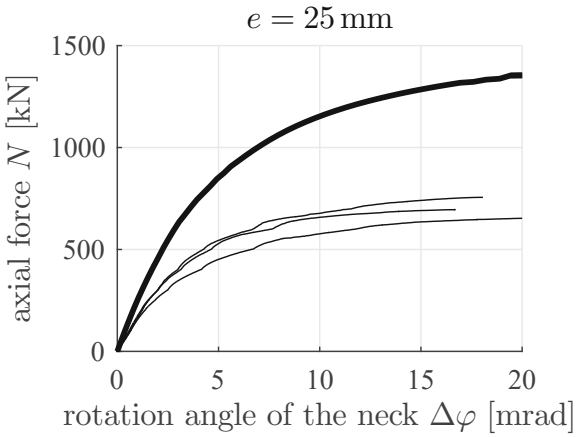

Figure 3.8: Comparison of (i) numerical results of 3D FE simulation obtained with the mesh shown in Fig. 3.5 as well as with input parameters listed in Eqs. (2.3) and Table 3.1 (thick line) with (ii) measurements from eccentric compression tests with $e = 25\,\text{mm}$ (thin lines)

3.4 Which essential mechanical features need to be considered in order to obtain also quantitatively reliable simulation results?

The obtained simulation results underline that FE simulations based on measured values of cube compressive strength and Young's modulus of concrete as well as on default values of Atena science (Table 3.1) do not delivery quantitatively reliable results, but structural stiffness and strength are significantly overestimated. Consequently, mechanical features which are significantly influencing the structural performance of concrete hinges have remained unconsidered. In the sequel, it is checked whether or not the differences between FE simulation results and experimental observations can be explained based on damage resulting from shrinkage of concrete and based on the potential overestimation of the strengthening effect resulting from the confinement of highly triaxial compressive stress states.

Shrinkage of concrete is restrained by the reinforcement of the concrete hinges, because the upper and lower reinforcement cages are connected by three pairs of rebars. Therefore, increasing shrinkage of concrete results in tensile stresses of concrete and in compression of the crossed reinforcement bars. Once tensile stresses in concrete reach

the tensile strength, shrinkage-induced cracking occurs. Notably, shrinkage increases typically proportionally to hydration degree, such that the advanced maturity of concrete after 28 days renders it likely that the tested concrete hinges suffered from significant shrinkage-induced damage. This will be investigated in Section 3.5.

Under the strong confinement of triaxial compressive stress states with principal normal stress ratios amounting to $1 : 0.5 : 0.\dot{3}$, ATENA science predicts a maximum principal compressive stress at failure which amounts to 6.9 times the unconfined uniaxial compressive strength. In this context, it is noteworthy that typical applications of FE software for reinforced concrete structures are beams and columns as well as plates and shells; and these structures exhibit either predominantly uniaxial or predominantly biaxial stress states. In other words, numerical simulations of standard civil engineering structures challenge the Menétrey-Willam failure surface in the vicinity of the uniaxial and the biaxial compressive strength, but the regime of *triaxial* compressive stress states remains untested. While this underlines that simulation of the structural behavior of concrete hinges is a particularly challenging task, one may also speculate that confinement-induced strengthening of concrete is overestimated by the default Menétrey-Willam failure surface. This will be investigated in Section 3.6.

3.5 Sensitivity analysis regarding shrinkage of concrete

The following sensitivity analysis regarding shrinkage consists of extending the FE analysis described in Section 3.1 by first simulation steps in which shrinkage of concrete is prescribed in terms of eigenstrains. Since concrete shrinkage was, unfortunately, not measured in the experiments of Chapter 2, the influence of *different* shrinkage intensities on the simulated structural behavior is studied. To this end, each one of the two FE simulations providing insight into the extensional stiffness and the bending stiffness of concrete hinges, is repeated four times, with shrinkage-related eigenstrains amounting to 0.15 ‰, 0.30 ‰, 0.45 ‰, and 0.60 ‰, respectively. This result in eight additional FE simulations which are based on the default input values listed in Table 3.1.

Simulation results suggest that increasing initial shrinkage of concrete decreases the initial stiffness of concrete hinges, both under centric and eccentric compression (Figs. 3.9 and 3.10). While the simulated relation between axial force and shortening of the neck remains in good approximation linear (Fig. 3.9), simulation of larger shrinkage intensities results in nonlinear relations between loading of the concrete hinge and the rotation angle of the neck (Fig. 3.10). These nonlinearities imply (i) that progressive load increase results initially in *stiffening* of the concrete hinge and (ii) that once a force

level exceeds some 150 kN, further load increase results in *softening* of the concrete hinge (Fig. 3.10). This can be explained as follows. Restrained shrinkage results in tensile cracking of concrete and in an associated decrease of the stiffness of the material. This damaged stiffness of concrete is relevant at the very beginning of compressive loading of the concrete hinge, because stress trajectories have to run around the open cracks. Load increase, in turn, progressively reduces the crack openings. Once a crack closes, the original material stiffness is practically restored, because stress trajectories no longer need to run around the cracks, but direct force transfer from one crack surface to the other becomes possible. This explains the initial stiffening, see also [10]. At larger load intensities, in turn, bending-induced tensile stresses (from eccentric loading) result in additional damage, and this explains the obtained softening at larger load intensities.

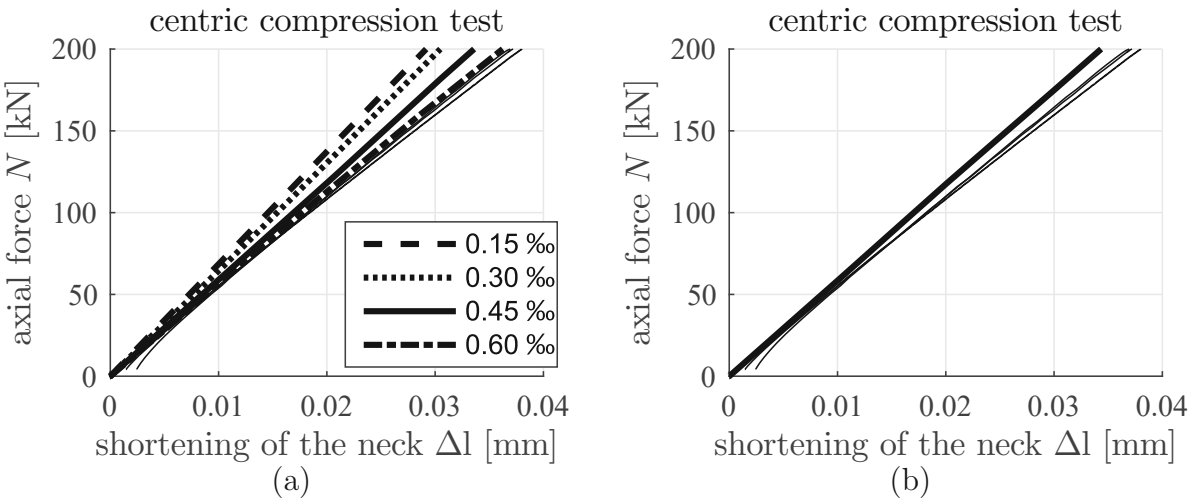

Figure 3.9: Sensitivity analysis regarding the role of shrinkage of concrete: Comparison of (i) numerical results of 3D FE simulation obtained with the mesh shown in Fig. 3.5 as well as with input parameters listed in Eqs. (2.3) and Table 3.1 and shrinkage (thick lines) with (ii) measurements from centric compression tests (thin lines): (a) stiffness decrease due to increasing shrinkage intensities, and (b) Simulation results obtained with "optimal" value of shrinkage amounting to 0.5 ‰

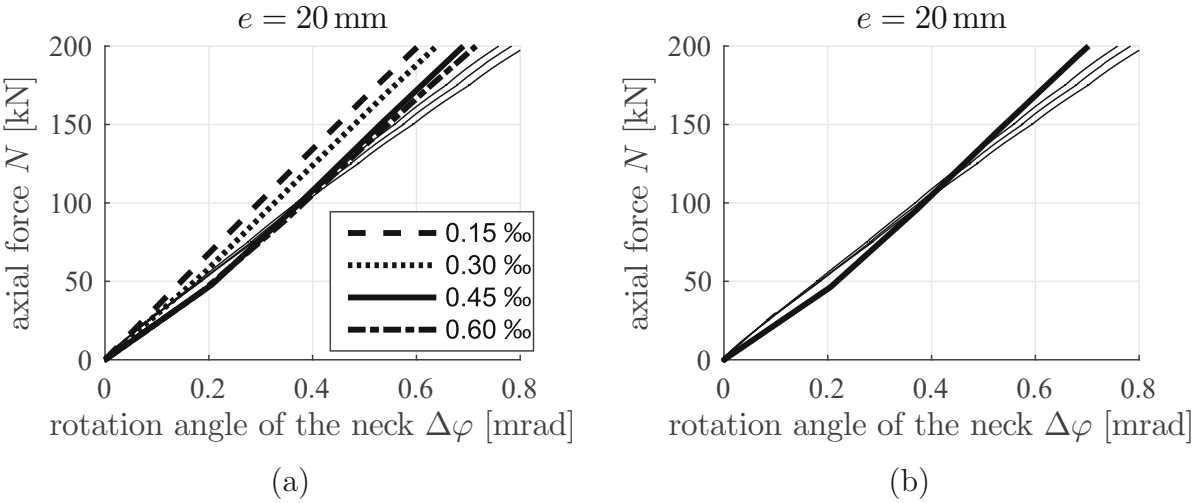

Figure 3.10: Sensitivity analysis regarding the role of shrinkage of concrete: Comparison of (i) numerical results of 3D FE simulation obtained with the mesh shown in Fig. 3.5 as well as with input parameters listed in Eqs. (2.3) and Table 3.1 and shrinkage (thick line) with (ii) measurements from eccentric compression tests with $e = 20\,\text{mm}$ (thin lines): (a) stiffness decrease due to increasing shrinkage intensities, and (b) Simulation results obtained with "optimal" value of shrinkage amounting to 0.5 ‰

Summarizing, the simulation results suggest that shrinkage strains might have resulted in considerable damage of the concrete hinges. Based on interpolation, it is found that a shrinkage intensity of 0.5 ‰ allows for reproducing the experimentally observed extensional and bending stiffness of the tested concrete hinges in a quantitatively satisfactory fashion.

Consideration of shrinkage does not only reduce the simulated initial stiffness of concrete hinges, but also the simulated ultimate load carrying capacity (Fig. 3.11). In more quantitative detail, the found "optimal" shrinkage intensity (0.5 ‰) reduces the model-simulated ultimate load carrying capacity of the tested concrete hinges by 22 %, see Fig. 3.11. Still, even the shrinkage-based FE simulation significantly overestimates the load carrying capacity of the tested concrete hinges, and this provides the motivation for the following sensitivity analysis regarding the triaxial compressive strength of concrete.

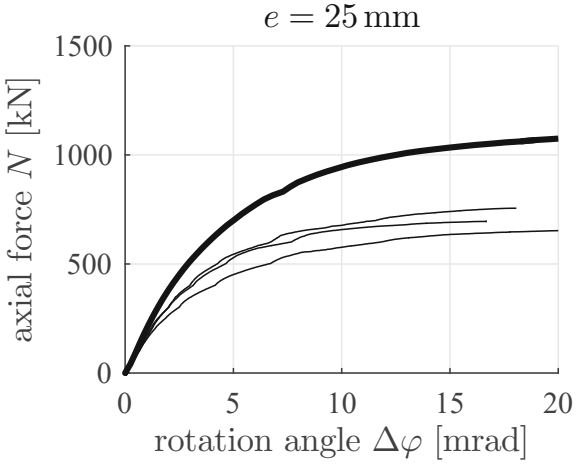

Figure 3.11: Comparison of (i) numerical results of 3D FE simulation obtained with the mesh shown in Fig. 3.5, and with input parameters listed in Eqs. (2.3) and Table 3.1, and with 0.5 ‰ shrinkage of concrete (thick line) with (ii) measurements from eccentric compression tests with $e = 25\,\text{mm}$ (thin lines)

3.6 Sensitivity analysis regarding confinement-induced strengthening of concrete

The following sensitivity analysis regarding the confinement-induced strengthening of concrete consists of repeating the FE analysis described in the previous Section (Fig. 3.11), based on FE input quantities which are deviating from the default values (Table 3.1), in order to simulate a more moderate strength increase with increasing confinement pressure. Reducing the triaxial compressive strength, in turn, shall neither modify the uniaxial compressive strength nor the uniaxial tensile strength. This can be achieved by increasing the input parameter λ_t, quantifying the ratio between the *fictitious* uniaxial tensile strength f_t' related to the Menétrey-Willam failure surface and the *realistic* uniaxial tensile strength f_t related to the Rankine failure surface. Notably, this modification is carried out exclusively in the immediate vicinity of the "compressive" half of the neck region, see the Finite Elements illustrated in red color in Fig. 3.12.

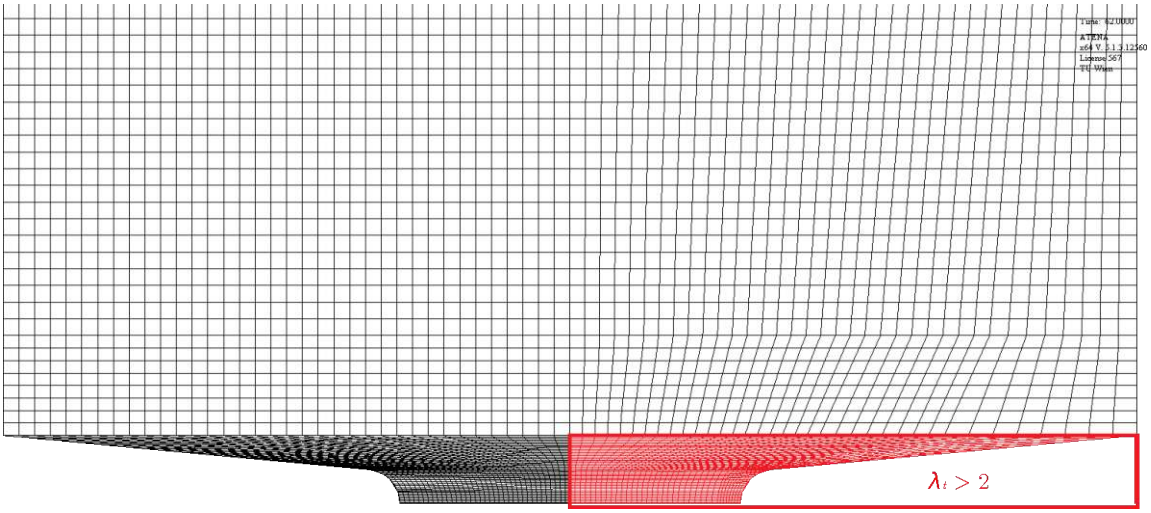

Figure 3.12: Finite Element mesh used for three-dimensional simulation of concrete hinges: elements in which the standard value $\lambda_t = 2$ is used are shown in black; elements in which increased values of λ_t are prescribed are shown in red (increase λ_t values result in decreased strength of concrete under triaxial compression)

Increasing the ATENA science input parameter λ_t from 2 to 4, 6, and 8, respectively, and considering all other required input values as listed in Table 3.1, delivers Menétrey-Willam failure surfaces with decreasing slopes in the ξ,ρ-diagrams, i. e. with less pronounced confinement-induced strengthening of concrete, see Fig. 3.13. Using these modified failure surfaces as the basis for FE simulations of eccentric compression tests of concrete hinges, delivers simulation results describing the *same* initial bending stiffness, but progressively decreasing ultimate load carrying capacities (Fig. 3.14). Based on interpolation it is found that

$$\lambda_t = 6.86 \tag{3.9}$$

allows for reproducing the experimentally observed ultimate load carrying capacities of the tested concrete hinges in a quantitatively satisfactory fashion, see Fig. 3.14.

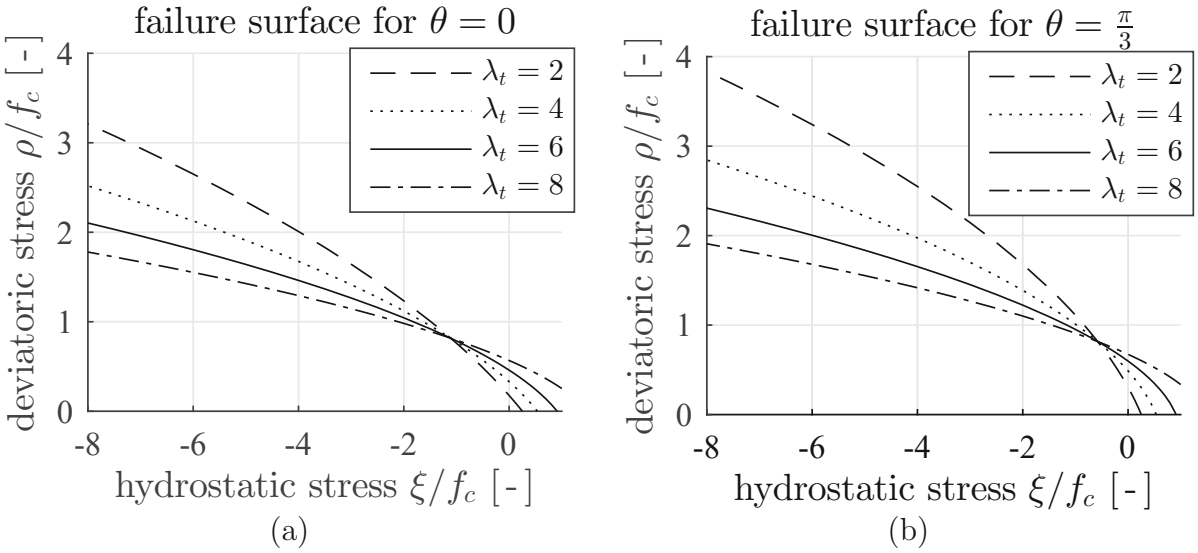

Figure 3.13: Failure meridians of Menétrey-Willam failure surface illustrated in sections through principal stress space containing the hydrostatic axis (see abscissa), see Eqs. (3.1) to (3.5), evaluated for input quantities listed in Table 3.1 and strength ratios $\lambda_t \in [2, 4, 6, 8]$: (a) tensile meridian with Lode angle $\theta = 0$; (b) compression meridian with Lode angle $\theta = \pi/3$

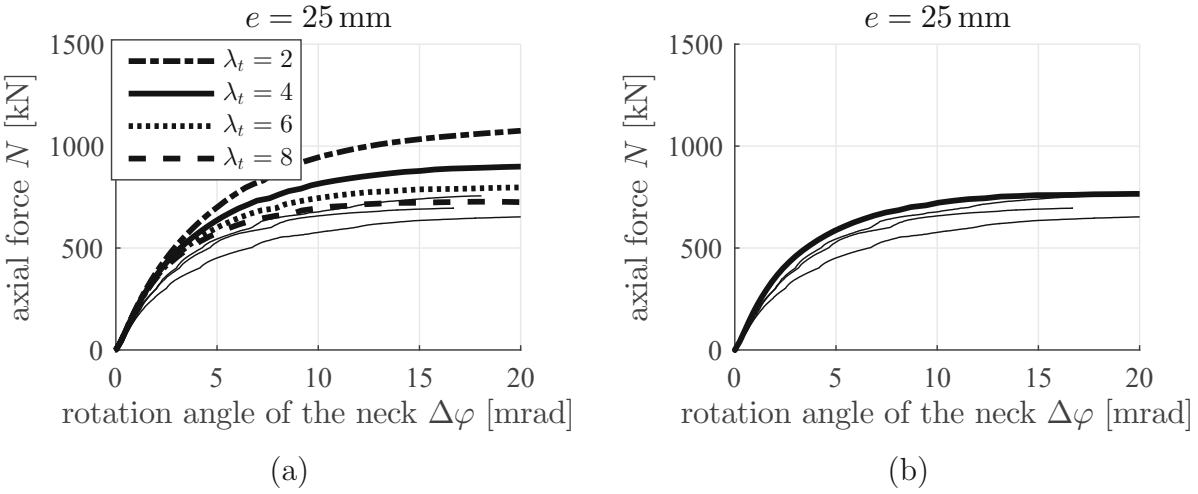

Figure 3.14: Sensitivity analysis regarding the role of triaxial strength of concrete: Comparison of (i) numerical results of 3D FE simulation obtained with the mesh shown in Fig. 3.5 as well as with input parameters listed in Eqs. (2.3) and Table 3.1 except $\lambda_t = [2; 4; 6; 8]$ and with 0.5 ‰ shrinkage of concrete (thick lines) with (ii) measurements from eccentric compression tests with $e = 20$ mm (thin lines): (a) load-carrying-capacity decreases with increasing tensile strength for the Menétrey-Willam failure surface, and (b) Simulation results obtained with "optimal" value of $\lambda_t = 6.86$ ($\Rightarrow f_t' = \frac{f_c}{2}$)

3.7 Micromechanics-assisted quantification of damage resulting from hindered shrinkage of concrete

The further improved FE simulation of concrete hinges (Fig. 3.14) reproduces the experimentally observed behavior of the tested concrete hinges in a qualitatively and quantitatively satisfactory fashion. This underlines the particular importance of considering shrinkage-induced damage. However, prescribing shrinkage-related eigenstrains in nonlinear FE simulations does not provide straightforward quantitative insight into the questions how much hindered shrinkage of concrete reduces the stiffness and strength of the material. As a remedy, a recently developed multiscale model for concrete, see [13], is used to quantify (i) the shrinkage-induced damage and (ii) the relation between damage-induced reduced stiffness and tensile strength, respectively. This results in micromechanics-assisted FE simulations of concrete hinges, i. e. in multiscale structural analysis.

The multiscale model of Hlobil et al. [13] envisions a microcracked composite consisting of a sane (= uncracked) concrete matrix damaged by parallel and interacting microcracks (Fig. 3.15). Using a Mori-Tanaka stiffness estimate from continuum micromechanics

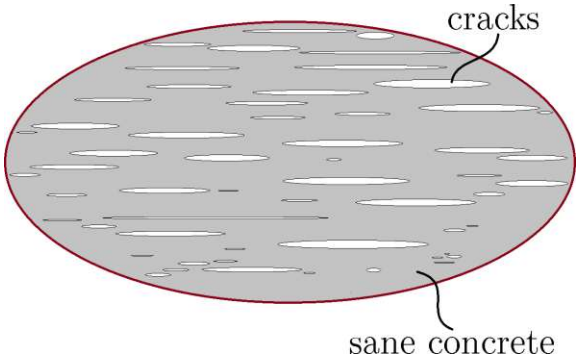

Figure 3.15: Idealization of concrete damaged by parallel cracks according to [13]; the two-dimensional figure refers to a three-dimensional representative volume element

[1, 31], the model suggests that the Young's modulus of microcracked concrete, in the direction normal to the crack planes, $E_{c,dam}$, decreases with increasing damage variable ω, and the mathematical formulation of this relation reads as [13]

$$E_{c,dam}(\omega) = E_c \cdot \left[1 + \frac{16 \cdot \omega}{3} \cdot \left(1 - \nu_c^2\right)\right]^{-1} \tag{3.10}$$

where E_c, ν_c, and ω denote the Young's modulus and the Poisson's ratio of sane concrete, as well as Budiansky and O'Connel's crack density parameter [3]. The relation between

the damage variable ω and the softening tensile strength, $f_{t,dam}$, was (i) identified in [13] from direct tension tests on dog-bone shaped concrete specimens and (ii) validated in the framework of blind predictions regarding three-point bending tests on notched mortar prisms; the mathematical formulation of this relation reads as [13]

$$f_{t,dam}(\omega) = \frac{K_{Ic}}{2}\sqrt{\frac{\pi}{a_g}\cdot\left[0.3148 + 0.385\cdot\omega\right]^{-1}}\,, \tag{3.11}$$

where K_{Ic} and a_g, respectively, denote the fracture toughness and the maximum aggregate size of concrete.

As for identification of the damage variable ω_s, resulting from hindered shrinkage of concrete, the undamaged Young's modulus of concrete is taken from Eqs. (2.3), the Poisson's ratio of concrete is set equal to the standard value $\nu_c = 0.2$, and the damaged Young's modulus of concrete is estimated from Fig. 3.6 as

$$E_{c,dam} = 26\,\text{GPa}\,. \tag{3.12}$$

Specializing Eq. (3.10) for these quantities and solving the resulting expression for the damage variable ω delivers

$$\omega_s = 6.5\%\,. \tag{3.13}$$

The fracture toughness of concrete is identified by specializing Eq. (3.11) for the undamaged tensile strength $f_t = 3.57\,\text{MPa}$ (see Table 3.1) and for $\omega = 0$, as well as from solving the resulting expression for K_{Ic} as

$$K_{Ic} = 0.286\,\text{MPa}\sqrt{\text{m}}\,. \tag{3.14}$$

The sought damaged tensile strength follows from specializing Eq. (3.11) for the damage variable from (3.13) and the fracture toughness from (3.14) as

$$f_{t,dam} = 3.44\,\text{MPa}\,. \tag{3.15}$$

Shrinkage-induced damage in form of microcracking is related to energy dissipation, and this dissipated energy must be accounted for when it comes to defining the input parameter "fracture energy G_f" of the "CC3DNonLinCementitious2" model of Atena science, where tensile softening is modeled based on a smeared crack approach. The corresponding relation between softening tensile strength σ and increasing crack opening w of the smeared crack is modeled based on the following relationship after Hordijk [14], see also Fig. 3.16

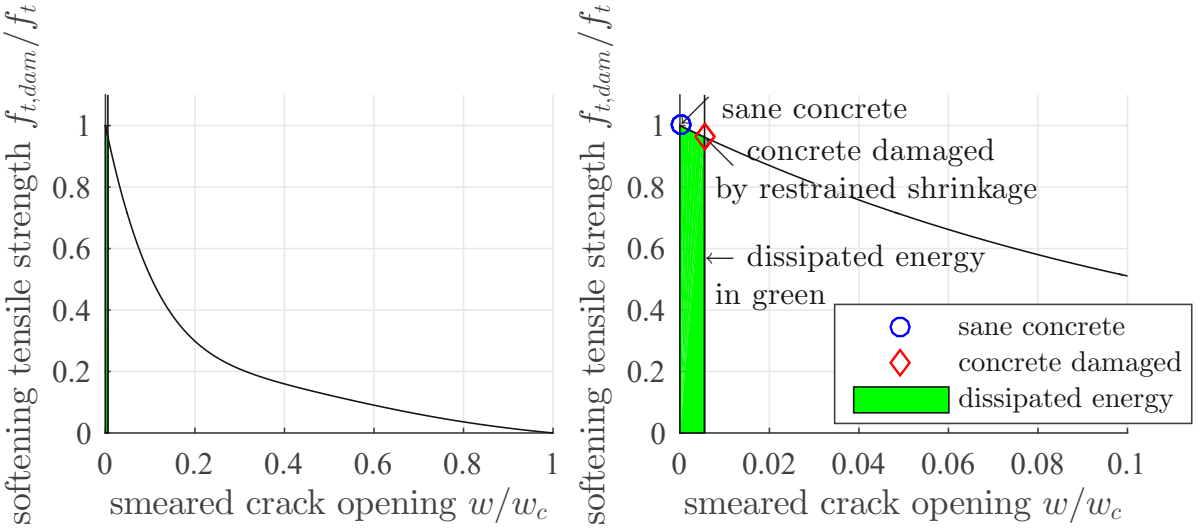

Figure 3.16: Tensile softening law of material model "CC3DNonLinCementitious2" of ATENA science: softening tensile strength of concrete over opening of smeared crack, see also Eqs. (3.16) and (3.17) as well as Table 3.1; the green area is equal to the energy dissipated, because of shrinkage-induced cracking

$$\frac{\sigma(w)}{f_t} = \left\{1 + \left(c_1 \cdot \frac{w}{w_c}\right)^3\right\} \cdot \exp\left(-c_2 \cdot \frac{w}{w_c}\right) - \frac{w}{w_c} \cdot \left(1 + {c_1}^3\right) \left(\exp\left(-c_2\right), \tag{3.16}$$

with

$$c_1 = 3\,, \qquad c_2 = 6.93\,, \qquad w_c = 5.14\,\frac{G_f}{f_t}\,. \tag{3.17}$$

Our next aim is to quantify the energy which is dissipated by shrinkage-induced cracking which has resulted in a crack density amounting to $\omega_s = 6.5\,\%$, see Eq. (3.13). This requires quantification of the crack opening w according to Hordijk's relation (3.16). To this end, Eq. (3.16) is specialized for Eqs. (3.17), for $\sigma = f_{t,dam}$, with $f_{t,dam}$ according to Eq. (3.15), and for numerical values of G_f and f_t taken from Table 3.1. Solving the resulting expression for the crack opening displacement delivers

$$w_s = 1.17\,\mu\mathrm{m}\,. \tag{3.18}$$

see also the point labeled as "concrete damaged by restrained shrinkage" in Fig. 3.16. The energy dissipated because of shrinkage-induced cracking is equal to the area under the softening curve, see the shaded area in Fig. 3.16. It follows from the following integration

$$\Delta G_f(w_s) = f_t \cdot \int_0^{w_s} \left[\left\{1 + 27 \cdot \left(\frac{w}{w_c}\right)^3\right\} \left(\exp\left(-6.93 \cdot \frac{w}{w_c}\right) \left(- 28 \cdot \frac{w}{w_c} \cdot \exp\left(-c_2\right)\right] \cdot \mathrm{d}w\,. \tag{3.19}$$

Specializing Eq. (3.19) for Eqs. (3.17) as well as for numerical values of G_f and f_t taken from Table 3.1, and integrating the resulting expression delivers the shrinkage-related energy dissipation increment as

$$\Delta G_f(w_s) = 4.08 \cdot 10^{-6}\,\mathrm{J/m^2}\,. \tag{3.20}$$

Finally, the residual fracture energy follows as the difference between the initial fracture energy G_f (see Table 3.1) and the shrinkage-related energy dissipation increment according to Eq. (3.20) as

$$G_f(w_s) = G_f - \Delta G_f(w_s) = 143\,\mathrm{J/m^2}\,. \tag{3.21}$$

It remains to be check whether or not consideration of shrinkage in form of eigenstrains amounting to 0.5 ‰ (see Fig. 3.14) is indeed quasi-equivalent to a reduction of Young's modulus from 34.75 GPa to 26 GPa, a simultaneous reduction of tensile strength from 3.57 MPa to 3.44 MPa see Eq. (3.15), and a simultaneous reduction of fracture energy from 147 J/m^2 to 143 J/m^2, see Eq. (3.21) and Table 3.2. Therefore, the FE simulation of eccentric compression right up to the load carrying capacity is repeated, using the default input values of Table 3.1, except for the modified input quantities listed in Table 3.2. The two different simulations indeed deliver quite comparable results, i. e. both the initial bending stiffness and the ultimate load carrying capacity of the simulated concrete hinges are very similar, see Fig. 3.17 to 3.19. This underlines that the usefulness of the presented mode of quantifying shrinkage induced damage based on a recently developed multiscale model for tensile failure of concrete.

Table 3.2: Modified input values of concrete model "CC3DNonLinCementitious2" of ATENA science, for consideration of shrinkage-induced damage based on an micromechanical approach and less confinement-induced strengthening under triaxial compression

description	name	value, unit
Young's modulus	E	26063 MPa
uniaxial tensile strength	f_t	3.44 MPa
fracture energy	G_f	143 J/m^2
ratio of tensile strength of Menétrey-Willam failure surface to the tensile strength of Rankine criterion; modified only in the immediate vicinity of the "compressive" half of the neck region, see the Finite Elements illustrated in red in Fig. 3.12	λ_t	6.86

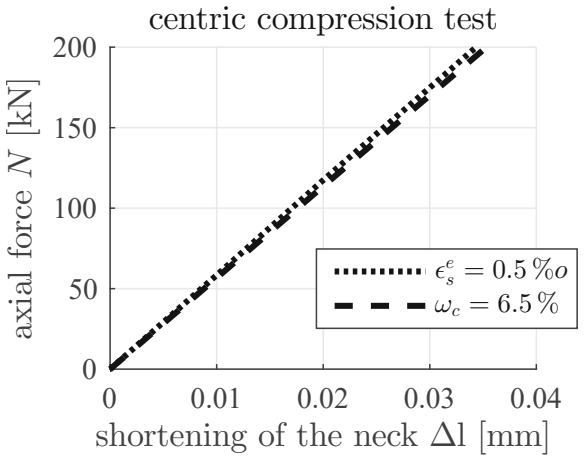

Figure 3.17: Comparison of simulation results, for centric compression, obtained for two different approaches to consideration of shrinkage: dotted line = results obtained with prescription of eigenstrains; dashed line = results obtained with reduced values of Young's modulus, tensile strength, and fracture energy, compare Table 3.2, with Table 3.1; both simulations are simulated with $\lambda_t = 6.86$

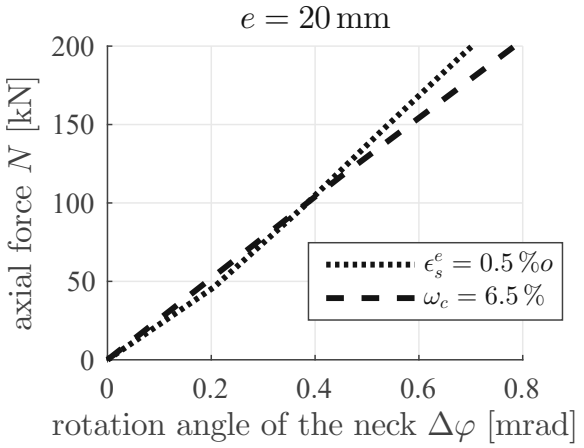

Figure 3.18: Comparison of simulation results, for eccentric compression with $e = 20\,\text{mm}$, obtained for two different approaches to consideration of shrinkage: dotted line = results obtained with prescription of eigenstrains; dashed line = results obtained with reduced values of Young's modulus, tensile strength, and fracture energy, compare Table 3.2, with Table 3.1; both simulations are simulated with $\lambda_t = 6.86$

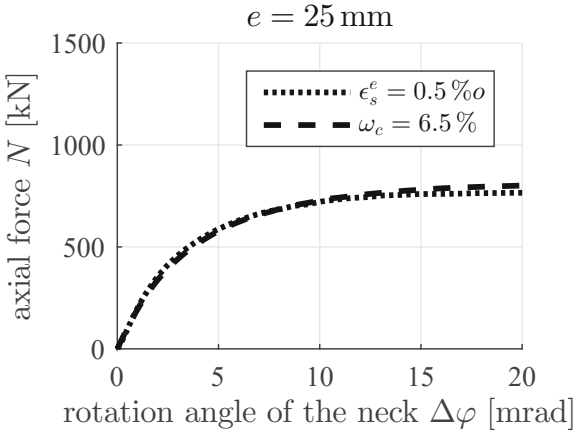

Figure 3.19: Comparison of simulation result, for eccentric compression with $e = 25\,\mathrm{mm}$, obtained for two different approaches to consideration of shrinkage: dotted line = results obtained with prescription of eigenstrains; dashed line = results obtained with reduced values of Young's modulus, tensile strength, and fracture energy, compare Table 3.2, with Table 3.1; both simulations are simulated with $\lambda_t = 6.86$

Chapter 4

Discussion

In this Chapter, simulation results are discussed with the aim to verbalize the gained insight into the structural behavior of concrete hinges. This includes the discussion of the triaxiality of compressive stress states in the neck region, the associated functionality of front-side notches, the triaxial compressive strength of concrete, ductile surface failure under biaxial compression, its implication on the durability of concrete hinges, the influence of shrinkage of concrete on the structural performance of concrete hinges, and the question whether or not consideration of creep deformation is important.

4.1 Triaxiality of compressive stress states in the neck region of concrete hinges and the functionality of front-side notches

Two-dimensional plane strain simulations have shown that compressive stress states in the neck region of concrete hinges are triaxial with principal stress ratios amounting to $1 : 0.5 : 0.\dot{3}$. Compressive stresses in lateral and thickness direction result from stress trajectories that run around the lateral and the front-side notches. While lateral notches are required to achieve the desired rotation ability of concrete hinges, the importance of front-side notches is not similarly evident.

The functionality and importance of front-side notches can be assessed in the context of three-dimensional Finite Element simulations, carried out in the framework of sensitivity analyses regarding the depth of front-side notches, (Section 11.2). Stress boundary conditions prevailing at free surfaces indicate a vanishing normal stress in the direction orthogonal to the surface. This implies that vanishing normal stresses in thickness

direction prevail not only at the plane front-side face of a concrete hinge without front-side notch, but also at the innermost free surface of a front-side notch, where the surface normal is pointing in thickness direction. In other words, the compressive stress in thickness direction is always zero *directly at the discussed surfaces*, and the most important question regards the distance from the surface, which is required for built-up of significant compressive stresses.

In the *absence* of a front-side notch, the built-up of compressive stresses in thickness direction is controlled by the Poisson effects: directly at the front-side surface, lateral strains in thickness directions are not restrained, but the restraint increases with increasing distance from the surface. In the present context, simulation results suggest that some 80 % of the reachable compressive normal stress in thickness direction are built-up within a 5 cm distance from the surface, and that the reachable stress is practically reached 10 cm from the surface (Fig. 4.1); whereby the "reachable stress" is equal to the one quantified by the two-dimensional plane strain simulations mentioned above.

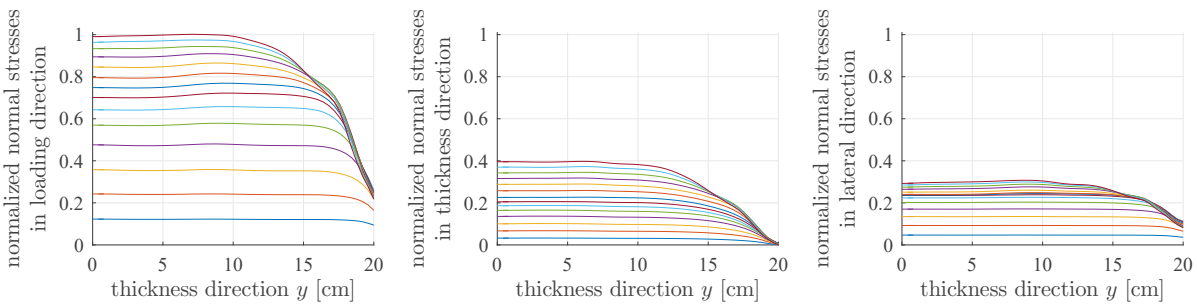

Figure 4.1: Normal stress distributions in thickness direction obtained from 3D FE simulations of concrete hinges *without* front-side notches, $y = 0$marks the center of concrete hinges, $y = 20$ cm the front side surface

A front-side notch significantly promotes the built-up of significant compressive normal stresses in thickness direction, already in the close vicinity to the free surface of the notch, because stress trajectories have to run around the notches, and the corresponding inclination angles of the stress trajectories provide the desired compressive stresses. A front-side notch with a depth of 3.5 cm appears to be optimal for the studied dimensions of a concrete hinge, because the reachable compressive stress in thickness direction is reached very quickly (Fig. 11.37 to 11.39). Further increasing the notch depth to 5 cm has the interesting effect that the compressive stresses in thickness direction (i) increase sharply with increasing distance from the notch, (ii) reach a maximum which is larger than the typical stress level quantified by means of the plane strain analyses, and (ii) finally decrease to the typical stress level quantified by means of the plane strain analyses (Fig. 11.8 to 11.10). Such a concentration of compressive stresses in the immediate vicinity of the front-side notch might well have a positive influence on the durability of

concrete hinges, but this cannot be answered based on the performed *time-independent* simulations.

Anyway, the characteristic principal compressive strength ratio $1 : 0.5 : 0.\dot{3}$ implies the existence of an isotropic stress part ("confinement pressure") that amounts to 60 % of the principal stress acting in loading direction. The confinement results in a considerable increase of the strength of concrete, as discussed next.

4.2 The triaxial compressive strength of concrete

It is well known that confinement pressure increases the strength of concrete. Still, the available experimental database regarding failure of concrete under triaxial compression is, unfortunately, rather small, because of the challenges associated with the realization of a triaxial compressive strength tests. As for the related discussion, it is useful to recall the state-of-the-art knowledge regarding failure of concrete in uniaxial and biaxial compressive strength tests.

Failure of concrete under *uniaxial* compression is very well documented in the open literature, e. g. there even exist computer tomography images taken *during* a strength test, clarifying that (i) at the peak load, failure starts in form of *distributed* damage with microcracks propagating in loading direction ("axial splitting"), (ii) at the beginning of the post-peak regime, microcracking localizes into a band which is inclined with respect to the loading direction, and (iii) later in the post-peak regime, this band turns into a shear band, i. e. the failure mode switches from invisible and distributed microscopic axial splitting to a macroscopically apparent shear failure mode, see [9].

Failure of concrete under *biaxial* compression is significantly less well documented in the literature. Even nowadays, state-of-the-art insight goes back to the landmark experiments by Kupfer et al. [16], who showed that the symmetric biaxial compressive strength is by a typical factor of 10 to 20 % larger than the uniaxial compressive strength of concrete.

Failure under triaxial compression is even less well understood. The employed Menétrey-William failure surface, for instance, was initially developed based on experimental data from triaxial compression tests by Kupfer et al. [16], by Mills and Zimmerman [20], and as well by Chinn and Zimmerman [8], who constructed one of the first triaxial compression test facilities which was large enough to characterize representative concrete cylinders produced with realistic maximum aggregate diameters. Strength values obtained in experiments, in which the isotropic confinement pressure was comparable to the one quantified in the neck region of concrete hinges (see above), suggest that the largest compressive stress at failure amounts to some 12 times the uniaxial

compressive strength. However, photos showing tested specimens after their failure, indicate a barrel-type shape of the unloaded specimens [8]. These residual deformations are very strong indicators that the performance of the tested concrete specimens was significantly influenced by undesired but unavoidable, friction-induced and self-balanced shear stresses, activated in the interfaces between load platens and specimen. Such shear stresses are well known to significantly increase the strength of the tested sample, but quantification of the shear-induced strengthening of concrete remains to be impossible in practical testing. Summarizing, it might well be that experimentally observed strength values significantly overestimate the actual load carrying capacity of the material.

It is interesting to discuss implications for strength modeling of concrete, resulting from the described uncertainties associated with the available triaxial compressive strength data. Notably, the default input values of the Menétrey-Willam failure surface, used by ATENA science, *deviate* from the counterparts originally suggested by Menétrey and William themselves. ATENA-science-simulated strength values, obtained for triaxial compression stress states with principal stress ratios $1 : 0.5 : 0.\dot{3}$, suggest that the largest compressive stress at failure amounts to some 6 times the uniaxial compressive strength, and this is by a factor of 2 smaller than the original version of the Menétrey-William failure surface.

In the present master thesis, the Menétrey-William failure surface was further modified such that simulated strength values, obtained for triaxial compression stress states with principal stress ratios $1 : 0.5 : 0.\dot{3}$, suggest that the largest compressive stress at failure amounts to only 2.5 times the uniaxial compressive strength. This raises the question whether or not such a comparably small confinement-induced strengthening may be realistic, compare with the approaches discussed above: $2.5 < 6 < 12$. In the context of Eurocode-consistent Finite Element simulation, this question can be answered affirmatively, as explained next. For partially loaded areas, namely, the Eurocode considers that the strength is larger than the uniaxial compressive strength, and the strength increase factor is a function of the necking ratio. Considering the neck of concrete hinges to represent a partially loaded area, and specializing Eurocode formulas for the geometric dimensions of the tested concrete hinges delivers a strength increase by a factor of 2.0, and this is quite close to the strength increase obtained with the stress ratio parameter $\lambda_t = 6.86$.

4.3 Ductile surface failure under biaxial compression explains the durability of concrete hinges

Stress triaxiality alone does not explain why concrete hinges are durable structural elements. At the air-exposed surfaces in the innermost regions of the lateral necks, namely, a free-surface boundary condition applies, such that a *plane* stress state prevails there. In this context, it is noteworthy that the biaxial compressive strength of concrete is by only a few percent larger than the uniaxial compressive strength of the material. Consequently, the stress state in an air-exposed surface layer of the neck region reaches its ultimate load carrying capacity already at loading stages which are smaller than or equal to regular service loads of concrete hinges. Still, the surface layer does not spall away, but it remains in place, and – even more importantly – also the stress state does not decrease significantly, although the strains increase very significantly. In other words, the surface layer exhibits a *ductile* rather than a brittle behavior. The continued integrity of the surface layer, in turn, is essential for the built-up of the triaxial compressive stress state. If the surface layer would spall away, namely, the neighboring layer (which was initially *inside* the volume of the structure) would become the new surface layer, it would all over sudden exhibiting a plane stress state, and the strength of the material would drop from the large strength under confined triaxial compression to the much smaller strength under biaxial compression. This would make it likely that initiation of spalling would result in a catastrophic domino effect with the spalling front propagating quickly in the direction towards the center of the concrete hinge. Anyway, there is plenty of evidence from testing of concrete hinges and from practical applications that spalling does not take place as long as the loading is not close to the load carrying capacity of a concrete hinge.

4.4 Shrinkage of concrete influences the structural performance of concrete hinges

Concrete is an aging material which is shrinking with time. Total shrinkage is typically decomposed into autogenous shrinkage, resulting from the chemical reaction between cement and water, and drying shrinkage.

Autogenous shrinkage is typically assumed to increase proportionally to the strength of concrete, but this oversimplifies the situation to a considerable extent. The actual origin of autogenous shrinkage is that hydration products, resulting from the chemical reaction between cement and water, occupy a slightly smaller volume than the reactants. Therefore, autogenous shrinkage increases practically linearly with increasing reaction

degree, referred to as "hydration degree". Notably, also uniaxial compressive strength is frequently assumed to be a linear function of hydration degree. Given that both autogenous shrinkage and uniaxial compressive strength are proportional to hydration degree, it is a logic consequence that there exists also a linear correlation between shrinkage and strength, although they are not etiologically linked to each other. As for quantitative aspects of autogenous shrinkage, it is noteworthy that typical concretes reach, 28 days after their production, hydration degrees between 70 and 80 %. This implies that most of the autogenous shrinkage strains develop within the first four weeks after production. Typical shrinkage intensities amount to 0.05 ‰ [2].

Drying shrinkage is a structural (and not a material) problem, because it is related to water transport at the microscale of concrete, and the driving force for the latter are moisture *gradients*. Gradients, in turn, contradict the requirement of a *material problem* which is, by definition, free of gradients. Given the diffusion driven nature of water transport in mature concrete, drying shrinkage develops over months, years, and decades. Thereby, shrinkage strains are the larger, the larger the reduction in internal relative humidity. Right after production, concrete samples are typically completely saturated, i. e. the internal relative humidity is practically equal to 100 %. Drying shrinkage comes to an end, once the internal relative humidity is uniform and equal to the external relative humidity of the ambient air. This equilibrium configuration is reached the faster, the shorter the required water transportation distances. The latter are typically quantified by the ratio obtained from dividing the concrete volume by the surface area exposed to the dry air. Given that necks of concrete hinges occupy a quite small volume but a quite larger surface area, concrete in the neck region is very prone of developing drying shrinkage strains much faster than typically expected in more standard concrete structures. As for quantitative aspects of drying shrinkage, drying to a relative humidity of 50 %, which is a typical value for indoor applications, results in drying shrinkage of normal concrete between 0.5 ‰ and 0.6 ‰ [12]. 28 days after production typically half of these values can be expected.

The presented FE simulations were based on shrinkage intensities amounting to 0.5 ‰, and this might appear as slightly too large compared to what is expected to be realistic after 28 days. Reducing shrinkage to the expected level, in turn, would result in an overestimation of the experimentally observed stiffness of concrete hinges. Two effects can explain this difference between simulation and experiment. Firstly, less initial stiffness of the neck region may results from entrapped air, given the difficulties to compact fresh concrete poured into formworks used for the production of concrete hinges. Secondly, the experimentally observed stiffness might be smaller than the actual stiffness, because of undesired concentration of loading and support forces. The top and

bottom steel plates of the concrete hinges, namely, were connected to the top and bottom reinforcement cages by means of welding. This results in eigenstresses and, hence, the steel plates are slightly curved rather than perfectly flat after welding. This implies that the loading and support forces are concentrated in the middle of the concrete hinge, rather than being equally distributed along the entire thickness direction, at least at the beginning of a loading sequence. At later stages of the loading process, full-line contact prevails, but residual imprints in the steel plates, resulting from the load application system and from the support system, respectively, indicate that external forces were – also close to the peak load – not perfectly uniformly distributed in thickness direction. A FE sensitivity analysis regarding the load application length in thickness direction, in turn, clarifies that load concentration results in a reduced structural stiffness of concrete hinges (Fig.11.113). This explains why realistic shrinkage intensities combined with perfectly distributed loading in thickness direction overestimate the experimentally observed stiffness of concrete hinges.

4.5 Is consideration of creep important?

The presented time-independent FE simulations cannot be expected to reproduce experimentally observed behavior in a perfect fashion, because concrete exhibits creep, but time-dependent behavior remained unconsidered in the numerical simulations. Extending the FE simulations towards consideration of creep turned out to be impossible, because creep modeling approaches provided by ATENA science are developed to assess *long-term* creep behavior, i. e. creep developing over years and decades. Numerical simulation of short-term creep, evolving within some tens of minutes, does not yield qualitatively realistic results.

Still, creep must be expected to play an important role when it comes to quantification of deformations close to the peak load, because concrete is well known to exhibit *nonlinear* creep. This is typically modeled by the affinity concept of Ruiz [22], which envision that the regular *linear creep function* of concrete is valid for load intensities up to 40 % of the strength. At larger load intensities, the *linear creep function* is to be amplified by an affinity parameter. The latter increases with the fourth power of the utilization degree, i. e. the ratio of applied stress to the strength of the material. While this concept was originally developed for uniaxial creep functions, the extension to three-dimensional stress states is straightforward, see [28, 29, 30]. Once the load carrying capacity is reached, the creep activity of concrete is three times as large as the creep activity in the linear creep regime.

Chapter 5

Conclusions

Testing provides very valuable insight into the structural performance of concrete hinges, but available deformation and displacement measurement are typically limited to the easily accessible *surface* of concrete hinges. What is happening *inside the volume* of concrete hinges, in turn, remains to a considerable extent an enigma. Therefore, Finite Element simulations are very valuable, because they provide complementary insight into the structural behavior of concrete hinges. They essentially allow for quantifying the *triaxial* compressive stress states prevailing in the neck region, which are responsible for the high load carrying capacities of concrete hinges.

From the numerical simulations documented in the current master thesis, the following conclusions are drawn:

- As for the investigated concrete hinges, the triaxial compressive stress state in the neck region exhibits characteristic ratios of principal stresses in loading direction, in thickness direction, and in lateral direction, amounting to $1 : 0.5 : 0.\dot{3}$.
- This stress triaxiality results to considerable extent from the existence of the notches, because stress trajectories must run around the notches, and the inclination angles of the stress trajectories create the desired compressive stresses acting orthogonal to the loading direction. This underlines the importance of front-side notches.
- The principal compressive stress ratio $1 : 0.5 : 0.\dot{3}$ implies that the isotropic part of the stress state (= "confinement pressure") amounts to 60 % of the compressive stress in loading direction.
- The significant confinement pressure results in a significant strengthening of concrete.

- Failure surfaces implemented in Finite Element software for concrete apparently overestimate the triaxial strength of the material significantly. This can be explained with the unsatisfactory experimental insight into triaxial strength of concrete and the big challenges associated with such test.

- Modifying standard failure surfaces, such that they are consistent with Eurocode regulations for *partially loaded areas*, allows for simulating realistic load carrying capacities of concrete hinges.

- As for the investigated concrete hinges, where the top and bottom reinforcement cages are connected by three pairs of crossed steel rebars, consideration of restrained shrinkage of concrete is important. Desirably, shrinkage is to be simulated in form of eigenstrains.

- Restrained shrinkage of concrete results in tensile microcracking of the material, and the created damage can be quantified based on a recently developed multiscale model for tensile strength and softening of concrete [13].

- The load carrying capacity of concrete hinges can be well simulated based on time-independent FE analyses, but corresponding rotation angles will be underestimated by such simulation approaches, because concrete exhibits nonlinear creep, and this time-dependent phenomenon significantly contributes to the overall deformations.

- Softening of concrete hinges in the post-peak regime is rather ductile than brittle. This manifests itself in strongly increasing rotation angles, while external loading decreases only marginally.

- The durability of concrete hinges results from a similarly ductile failure mode of concrete at the innermost surface of the lateral notches, where a *biaxial compression* stress state prevails. This ductile failure enables the built-up of the triaxial stress states described above.

Bibliography

[1] Y. Benveniste. A new approach to the application of mori-tanaka's theory in composite materials. *Mechanics of Materials*, 6(2):147–157, 1987.

[2] British Standards Institution and CEN European Committee for Standardization. EN *1992-1-1:2015-07-31 Eurocode 2: Design of concrete structures – Part 1-1: General rules and rules for buildings*. EN 1992-1-1:2015-07-31. British Standards Institution and CEN European Committee for Standardization, 2014.

[3] B. Budiansky. On the elastic moduli of some heterogeneous materials. *Journal of the Mechanics and Physics of Solids*, 13(4):223–227, 1965.

[4] B. Budiansky and R. J. O'Connell. Elastic moduli of a cracked solid. *International Journal of Solids and Structures*, 12(2):81–97, 1976.

[5] J. Červenka and V. Červenka. Three dimensional combined fracture-plastic material model for concrete including creep and rate effect for dynamic loading. http://www.cervenka.cz/assets/files/papers/3D Fracture-Plastic Model v5.pdf; last access: April 12, 2016.

[6] J. Červenka and V. K. Papanikolaou. Three dimensional combined fracture–plastic material model for concrete. *International Journal of Plasticity*, 24(12):2192–2220, 2008.

[7] V. Červenka, L. Jendele, and J. Červenka. *ATENA program documentation Part 1 - Theory*, 2014.

[8] J. Chinn and R. M. Zimmerman. Behavior of plain concrete under various high triaxial compression loading conditions. Technical report, COLORADO University AT BOULDER, Defense Technical Information Center Document, New Mexico, 1965. WL TR 64-163, Air Force Weapons Laboratory.

[9] J. Desrues, P. Bésuelle, and H. Lewis. Strain localization in geomaterials. *Geological Society, London, Special Publications*, 289(1):47–73, 2007.

[10] V. Deudé, L. Dormieux, D. Kondo, and S. Maghous. Micromechanical approach to nonlinear poroelasticity: Application to cracked rocks. *Journal of Engineering Mechanics*, 128(8):848–855, 2002.

[11] J. Dix. Betongelenke unter oftmals wiederholter Druck- und Biegebeanspruchung: Bericht [Concrete hinges under many times repeated compression and bending: report.]. *Deutscher Ausschuß für Stahlbeton*, 150:1–41, 1962. In German.

[12] fib (the International Federation for Structural Concrete), J. Walraven, A. Bigaj-van Vilet, P. Beverly, L. Taerwe, S. Matthys, Balázs, Cairns, Cervenka, Corres, Cosenza, di Pisco, Eligehausen, Falkner, Fardis, Foster, Ganz, Helland, Høj, Keuser, Klein, Kollegger, Mancini, Marti, Matthews, Menegotto, Müller, Randl, Rostam, Sakai, Schissl, Sirist, Ueda, van der Horst, Yamazaki, Benz, Breiner, Burkat-Andres, Chiorino, Creton, Curbach, Demonté, Dehn, F. Ruiz, Gehlen, Glavind, Gylltoft, Häussler-Combe, Mechtcherine, Muttoni, Pinto, Plizzari, Prota, Reinhardt, Triantafillou, Vandewalle, Vrouwnvelder, Wight, et al. *fib model code for concrete structures 2010*. Ernst & Sohn, Wiley, 2013.

[13] M. Hlobil, M. Göstl, J. Burrus, C. Hellmich, and B. Pichler. Molecular-to-macro upscaling of concrete fracture: theory and experiments. Paper draft which is planed to be submitted to the Journal for the Mechanics and Physics of Solids, 2016.

[14] D. A. Hordijk. *Local approach to fatigue of concrete*. Doctor dissertation, Delft University of Technology, The Netherlands, 1991. ISBN 90/9004519-8.

[15] J. Kalliauer. Finite Element-based sensitivity analyses regarding concrete hinges subjected to short-term eccentric compression. Project Work, TU Wien – Vienna University of Technology, 2016.

[16] H. Kupfer, H. K. Hilsdorf, and H. Rusch. Behavior of concrete under biaxial stresses. In *Journal Proceedings of the American Concrete Institute*, volume 66, No. 8, pages 656–666, 1969.

[17] F. Leonhardt and H. Reimann. *Betongelenke: Versuchsbericht, Vorschläge zur Bemessung und konstruktiven Ausbildung. Kritische Spannungszustände des Betons bei mehrachsiger, ruhender Kurzzeitbelastung [Concrete hinges: test report, recomendations for structural design. Critical stress states of concrete under multiaxial static short-term loading]*, volume 175. Ernst und Sohn, Berlin, 1965. In German.

[18] S. Marx and G. Schacht. Betongelenke im Brückenbau [Concrete hinges in bridge construction]. *Berlin Deutscher Beton- und Bautechnik Verein*, 18, 2010. In German.

[19] P. Menétrey and K. J. Willam. Triaxial failure criterion for concrete and its generalization. *ACI structural Journal*, 92(3):311–318, 1995.

[20] L. L. Mills and R. M. Zimmerman. Compressive strength of plain concrete under multiaxial loading conditions. In *Journal Proceedings of the American Concrete Institute*, volume 67, No. 10, pages 802–807, 1970.

[21] G. Morgenthal and P. Olney. Concrete hinges and integral bridge piers. *Journal of Bridge Engineering*, 21(1):06015005, 2015.

[22] M. Ruiz, A. Muttoni, and P. Gambarova. Relationship between nonlinear creep and cracking of concrete under uniaxial compression. *Journal of Advanced Concrete Technology*, 5(3):383–393, 2007.

[23] G. Schacht and S. Marx. Unbewehrte Betongelenke – 100 Jahre Erfahrung im Brückenbau [Unreinforced concrete hinges – 100 years experience in bridge concstructions]. *Beton-und Stahlbetonbau*, 105(9):599–607, 2010. In German.

[24] T. Schlappal, M. Schweigler, S. Gmainer, M. Peyerl, and B. Pichler. Creep and cracking of concrete hinges. Paper draft which is planed to be submitted to Experimental Mechanics, 2016.

[25] Austrian Standards Institute. ONR 23303:2010-09-01 *Prüfverfahren Beton (PVB) - Nationale Anwendung der Prüfnormen für Beton und seiner Ausgangsstoffe [Test protocol concrete - National application of testing standards for concrete and its raw materials]*. Austrian Standards Institute, 2010. In German.

[26] M. M. Tourasse. Essais sur articulation Freyssinet [Tests on Freyssinet hinges]. *Annales de l'Institut Technique du Bâtiment et des Travaux Publics*, 40(57):62–87, 1961. In French.

[27] N. V. Tue and H. Jankowiak. Betongelenke aus selbstverdichtendem und hochfestem Beton bei der neuen Elbebrücke Mühlberg [Concrete hinges made of self-compacting and high performance concrete, of the new Elbe bridge Mühlberg]. *Bautechnik*, 86(10):637–646, 2009. In German.

[28] S. Ullah, B. Pichler, and C. Hellmich. Modeling ground-shell contact forces in natm tunneling based on three-dimensional displacement measurements. *Journal of Geotechnical and Geoenvironmental Engineering*, 139(3):444–457, 2013.

[29] S. Ullah, B. Pichler, S. Scheiner, and C. Hellmich. Shell-specific interpolation of measured 3D displacements, for micromechanics-based rapid safety assessment

of shotcrete tunnels. *CMES - Computer Modeling in Engineering and Sciences*, 57(3):279–314, 2010.

[30] S. Ullah, B. Pichler, S. Scheiner, and C. Hellmich. Influence of shotcrete composition on load-level estimation in natm-tunnel shells: Micromechanics-based sensitivity analyses. *International Journal for Numerical and Analytical Methods in Geomechanics*, 36(9):1151–1180, 2012.

[31] A. Zaoui. Continuum micromechanics: survey. *Journal of Engineering Mechanics*, 128(8):808–816, 2002.

Chapter 6

Appendix

Finite Element-based sensitivity analyses regarding concrete hinges subjected to short-term eccentric compression

Abstract. This Project Work reports on comprehensive non-linear Finite Element simulation studies regarding the structural behavior of reinforced concrete hinges loaded up to their load carrying capacity. The aim is to investigate sources for possible deviations between simulation results and experimentally observed behavior. This includes quantification of numerical errors stemming from the discretization of the problem and from the used incremental-iterative solution strategy. In addition, it is shown that two-dimensional simulations deliver results which are significantly different from the ones obtained with three-dimensional simulations. As for the material model of concrete, the relations between input parameters and simulation results are studied by means of deterministic and stochastic sensitivity analyses. It is also shown that knowledge regarding the actual support and loading conditions of concrete hinges is important for reliable Finite Element simulations. Putting together all simulation results, it is finally recommended to check the predictive capabilities of any developed Finite Element model in comparison with independent experimental data, whereby "independent" means that the considered experimental data were not used to develop the model. If such an assessment is impossible, for instance because no additional experimental data are available, parameter fitting should be handled very carefully. It is recommended to accept only as few fitting parameters as possible, to chose fitting parameters which exhibit a clear mechanical interpretation, and to check the plausibility of the finally obtained values of the fitting parameters. This is setting the scene for a follow-up Master Thesis, in which recently performed experiments on reinforced concrete hinges will be re-analyzed. Therein, it will be shown that highly non-linear behavior of concrete hinges (loaded up to their load carrying capacity) can be explained by considering (i) default input values which depend of the actual stiffness and the actual cube compressive strength of the used concrete, (ii) damage resulting from hindered shrinkage of concrete, and (iii) a realistic approach to modeling strength of the material under triaxial compression. This investment into essential mechanical features renders mathematically motivated fitting of material input parameters unnecessary.

Contents

7 Introduction

Concrete hinges are un-reinforced or marginally reinforced necks in beam-like or column-like reinforced concrete structures. Typically, a few pairs of crossed steel rebars run across a concrete hinge, and the cross-over point is at the center of the neck. Therefore, the bending stiffness of the neck is significantly smaller than the one of the full beam or column cross-section. This results in a desired concentration of bending deformations at the concrete hinge. In addition, it is part of the structural concept, that concrete hinges exhibit bending-induced tensile cracking even under regular service loads. Cracking further reduces the bending stiffness of the neck, and this further promotes the ability of a concrete hinge to develop desired relative rotation angles. The large rotation ability of concrete hinges is evidenced by several test series see, e. g. [Tourasse, 1961], [Dix, 1962], [Leonhardt, 1965], [Schlappal, 2016].

Concrete hinges were invented before world war II by Eugène Freyssinet, and they enjoyed great popularity after the war. In the 1960s, Leonhardt [Leonhardt, 1965] developed pioneering design guidelines for concrete hinges, see also the reformulation of these guidelines in the

nomenclature of modern European design standards by Marx [Marx, 2010]. Anyway, decades-long durability of concrete hinges remained questionable at the end of the 1960s. Therefore, the civil engineering community decided to gain practical experience from quasi-continuous monitoring of existing structures. Now, more than five decades later, there is plenty of practical evidence that concrete hinges indeed provide the expected long-term durability associated with reliable services and small costs for maintenance and repair. Therefore, concrete hinges experience a renaissance in practical engineering, particularly so in integral bridge construction, see, e. g. [Tue, 2009], [Schacht, 2010], [Morgenthal, 2015].

Nowadays, several powerful software products for the numerical simulation of reinforced concrete structures are commercially available. This may create the unjustified expectation that using such products automatically delivers reliable Finite Element simulations of reinforced concrete structures. However, the macroscopically apparent mechanical behavior of concrete is very complex, because it is triggered by processes happening at the microstructure of the material, and these processes are not yet completely deciphered; not to mention that it is also an open research question how to upscale such microscopic processes, once they are well understood, from the microstructure to the macroscopic material scale of concrete. A few examples for such links between microstructure and macroproperties are as follows:

1. Concrete is a chemically active material, because of the chemical reaction between cement and water. The kinetics of the chemical reaction typically reach a maximum a few hours after mixing, and they decay progressively afterwards, but they never come to an end, given the diffusion driven nature of the reaction at mature ages of the material. Since reaction products occupy a slightly smaller volume than the initial reactants, concrete exhibits macroscopically so-called autogenous shrinkage.
2. Concrete is a porous material with pore sizes down to single nanometers. Drying of concrete changes the effective pore pressures which are acting on the solid skeleton. Therefore, simple macroscopic drying of the material results in significant stress redistributions at the microscale, and they manifest themselves macroscopically as drying shrinkage.
3. Concrete exhibits time-dependent stiffness and compliance, referred to as macroscopic creep and relaxation of the material. The microstructural origin of these macroscopic properties is still not clear, but it is likely that creep and relaxation are related to shear dislocations of nanoscopic water-filled interfaces, where water is in an adsorbed “liquid crystal” state and serves as a viscous lubricant.
4. Concrete exhibits strength values and associated failure modes, which strongly depend on the loading type. The uniaxial tensile strength, for instance, is one order of magnitude smaller than the uniaxial compressive strength, and the latter is significantly smaller than the strength of the material under triaxial compressive loading. While tensile failure is related to catastrophic (“instable”) crack propagation, failure under uniaxial compression starts with non-catastrophic damage in form of

debonding of aggregates from the surrounding cement paste matrix, once the loading exceeds 30 percent of the strength. Under triaxial compression, in turn, a transition from brittle to ductile failure is observed. Again, the microstructural mechanisms and processes standing behind these macroscopic observations are even nowadays not fully understood.

As a matter of fact, available simulation tools for concrete are of macroscopic and phenomenological nature. Therefore, material input parameters for Finite Element simulations must be prescribed such that the numerical calculations are customized for the concrete of interest, and this provides the motivation for the current Project Work.

The current Project Work investigates different origins for possible deviations between Finite Element simulation results and experimentally or practically observed behavior. This is done in a well-structured and systematic fashion.

- Deviations could result from numerical errors. On the one hand, the Finite Element discretization needs to be fine enough such that objective simulation results are obtained, whereby "objective" means that simulation results do virtually not change, even if a significantly finer discretization would be used. This calls for an investigation regarding the mesh fineness, with the aim to find an optimal trade-off between required simulation efforts and reliability of the obtained results. On the other hand, the mechanical behavior of concrete exhibits several sources of non-linearities, and this requires an incremental-iterative solution strategy in the framework of non-linear Finite Element analyses. This calls for an investigation regarding convergence indicators.
- Deviations could result from inappropriately chosen material input parameters. In this context, it is beneficial to have insight into the sensitivity of simulation results with respect to changes of input parameters, and this calls – on the one hand – for deterministic sensitivity analyses. In addition, concrete is a heterogeneous material, and this implies that even homogenized material properties will exhibit certain fluctuations within the volume of a reinforced concrete structure, even though nominally the same concrete is used to produce such structures. This calls – on the other hand – also for stochastic sensitivity analyses considering statistically fluctuating concrete properties.
- Deviations could result from uncertainties regarding the actual loading and support conditions. This calls for investigating loading and support scenarios which deviate from the nominally expected configurations.
- Deviations could result from oversimplifications related to two-dimensional simulations approaches, although the actual problem at hand is of three-dimensional nature. This calls for a comparison of simulation results obtained under consideration of plane stress states and plane strain states, respectively, with simulation results obtained with three-dimensional simulations.

All studies described in the sequel are carried out with help of the Finite Element analysis software ATENA® 5.1. This program is used for the simulation of short-term eccentric compression tests on concrete hinges, performed right up to their ultimate load carrying capacities.

The current report is structured as follows: The analyzed concrete hinges are described in Section 8. This includes their geometric shape, the material behavior of steel and concrete, as well as the support and loading conditions. The sensitivity of simulation results with respect to the fineness of the Finite Element mesh and other convergence studies are given in Section 9. Different material models for concrete are compared in Section 10. Deterministic sensitivity analysis are carried out in Section 11. This includes (i) the comparison of simulation results obtained with 2D models and with 3D models, respectively, (ii) a sensitivity analysis regarding the size of the front-side notch, (iii) sensitivity analyses studying the influence of every single material input parameter on the simulated structural behavior of concrete hinges, and (iv) a sensitivity analysis regarding the effective load application length. Stochastic sensitivity analyses are the topic of Section 12. Therein, input parameters are considered as statistical quantities, fluctuating around an expected value. Uncorrelated sensitivity analyses are carried out first, and this might well result into the situation where a rather large Young's modulus is combined with a rather small compressive strength. This provides the motivation to perform also correlated stochastic analyses, where stiffness and strength are assumed to be correlated such that a rather large Young's modulus implies also a rather larger compressive strength. While the first two types of stochastic analyses considered spatially *uniform* properties of concrete within a concrete hinge, sensitivity analyses based on "random fields" are used to study the structural behavior of concrete hinges under the assumption that properties of concrete are not uniform within the volume of a concrete hinge, but that they fluctuate around a mean value. The results of this Project Work are discussed in Section 13, where also final conclusions are drawn.

8 Statement of the problem

Concrete hinges are established over decades [Bernhardt, 2003], and shown that they can sustain some millions of load alternations [Bernhardt, 2003] [Marx, 2009]. They fall into oblivion [Bernhardt, 2003] [Schacht, 2010], but now they have a renaissance [Schacht, 2010], because they are economic and durable [Schacht, 2010].

Dix [Dix, 1962] and Leonhardt [Leonhardt, 1965], recommend to use less reinforcement in the neck due to

- Reinforcement will lead to shrinkage cracks, especially in the hinge neck. [Leonhardt, 1965]
- The bars reduce creeping. Creeping has a very good effect in concrete hinges: It makes the hinge less rotational stiff and that it reduces peak-stresses. [Leonhardt, 1965]

- The bars increase the rotational stiffness. [Leonhardt, 1965]
- Strong reinforcements under compression, near the yield stress, tend to buckle. Which lead to unbind/detach from the concrete, and crush the concrete even more. Those reinforcement bars reduce in most cases the Peak-load. ([Dix, 1962] mentioned Eugène Freyssinet (1925) as original author.)

Both mention the possibility to use a small amount of reinforcement bars in the middle of the hinge, which is realized in all hinges in this work.

8.1 Geometric dimensions

The basic model has a height of 34.9cm (load-direction), a width of 25cm and an out-of-plane-thickness of 40cm (see **Fig. 8.1**). Models with front notches on all four sides were simulated (see **Fig. 8.5**) in this work. The concrete-hinges are according the recommendations of Freyssinet und Leonhardt, but also smaller front-notch-deepness's, then recommended, were simulated. For 3D-Analysis a model using both symmetry-surfaces are used

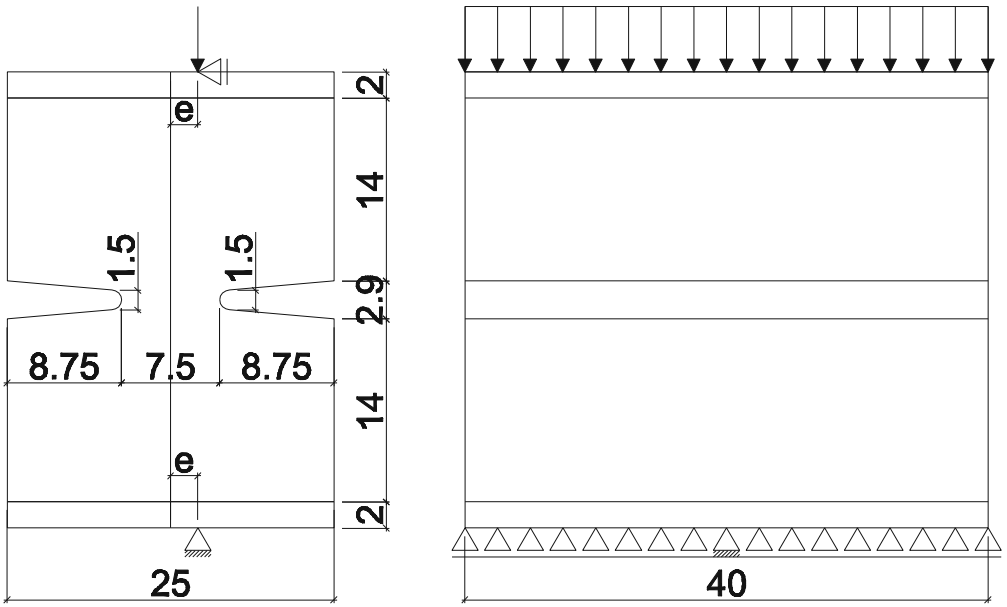

Fig. 8.1: The basic Geometry of the Concrete Hinges

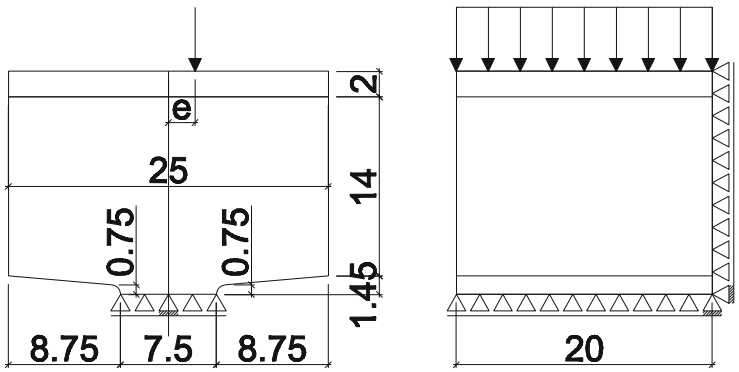

Fig. 8.2: The Model using Symmetry-conditions

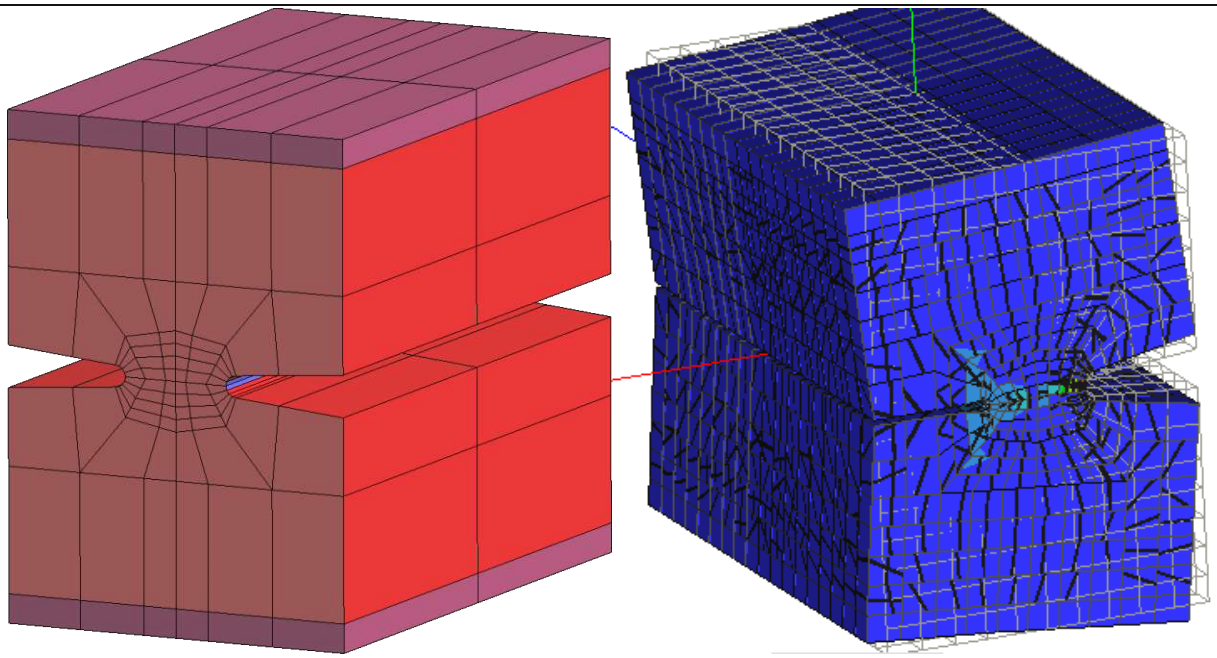

Fig. 8.3: 3D-View of the undeformed (left) and deformed (right) model

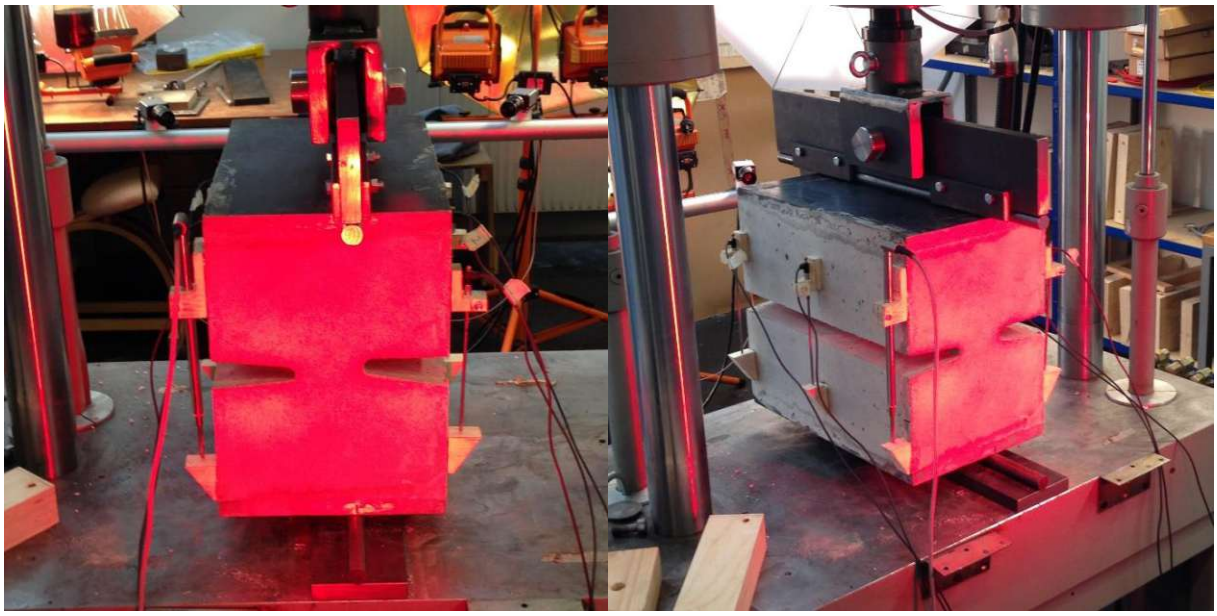

Fig. 8.4: Model in Reality

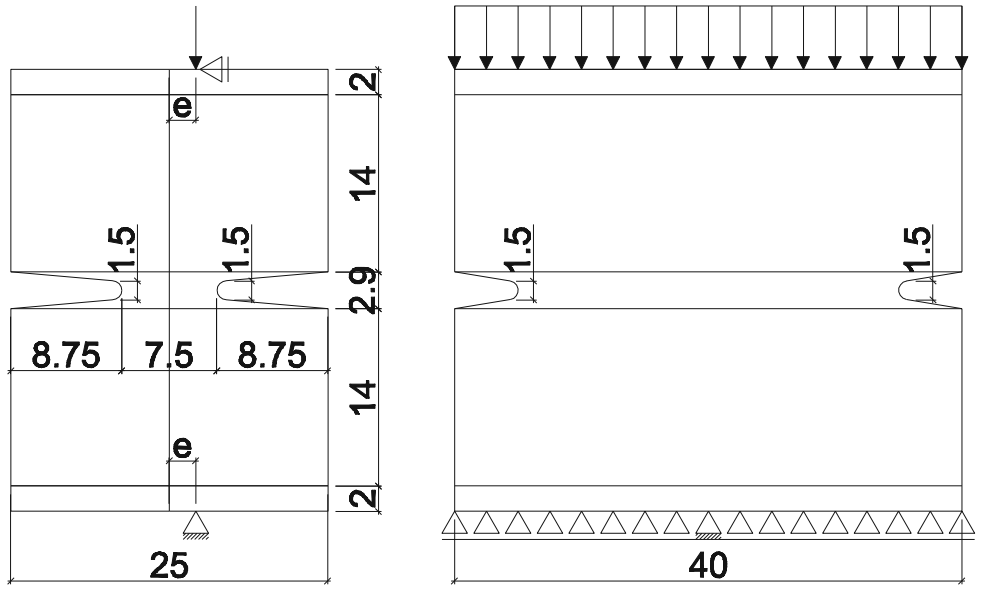

Fig. 8.5: The basic Geometry of the Concrete Hinges with front notch

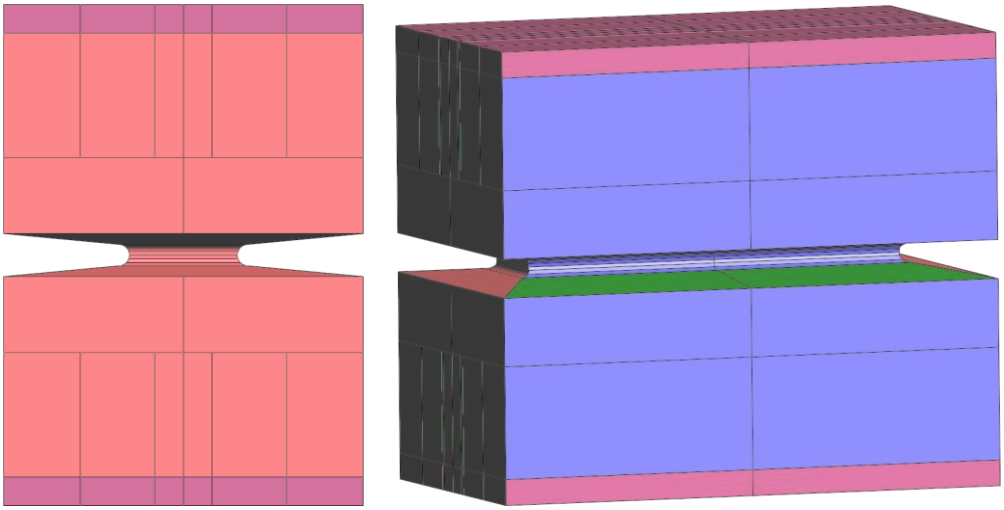

Fig. 8.6: The basic Geometry of the Concrete Hinges with front notch in GiD [GiD 12.0,2015]

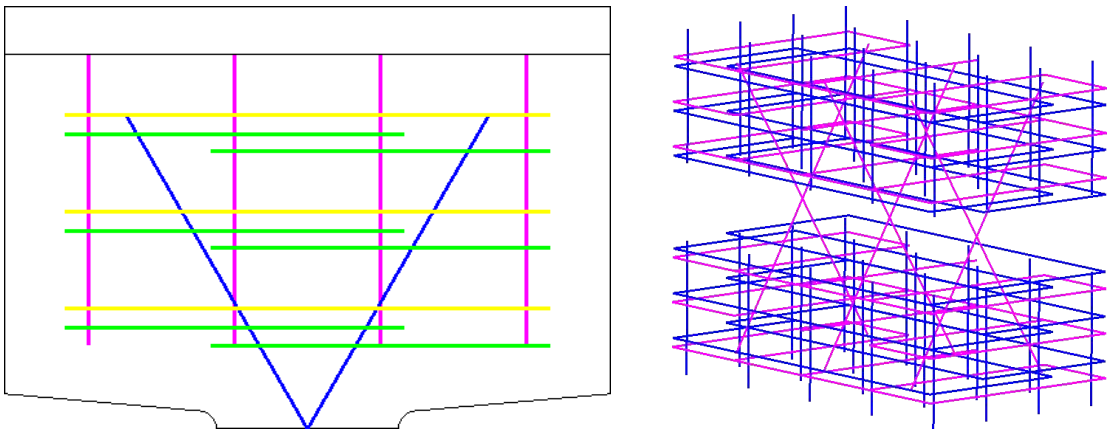

Fig. 8.7: Reinforcement Bars – 2D (left) and 3D (right)

8.2 Field equations including material behavior of concrete

For the original basic configuration of this model, the standard values of "SOLID Concrete" of "Concrete EC2" for the "Mean"-Values of "C30/37" with an aggregate size of 8mm are chosen:

Table 1: Default Material Data for C30/37 Mean

	C30/37
Young's Modulus-E	32000 MPa
Poisson's Ratio	0.2
Tension Strength-FT	2.9 MPa
Compression Strength-FC	-38MPa
Fracture Energy-GF	72.5 N/m
Critical Comp Disp.-WD	-0.000 5 m
Plastic Strain-EPS_CP	-0.00 097 438
Onset of Crushing-FC0	-6.09 MPa
Eccentricity-EXC	0.52
Dir of pl. Flow-BETA	0.0
Fixed Crack	1
FCR	0.8
Agg	0.008

Table 2: Material Data for without front notch

	Standard for $FC_{Cu,m}$=54.267[1]	used Values	Compressive neck-zone
Young's Modulus-E	36 097.2 MPa	24 600 MPa[2]	24 600 MPa
Poisson's Ratio	0.2	0.2	0.2
Tension Strength-FT	3.47 MPa	3.386 67 MPa	23.65 MPa[3]
Compression Strength-FC	-47.3 MPa	-47.3 MPa	-47.3 MPa
Fracture Energy-GF	146 N/m	142.464 N/m	146 N/m
Critical Comp Disp.-WD	-0.000 5 m	-0.000 5 m	-0.000 5 m
Plastic Strain-EPS_CP	-0.001 24	-0.001 24	-0.001 24
Onset of Crushing-FC0	-7.29 MPa	-7.29 MPa	-7.29 MPa
Eccentricity-EXC	0.52	0.52	0.52
Dir of pl. Flow-BETA	0.0	0.0	0.0
Fixed Crack	1	1	1

[1] The "Cubic-Mean" strength was 54.2$\dot{6}$ MPa out of three tests: 54.5 MPa; 54.2 MPa; 54.1 MPa.

[2] 32 800MPa were tested. Due to shrinkage-cracks especially in the neck and due to difficult concrete compacting in high reinforced areas the Young's Modulus is reduced to 24 600 MPa(75%). This leads also to a reduction of the tensile strength and the Fracture Energy according to

[3] To reduce the triaxial stresses near hydrostatic loading the tensile strength is increased to half of the compressive strength, due to data check in GiD, this has to be done manually in the inp-File.

FCR	0.8	0.8	0.8
Agg	-	0.008 m	0.008 m

Table 3: Material Data for with front-side-notch

	Standard for $FC_{Cu,m}$=56.25[4]	used Values	Compressive neck-zone
Young's Modulus-E	36 520.8 MPa	26 062.5 MPa[5]	26 062.5 MPa
Poisson's Ratio	0.2	0.2	0.2
Tension Strength-FT	3.57 MPa	3.474 18 MPa	24.5 MPa[6]
Compression Strength-FC	-49 MPa	-49 MPa	-49 MPa
Fracture Energy-GF	147 N/m	143.055 N/m	147 N/m
Critical Comp Disp.-WD	-0.000 5 m	-0.000 5 m	-0.000 5 m
Plastic Strain-EPS_CP	-0.001 24	-0.001 24	-0.001 24
Onset of Crushing-FC0	-7.49 MPa	-7.49 MPa	-7.49 MPa
Eccentricity-EXC	0.52	0.52	0.52
Dir of pl. Flow-BETA	0.0	0.0	0.0
Fixed Crack	1	1	1
FCR	0.8	0.8	0.8
Agg	-	0.016 m	0.016 m

The (symmetric) 3D-Stresstensor has three coordinate independent Values, this values can be split into the three principal strains, or the Haigh-Westergaard coordinates, or other invariants [IMWS, 2011][Thomson, 2015]. By the state of the art many failure surfaces for concrete can be most easily represented by using Haigh-Westergaard coordinates. Also Atena uses such a failure surface expressed in Haigh-Westergaard coordinates:

$$F_{3P}^{p}(\xi,\rho,\theta)_{e,ft,fc} = \tfrac{3}{2}\tfrac{\rho^2}{f_c'^2} + \tfrac{m}{f_c'}\cdot\left(\rho\cdot\tfrac{r(\theta)}{\sqrt{6}} + \sigma_m\right) - c = 0 \qquad (1)^{7}$$

$$m = 3\tfrac{f_c'^2 - f_t'^2}{f_c'\cdot f_t'}\tfrac{e}{e+1}, \quad r(\theta) = \tfrac{4\cdot(1-e^2)\cdot\cos(\theta)^2 + (2e-1)^2}{2\cdot(1-e^2)\cos(\theta) + (2e-1)\cdot\sqrt{4\cdot(1-e^2)\cos(\theta)^2 + 5\cdot e^2 - 4e}}, \quad e = 0.52 \qquad (1a,b)$$

— [Červenka, 2008] equation 25 and 26 and ATENA Theory [Červenka, 2014] equation 2.54 referring on the failure surface of MENETREY, WILLAM.

The strains in concrete can be elastic, viscoelastic or inelastic strains [Grassl, 2014] (like plastic, viscoplastic and damage or fracturing strain) and most of them not (only) depend on

[4] The "Cubic-Mean" strength was 56.25 MPa out of two tests: 55.0 MPa; 57.5 MPa.

[5] The Mean Young's Modulus was 34 750 MPa out of two tests: 34 300 MPa and 35 200 MPa were tested. Due to shrinkage-cracks especially in the neck and due to difficult concrete compacting in high reinforced areas the Young's Modulus is reduced to 26 062.5 MPa(75%). This leads also to a reduction of the tensile strength and the Fracture Energy according to

[6] To reduce the triaxial stresses near hydrostatic loading the tensile strength is increased to half of the compressive strength, due to data check in GiD, this has to be done manually in the inp-File.

[7] simplified equation from ATENA Theory [Červenka, 2014]: $F_{3P}^{p} = \left[\sqrt{1.5}\,\tfrac{\rho}{f_c'}\right]^2 + m\left[\tfrac{\rho}{\sqrt{6}f_c'}\,r(\theta,e) + \tfrac{\xi}{\sqrt{3}f_c'}\right] - c = 0$

the current stress, but also on the stress-strain-history of this element. In the static problem-type of Atena, the software makes the assumption that the strain of an integration point is the sum of elastic, plastic and fracture strain. The elastic strain is the stress[8] over the stiffness[9]. The plastic strain is in general the time-independent[10] strain that would be still in the unfractured specimen after removing all loads. The fracturing strain can in general be considered as the strain, which is due to cracks and damage.

$$\varepsilon_{ij} = \varepsilon_{ij}^{e} + \varepsilon_{ij}^{p} + \varepsilon_{ij}^{f} \tag{2}$$

— ATENA Theory [Červenka, 2014] equation 2.36 referring on DE BORST (1986).

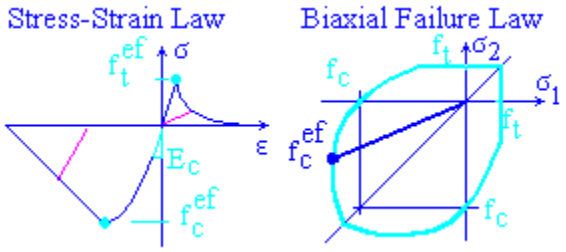

Fig. 8.8: Failure-Curves in Atena [GiD 12.0,2015][ATENA, 2015][Červenka, 2014]

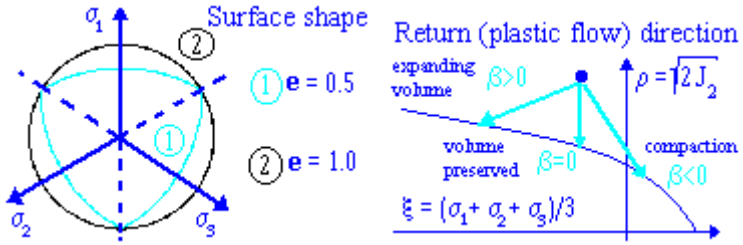

Fig. 8.9: Failure-Surface [GiD 12.0,2015][ATENA, 2015][Červenka, 2014]

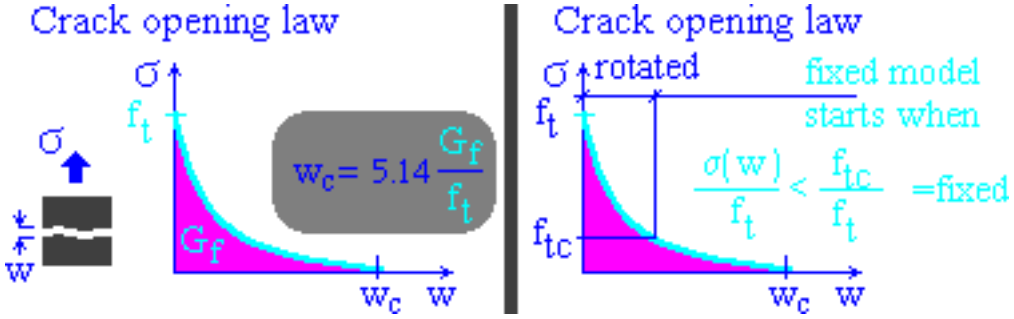

Fig. 8.10: Fracture Energy and Crack opening law [GiD 12.0,2015][ATENA, 2015][Červenka, 2014]

[8] There are different kind of stress-measurements, like true stress (σ=F/A) or nominal stress (σ=F/^{0}A) [Thomson, 2015] [Grassl, 2014]

[9] In 2D or 3D it is a little bit more complicated: Then you are can pre-"multiply" with the inverse of the stiffness-tensor: $\underline{\underline{\varepsilon}} = \underline{\underline{C}}^{-1} : \underline{\underline{\sigma}}$ [Hellmich, 2012] [Thomson, 2015]

[10] but dependent on the load-history

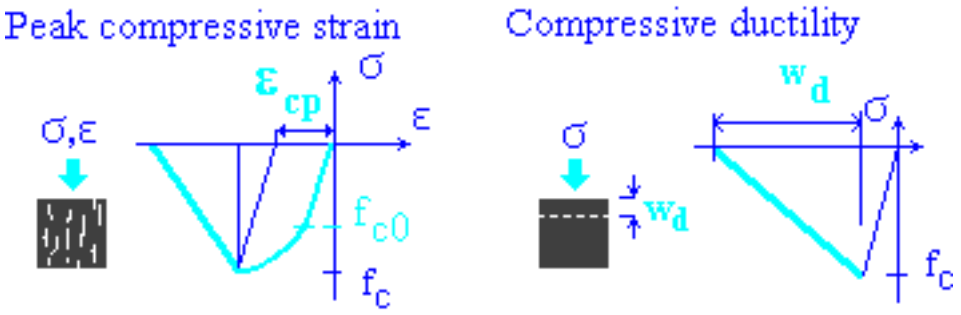

Fig. 8.11: compressiv behaviour [GiD 12.0,2015][ATENA, 2015][Červenka, 2014]

There is a quite similar, but more advanced Version, of this material-model, which is described in the Manual as follows:

> *"The CC3DNonLinCementitious3 fracture plastic constitutive model is an advanced version of the CC3DNonLinCementitious2 material that can handle the increased deformation capacity of concrete under triaxial compression."*
>
> — ATENA_Theory.pdf [Červenka, 2014]

This Material-model needs small load-steps to convert, and uses plastic potential. [Červenka, 2008] There are negligible differences for the load-displacement curve till service load, so in many cases it is not necessary to use this advantaged material-model. In this work mostly the material-models Cementitious 2 and Cementitious 3 were used.

Material failure surface.

Concrete Hinges have high triaxial hydrostatic stresses, with a stress-ratio of about 1:0.5:0.3 (see Chapter 11.1.2); therefore it is important to check the material behavior for triaxial stress states. The failure surface is for CEM2 and CEM3 according to equation **(1)**. This equation with C30/37-Mean-Values ($f_c'=f_c=38$MPa; $f_t'=f_t=2.9$MPa; e=0.52) is used to show the figures **Fig. 8.12**, **Fig. 8.13**, and **Fig. 8.14**. To understand what such triaxial stress means they are plotted in a graph with uni- and biaxial-stress-states and zoomed out the typical area where FEM-Software is tested.

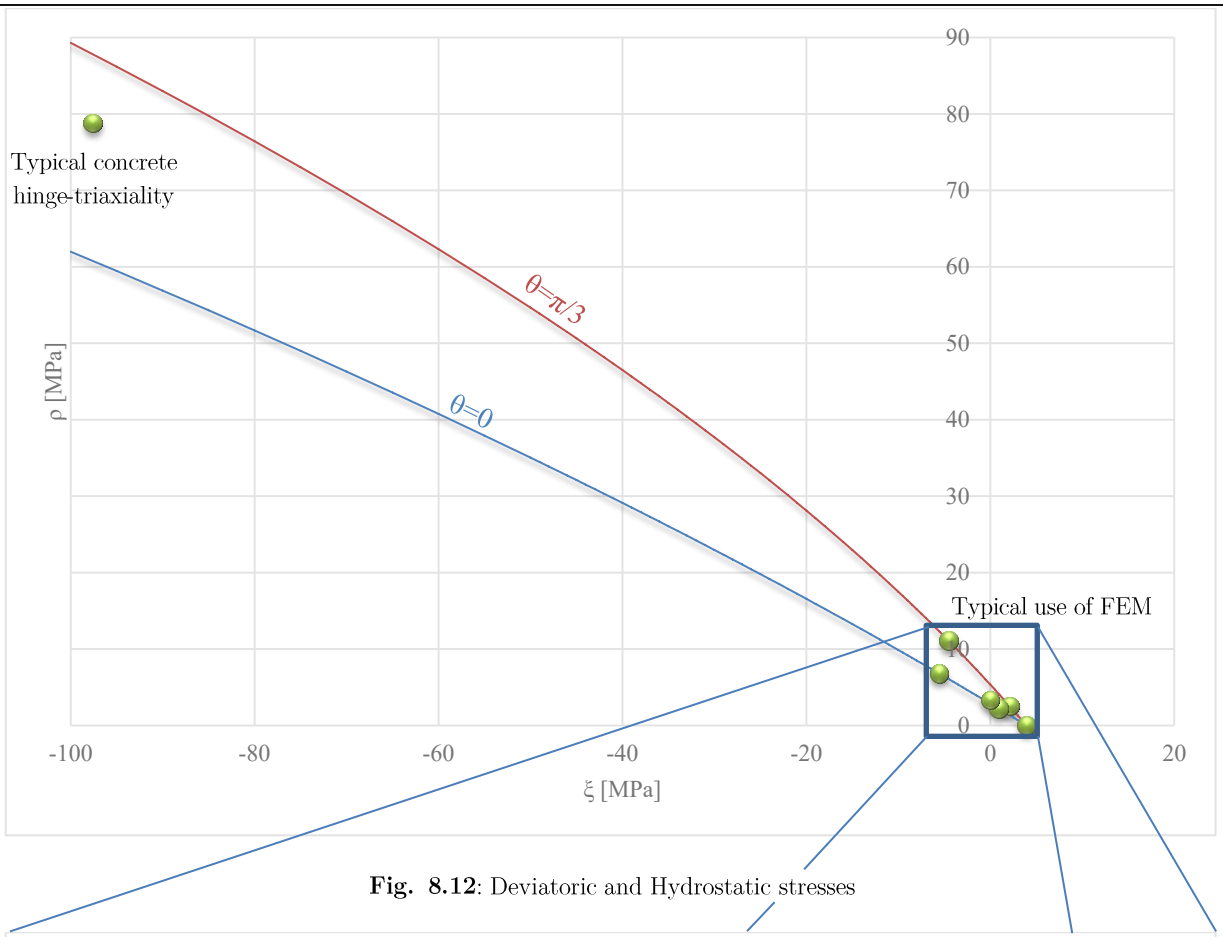

Fig. 8.12: Deviatoric and Hydrostatic stresses

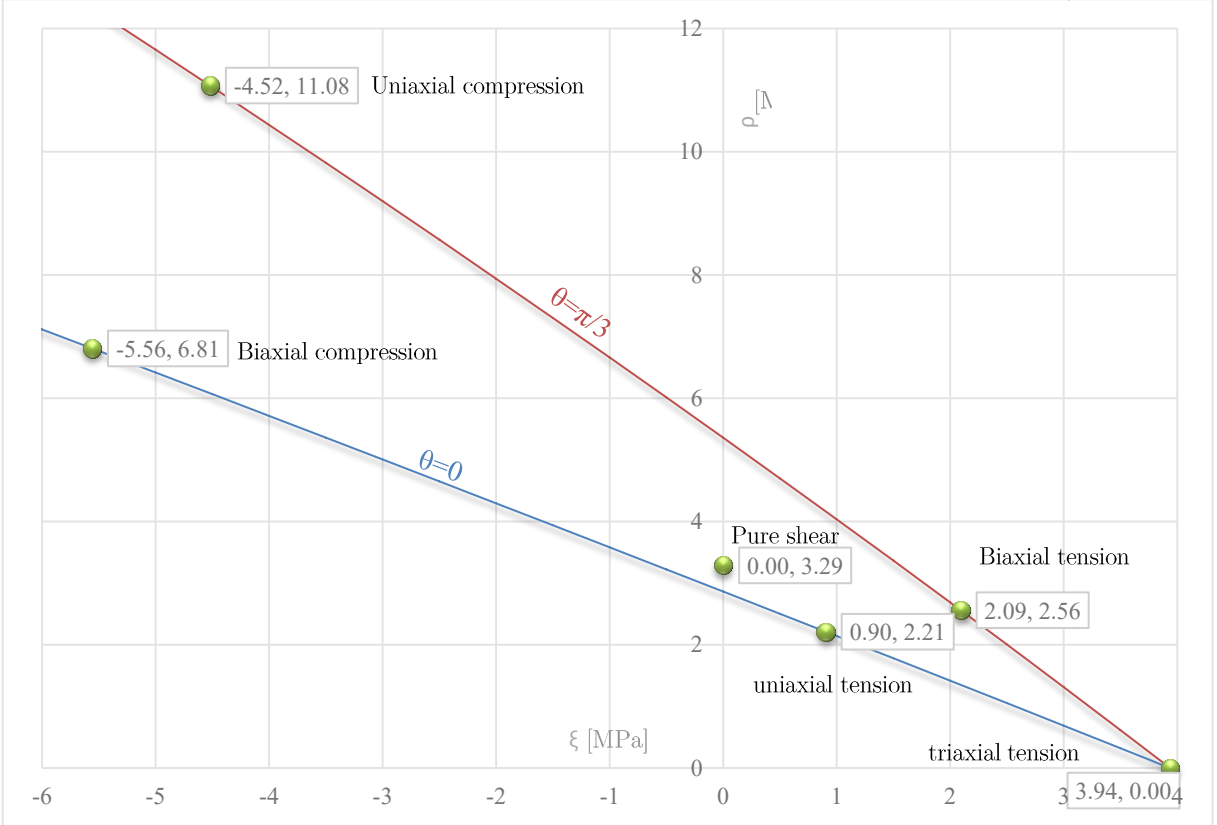

Fig. 8.13: Deviatoric and Hydrostatic stresses

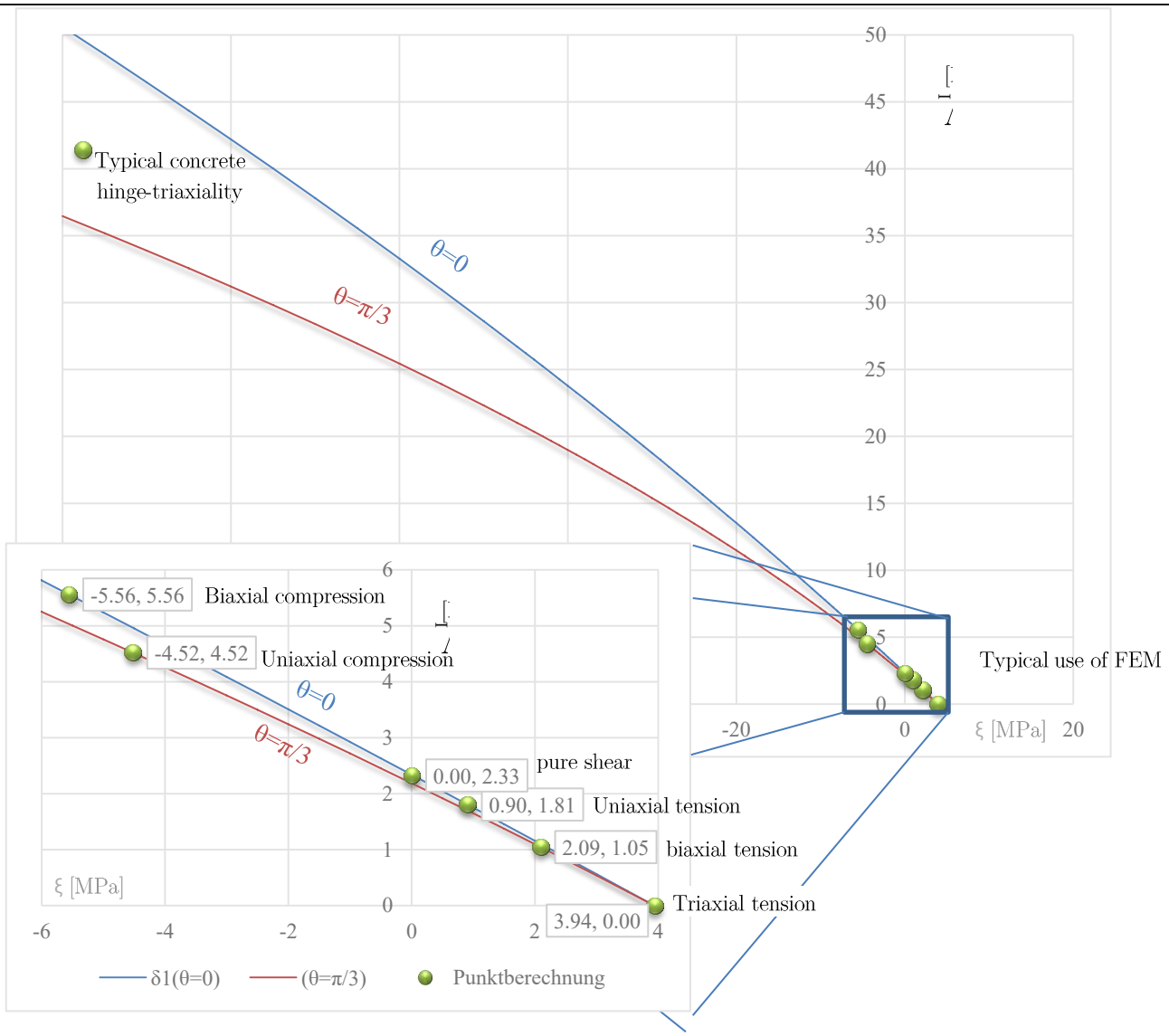

Fig. 8.14: failure-surface in Λ1-ξ-Diagramm

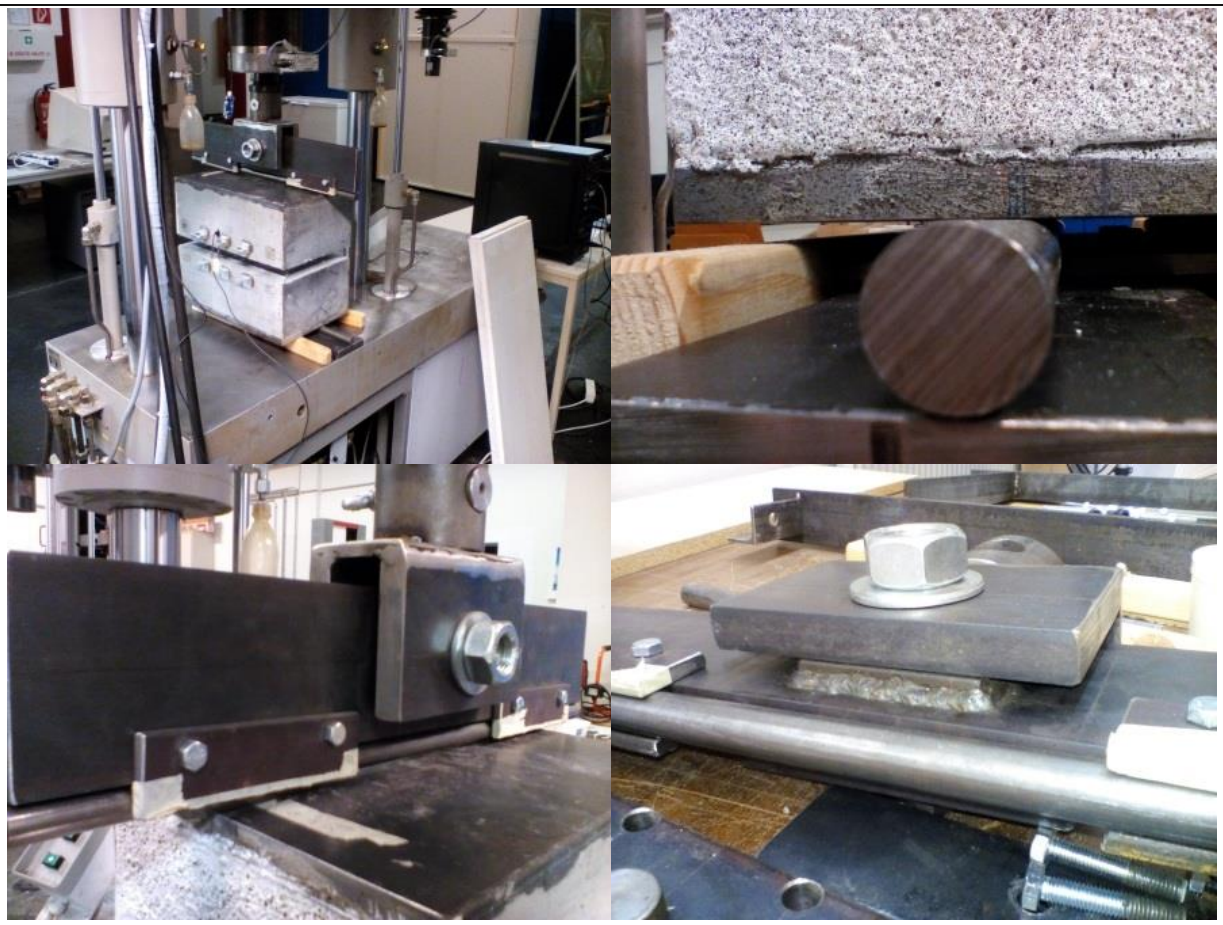

Fig. 8.15: Boundary-Conditions in Reality a)Model, b) bottom support; c,d)Loaidng plate

9 Finite Element models and convergence studies

9.1 Convergence regarding discretization error (mesh fineness)

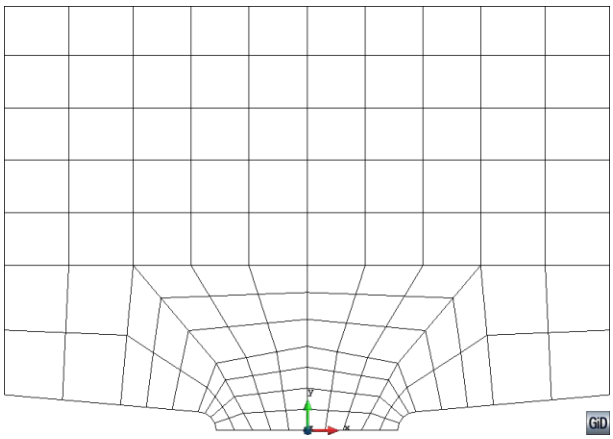

Fig. 9.1: The meshed 2-D-Half-Model

The mesh should be quite big, compared to the model-size, because the size of one element should represent the characteristic length of the damage zone; also mechanism like Fracture-Energy makes the model generally independent on the Mesh-Size[Grassl, 2014]. This first mesh-size lead that the stresses orthogonal to the free surface are not zero, they were in the

pre-peak up to -190MPa for a concrete, which sustain an uniaxial compression of -38MPa (≙C30/37) (see **Fig. 9.2**)

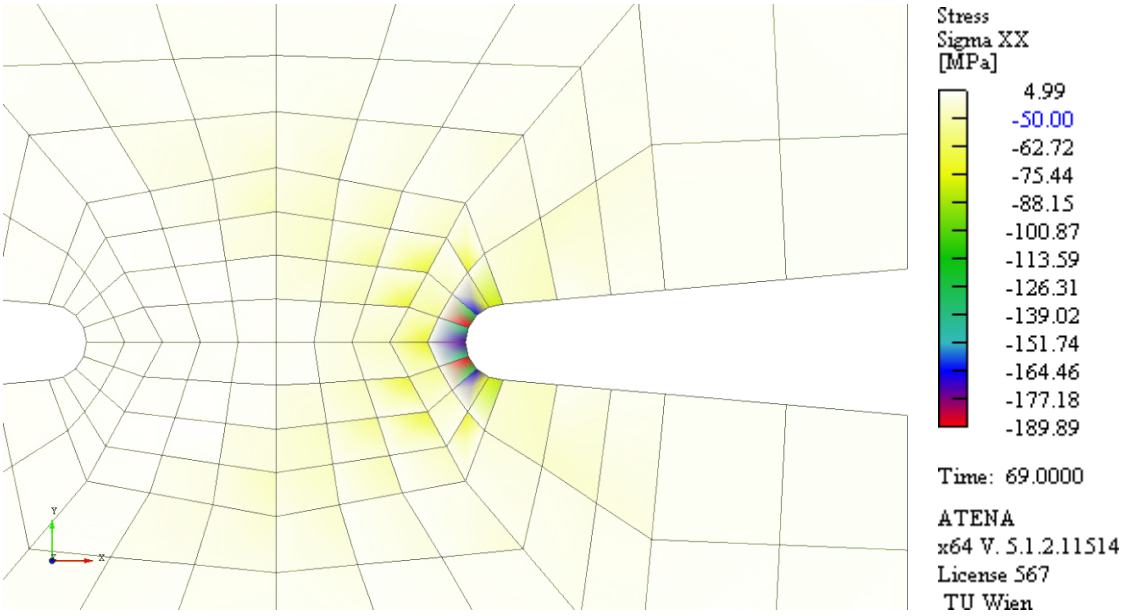

Fig. 9.2: The horizontal Stress at the quadrant-point is -173MPa (white are compressiv-stresses lower than 50MPa)

If you look at a 100-times-finer mesh you see that the gradient at this area is extremely high. (See **Fig. 9.3**) So for finite Analysis you have to be careful with choosing the mesh-size. Many think that a finer mesh would have better results, but especially if you look at tension cracking, the mesh-size has to have a reasonable size, depending on the Aggregate Size. If the mesh is smaller than the aggregate Size it cannot represent it as a homogeneous continuum and it is not possible to represent the damage-zone at all, which has a certain size. A crack in Finite Elements starts in general the "weakest" Element, which leads to stress concentration in the next element, which leads to crack which follows the mesh. And this crack is generally one element thick[11]. Because the crack opening is calculated in FE-Software as a big strain in one element, which leads to bigger strains in smaller elements, also the have the same crack opening. Because in FE-Software stresses are calculated as a function of strain, the parameters like post-peak-strains (post-peak of one element) and fracture energy have to be adapted.

[11] Except you use discrete crack-modelling, which would take so much time that you often can hardly use it. Therefore it is not implemented in Atena, but the smeared-crack-approach seems to be one of the best implemented in FE-Software.

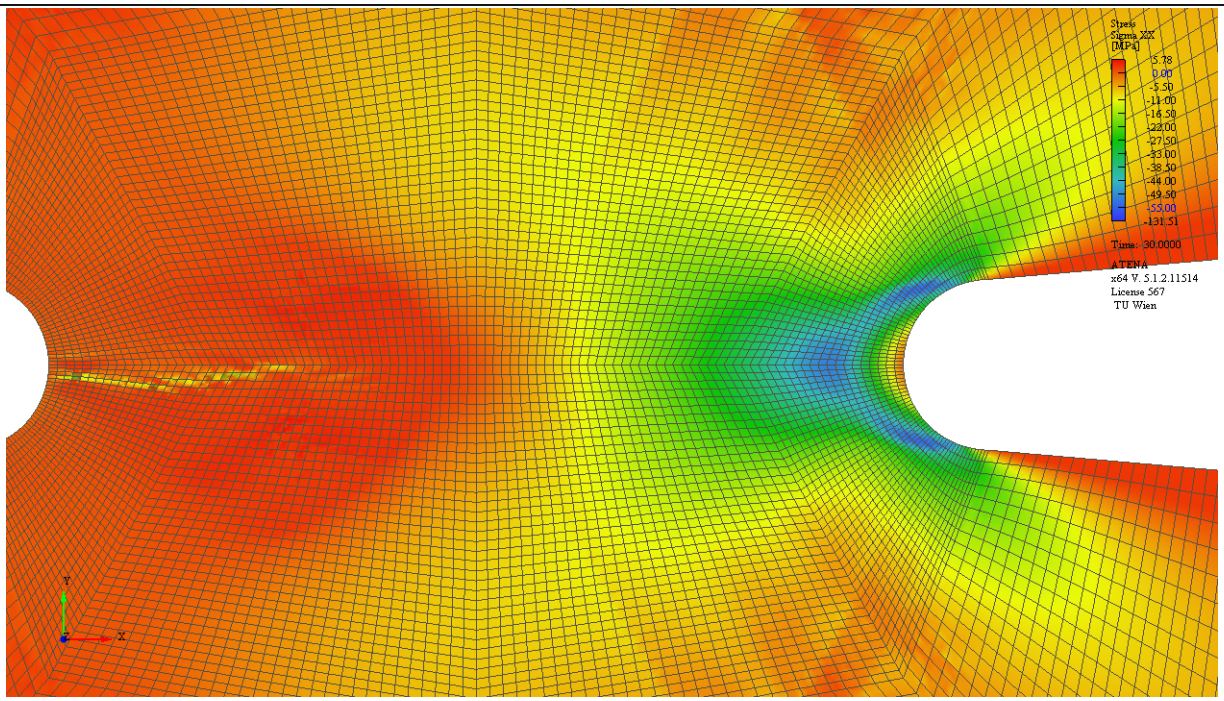

Fig. 9.3: σww in the area of the notch with a mesh of 0.6mm in the hinge-neck

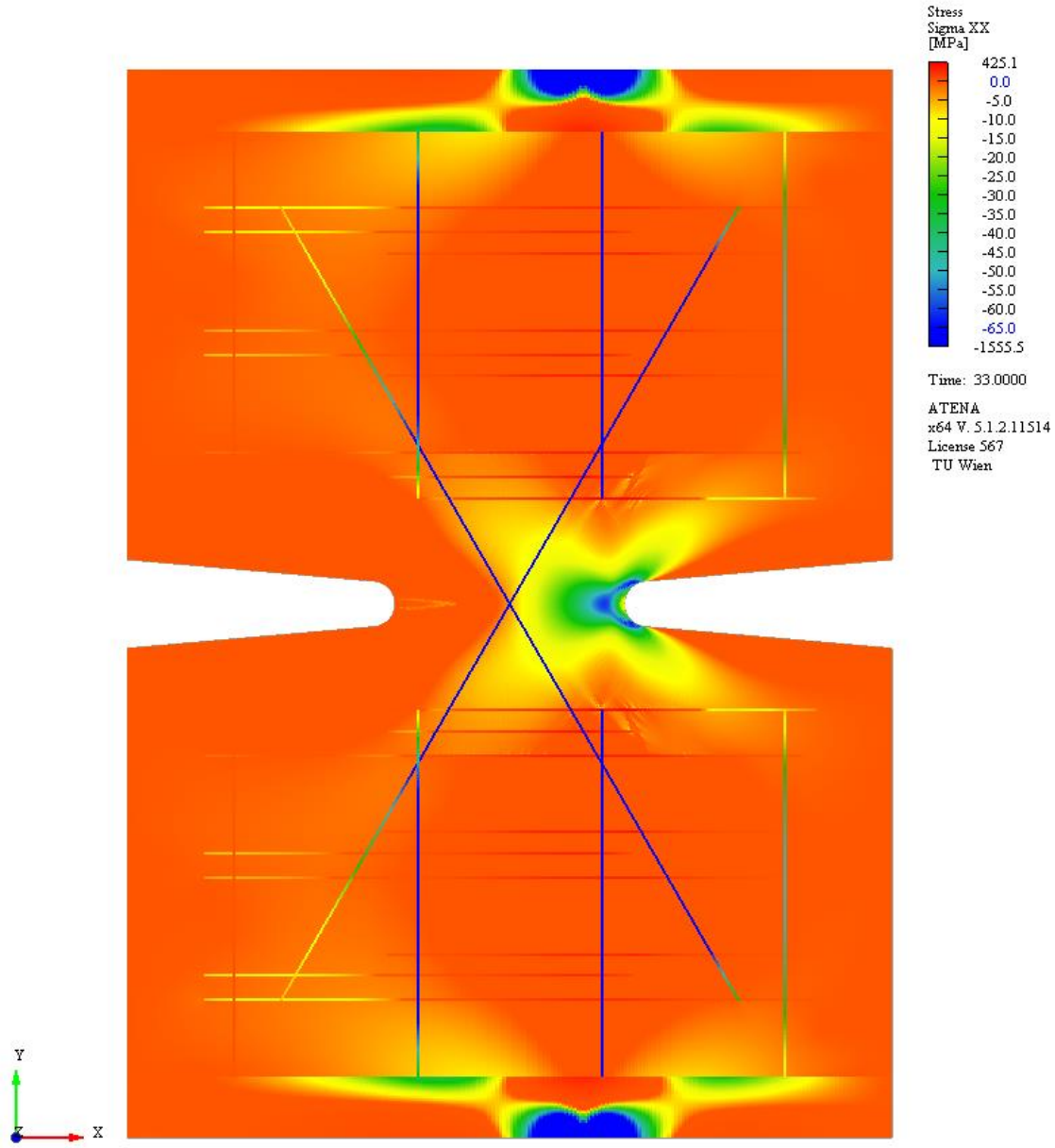

Fig. 9.4: σww in the area of the notch with a mesh of 0.3mm in the hinge-neck

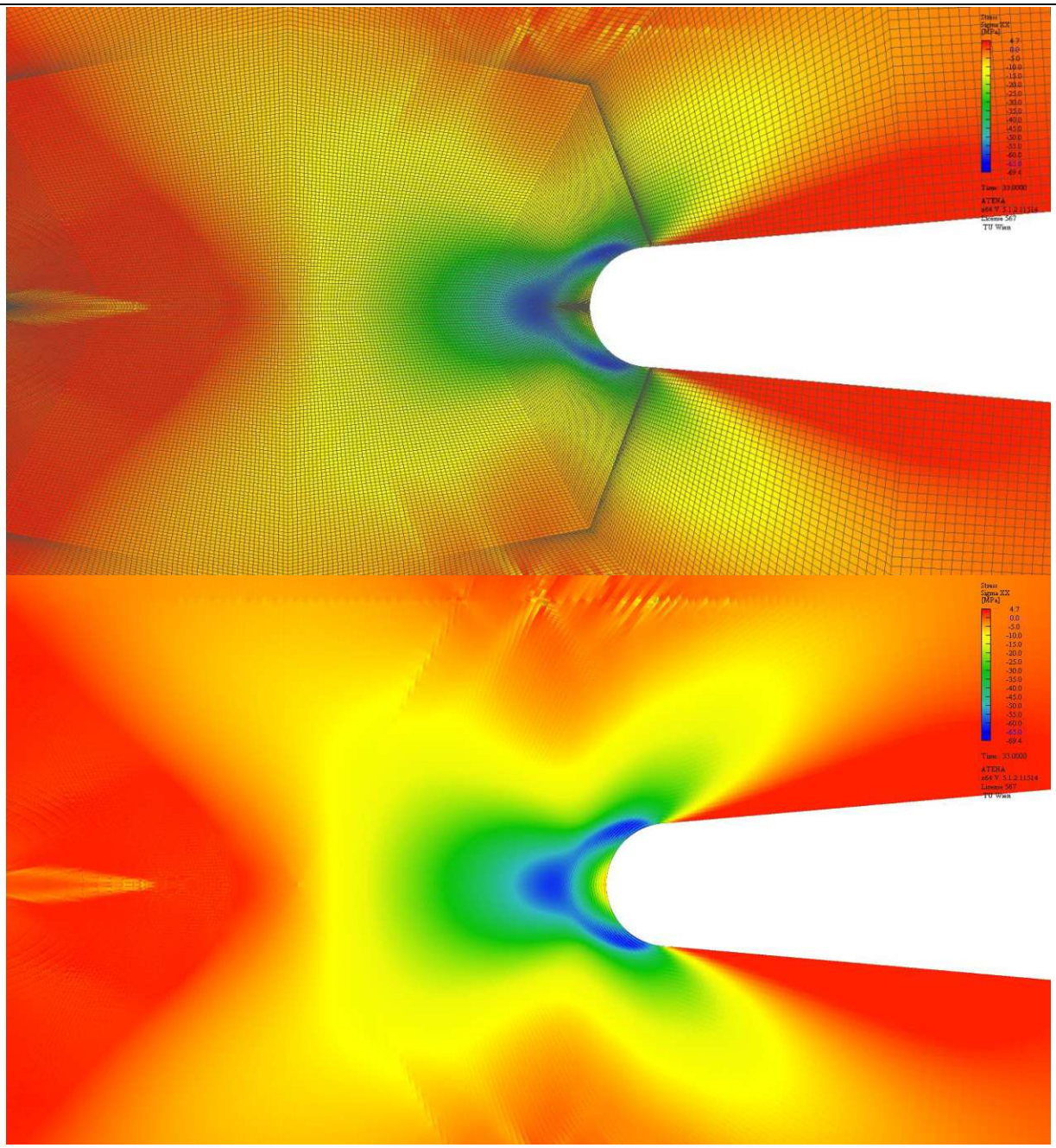

Fig. 9.5: σww in the area of the notch with a mesh of smaller than 0.3mm in the hinge-neck

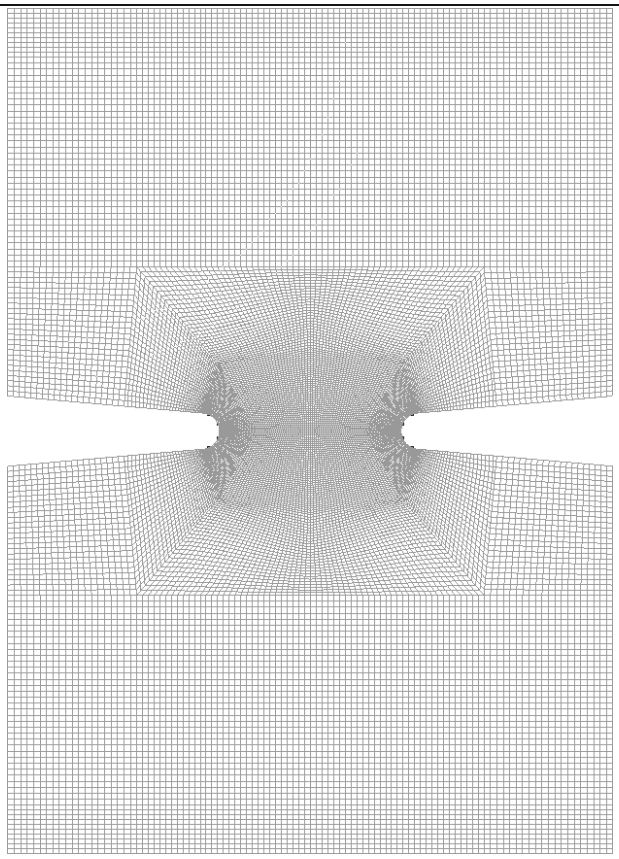

Fig. 9.6: The meshed 2-D-double-Mode, with a mesh-size of 0.7mm in the hinge-neck

This model with a finer mesh gets much better results for the stresses in the "hinge-neck". According to Dix [Dix, 1962] the Model of Stresses and Strains should be separated into the "Hinge-Neck", which is the part between the notch, and the "Hinge-Head", which is the part where the most important failure mode is the indirect tensile stress splitting (Brazilian Test). The stresses at the free surface must be zero by definition, so also the FEM-Model should come to the same solution, but the "coarse" mesh, with a mesh-size of about 7.5mm · 7.5mm returns compressive stresses at the free surface up to about 200 MPa (see **Fig. 9.9a**) for a concrete C30/37, with a mean-uniaxial compressive strength of 38 MPa. The mesh with a mesh-size of about 0.75mm · 0.75mm simulates compressive stresses of about 8 MPa till peak-load for the same concrete (see **Fig. 9.10b**) (after Peak up to about 10 MPa). Also 8 MPa are still about 20% of the compressive strength, but it is only one element-row of a thickness of 0.75mm, therefore it is negligible. A studies of a finer mesh (0.3-0.35mm), show that there are mostly differences in this last surface-element, and next to the 8mm-reinforcement bars. Also this finer mesh had the same problem of the last surface-element that has compressive stresses up to about 13 MPa (see **Fig. 9.11**) (16 MPa in Post-peak). Also the 7mm-Mesh looks quite coarse (see **Fig. 9.7a, Fig. 9.8a**, **Fig. 9.9a**, and **Fig. 9.12a**), but it is already finer than the reinforcement bar (8mm) or the aggregate-size (8mm), so a (much) finer mesh is in general not very meaningful in concrete. You can consider a material in a quite good approximation if the representative volume is about 2^3 to 3^3 bigger than the biggest aggregate size (reasons see [Hellmich, 2012]). Anyway to have a reasonable compromise between of representative homogenous material and a converted mesh-size a mesh-size in the hinge-

neck of 0.75mm (100Elements over the neck-thickness) (increasing up to 2.7mm) is chosen for analysis.

$\sigma_{LL,max}$ is for the 7mm-Mesh about 11times the compressiv strength (see **Fig. 9.7a**). It is very unlikely that a concrete can sustain such high loads, at the node on the free surfrace. Every common FE-Software calculates at some integration points and extrapolates the stresses and strains to the nodes, and afterwards the software takes an average of the calcuated value of each elementnode for the output of a node. [Trouble, 2015]
The following pictures shows you on the horizontal Achsis the coordinates of the With-Direction and on the vertical Achsis the Stresses.

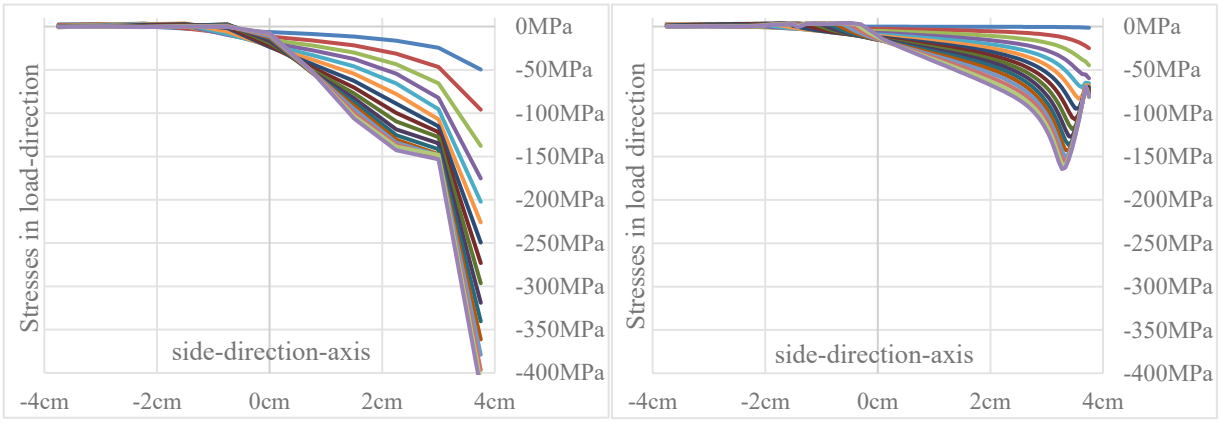

Fig. 9.7: Stresses of different load-steps in load-direction; left: coarse mesh (7.5mm), right: fine mesh (0.75mm)

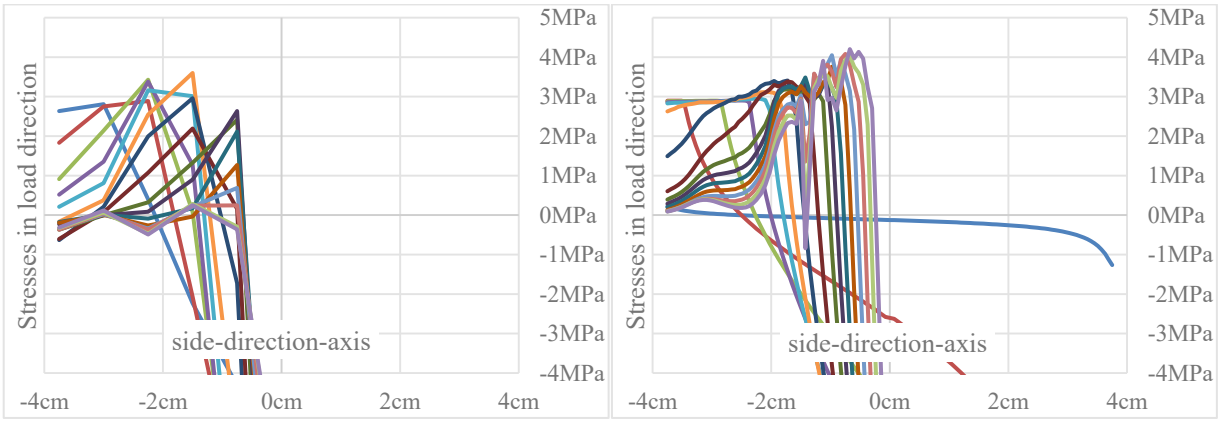

Fig. 9.8: Stresses of different load-steps in load-direction; left: coarse mesh (7.5mm), right: fine mesh (0.75mm)

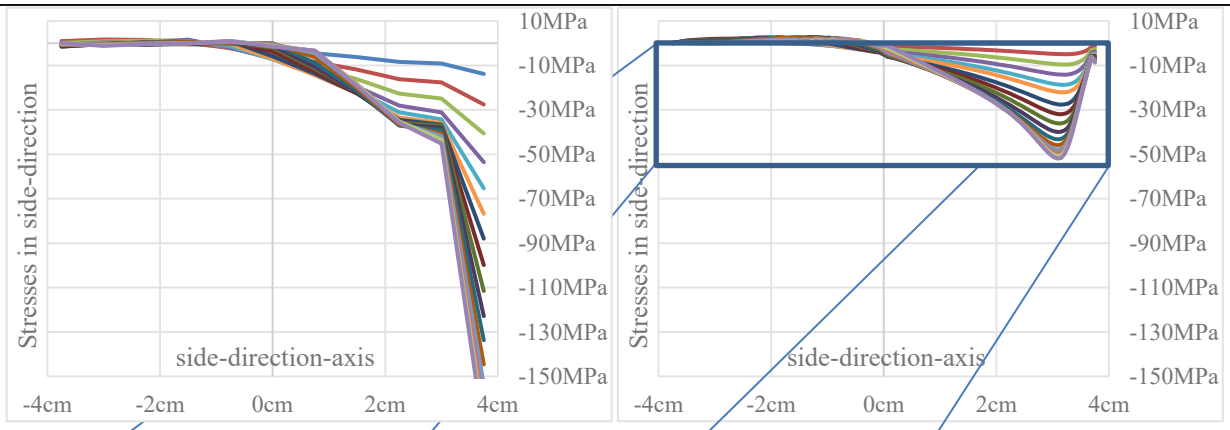

Fig. 9.9: Stresses of different load-steps in side-direction; left: coarse mesh (7.5mm), right: fine mesh (0.75mm)

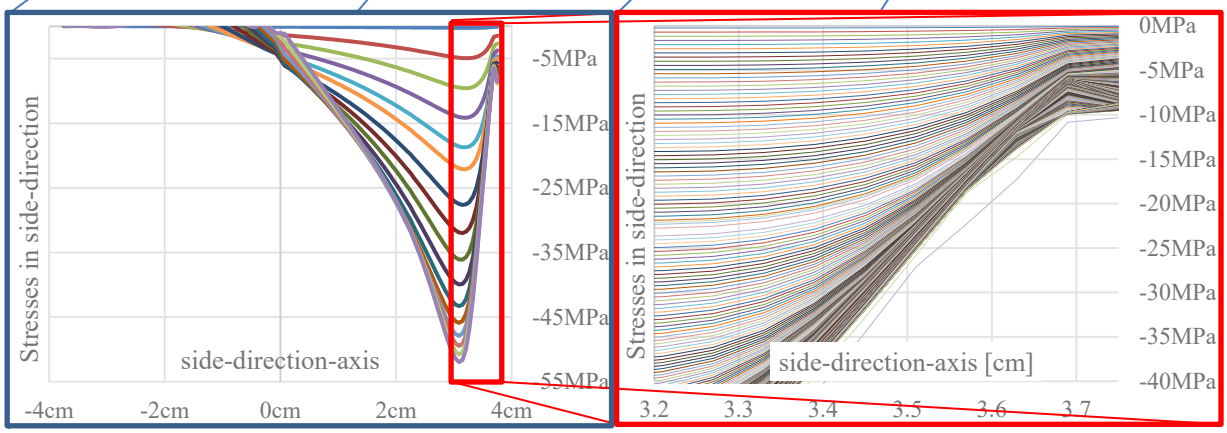

Fig. 9.10: Stresses of different load-steps in side-direction of the meshsize of 0.75mm more in detail

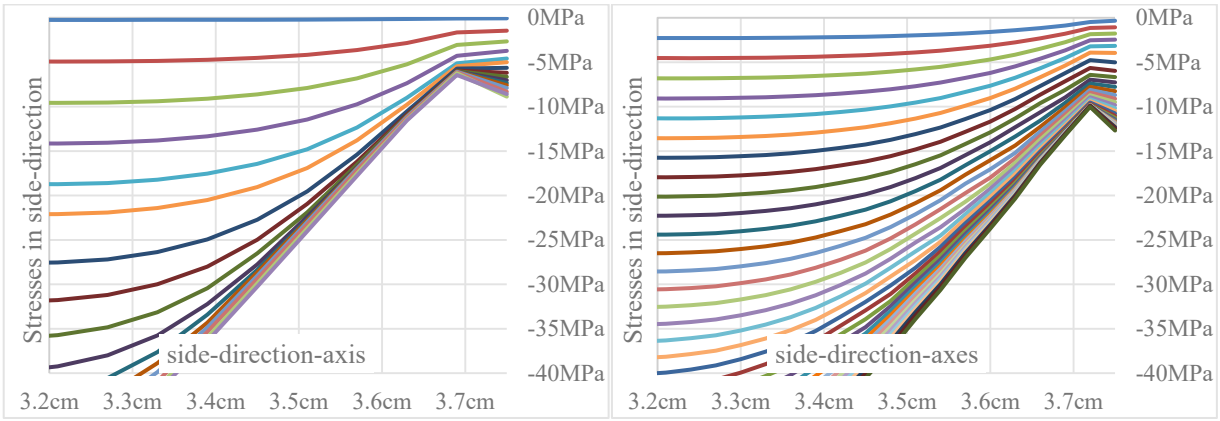

Fig. 9.11: Stresses of different load-steps in side-direction; left: 0.75mm-Mesh; right: 0.3mm-Mesh

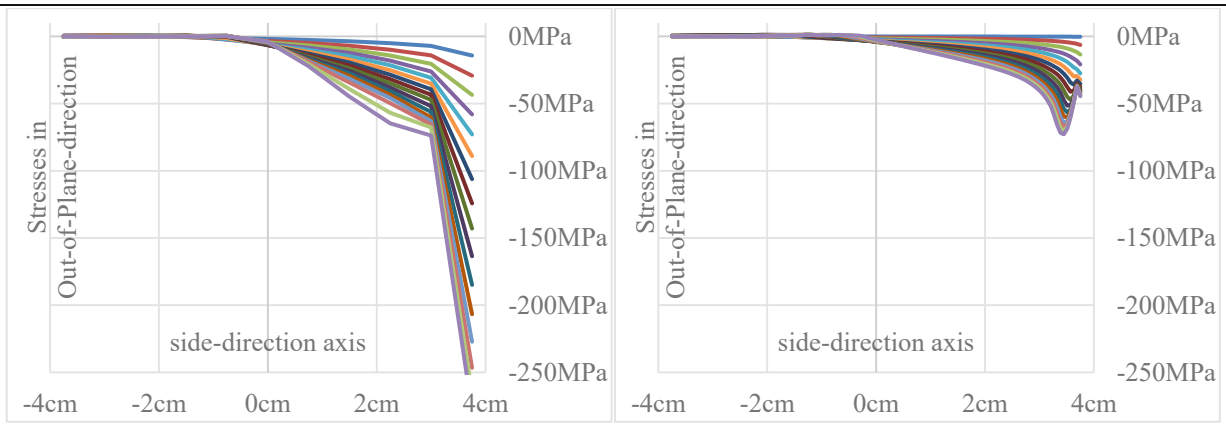

Fig. 9.12: Stresses of different load-steps in out-of-plane-direction; left: coarse mesh (7mm), right: fine mesh (0.7mm)

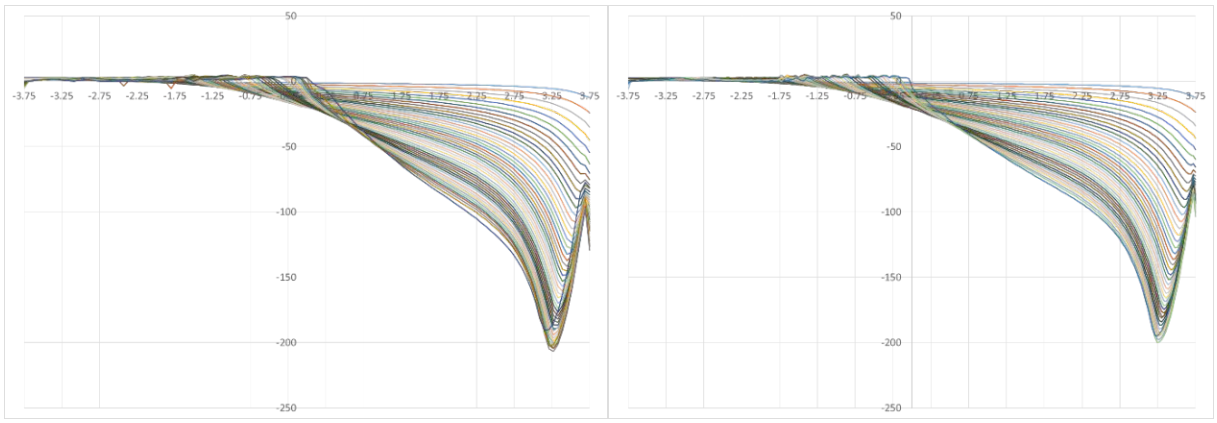

Fig. 9.13: comparison σ_{LL} between 0.75mm (left) and 0.3mm-Model (right)

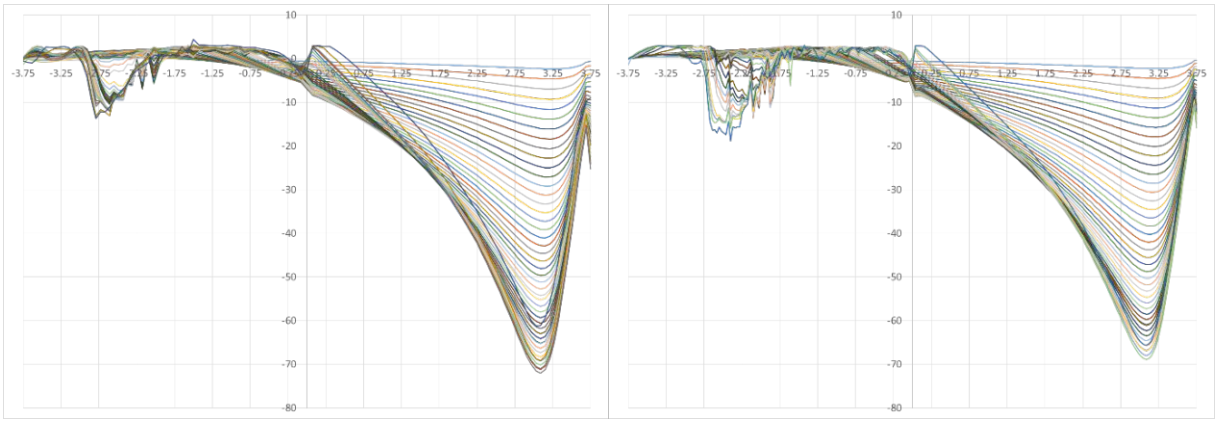

Fig. 9.14: comparison σ_{SS} between 0.75mm (left) and 0.3mm-Model (right)

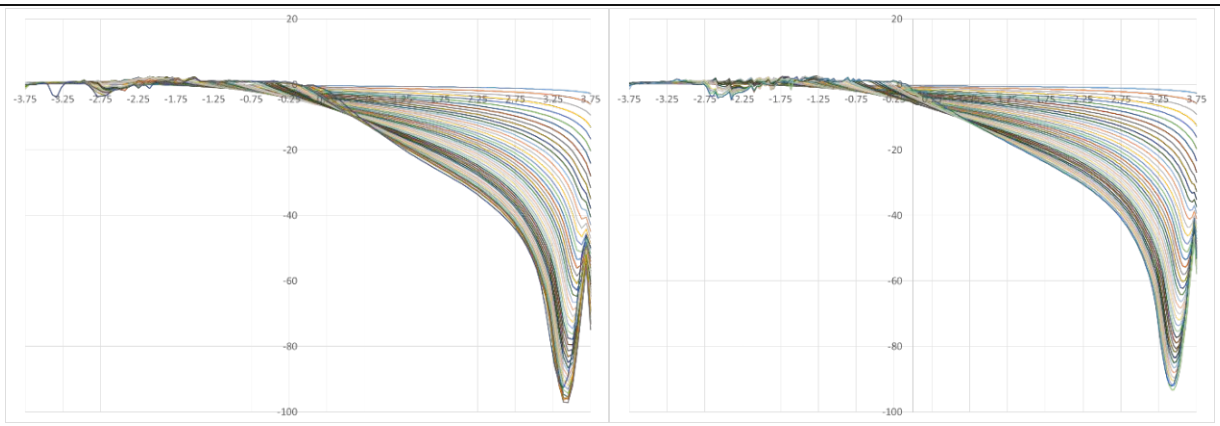

Fig. 9.15: comparison σ_{TT} between fine 0.75mm (left) and extra-fine-0.3mm-Model (right)

The load-displacement curve does not change that much, compared to the big differences in the neck. (see **Fig. 9.16**)

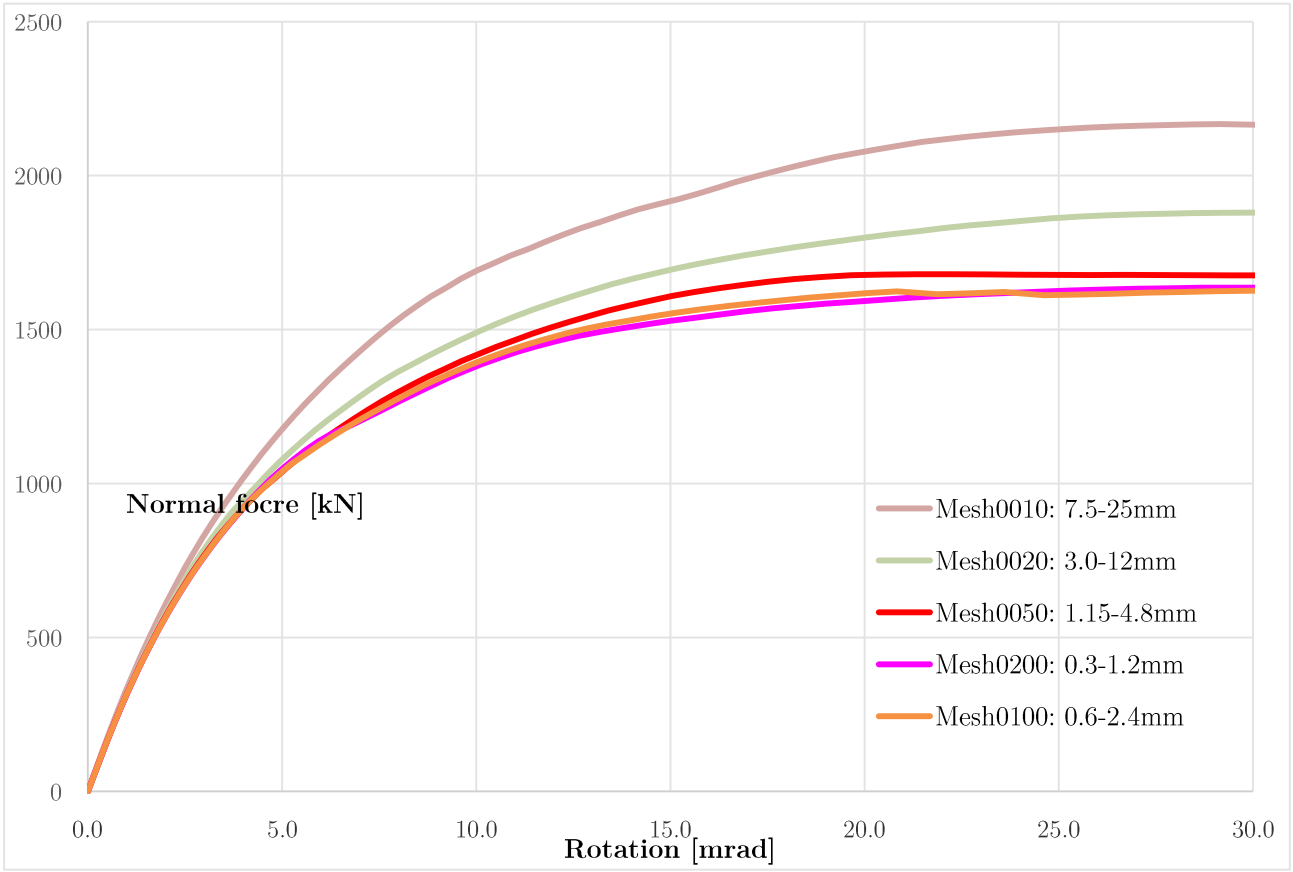

Fig. 9.16: comparison between coarse (7.5mm in brounish) and fine (lower lines) meshes

9.2 Convergence regarding iteration error in context of incremental-iterative solution concept

In **Fig. 9.17** you can see the difference results, with different convergence-Errors. The gray line is calculated with standard values, the others have 10times or 100times smaller allowed error, and there are almost no differences, so to have a converted results you should change the values according to **Table 4**. The iteration Limit should also be increased, because otherwise it would not reach the allowed tolerance for most of the steps, therefore you should check the convergence summary after the calculation, not all steps have to convert. The convergence error between the lines has a maximum of 10.3%, but because some calculations with a smaller convergence error finished before they reached the ultimate failure load the overestimation due to convergence error of the failure load might be a little bit higher.

The source of this convergence errors might be mostly in the hinge neck, where it is very likely that there are the biggest stress gradients.

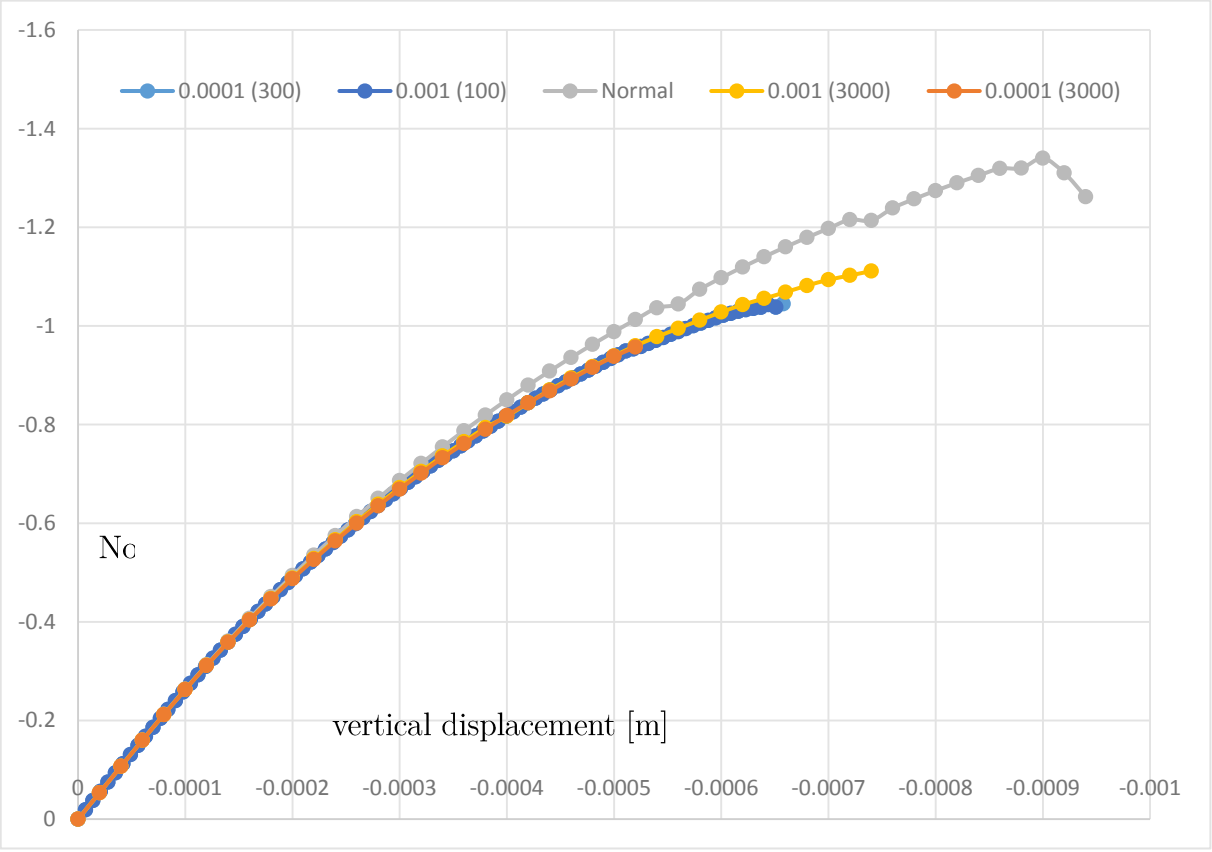

Fig. 9.17: comparison of different allowed convergence-Errors

Hinge-neck-stresses. The convergence error influences the failure load quite much, as you can see in **Fig. 9.17**. For a better understanding of the difference of the peak load, the following work looks also at the stresses in the hinge neck. The calculation for the smaller convergence error could not finish (error at 0.75mm vertical displacement), but the calculation with the standard configuration calculated further. To be able to compare the results all further load-steps were also deleted in the standard configuration, except the one step with the highest load, which is pink in the following three left graphs (**Fig. 9.18**a, **Fig. 9.19**a,

Fig. 9.20a). The peak-load at 0.75mm is about 10% higher in the standard configuration, the maximum of the Stresses in the Load-Direction are 15.1% higher and in the Thickness-Direction 14.8%, but the interesting is that with a stricter convergence error the stresses in the Side-Direction (With-Direction) are 34.7% to high, which you can clearly see in **Fig. 9.19**. The gradient of the stresses in the side-Direction are quite big in the area of the biggest stresses, as you can see in **Fig. 9.5**.

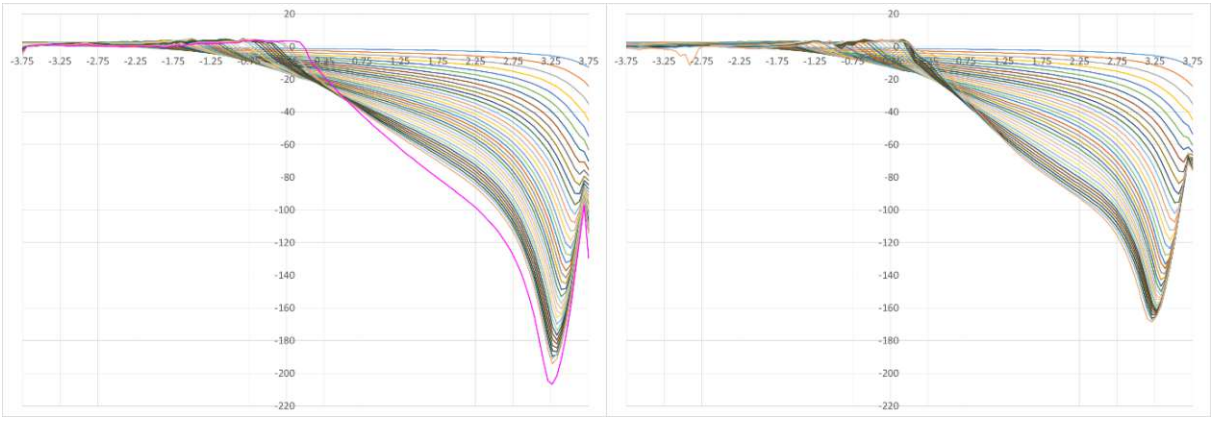

Fig. 9.18: comparison σ_{LL} between standard configuration (left) and strict errors (right)

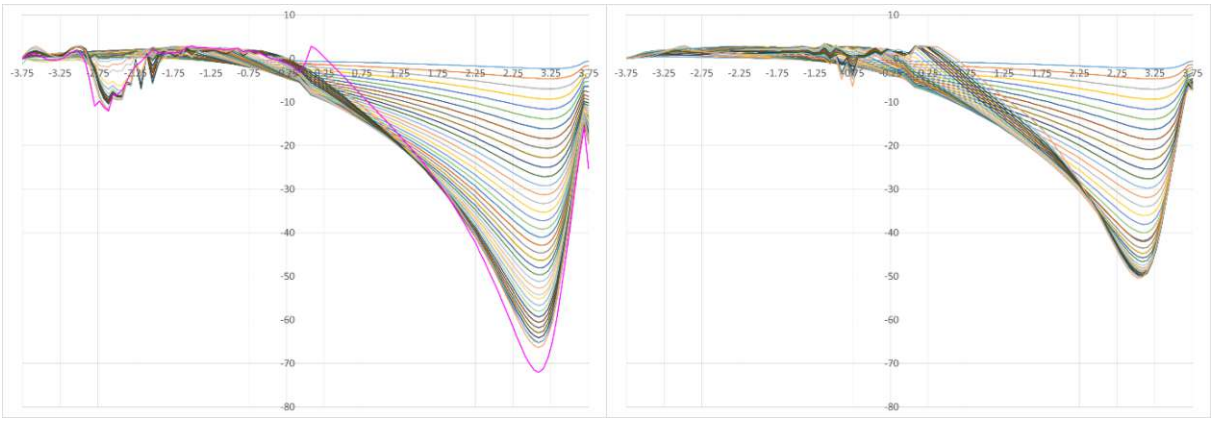

Fig. 9.19: comparison σ_{SS} between standard configuration (left) and strict errors (right)

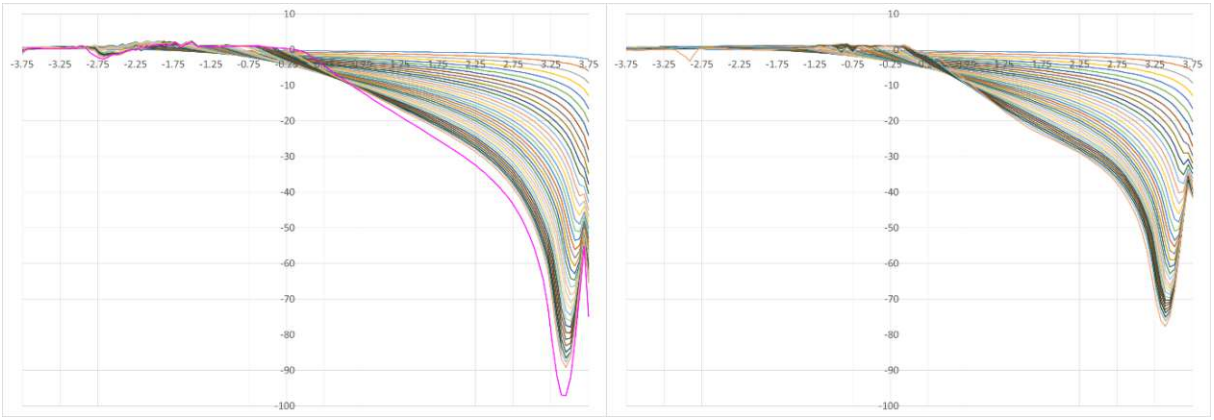

Fig. 9.20: comparison σ_{TT} between standard configuration (left) and strict errors (right)

Table 4. Recommended Error-Values.

	Default	Recommended
Displacement Error	0.01	0.001
Residual Error	0.01	0.001
Absolute Residual Error	0.01	0.001
Energy Error	0.001	0.0001
Negligible Size Relative	0.0001	0.00001
Integration Limit	30	100 (or more[12])
Conditional Break Criteria	Off	On

10 Comparison of different material models

Several Material-model implemented in Atena were tested and came to a conclusion that Cementious2 (CEM2) and Cementitious3 (CEM3)- Models are used for further calculations.

CEM3. The Model for big triaxial compression gave slightly different results at peak-load, but the calculating times rises with a factor of four, mostly due to smaller load-steps. (see **11.1.5 Comparison of the costs of calculation**).

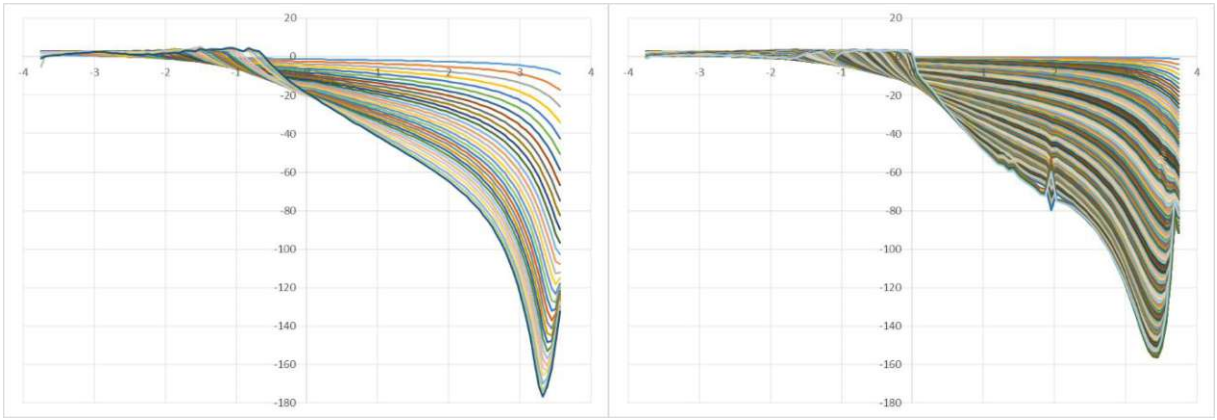

Fig. 10.1: comparison σ_{LL} between CEM2 (left) and CEM3 (right)

[12] Most of the load steps on the load path should convert; especially those load steps are important which are used for further results (for example the peak-load). In ATENA Studio v5 "Convergence summary" is a standard graph, which should always be checked for "Non-converged" steps.

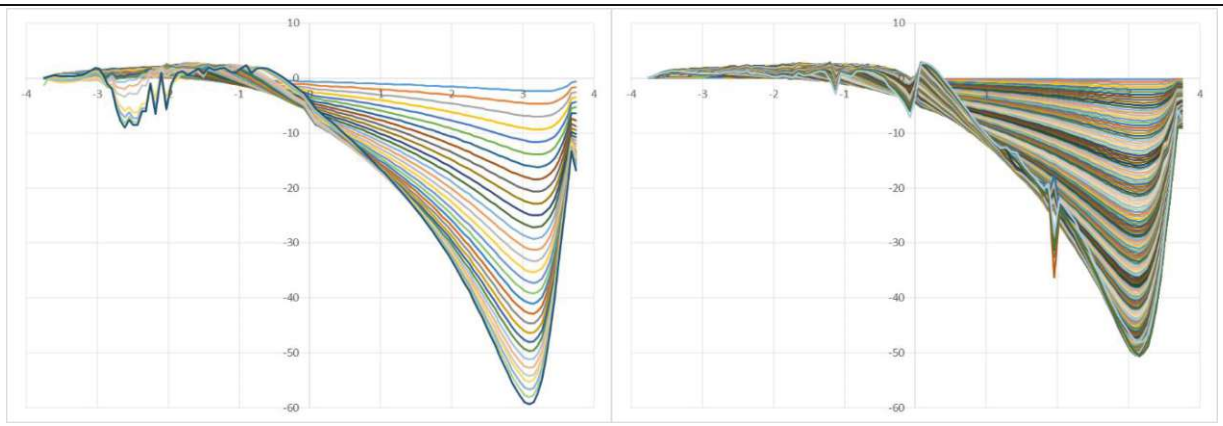

Fig. 10.2: comparison σ_{SS} between CEM2 (left) and CEM3 (right)

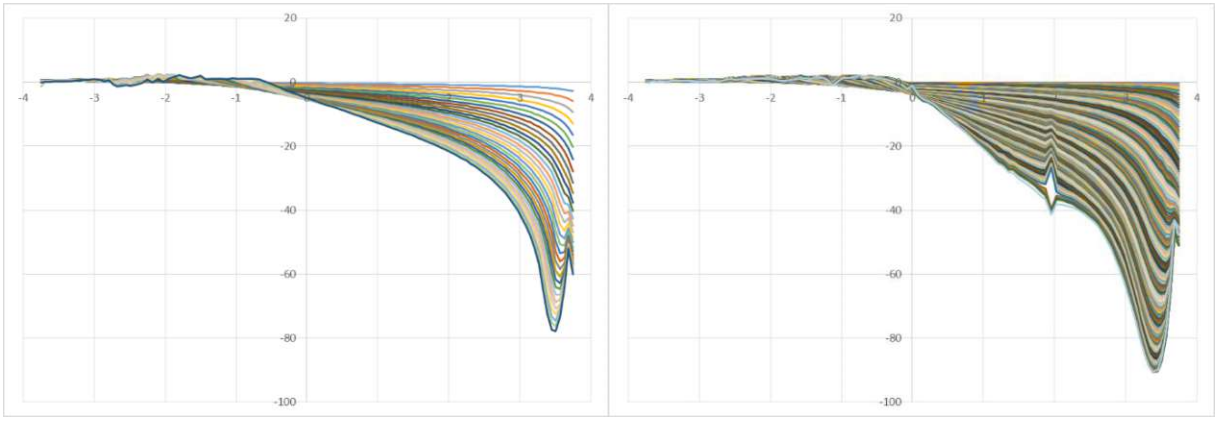

Fig. 10.3: comparison σ_{TT} between CEM2 (left) and CEM3 (right)

11 Deterministic Sensitivity Analyses carried out with ATENA Science

11.1 Comparison of plane stress, plane strain, and 3D simulations

11.1.1 2D plane stress

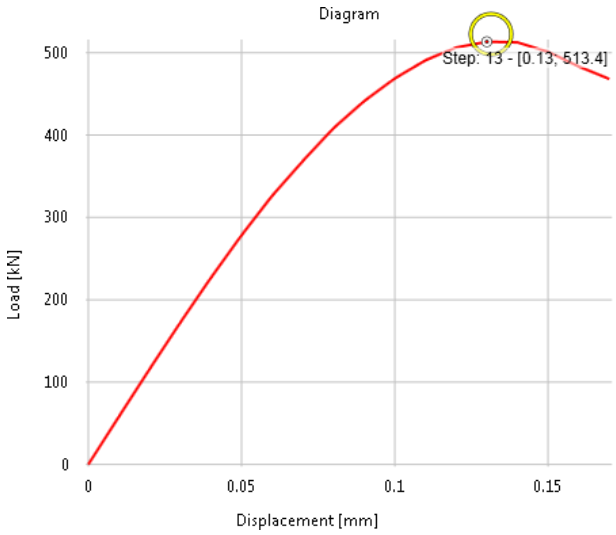

Fig. 11.1: Load Displacement – Curve Plain Stress

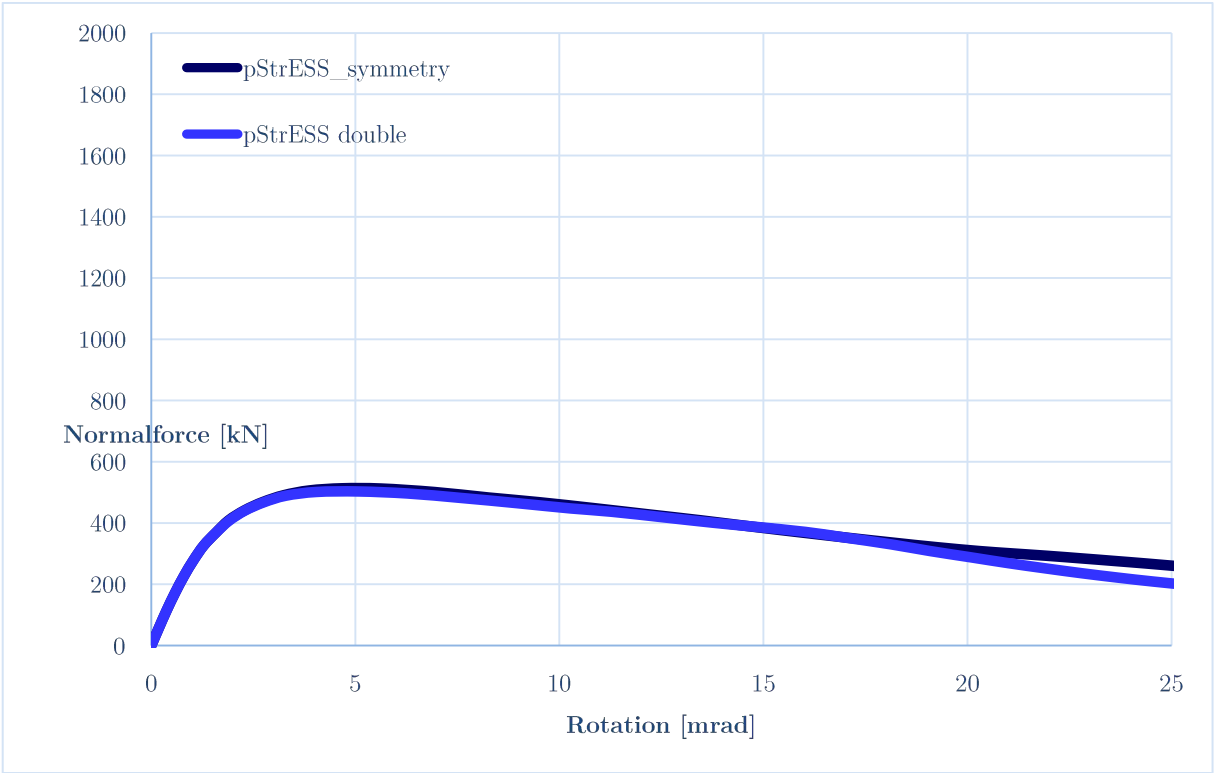

Fig. 11.2: Load Rotation – Curve; Plain Stress

The 40cm tick-plain-stress-model with an eccentricity of 24mm has a peak-load of about 510kN at a rotation of about 5.4mrad. Expressed in Model-independent values: m=e/a=0.32 and an average stress of about $0.45 \cdot f_c$. Assuming a triangular-stress-distribution a maximum stress of about $1.7 \cdot f_c$ is reached in the plain Stress-model. The differences of the plain-stress-model using symmetry-conditions and the double plain-stress-model are negligible. The plain-stress-model with symmetry-conditions reached a peak-load of about 513kN and the

double plain-stress-model reached a peak-load of about 503kN, which is a difference of 2%, which might be due to an "unsymmetrical" "dominant" crack, which unloads the "symmetrical" "opposite" crack.

Hinge-neck-stresses. The maximal compressive Stress of the plain Stress-Model is about 124% of the compressive strength, which is a reasonable number because the in the simpler 2-D-plain-Stress-Model of SBeta[13] the maximal compressive stresses are about 126%. The **Fig. 11.5** shows that seven load-steps did not convert and leads to tension-stresses of about 0.5MPa, and those load-steps, which converted within the tolerance, have compression-stresses of about 0.05MPa, which is about 1‰ of the compressive strength.

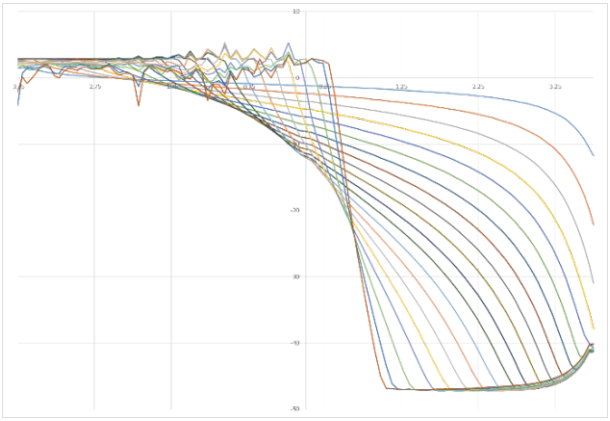

Fig. 11.3: σ_{LL}

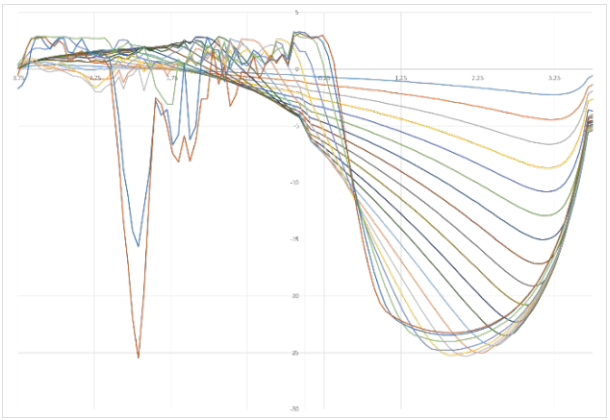

Fig. 11.4: σ_{SS}

[13] *"SBETA was our very first product developed in 80's for DOS operating system. It was a first user-friendly non-linear FE software package on the market for non-linear finite element analysis of concrete and reinforced concrete structures. […]"*
— [Trouble, 2015] in Question 2.1.3 of the Troubleshooting Manual of Atena

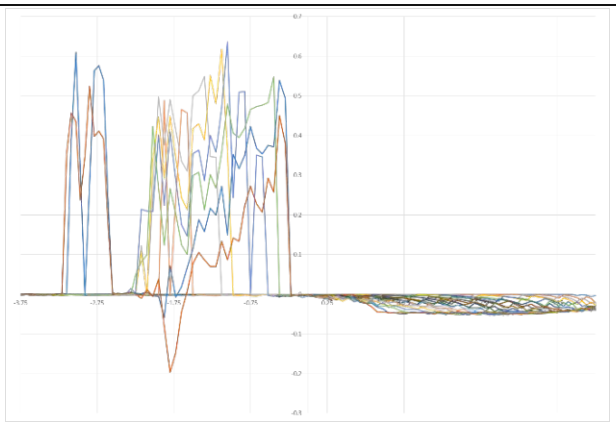

Fig. 11.5: σ_{TT}

11.1.2 2D plane strain

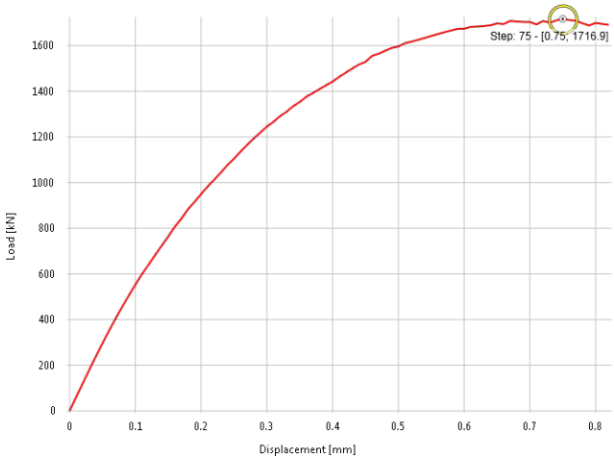

Fig. 11.6: Load-Displacement – Curve Plain Strain

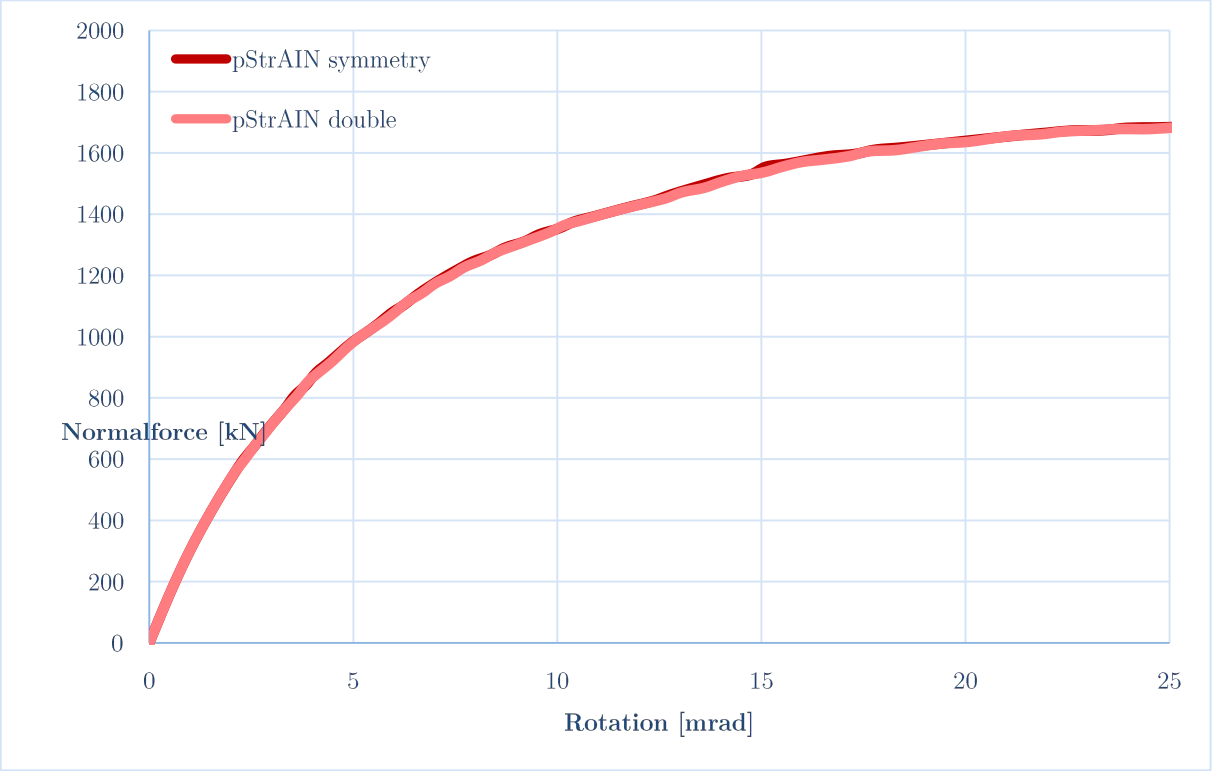

Fig. 11.7: Load Rotation – Curve; Plain Strain

Load carrying capacity. The 40cm tick-plain-strain-model with an eccentricity of 24mm has a peak-load of about 1710kN at a rotation of about 32mrad. Expressed in Model-independent values: m=e/a=0.32 and an average stress of about $1.5 \cdot f_c$. Assuming a triangular-stress-distribution a maximum stress of about $5.6 \cdot f_c$ is reached in the plain-stain-model. The differences of the plain-strain-model using symmetry-conditions and the double plain-strain-model are negligible. The plain-strain-model with symmetry-conditions reached a peak-load of about 1717kN and the double plain-strain-model reached a peak-load of about 1709kN, which is a difference of 5‰, which might be due to an "unsymmetrical" "dominant" crack, which unloads the "symmetrical" "opposite" crack.

Hinge-Neck-Stresses. The compressive-stresses in load-direction are up to 200MPa, the stresses in side-direction are up to about 70MPa and the out-of-plane-stresses are up to about 100MPa. Not considering that they occur on slightly different places, this stresses have a stress-ratio of about 1:0.3:0.5, which lead to a triaxial-stress behaviour with a high compressive-strength. The peak-stresses are up to about 5 times of the compressive strength, also they are very local. The Eurocode2 allows for this geometry without front notch (**Fig. 8.1**) a compressive strength of $\sqrt{3} \cdot f_{cd}$ and for the geometry with front notch (**Fig. 8.5**) a compressive strength of $2 \cdot f_{cd}$[EN1992, 2011][Marx, 2009].

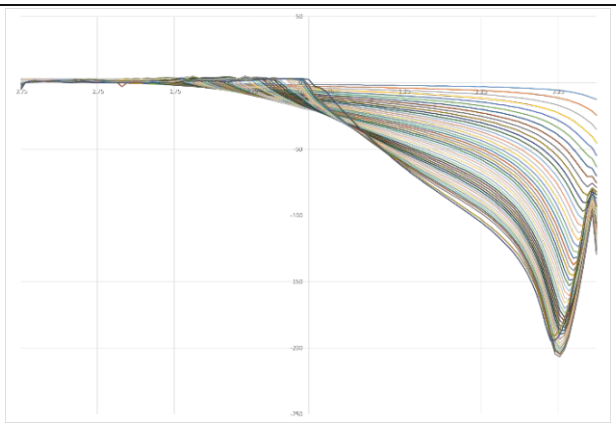

Fig. 11.8: σ_{LL}

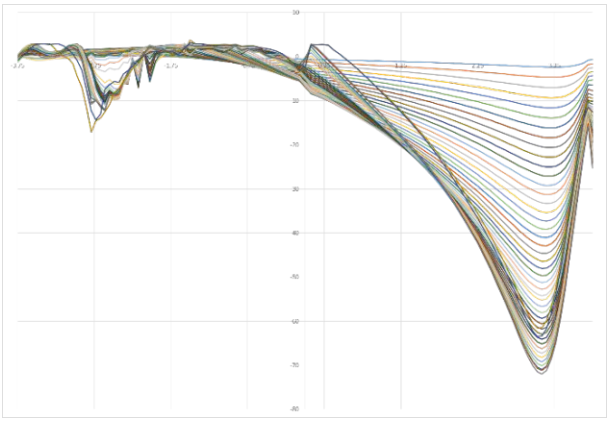

Fig. 11.9: σ_{SS}

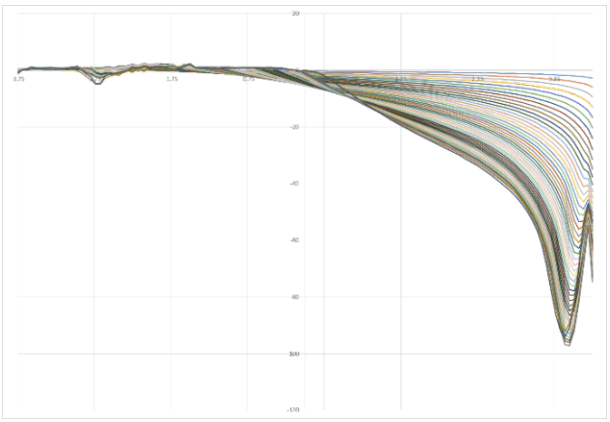

Fig. 11.10: σ_{TT}

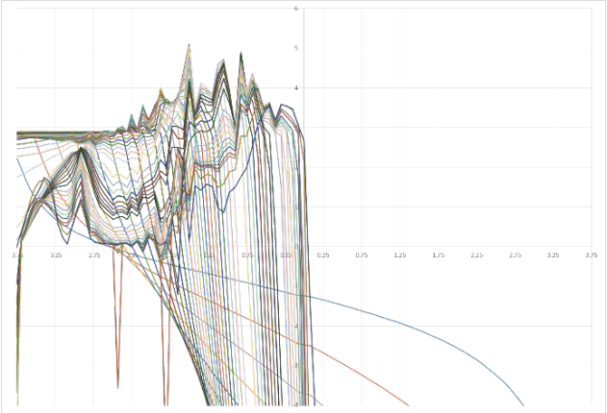

Fig. 11.11: Tension-stresses in σ_{LL}

11.1.3 3D

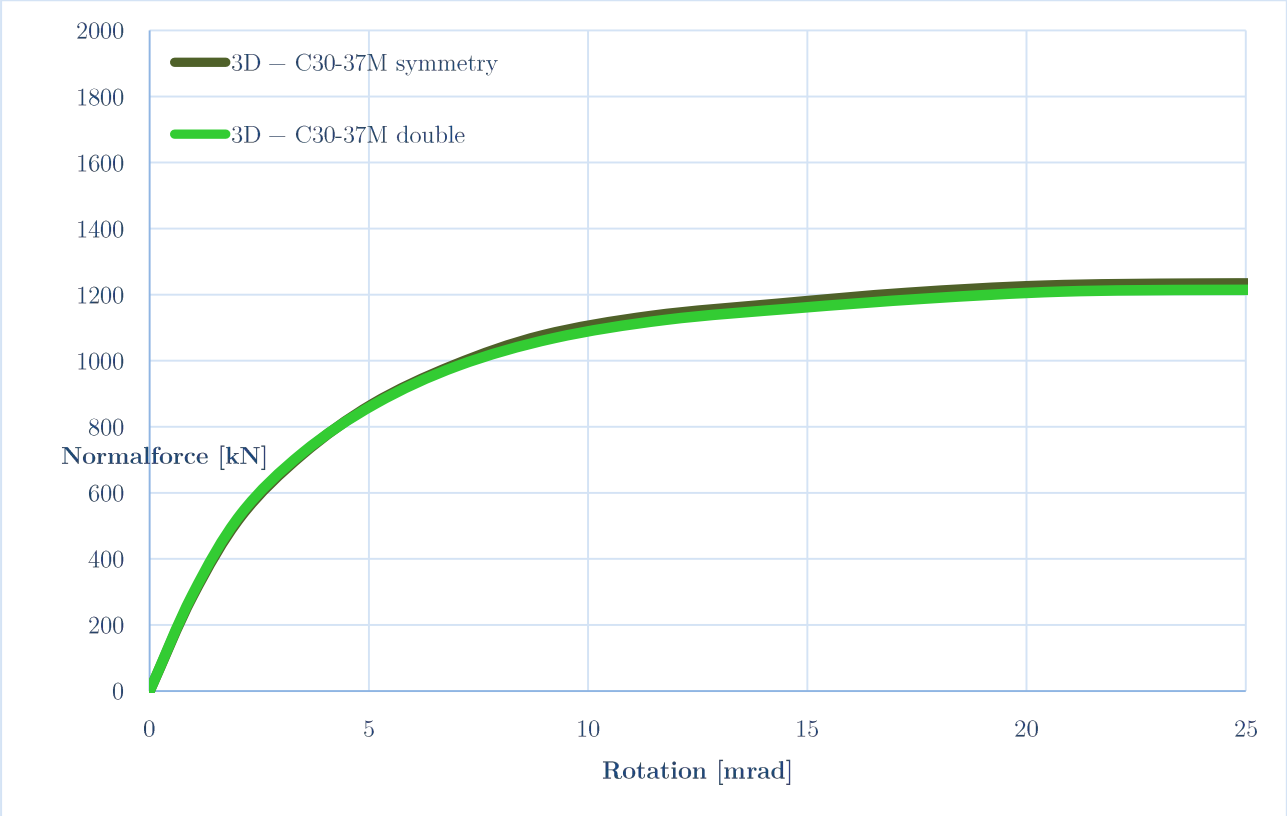

Fig. 11.12: Load Rotation – Curve; 3D

Load carrying capacity. The 40cm tick 3D-model with an eccentricity of 24mm has a peak-load of about 1220kN at a rotation of about 24mrad. Expressed in Model-independent values: m=e/a=0.32 and an average stress of about $1.1 \cdot f_c$. Assuming a triangular-stress-distribution according to Leonhard a maximum stress of about $4.0 \cdot f_c$ is reached in the 3D-model. The differences of the 3D-model using symmetry-conditions and the double 3D-model are negligible. The 3D-model with symmetry-conditions reached a peak-load of about 1233kN and the double plain-strain-model reached a peak-load of about 1214kN, which is a difference of 16‰, which might be due to an "unsymmetrical" "dominant" crack, which unloads the "symmetrical" "opposite" crack.

Hinge-Neck-stresses. The stress-dimension is plotted in color-dimension instead of in a geometric-dimension, because the hinge-neck is now a 2D-Area. In the following figures (**Fig. 11.13**, **Fig. 11.14**, and **Fig. 11.15**) you can see that the stresses, especially the stresses in load-direction, are over ¾ almost equal, only at the surface the stresses are decreasing, so plain-strain seems to be a good assumption for the concrete hinge.

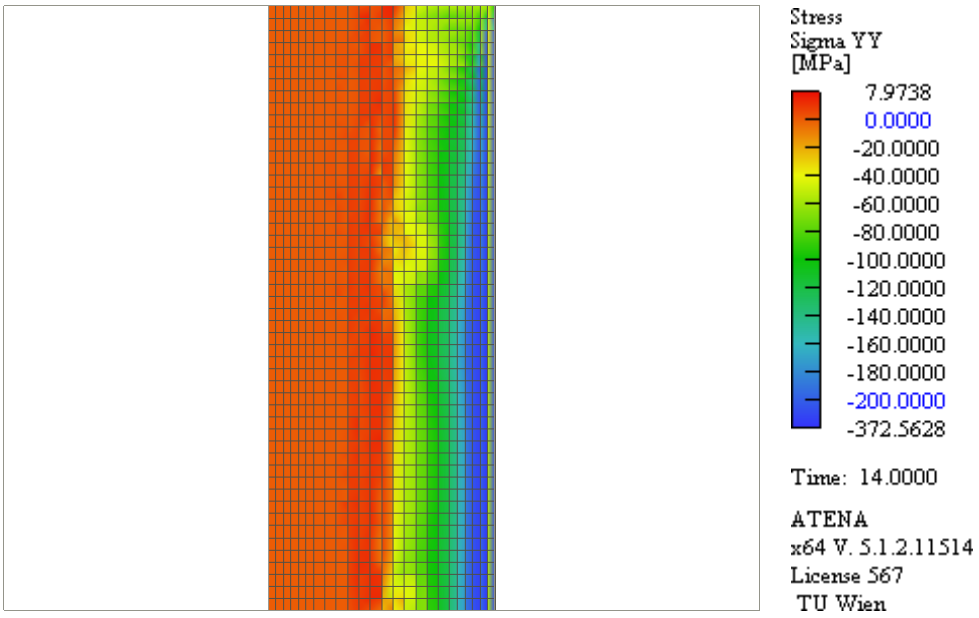

Fig. 11.13: σ_{LL} in the hinge-neck

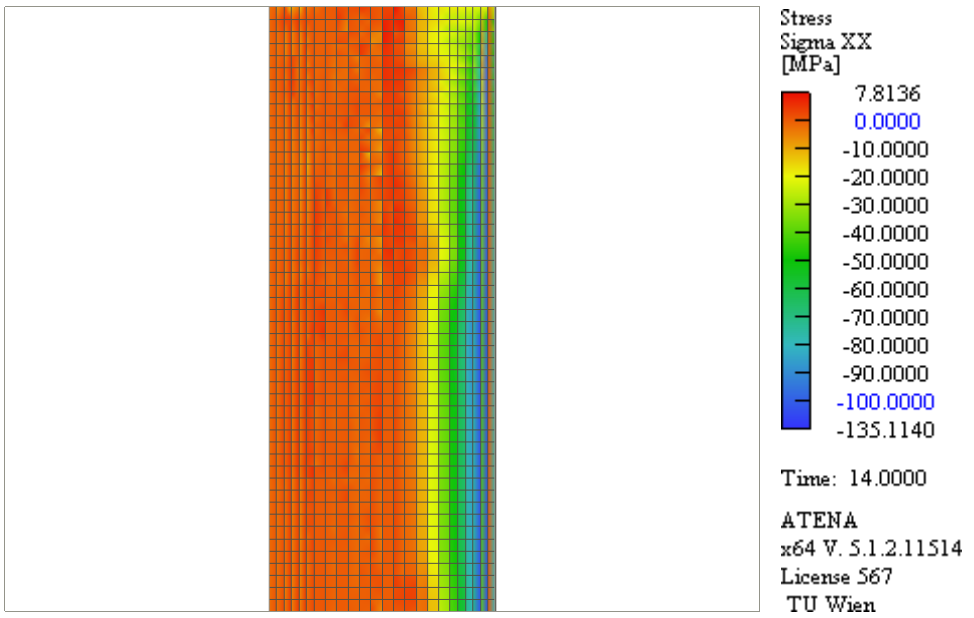

Fig. 11.14: σ_{ss} in the hinge-neck

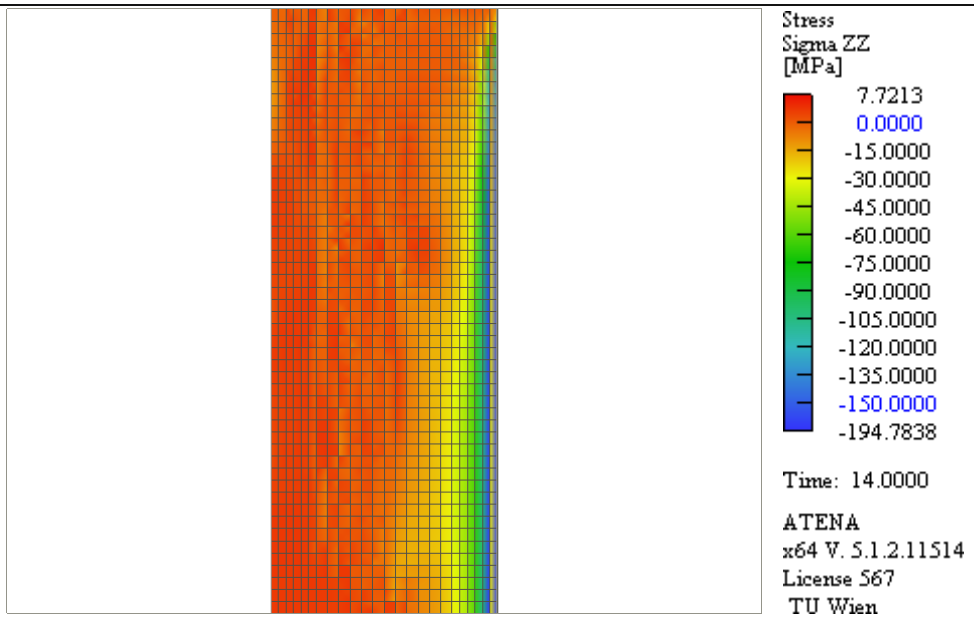

Fig. 11.15: σ_{TT} in the hinge-neck

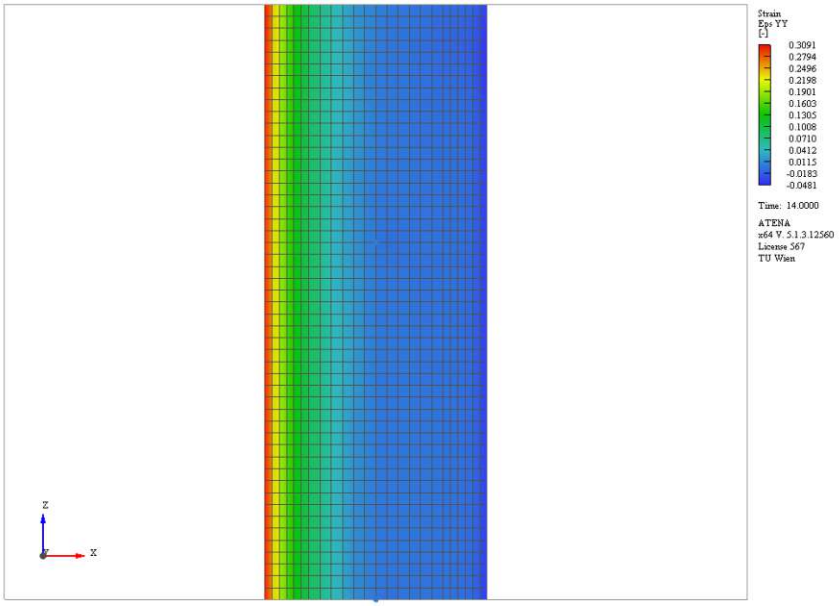

Fig. 11.16: ϵ_{LL} in the hinge-neck

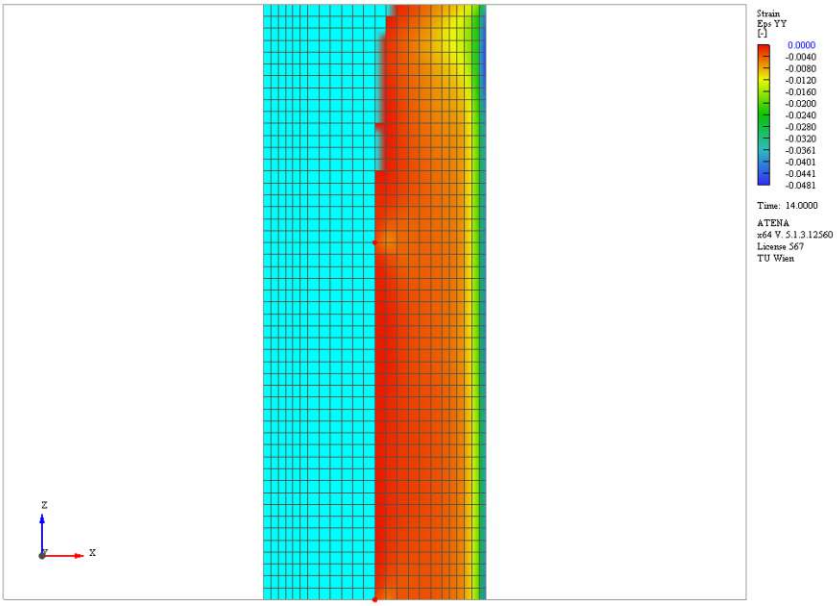

Fig. 11.17: ϵ_{LL} in the hinge-neck (compressive strains)

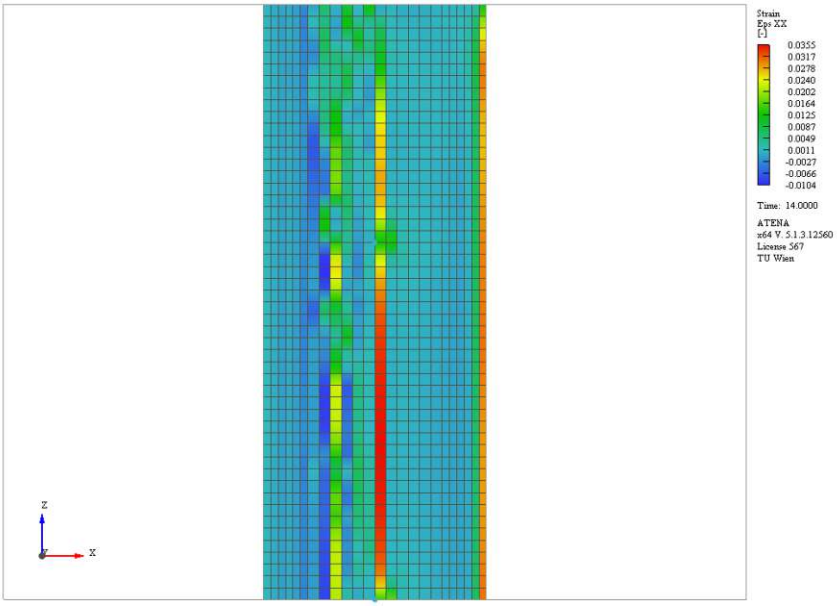

Fig. 11.18: ϵ_{SS} in the hinge-neck

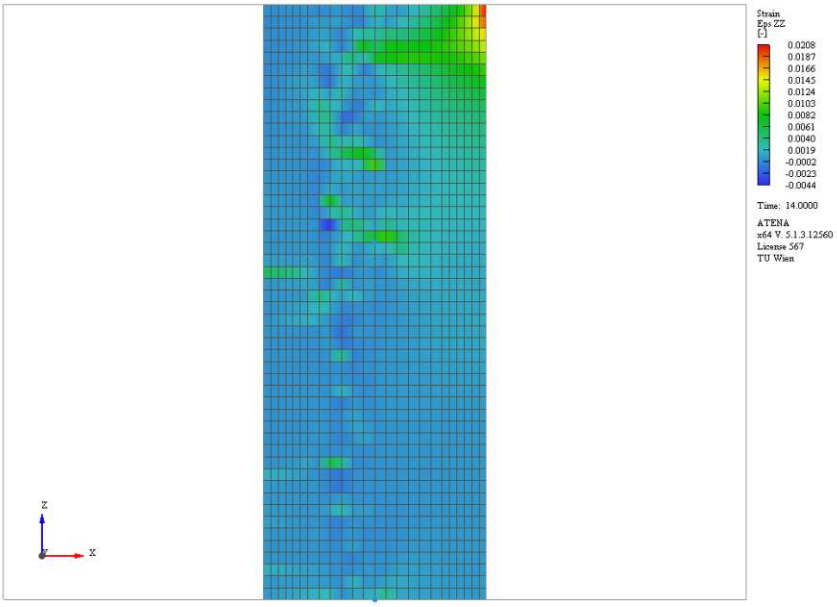

Fig. 11.19: ϵ_{TT} in the hinge-neck

The stresses at the hinge neck stresses on the compressive-side-surface **Fig. 11.20**, are almost constant in the middle and reduce to the front/back-surface (**Fig. 11.21**, **Fig. 11.22**, **Fig. 11.23**). The stresses orthogonal to the free surface (stresses in side-direction) are not zero, which is due to extrapolation. This Extrapolation from the Integration-Points is shown in **Fig. 11.13**, **Fig. 11.14** and **Fig. 11.15**. To reduce this problem also the stresses of 5mm to the inside **Fig. 11.24** are shown in **Fig. 11.25**, **Fig. 11.26**, and **Fig. 11.27**. The stresses to the free (front-) surface are Zero, like they should be (see **Fig. 11.23** and **Fig. 11.27**).

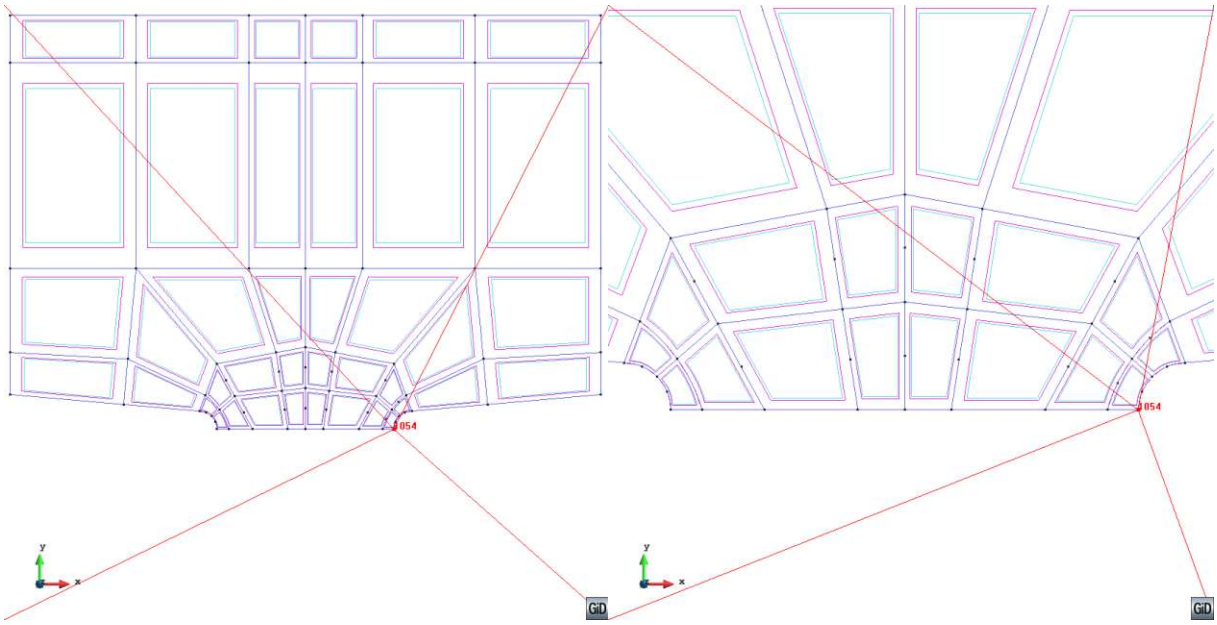

Fig. 11.20: line of evaluated results for stresses (surface of the compressive side)

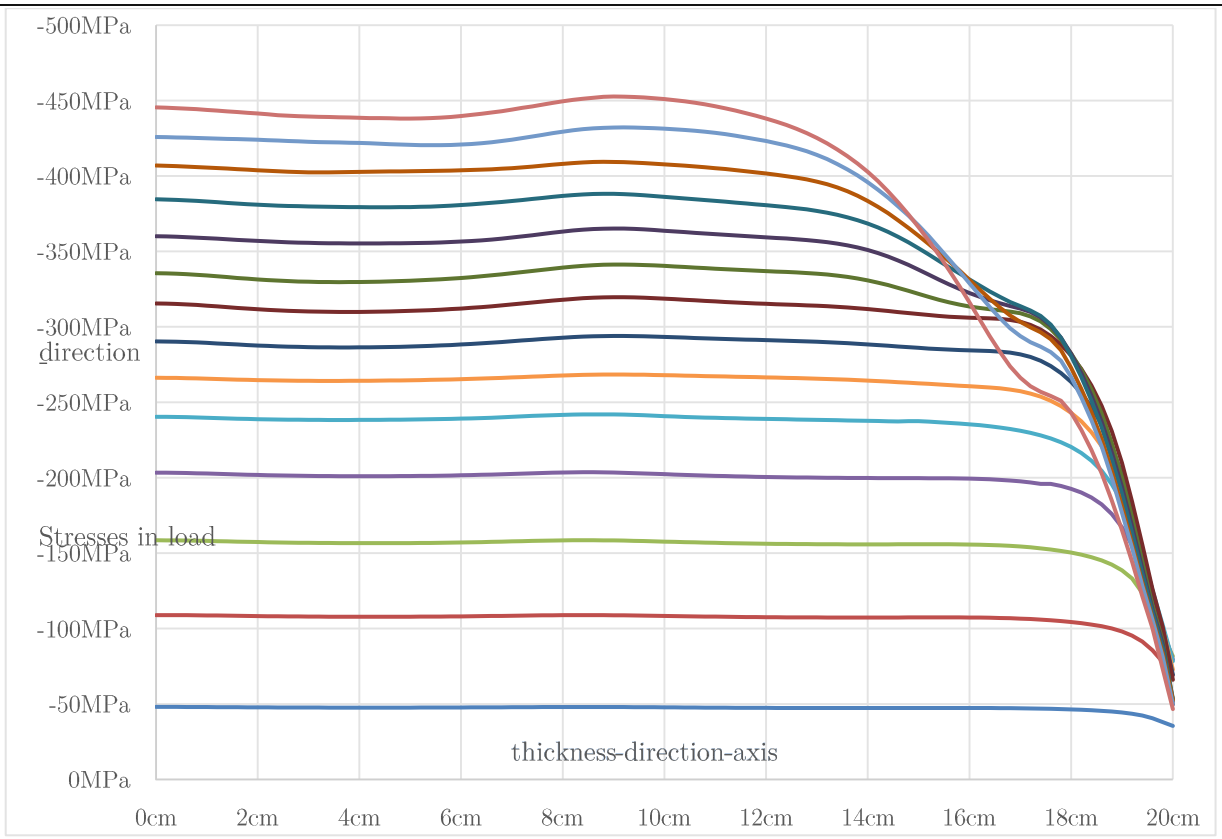

Fig. 11.21: stresses in load-direction

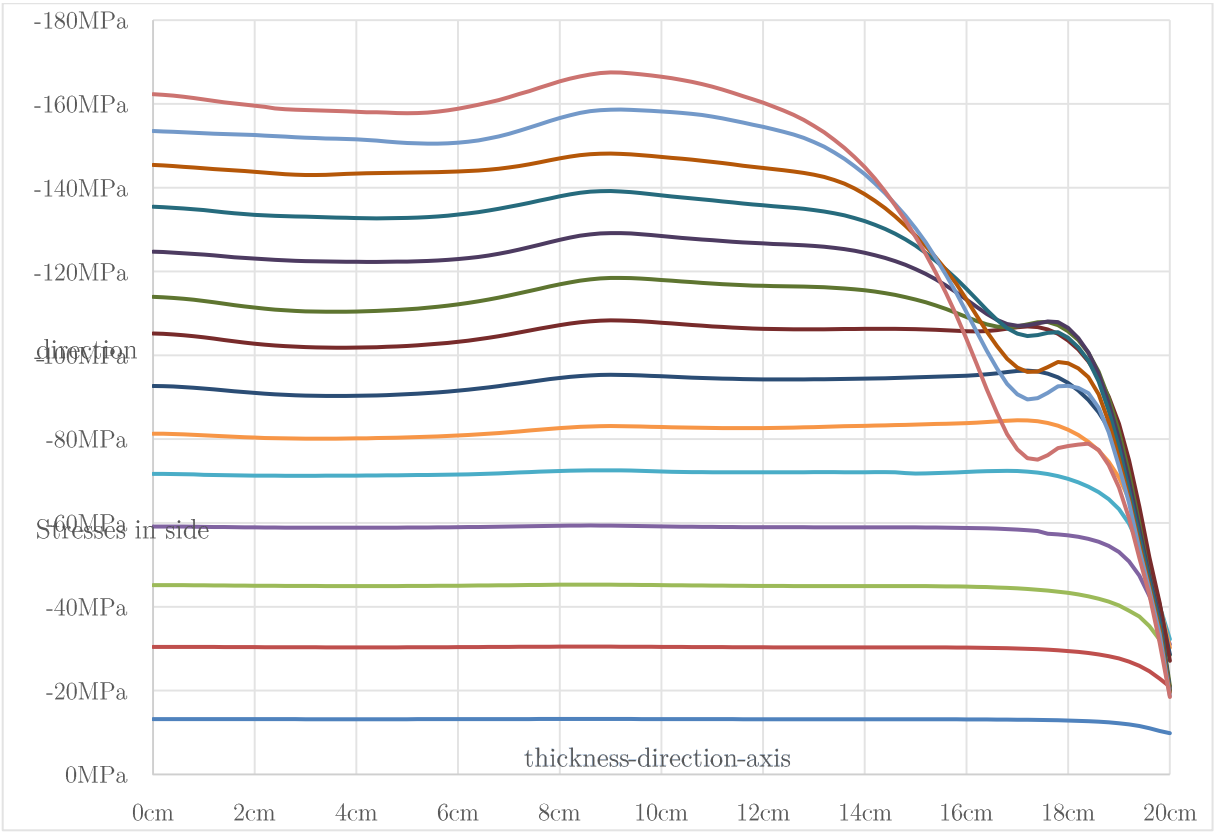

Fig. 11.22: stresses in side-direction

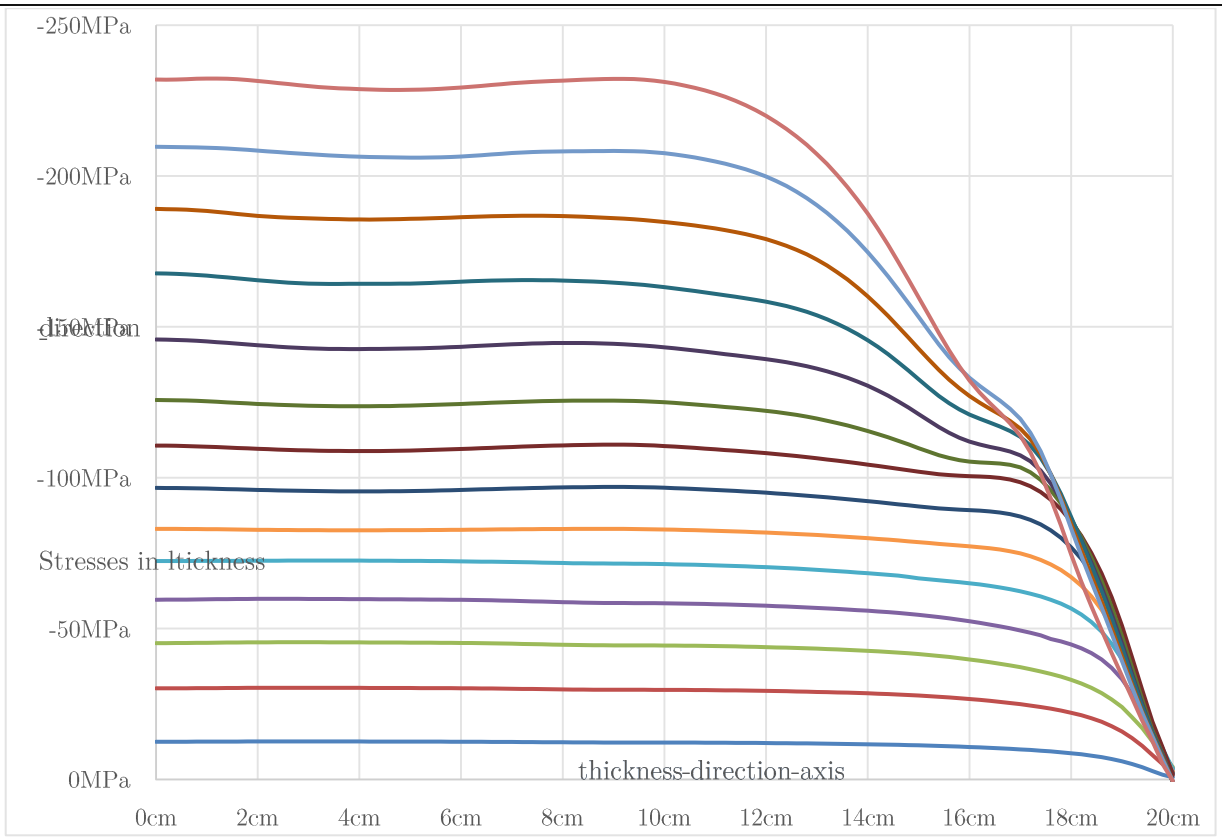

Fig. 11.23: stresses in thickness-direction

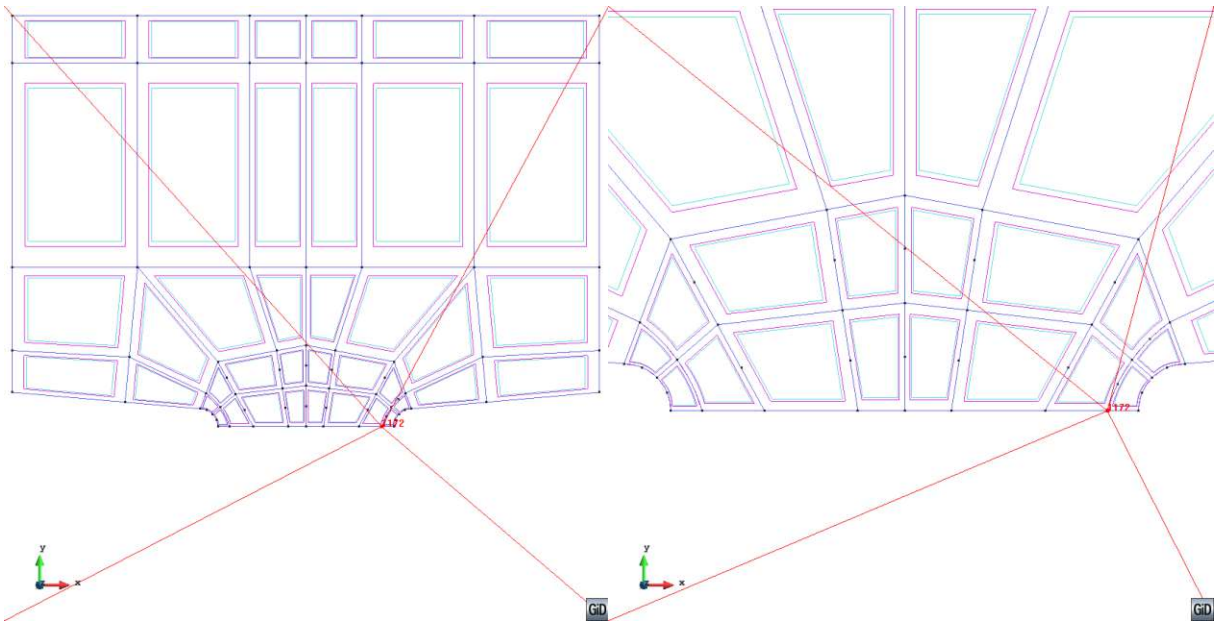

Fig. 11.24: line of evaluated results for stresses (inside, compressive side)

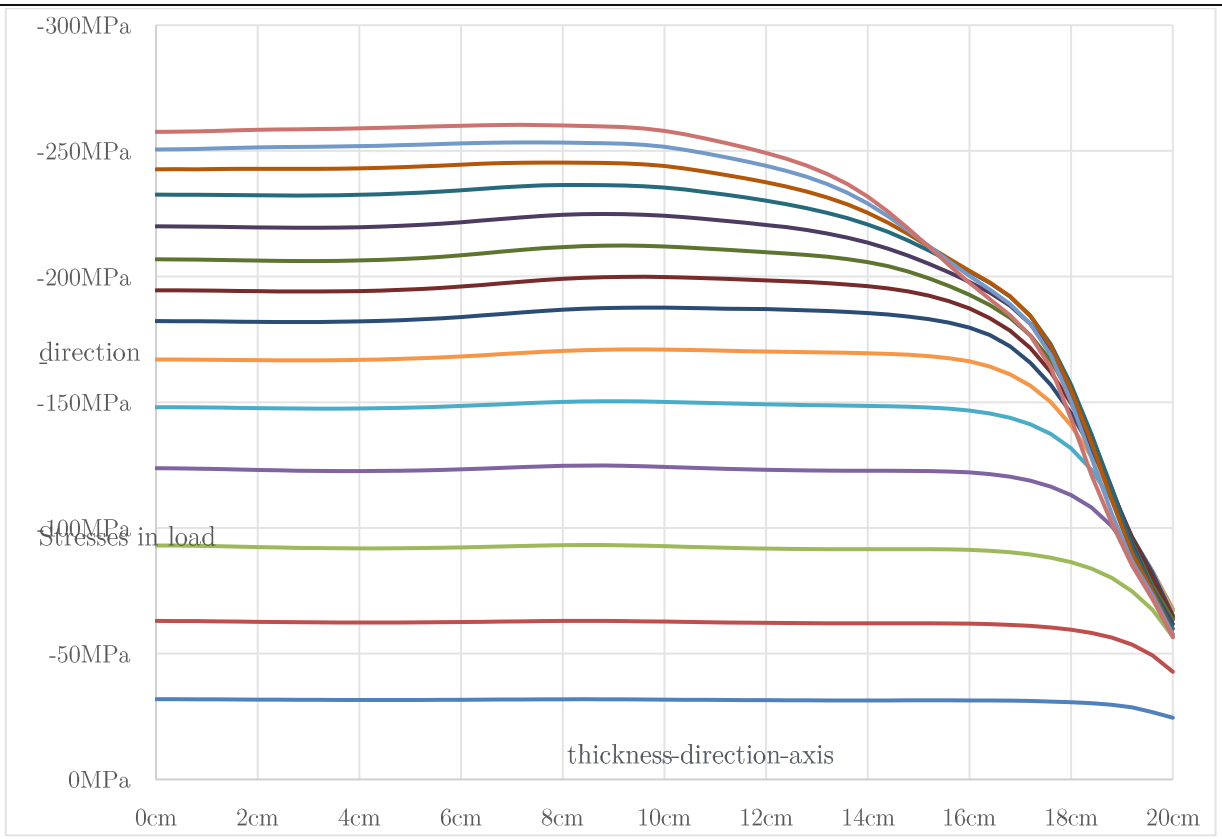

Fig. 11.25: stresses in load-direction

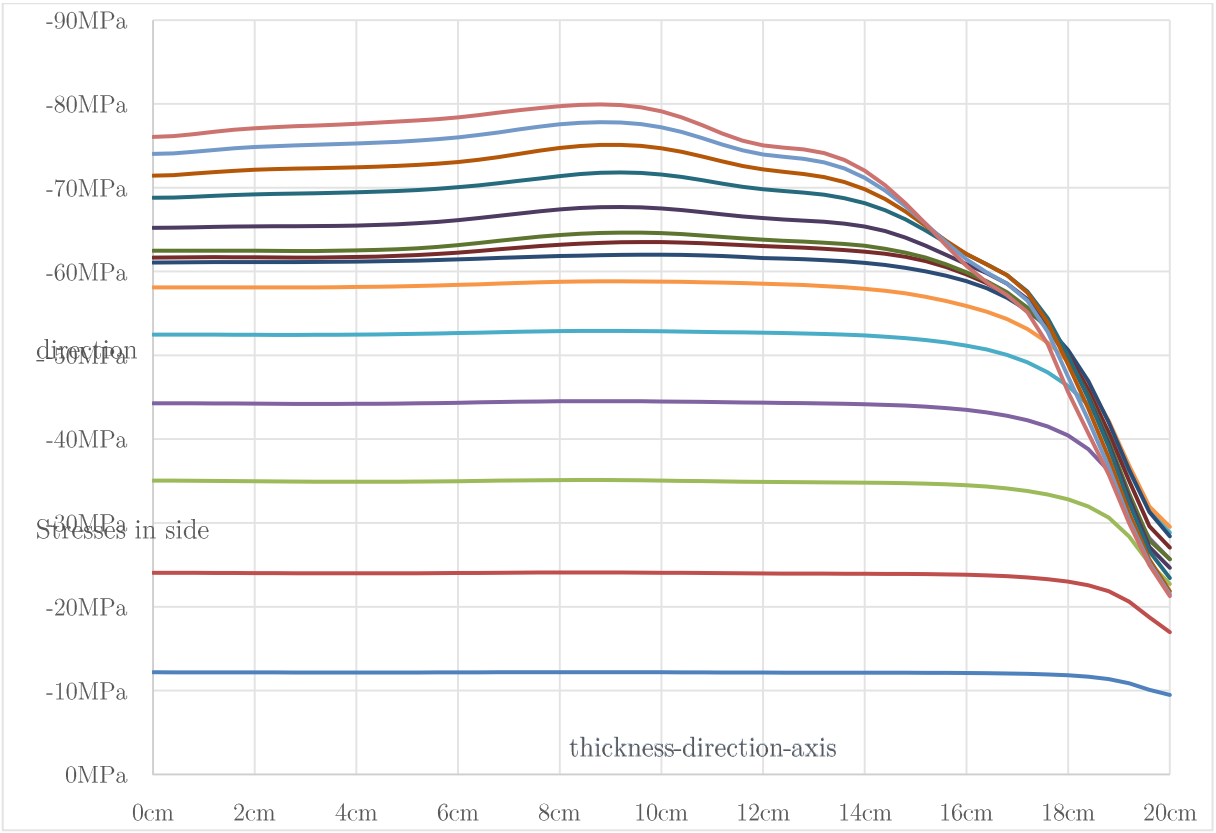

Fig. 11.26: stresses in side-direction

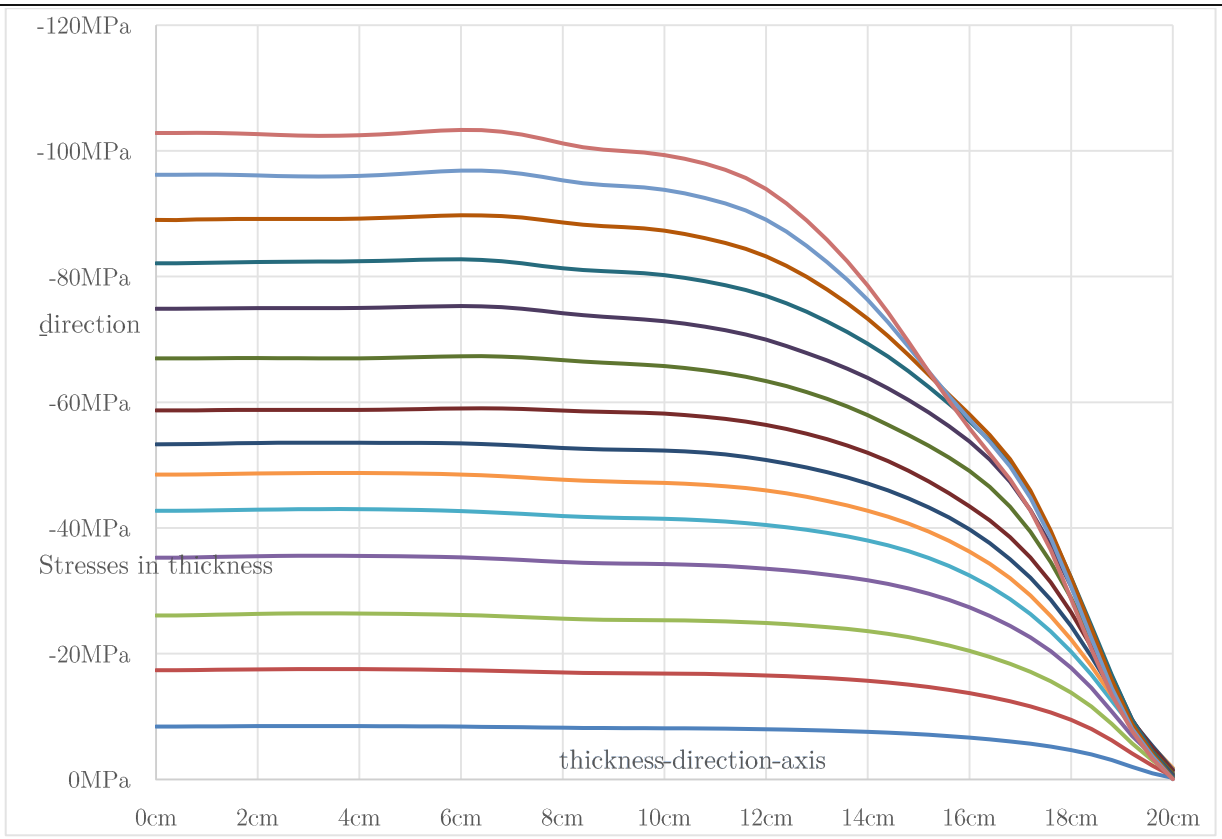

Fig. 11.27: stresses in tickness-direction

11.1.4 Comparison of results

The ultimate load in the Plain Strain Model is about 3.3[14] times bigger than in the Plain Stress-Model. The displacement of the loading-plate the peak-load is in the Plain-Strain-Model about 5.8 times higher than of the Plain-Stress-Model. At the rotation of the 3D-Peak-Load the Load of the 2-D-Plain-Stress Model would have been dropped to a quarter of the 2-D-Plain-Stress-Peak-Load, that means if you load the 3D-Model till failure, the resistance of the hinge will have been dropped massively on both free surfaces.

[14] This number has to be questioned, because of reasons mentioned later: In the Plain-Strain-Model Atena might over-guess the peak-load, because of high triaxial stresses.

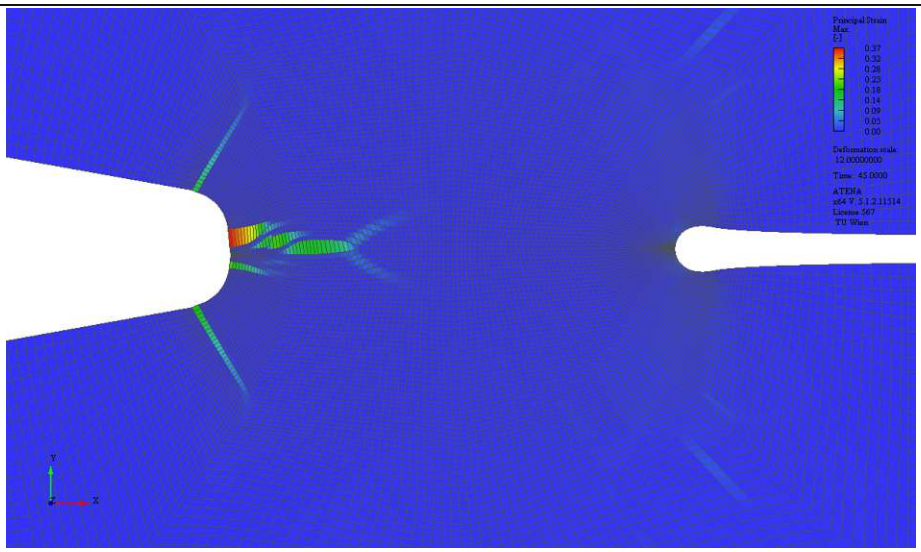

Fig. 11.28: Cracks in the double-2D-model

The red lines in **Fig. 11.29** and **Fig. 11.30** are the results of plain-Strain, the blue lines are the result of plain-Stress and the green lines between both are the curve of the 3D-Model. Each of those 3-2D-Models was calculated with both sides and with using symmetry (in 3D both symmetries), using the same color. The differences of those lines are so small, that you can only see differences in the post-peak. In the pre-peak, the differences are in the order of the thickness of those lines. The Peak-Load-Difference for the plain-Strain-model is 0.5%, for the 3DModel 1.5% and for Plain-Stress-Model is 2.1% in the post-peak the differences gets bigger, which is obvious because in a model using the whole model in most cases one crack is along one line of elements, the same is for the half model of the model with symmetry, which would mean two symmetric cracks. In **Fig. 11.28** it is shown, that two cracks starts symmetric, but almost at peak-load, the upper crack gets weaker and the crack somehow joins together. Therefore, the results are quite reproducible. For designing a concrete hinge the most important thing is to be on the save side to the peak-Load, so the post-peak is not that important, also it might could be interesting how ductile the failure mechanism is, because it might be possible to rehabilitate the structure after noticing big deformations or at least save peoples live before failure. Concrete hinges have alternating loading, so brittle fatigue failure [Dix, 1962] could occur, also due to high stresses creep failure might be possible, which is not further considered in this work.

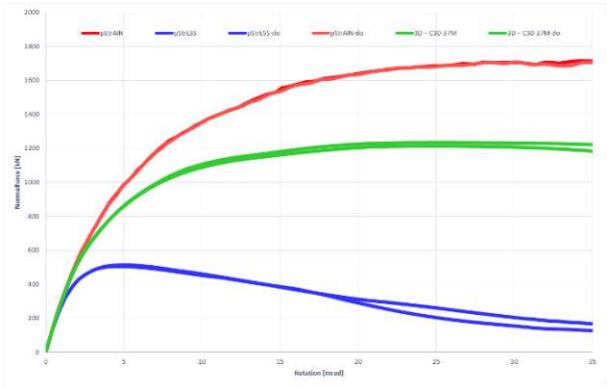

Fig. 11.29: Load-Rotation-Curves red: Plain-Strain, green: 3D; blue: plain stress

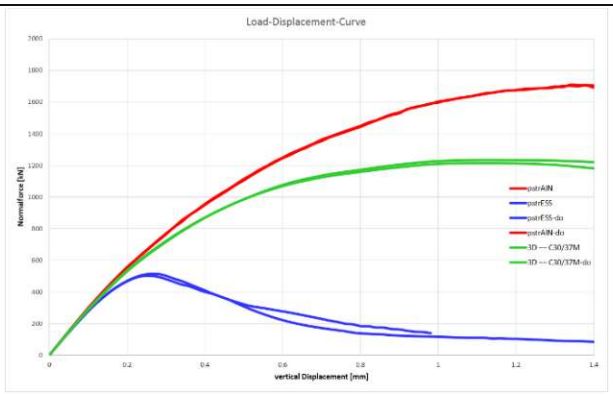

Fig. 11.30: Load-Displacement-Curves red: Plain-Strain, green: 3D; blue: plain stress

Both 2D-Models are quite the same until a rotation of about 2mrad, where you reached already 80% of the peak load of the Plain-Strain-Model. The plain-Strain-Model is a good approximation for the model for a rotation until 3mrad. For of a/b-ration of 0.1875 the peak load this 3D model is about 70% of the peak load of the plain-Strain-Model. For this a/b-ration, the 3D-model has a peak-load of about 240% of the plain-Stress-Model, but the curve of the 3D-Model looks qualitatively quite different. According to **Fig. 11.29** and **Fig. 11.30** it is necessarily to make a 3D-Model because of the big triaxial stresses. The principal stresses are in proportion of about 1:0.3:0.5.

11.1.5 Comparison of the costs of calculation

2D: The calculation time of the 2-D-Half-Model to the 2-D-Double-Model for the big mesh (7.5mm[15];see **Fig. 9.1**) increased from 19 seconds to 27 seconds. The big mesh to the fine mesh(0.6mm) (see **Fig. 9.6**) raised from 0,45 minutes to 12,02 minutes. The calculation-time to the even finer mesh (0,3mm) raised to 42.80 minutes.

The calculation time for a 10times lower convergence-tolerance raised from

The calculation time could be reduced from 12.02minutes to 7.02minutes with reducing the load steps from 82 to 15, which was only used for the parameter-studies, to be able to calculate hundreds of calculations in a reasonable time.

The CEM3-Double-Model (see Chapter **8.2** and Chapter **10**) needs smaller load-steps and failed earlier (vertical displacement of 0.63mm instead of 1.6mm), so it is difficult to compare but in the chosen case the calculation time rose to 44.77 minutes for the mesh-size 0.6mm after 315steps.

Creep. The 2-D-Model took 30,30min the creep model took 37,26min, which is 123%.

3D: To reduce the cost of calculation both symmetries were used, which reduced the calculating time from 6.13 minutes to 2.17 minutes for the mesh shown in **Fig. 9.1** (7.5mm in the “hinge-neck”) with an element “out-of-plane”-thickness of 2.22cm.

[15] The mentioned mesh-sizes are in the “hinge-neck” the biggest mesh-size-lengths are 3.2times bigger.

Those 2.17 minutes rose to 19.18 minutes for a mesh 2.5mm in the “hinge-neck” and out-of-plane 4mm, so the calculation time rise only by a factor of 8.8 also the finer model has 50times more elements.
For the CEM3-Model the calculation time rose from 19.18 minutes to 204.58 minutes. One of the reasons is that 300loadsteps instead of 14 were used, which were necessary to calculate the model without error.

11.2 Front-notch-related sensitivity analyses

The neutral line (yellow line in **Fig. 11.31**) of the 3-D-Model without front-notch is about between the centerline and 4mm to the compression side, so a constant crack-tip is a quite good assumption.

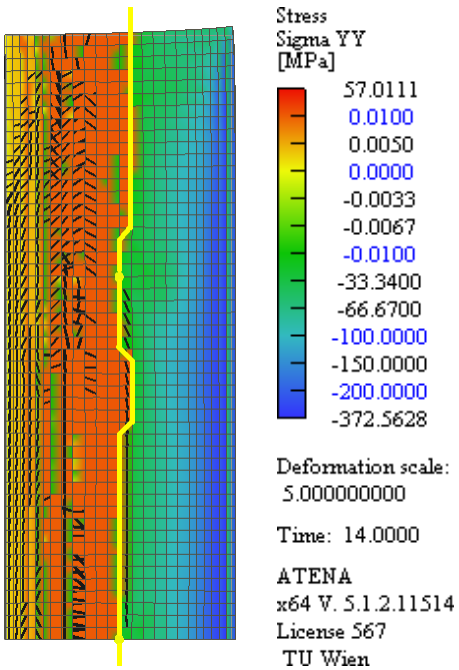

Fig. 11.31: The cutted neck-area using symmetry conditions, the yellow line symbols the newtral line red&orange:tension; yellow: newtral; green&blue: compression

Like in the 2D-Model, the crack-tip is not easily defined, because of many microcracs the Model has very much plasticity, so an intelligent way to define the crack-tip is to look at the maximal stresses in the Load-direction. At peak-load the peak-tension-stresses occur very near to the neutral line. Because the neutral line is almost parallel to the out-of-plane-thickness-direction, a crack-tip measured at the front-surface is for concrete hinges without front notch a good approach also for the crack-tip in the middle of the hinge.

without Front-notch: The stress-distribution over the thickness is shown in Chapter 11.1.3.

2cm-Front-Notch: The stresses are 5mm from the compressive surface **Fig. 11.32a**. That the stresses in thickness-direction are not zero at the free surface might be due to a problematic mesh in the neck-region, due to a complicated front notch-geometry (see **Fig. 11.32b**).

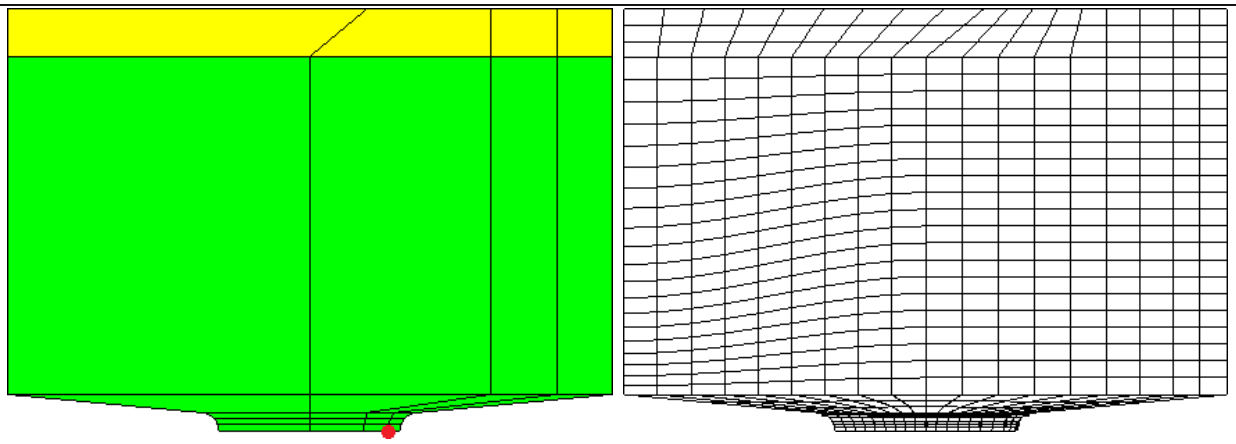

Fig. 11.32: left: point for elevation; right: mesh

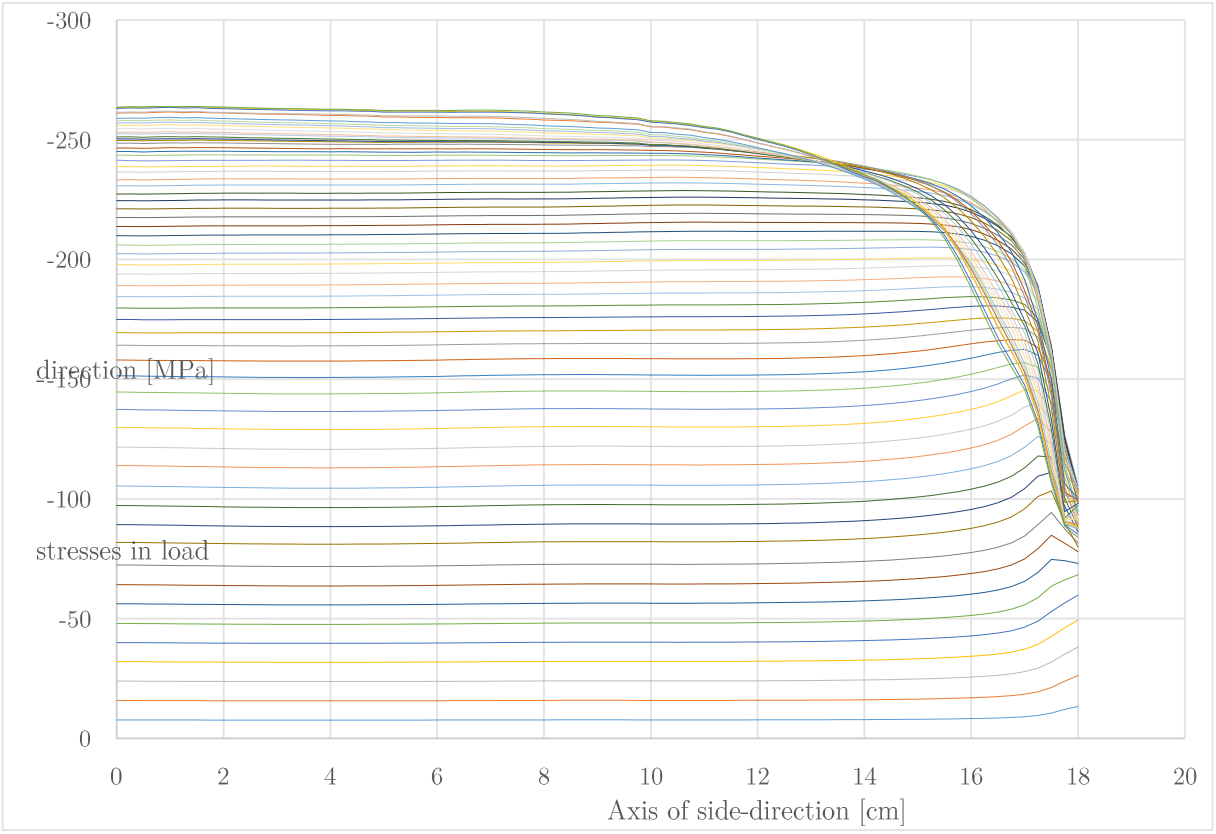

Fig. 11.33: stresses in load-direction

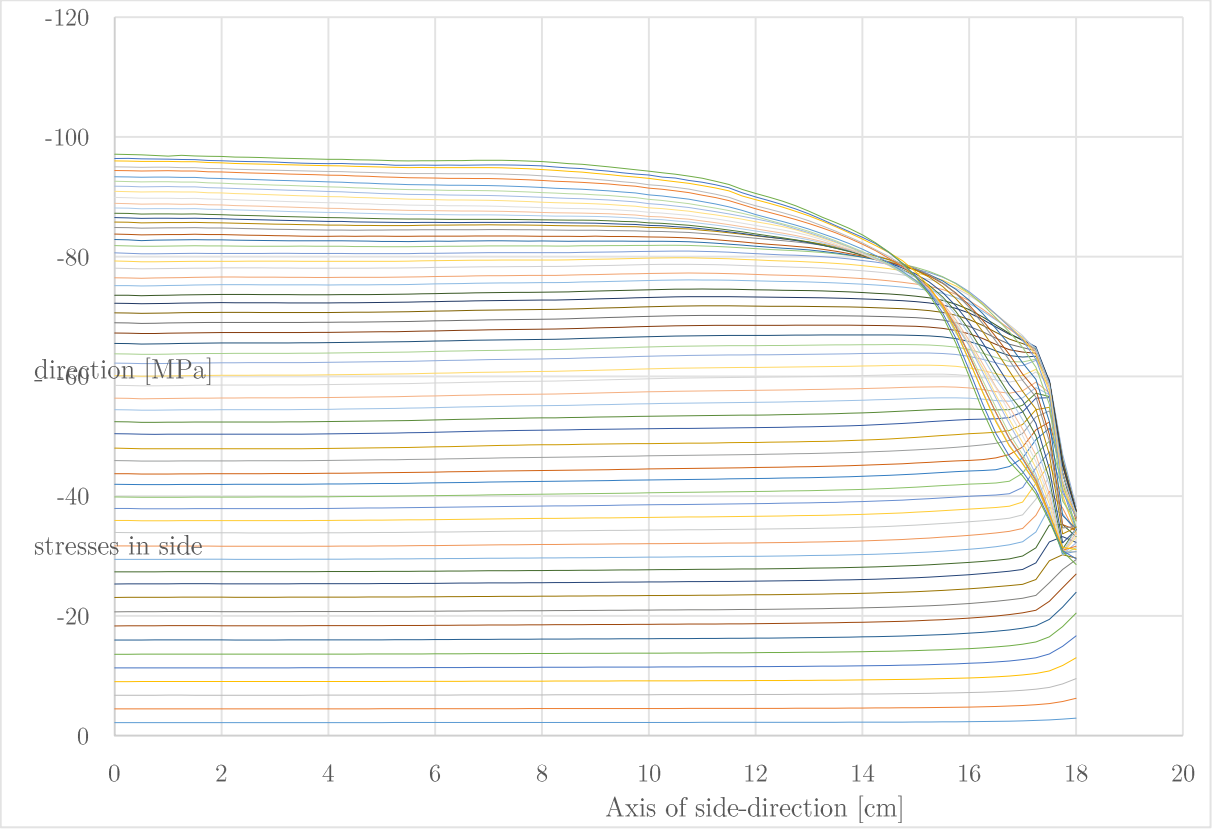

Fig. 11.34: stresses in side-direction

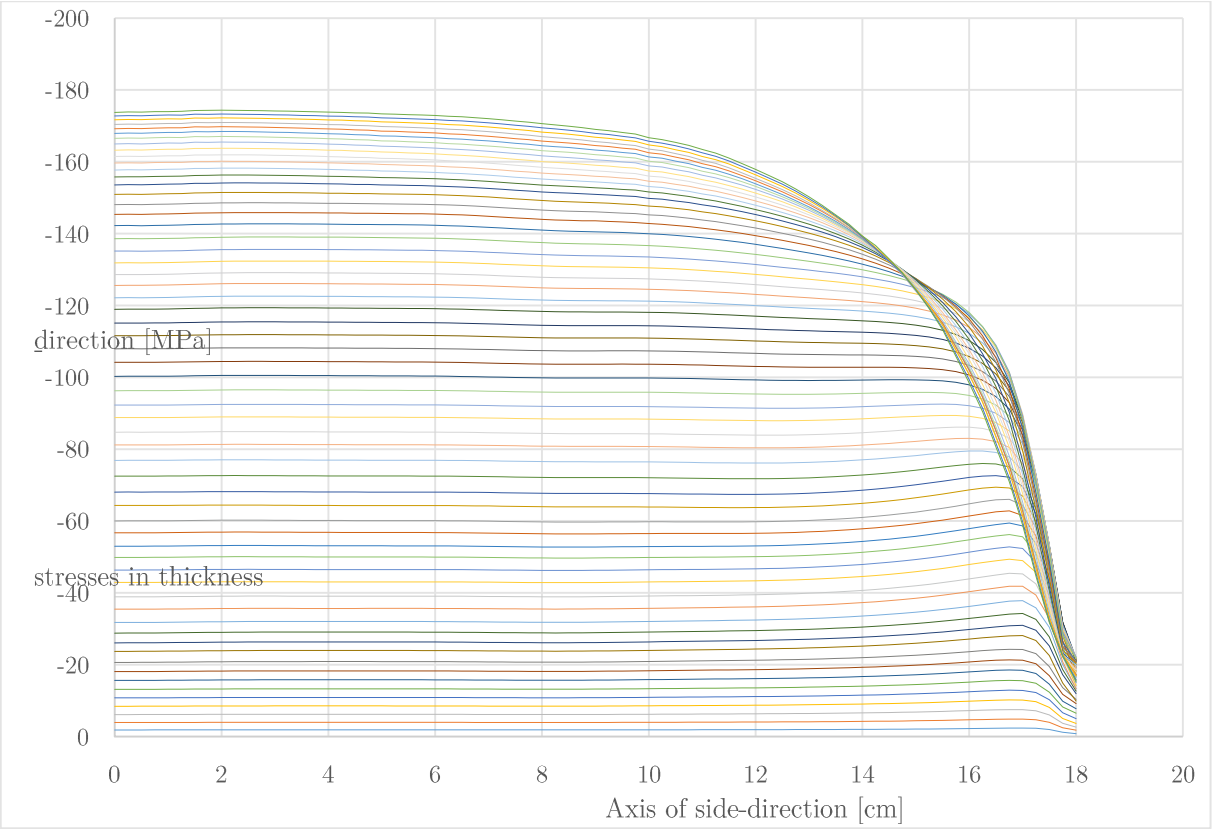

Fig. 11.35: stresses in thickness-direction

3.5cm-Notch-deepness: Different Lines are evaluated for stresses (**Fig. 11.36a**). The notch-deepness seems to be intelligent, because the stresses are at the line of highest load

quite constant (**Fig. 11.38**). At peak-load the stresses at the compressive side is already reducing (**Fig. 11.37**). The compressive stresses are near the front notch the highest, for the line 15mm from the compressive surface (**Fig. 11.39**).

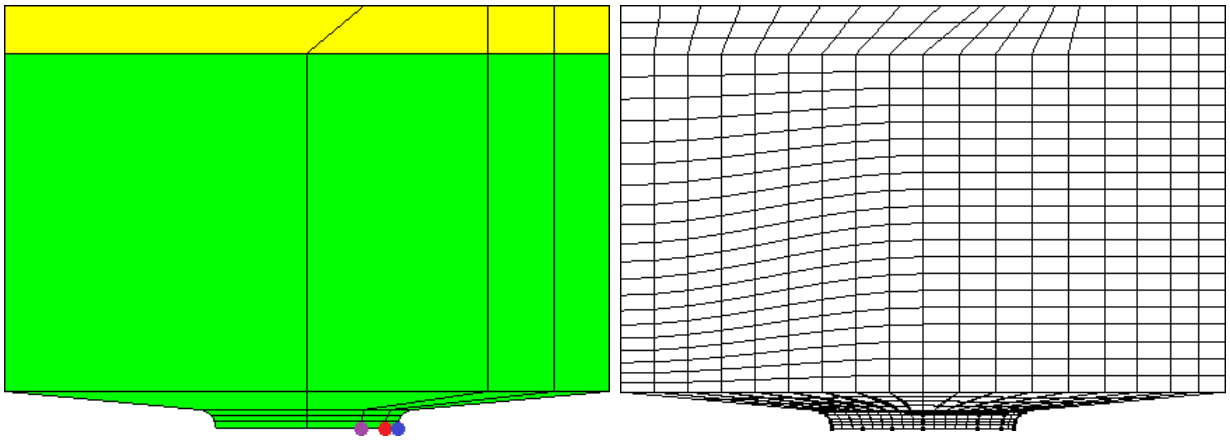

Fig. 11.36: left: points for elevation; right: mesh

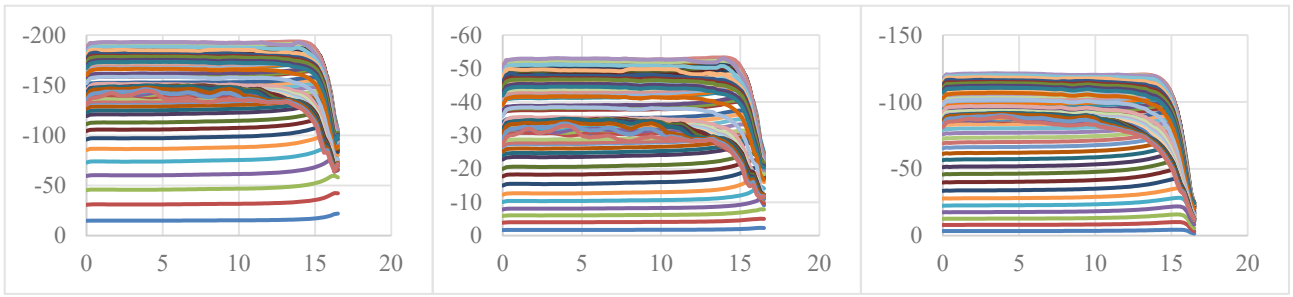

Fig. 11.37: stresses [MPa] at the compressive-surface in a)load-direction b)side-direction c)thickness-direction

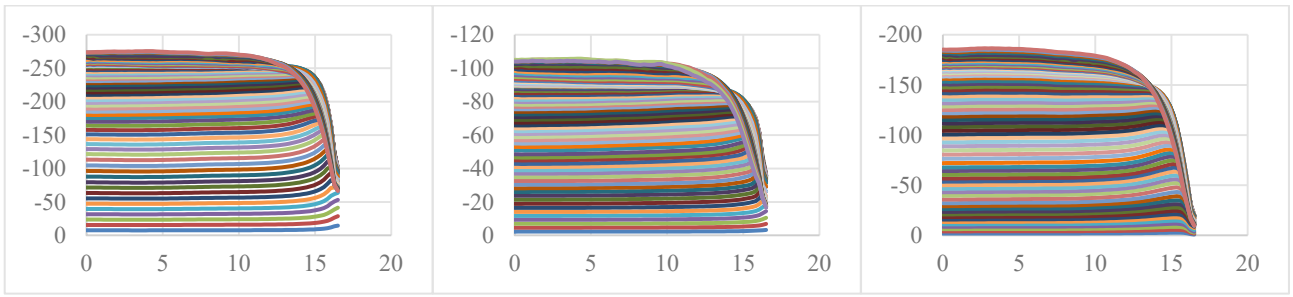

Fig. 11.38: stresses [MPa] at 5mm from the compressive-surface in a)load-direction b)side-direction c)thickness-direction

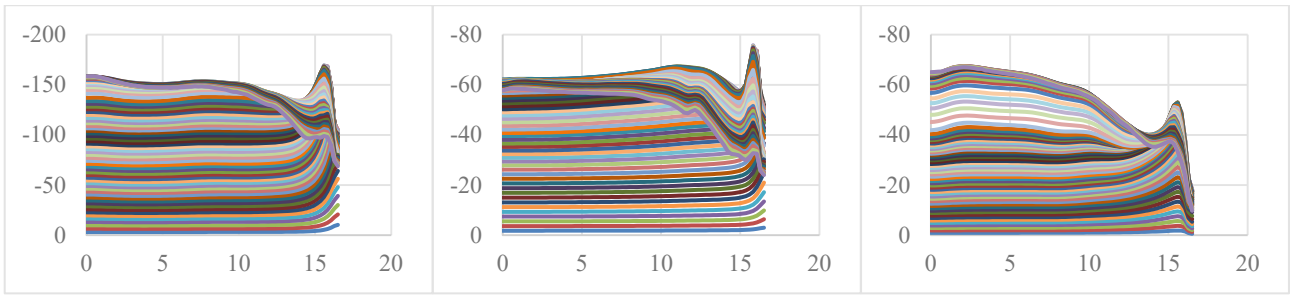

Fig. 11.39: stresses [MPa] at 15mm from the compressive-surface in a)load-direction b)side-direction c)thickness-direction

5cm-Notch-deepness: The automatic-mesh-generator (only for tetrahedra available) is used for this model due some problems with a brick-mesh. The stresses are evaluated for 15mm from the compressive surface.

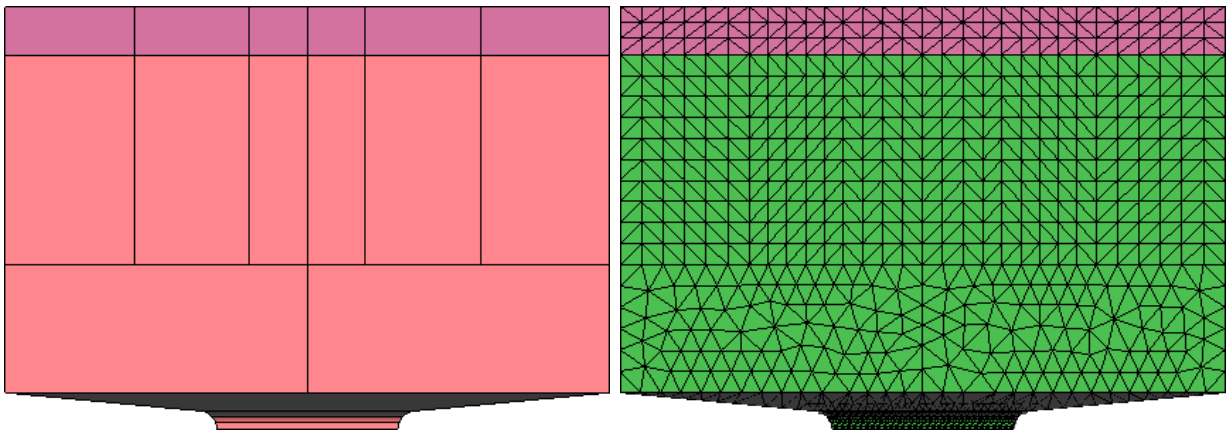

Fig. 11.40: Model with 5cm-front-notch

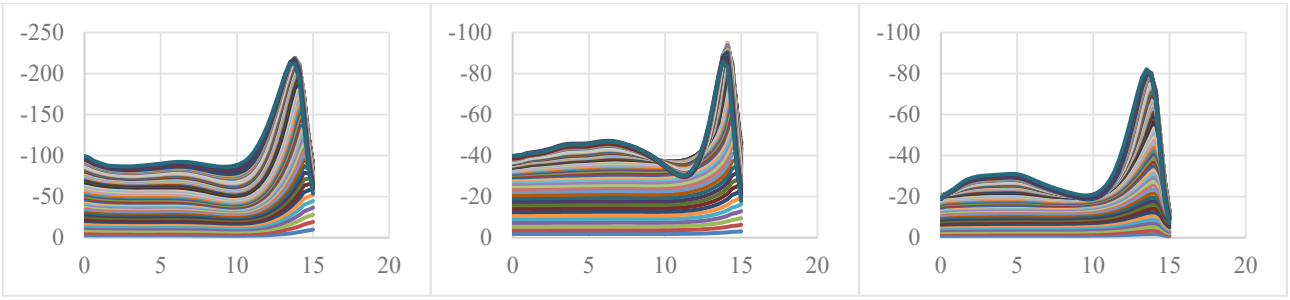

Fig. 11.41: stresses [MPa] at 15mm from the compressive-surface in a)load-direction b)side-direction c)thickness-direction

11.3 Material behavior

In this parameter studies is done with 2D-Plain-Strain-Model with Mean Values of C30/37 and only changing one parameter was compared with the experiment, without front notch, geometry shown in **Fig. 8.1** and with tested Material parameters of a compressive cubic strength of 54,27MPa (mean of 54.5MPa; 54.2MPa; 54.1MPa) and a Young's Modulus of 32800MPa. The differences between 2D-Plain-Strain-Model and 3D-Model are discussed in Chapter 11.1 Comparison of plane stress, plane strain, and 3D simulations (especially: **Fig. 11.29**). To get a first estimate in a reasonable time every load step has an increasing vertical displacement of 0.1mm[16], with standard convergence criteria, but still using a fine mesh (0.6mm), with 26 400 Quadrilateral Elements (26 885 Nodes). Due to further calculations, a higher number of load steps, until to a certain amount almost did not increase the computational time, because smaller load steps need less iterations, so for further works it would be intelligent to increase the load steps.

The standard configuration is shown in **Fig. 11.42**. The gray line is the experiment loaded for the first time up to a load of 225kN; the blue line is the experiment up to big defor-

[16] The standard configuration had 13 load steps, many configurations "errored" later (max 15) some "errored" (much) earlier.

mations, which can be assumed as peak-load. Because of creep-tests in the first loading the orange line shows the secant through the 0kN and 50kN, which can be assumed as the tangent at zero.

The pictures of the strains and stresses are those, which show the qualitative difference the best. The principal strain is in all plots from blue (zero) to orange (2.5%) the same[17], and zero stresses are in all plots orange. Often for failure is the crack-propagation shortly before failure. Due to different failure steps the loading for the pictures in this chapter of strains and stresses differ on purpose. The stresses have only the same-zero-point, but on purpose not equal stress-colors, because they sometimes differ decades, and you would not be able to see anything on one plot. The qualitative stress-distribution-differences are clearer in those plots. The Rotation-Load-Curve better explain the quantitative effects like peak-load or stiffness.

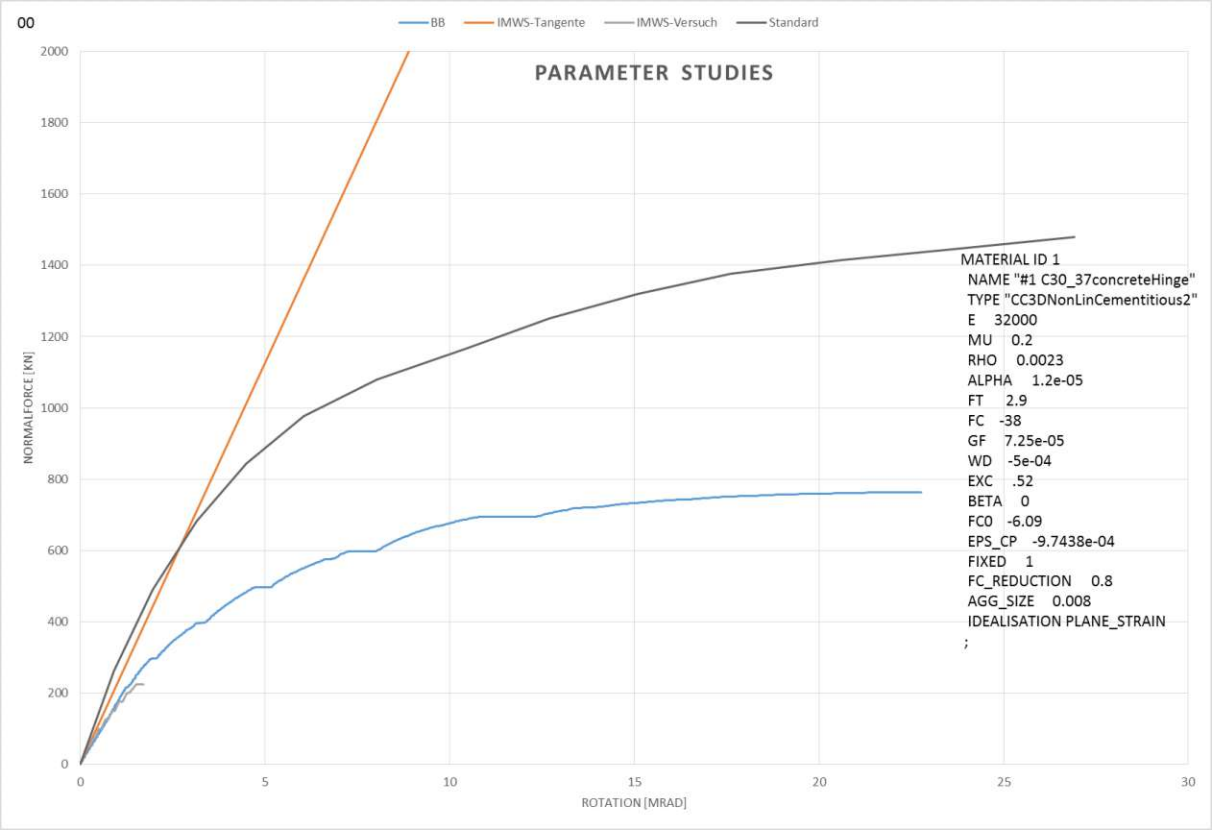

Fig. 11.42: Parameter Studies Standard configuration in the Rotation-Load-Curve

[17] Strains above 2.5% can be in general considered as fully cracked in this model. To see differences of crack-openings the colour (orange to red) of the stains above 2.5% are dependent on the biggest strain.

Table 5: Material Data

	Build11514[18]		Default Value	Tested range	
	Atena 5.1.2.11514		C30/37	Min	Max
FC	-∞	Max{FC0; -2FT}	-38MPa	-380MPa	FC0[19]
FT	0	-FC/2[20]	2,9MPa	0,029MPa	-FC/2[21]
E	0	+∞	32 000MPa	3 200MPa	320 000MPa
ν	-1	0.5	0,2	-0,9999	+0,49
GF	0	+∞	7,25E-5 MN/m	7,25E-8 MN/m	7,25E-4 MN/m
EXC	-∞	+∞	0,52	0.3[22]	2
EPSCP	-∞	0	-9,7‰	-1E+99	-1E-99
FC0	FC	0	-6,09 MPa	FC[23]	-1E-99 MPa
WD	-∞	0	-0,5 mm	-1E+99 m	-1E-99 m
β	-∞	∞	±0	-0,7	+0,7
ρ	-∞	∞	0.0023 kton/m³	0	1E+99 kton/m³
α	-∞	∞	0.000 012 C⁻¹	-1E+99 K⁻¹	1E+99 K⁻¹
fix	-∞	∞	1	0	≥1[24]
Fc_R	0	1	0,8	1E-99	1
Agg	0	∞	2 cm	1E-99 m	1E+99 m

[18] Values in Build11516 (GiD) differ, but they were reported and corrected. The newer builds still differ to the values of 5.1.2.11514, because they tell meaningful limits, also Atena has no input-control.
[19] FC0=-6.09MPa
[20] in newer GiD versions (not in Atena) it is according to the manual[Červenka, 2014]: FC0/2
[21] FC/2=19MPa
[22] EXC<0.5 means a concave failure surface
[23] FC=38MPa
[24] Values bigger than one were calculated, but they do not differ from 1, because of the definition (see **Fig. 11.90**)

11.3.1 Compressive Strength

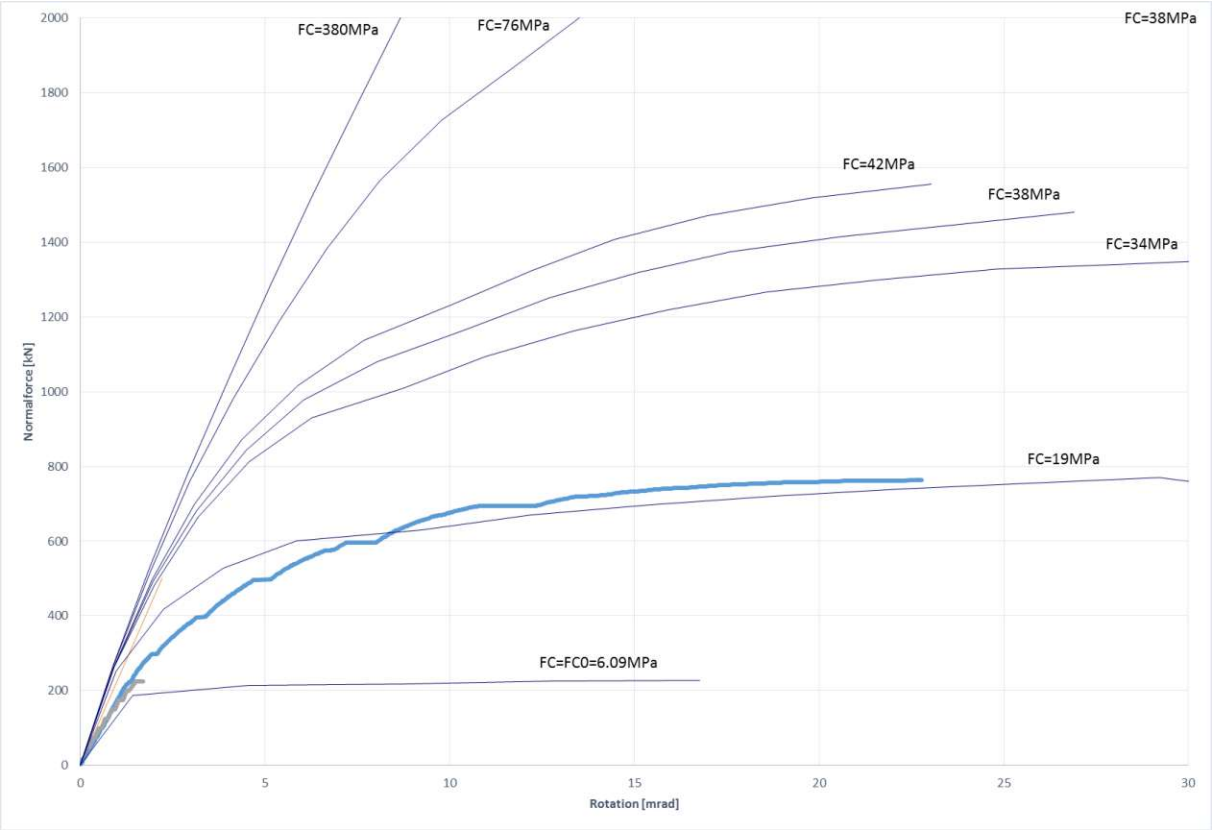

Fig. 11.43: Effect of the different Compressive-Strength in the Rotation-Load-Curve

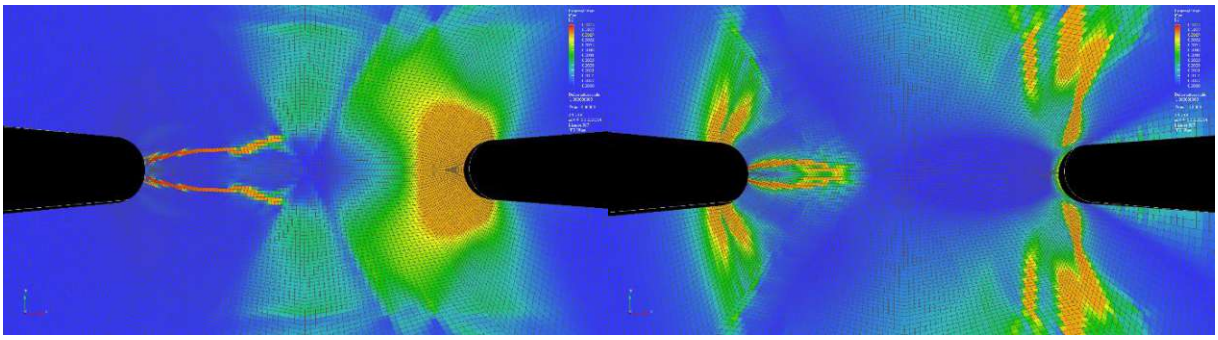

Fig. 11.44: ϵ_1 first principal strain for FC=FC0-6.09MPa (left) and FC=-380MPa (right)

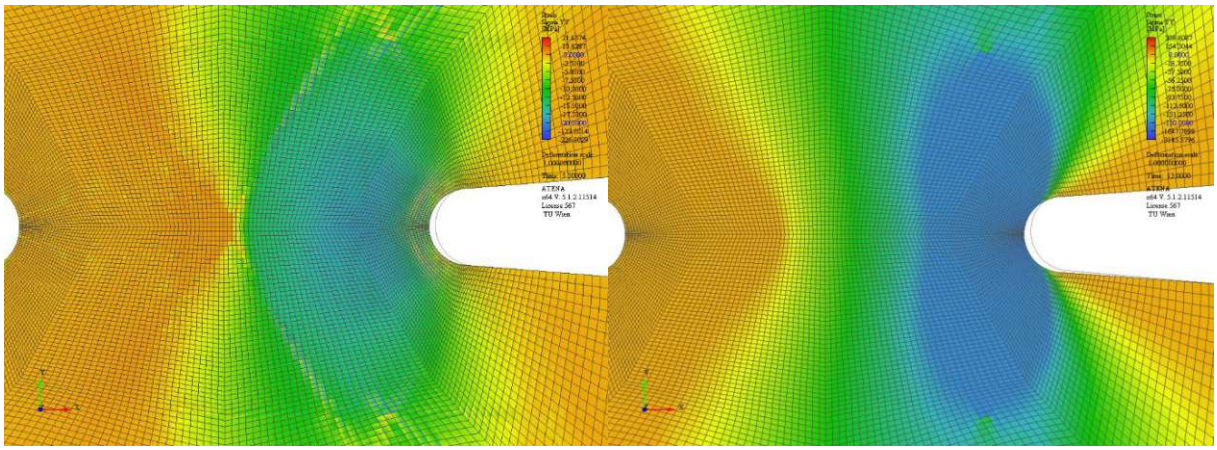

Fig. 11.45: σ_{LL} stresses in Load-Direction for FC=FC0=-6.09MPa (left) and FC=-380MPa (right)

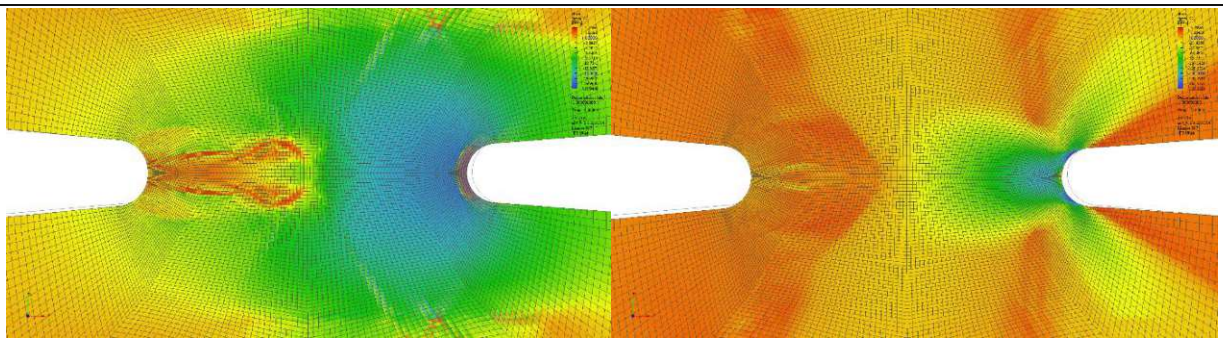

Fig. 11.46: σ_{SS} stresses in Side-Direction for FC=FC0=-6.09MPa (left) and FC=-380MPa (right)

11.3.2 FT-Tension strength (of the concrete)

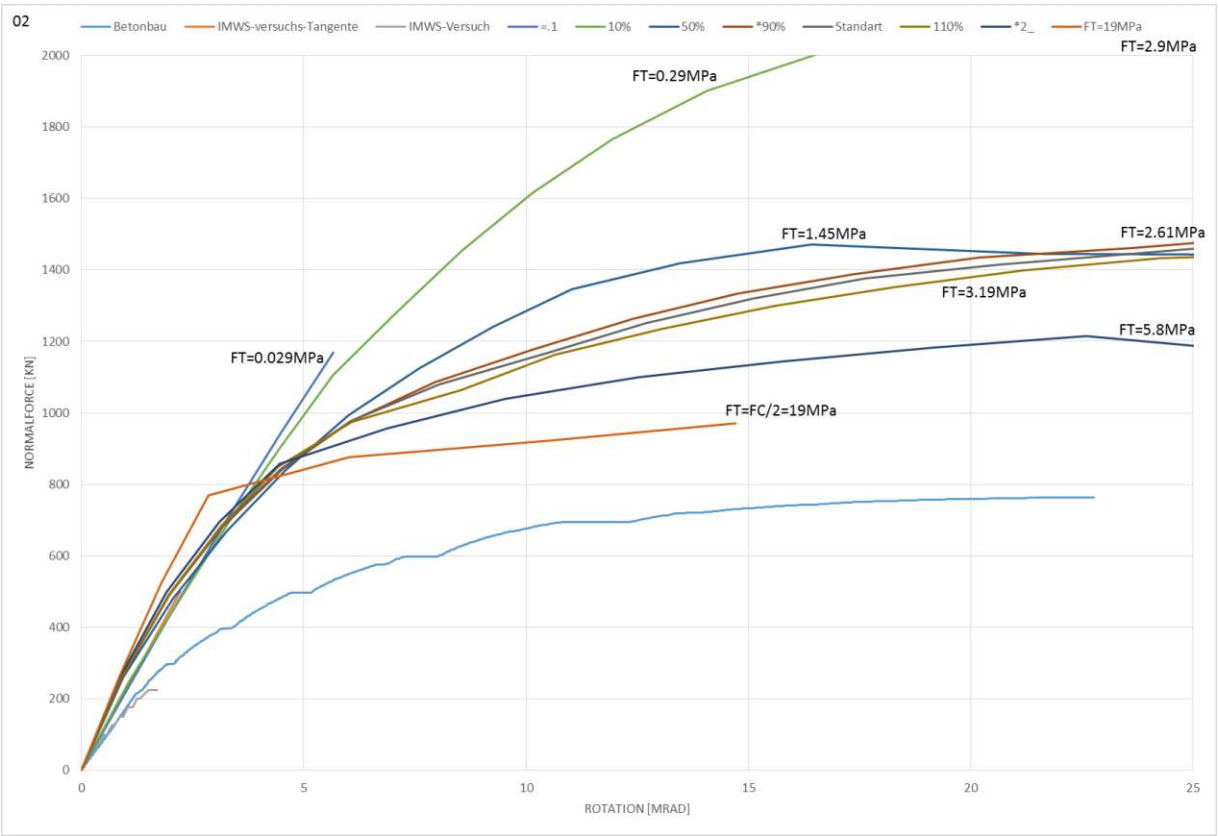

Fig. 11.47: Effect of the different Tension-Strength in the Rotation-Load-Curve[25]

[25] FC0=-6.09MPa, but the "Acceptable range" according to [GiD 12.0,2015] with [ATENA, 2015] is between -∞ and –2·FT, therefore Results with FT bigger than 3.045MPa, might not be realistic, without changing FC0 (see Chapter **11.3.8 Onset** of Crushing (FC0)

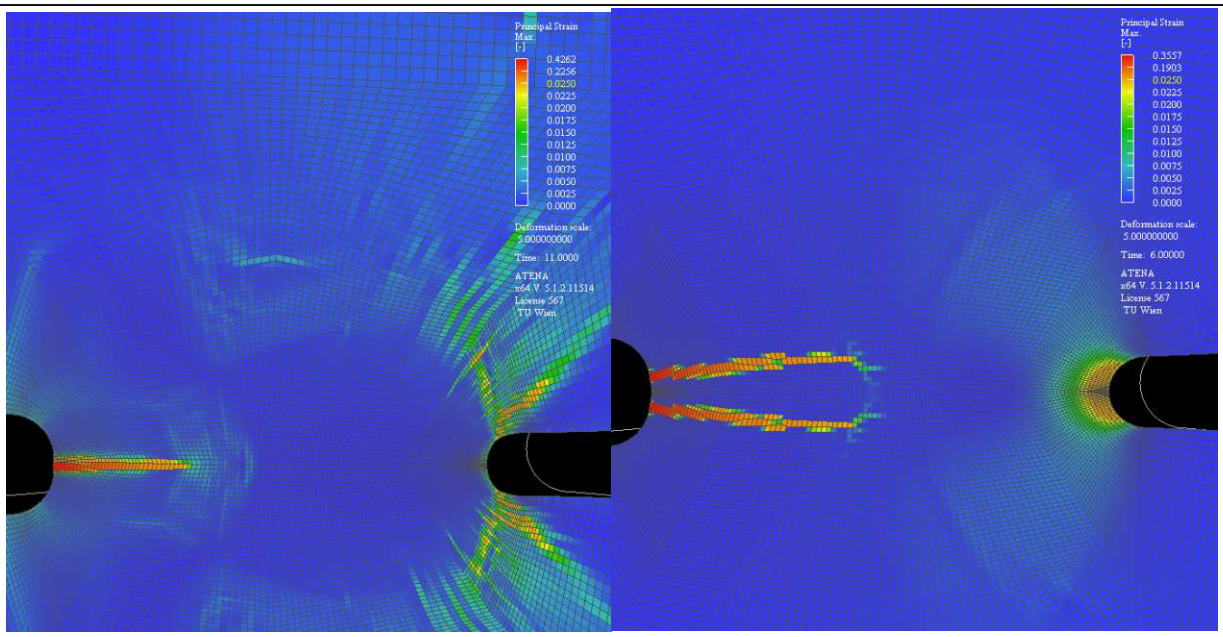

Fig. 11.48: ϵ_1 first principal strain for FT=0.29MPa (left) and FT=FC/2=19MPa (right)

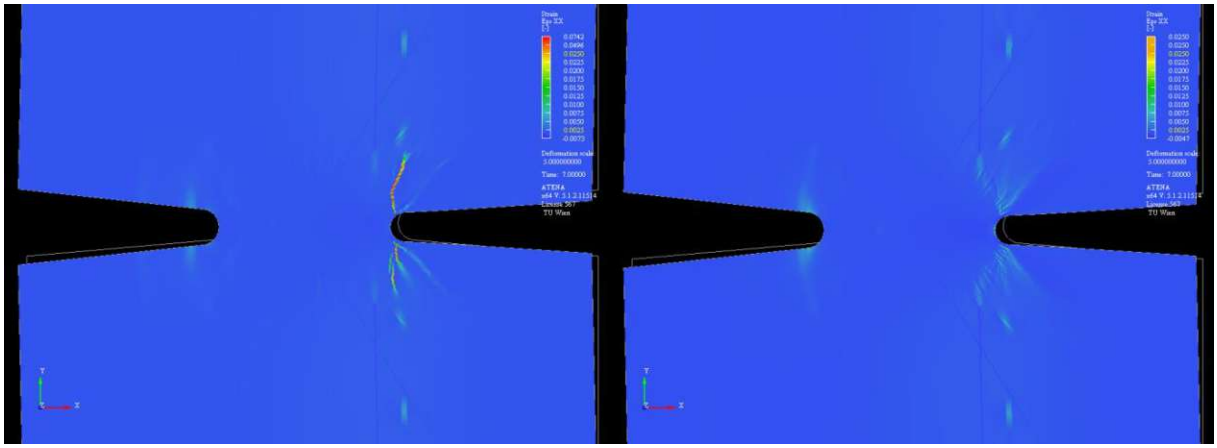

Fig. 11.49: ϵ_{xx} strain in side-direction for FT=0.1MPa (left) and FT=0.29MPa (right) at a vertical Displacement of 0.7mm

The final failure mechanism of tensile splitting (see **Fig. 11.53**), does not really occur in this Parameter Studies, it fails due to big rotations. Decreasing the Tensile Strength to 0.1MPa shows in this model some tensile splitting, already in the early pre-peak (see **Fig. 11.49**)

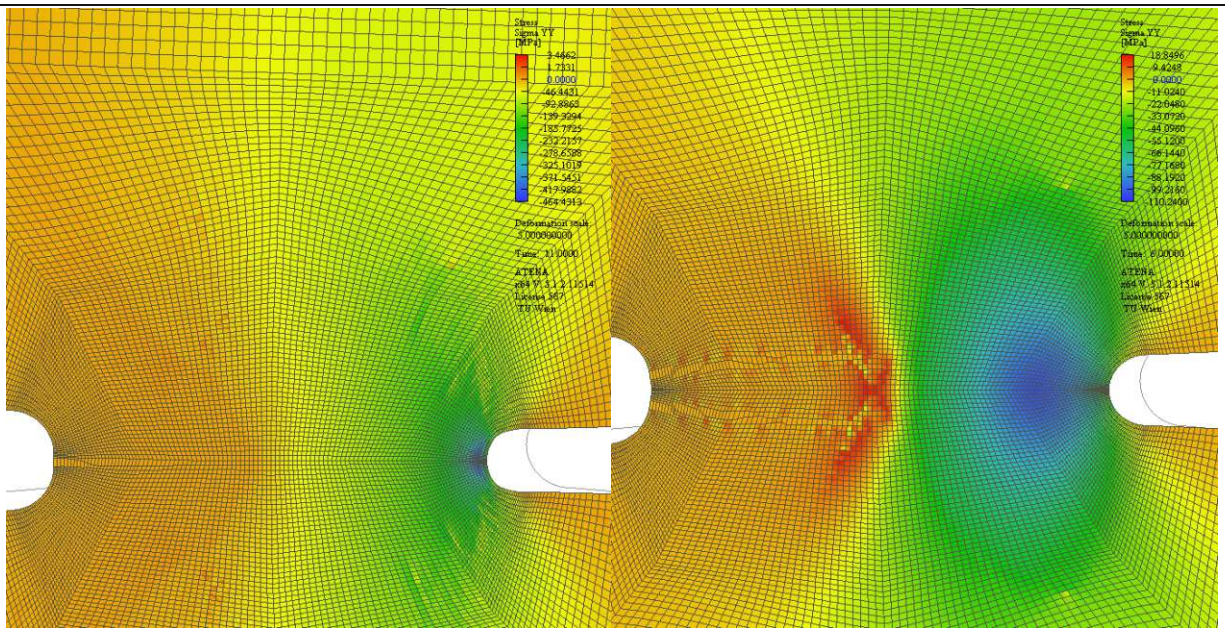

Fig. 11.50: σ_{LL} stresses in Load-Direction for FT=0.029MPa (left) and FT=FC/2=19MPa (right)

The influence of the tension strength is very interesting, because an increasing tension strength, of course increases the stiffness, but decreases the peak load. So a large crack is desired/wanted, because it reduces the eccentricity of the load compared to the balance point of the intact hinge-neck-Surface. Leonhard made two possible borderline cases: In one he assumed a stress distribution of a triangle and in the other one a stress distribution of a rectangle [Leonhardt, 1965] (see **Fig. 11.51**). In both cases he assumed that the crack-tip propagates to the "neutral line", which would lead to an overestimation of the failure load, but he assumes the compressive strength due to triaxiality of $\sqrt{(3)}$ of the uniaxial compressive strength, which might be an underestimation. As you can see in **Fig. 11.51** the rectangle-assumption has smaller peak-stress, under the assumption of the same Normal-force and same eccentricity (compared to the uncracked area). The eccentricity to the intact area is in the rectangle-model zero, therefore smaller tensile stresses are an advantage, because of less (rotational) stiffness and bigger peak loads. Also a lower Tensile-Strengh leads to higher compressive Stenght.

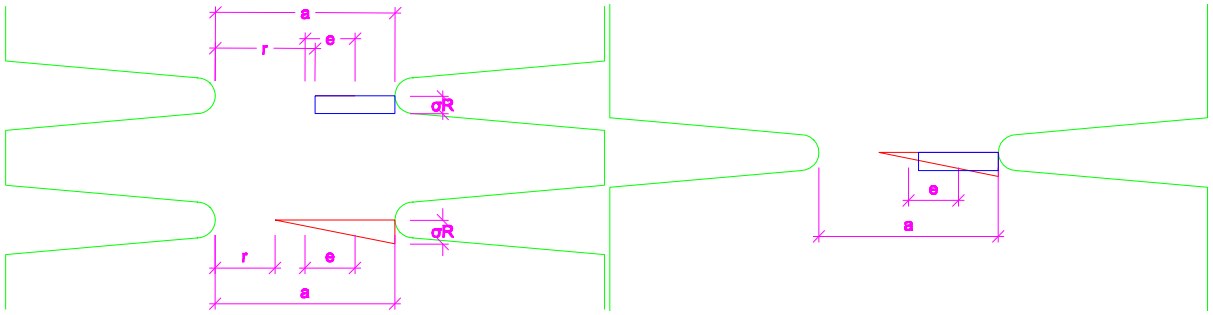

Fig. 11.51: comparison of rectangle and triangle-Model of Leonhard [Leonhardt, 1965]

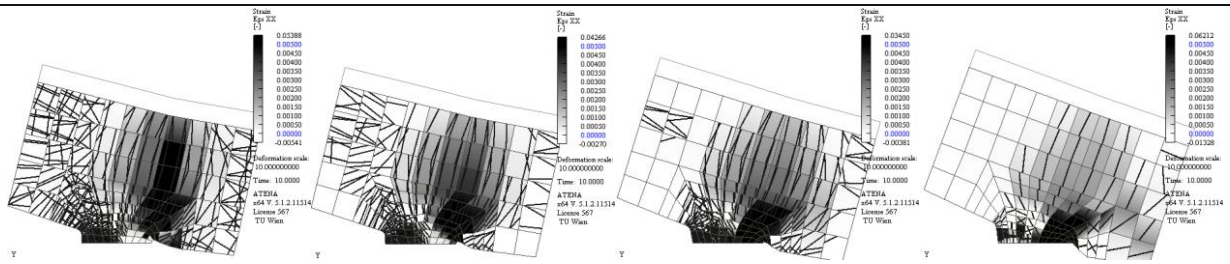

Fig. 11.52: Tension Strength FT=0.29MPa; FT=1.45MPa; FT=2.90MPa; FT=5.80MPa

In **Fig. 11.52**, with a bigger mesh, the Tension Strength has a bigger influence on the Brazilian splitting.

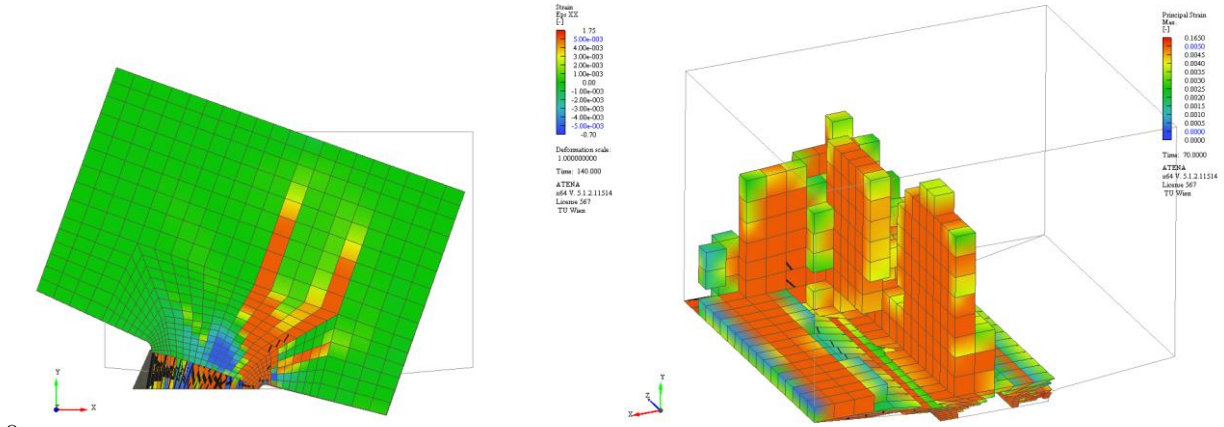

Fig. 11.53: Two 3-D-Model which show the final failure mechanism of tensile splitting.

11.3.3 Young's Modulus

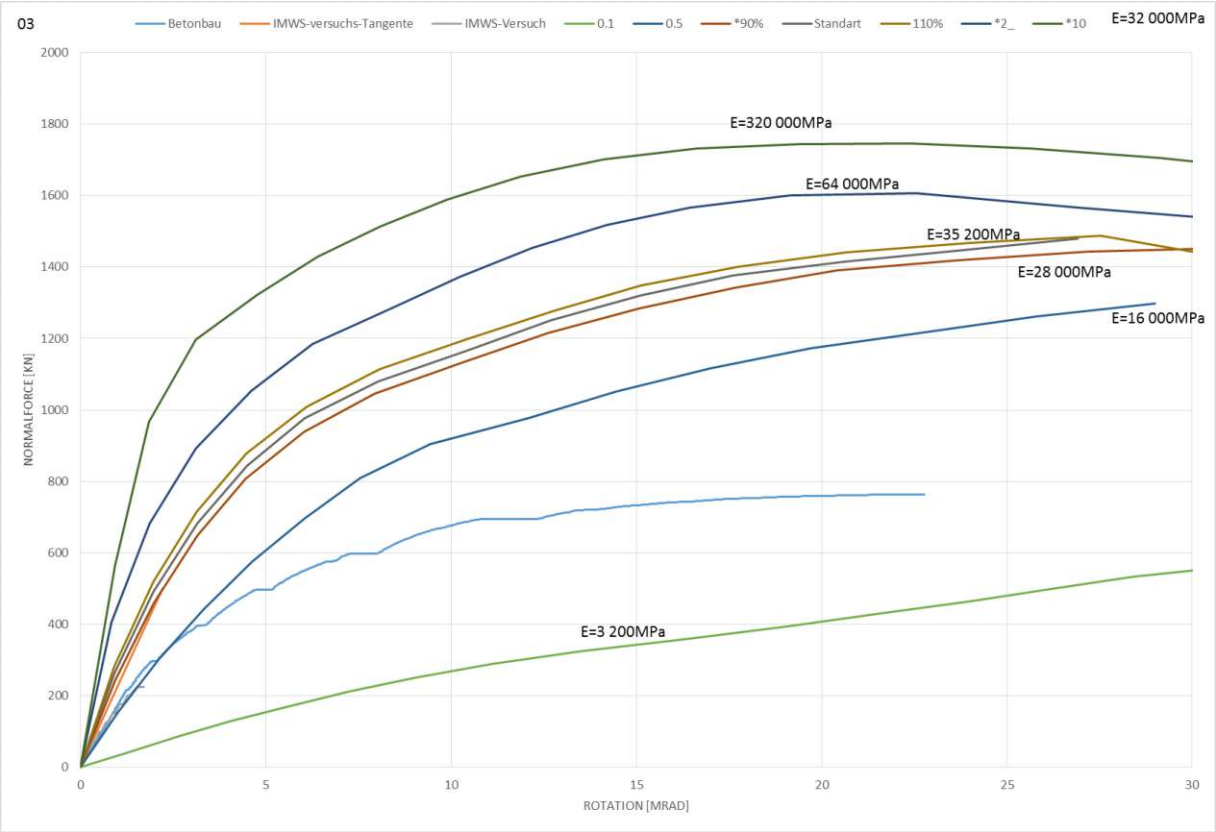

Fig. 11.54: Effect of the different Young's Moduli in the Rotation-Load-Curve

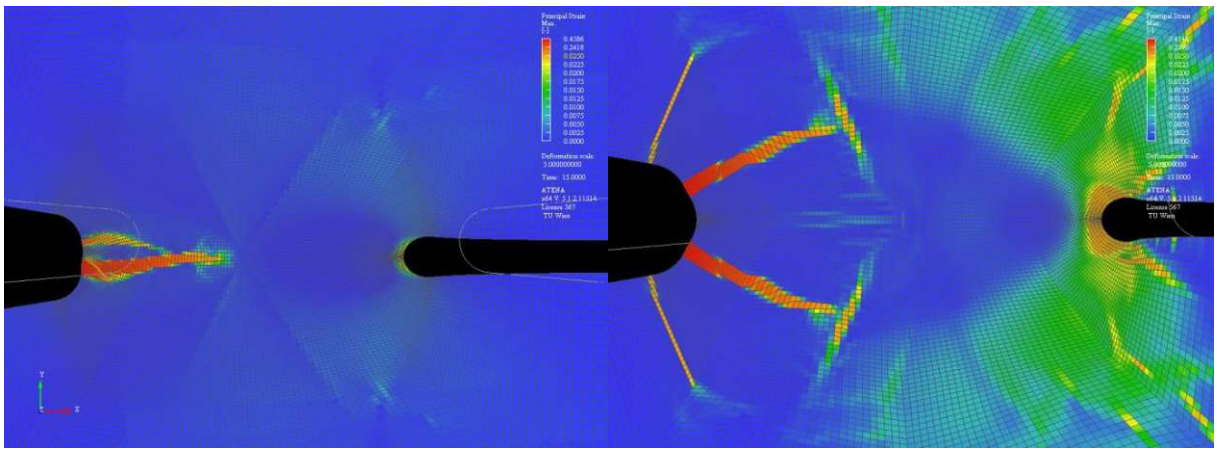

Fig. 11.55: ϵ_I first principal strain for E=3 200 MPa (left) and E=320 000 MPa (right)

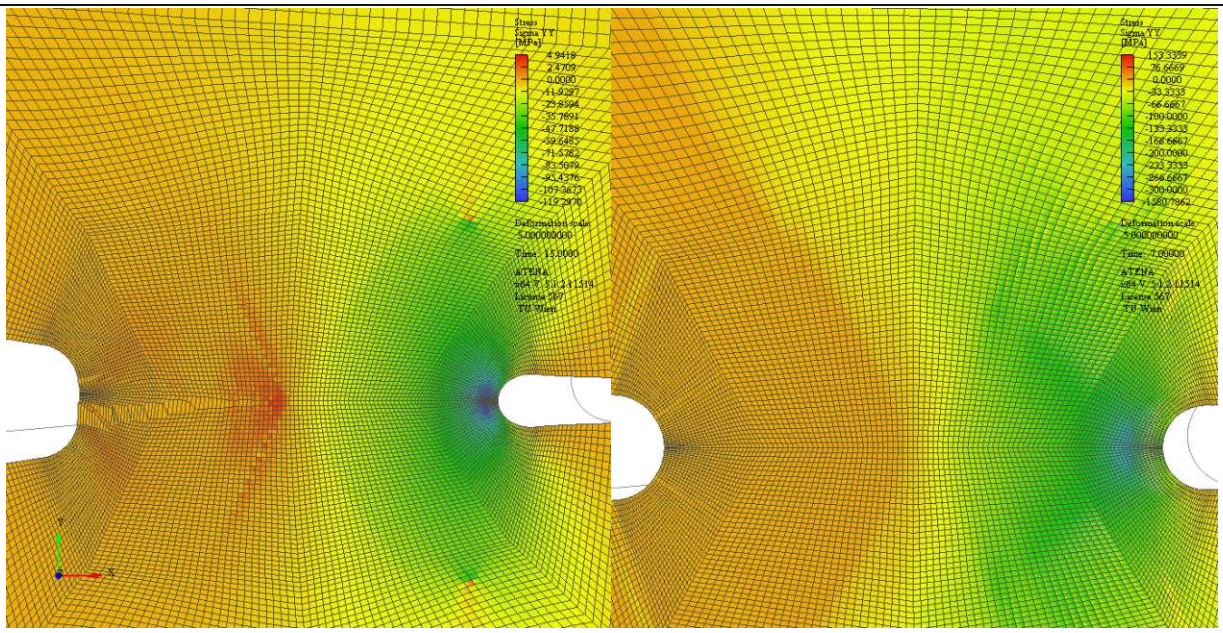

Fig. 11.56: σ_{LL} stresses in Load-Direction for E=3 200 MPa (left) and E=320 000 MPa (right)

11.3.4 Poisson's ratio

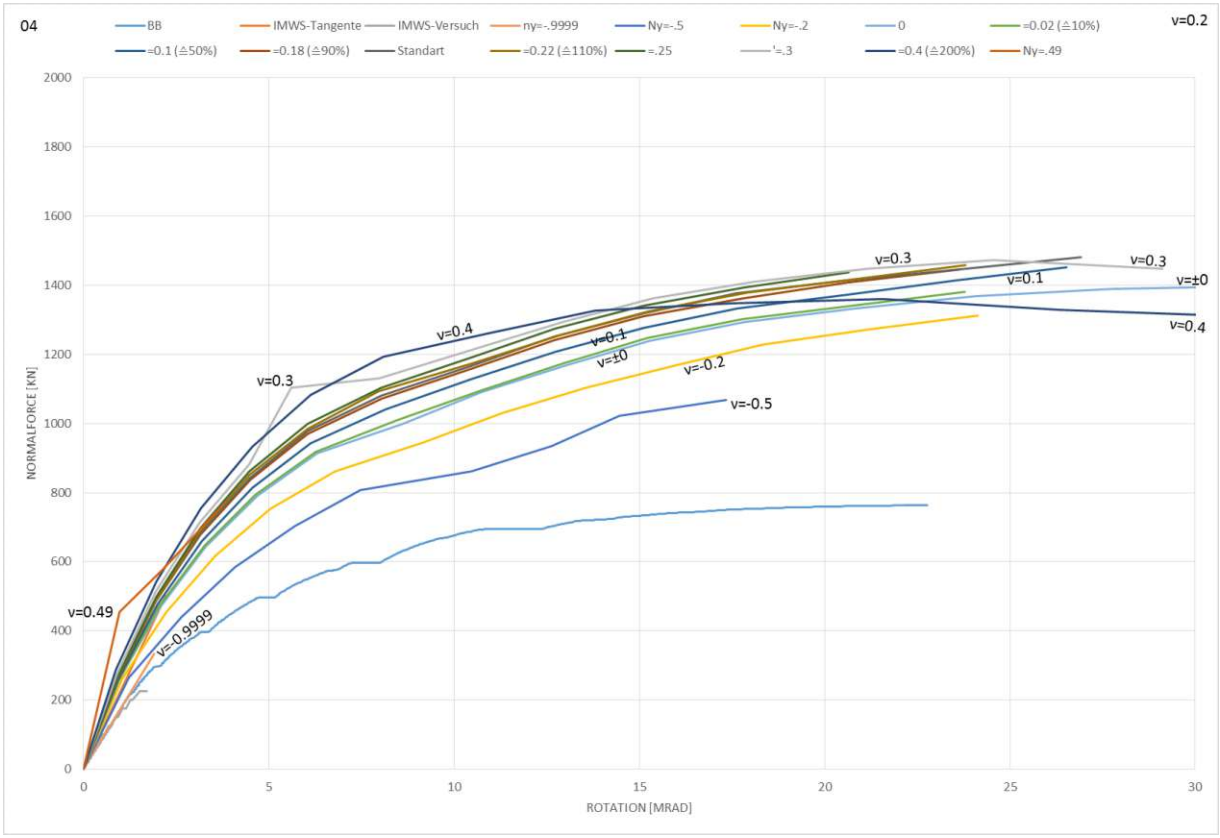

Fig. 11.57: Effect of the different Poisson's ratio in the Rotation-Load-Curve[26]

[26] "Acceptable range: <0;0.5)" according to [GiD 12.0,2015] with [ATENA, 2015]

According to

Fig. 11.57 a change of ν between 0.1 and 0.4, which is a quite wide region, the Load-Rotation-Curve does not change much.

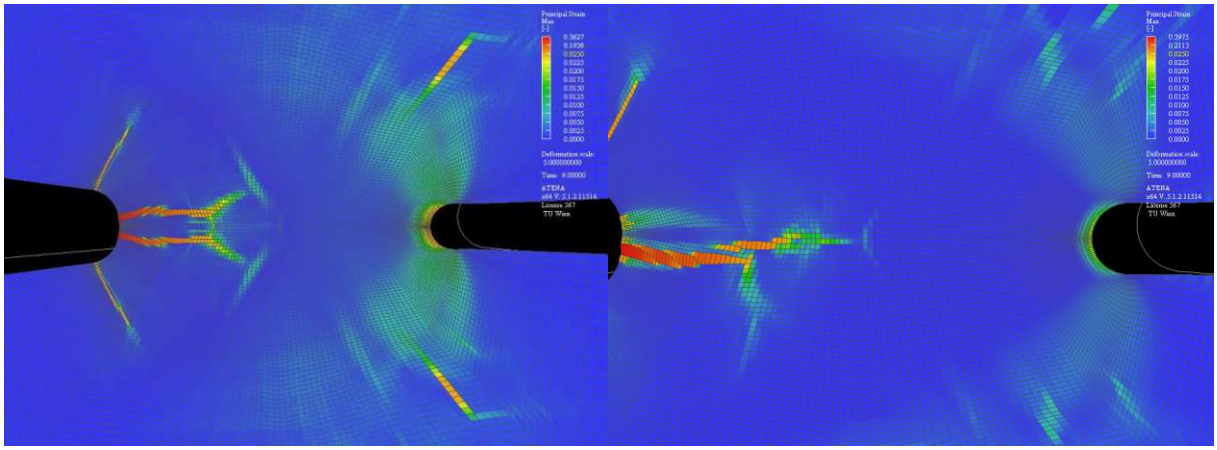

Fig. 11.58: ϵ_I first principal strain for ν=-0.5(left) and ν=+0.4 (right)

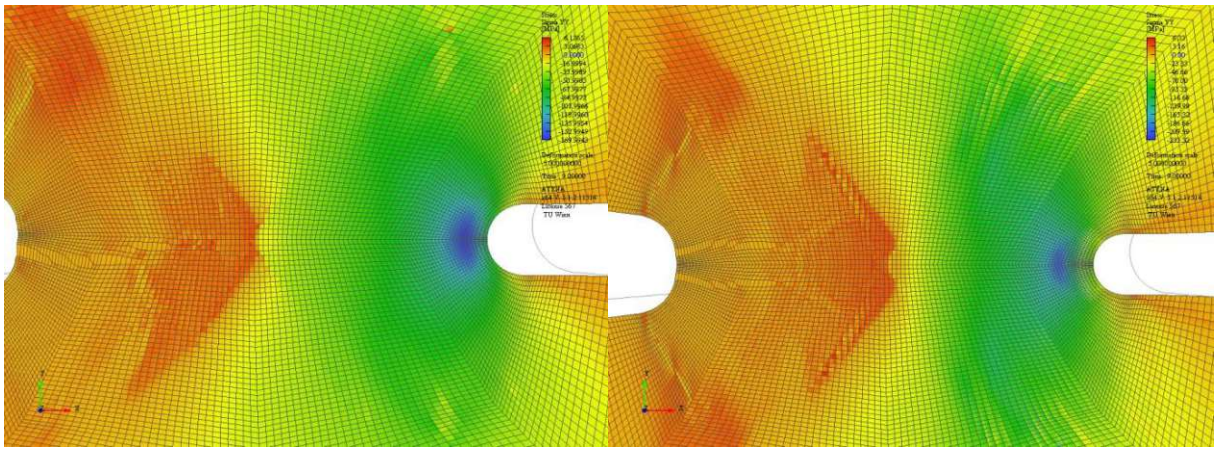

Fig. 11.59: σ_{LL} stresses in Load-Direction for ν=-0.5(left) and ν=+0.4 (right)

11.3.5 Fracture Energy

After reaching the tensile strength, the material gets cracks, but those cracks are not (fully) connected together, so there are still areas where the concrete can transmit stresses (and therefor also forces), also there might be some locally strong parts, which did not fail at all, but over a larger Area or Volume the stiffness decreases quite much, and the bigger the "mean" crack opening, the less areas, which are still connected together. Also this work is in general only interested in the pre-peak, but in general this local post-peak-behavior , or even failure in some elements, does not automatically lead to a decreasing load.

After reaching the tensile strength of an integration point, the FE-Model splits the strains into the elastic strains and the fracturing strains. Zero stresses are transmitted in the FE-Model, when the crack-with (w) reaches the "*full tension-failure-crack-opening-with*"[27] of this

[27] "Full" crack opening is the crack opening under tension, where crack is so wide open, that no connection between the parts (in this Area with this opening).

concrete (w_c), which is depending on the Fracture Energy. According to **Fig. 11.60** this model uses the *"Exponential Crack Opening Law"*. [ATENA, 2015] uses a function from experiments by "HORDIJK (1991)":

$$\frac{\sigma}{f_t'^{ef}} = \qquad (3)$$

— ATENA Theory [Červenka, 2014] equation 2.13 referring on HORDIJK (1991).

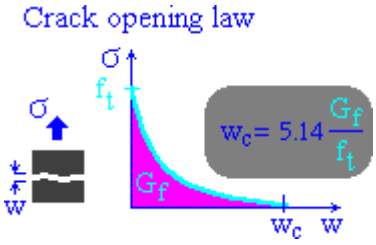

Fig. 11.60: Fracture Energy for CEM2 [GiD 12.0,2015][ATENA, 2015][Červenka, 2014]

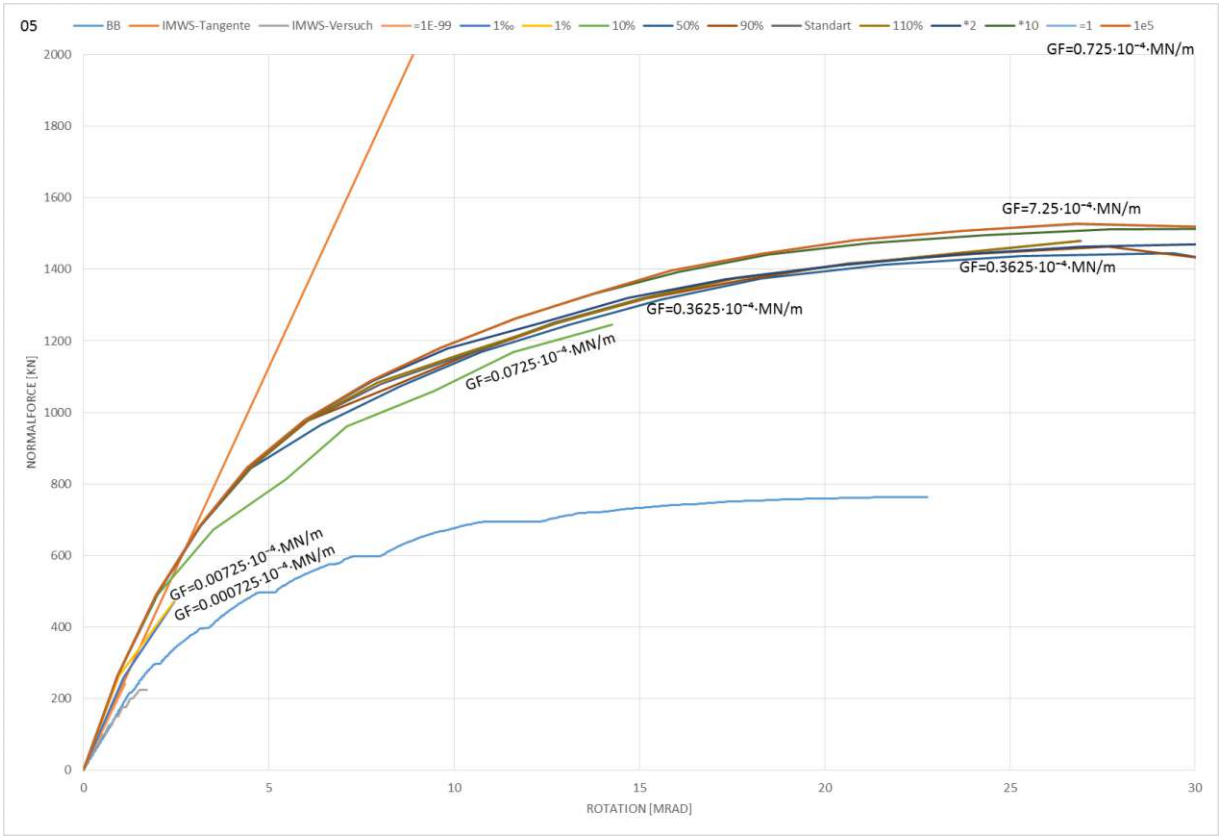

Fig. 11.61: Effect of the different Fracture Energy in the Rotation-Load-Curve

(Analyse mit feineren Lastschritten ergänzen)

Decreasing the fracture Energy more than 10times from the standard value makes the calculation unstable, and less than that, it does not affect much in the Load Rotation Curve (see **Fig. 11.61**) , but as you can see in Fig. 11.62 the strain plot looks quite different.

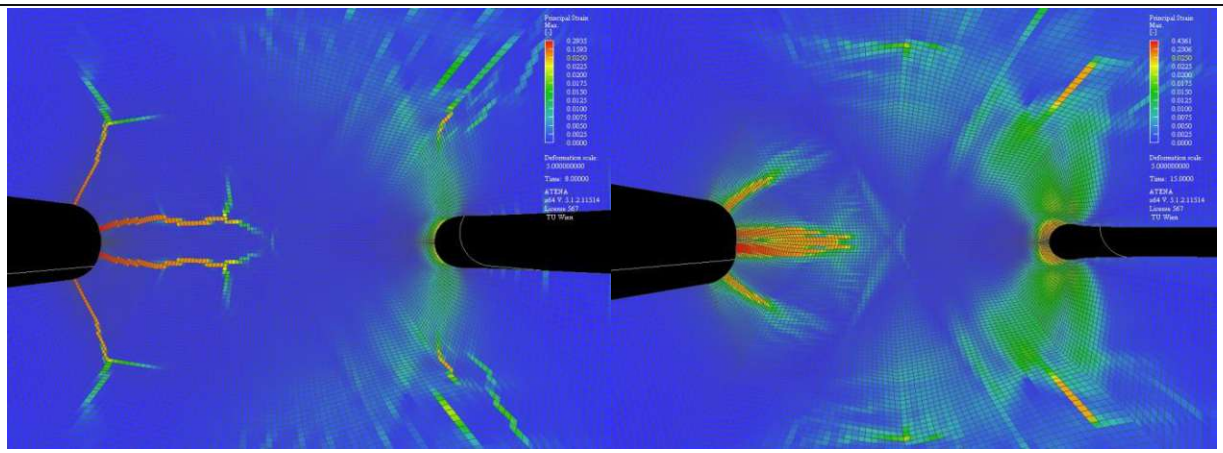

Fig. 11.62: ϵ_I first principal strain for GF=0.0725 kN/m (left) and GF=7.25 kN/m (right)

Fig. 11.62 shows the (quantitative) differences of the failure-Mode. **Fig. 11.62a** at a displacement of 0.8mm and **Fig. 11.62b** at a vertical displacement of 1.5mm, to compare qualitative at the same displacement-level see **Fig. 11.63**, both have a vertical displacement of 1mm, the one with the 100times higher Fracture Energy one has (only) about 17% bigger load, also the maximal principal strains in **Fig. 11.63a** looks quite different to/from **Fig. 11.63b.**

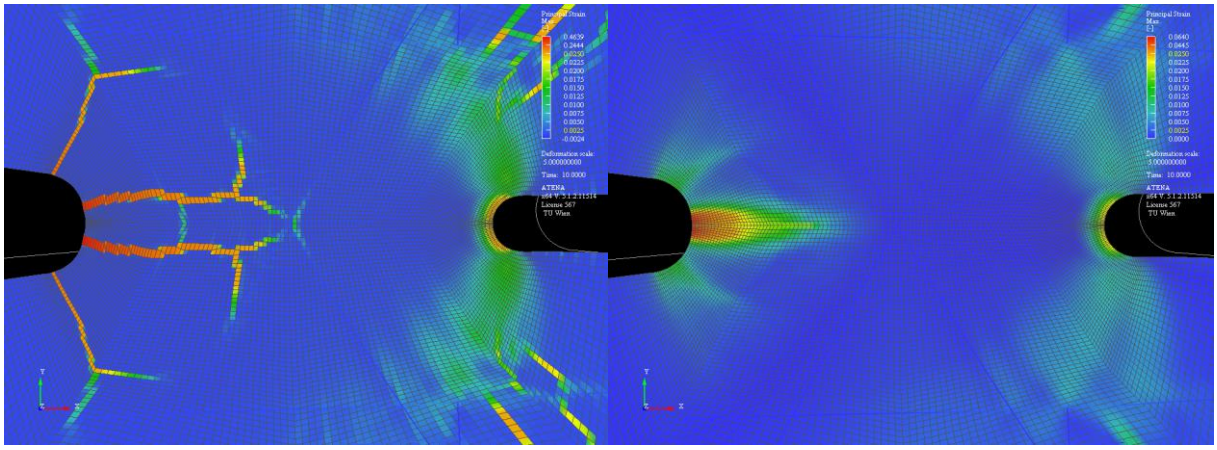

Fig. 11.63: ϵ_I first principal strain for GF=0.0725 kN/m (left[28]) and GF=7.25 kN/m (right) at a vertical displacement of 1mm

[28] Last load-Step of **Fig. 11.63b** did not convert (within the tolerance limits).

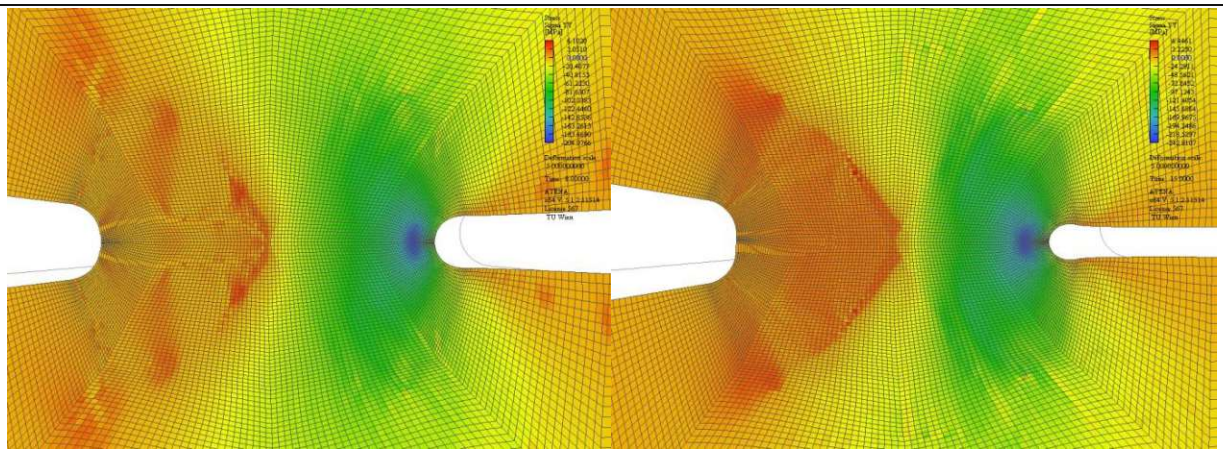

Fig. 11.64: σ_{LL} stresses in Load-Direction for GF=0.0725 kN/m (left) and GF=7.25 kN/m (right)

11.3.6 "Excentricity-EXC"[29]

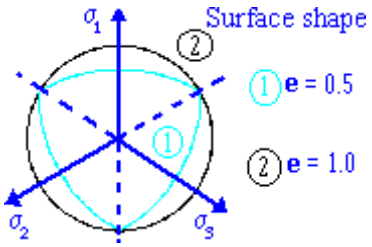

Fig. 11.65: Surface Shape in [GiD 12.0,2015][ATENA, 2015] [Červenka, 2014]

To understand Parameter for the *"deviatoric-plane-form"* EXC, which is used in the failure-surface-equation **(1)**, for calculate m and r in **(1a,b)**, written as a function of e:

$$F_{3P}^{p}(\xi,\rho,\theta,e)_{ft,fc} = \frac{1.5\cdot\rho^2}{f_c'^2} + \frac{m(e)}{\sqrt{6}\cdot f_c'}\cdot\left(\rho\cdot r(\theta,e)+\sqrt{2}\cdot\xi\right) - c = 0 \qquad (4)$$

Only values for e between[30] 0.5 and 1 are reasonable for concrete according to [GiD 12.0,2015] with [ATENA, 2015]

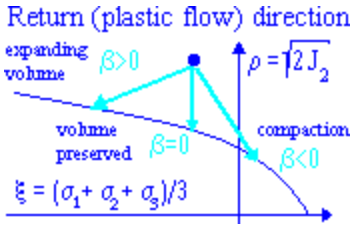

Fig. 11.66: Deviatoric plain in [GiD 12.0,2015][ATENA, 2015] [Červenka, 2014]

[29] "excentricity" … old word for eccentricity [Wiktionary, 2012]

[30] 0.5≤e≤1 (including both limits) e=0.5 and e=2 are both triangular (sharp corners) in the deviatoric plane for $1.5\cdot\frac{\rho^2}{f_c'^2} << Max\left(m\cdot\frac{\rho}{\sqrt{6}\cdot f_c'}\cdot r(\theta,e), m\cdot\frac{|\xi|}{\sqrt{3}\cdot f_c'}, c\right)$.
1<e≤2 will not be representative for concrete

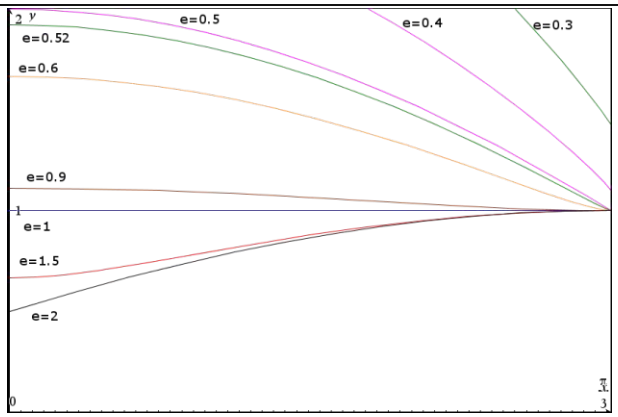

Fig. 11.67: θ-r-Diagram; r depending on θ, for different e-Values.

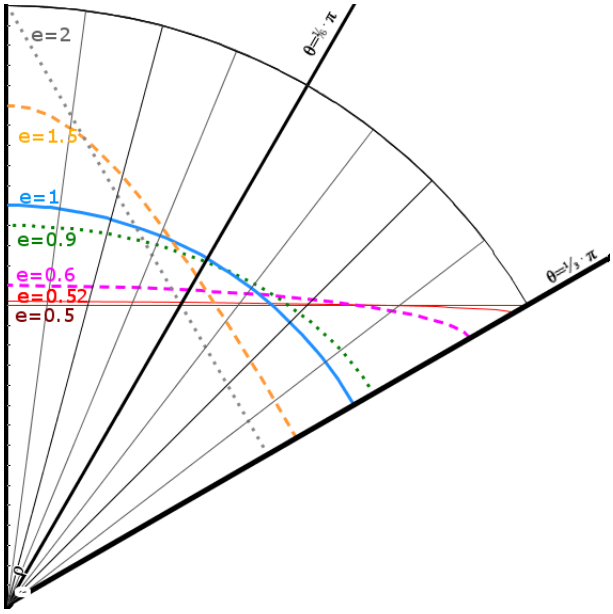

Fig. 11.68: $\theta - \frac{e+1}{e \cdot r}$-Diagram[31]

[31] representative for the deviatoric plain for

1. $1.5 \cdot \frac{\rho^2}{f_c'^2} << \frac{m(e) \cdot \rho \cdot r(\theta,e)}{\sqrt{6} \cdot f_c'}$ and
2. $\sqrt{2} \cdot |\xi| << \rho \cdot r(\theta,e)$ and therefore $\rho \approx \sqrt{6} \cdot f_c' \cdot c \cdot \frac{1}{m(e)} \cdot \frac{1}{r(\theta,e)}$

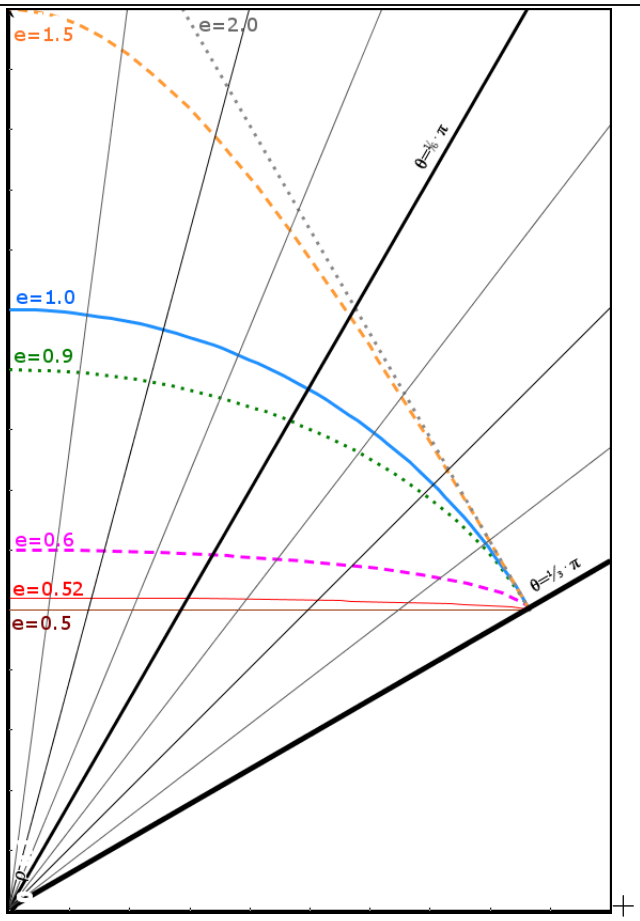

Fig. 11.69: θ $-\frac{1}{r}$-Diagram[32]

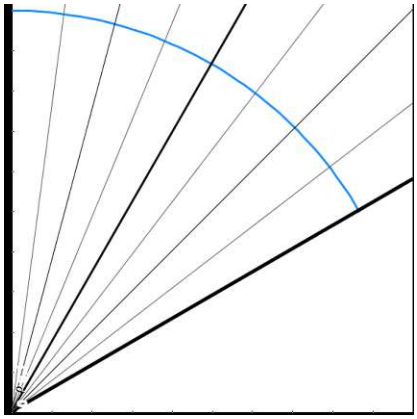

Fig. 11.70: θ −1 -Diagram[33]

[32] representative for the deviatoric plain at the failure surface for

1. $1.5 \cdot \frac{\rho^2}{f_c'^2} << \frac{m(e) \cdot \rho \cdot r(\theta,e)}{\sqrt{6} \cdot f_c'}$ and
2. $\xi \leq 0$ and
3. $\sqrt{6} \cdot f_c' \cdot c << m \cdot \rho \cdot r(\theta,e)$ and therefore $\rho \approx -\sqrt{2} \cdot \xi \cdot \frac{1}{r(\theta,e)}$

[33] representative for the deviatoric plain at the failure surface for

1. $\frac{m(e) \cdot \rho \cdot r(\theta,e)}{\sqrt{6} \cdot f_c'} << 1.5 \cdot \frac{\rho^2}{f_c'^2}$

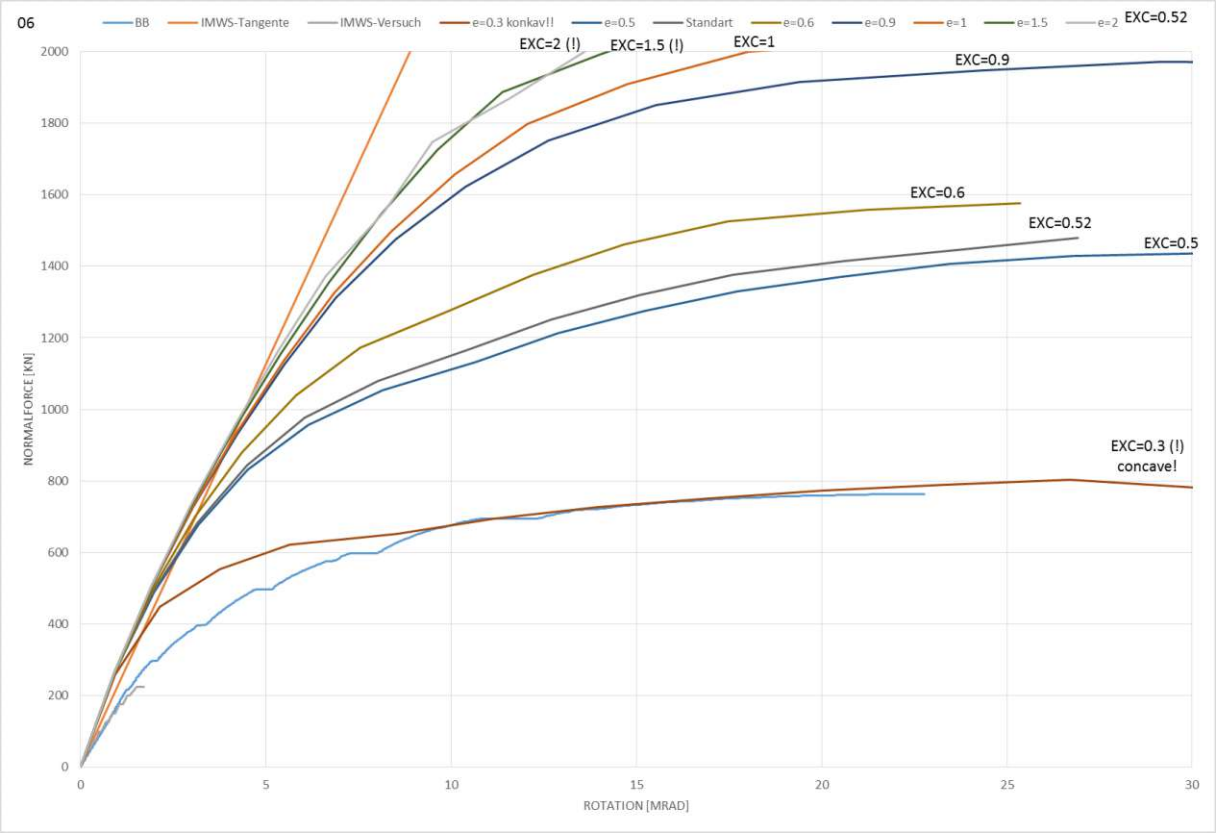

Fig. 11.71: Effect of the different "Excentricities" in the Rotation-Load-Curve[34]

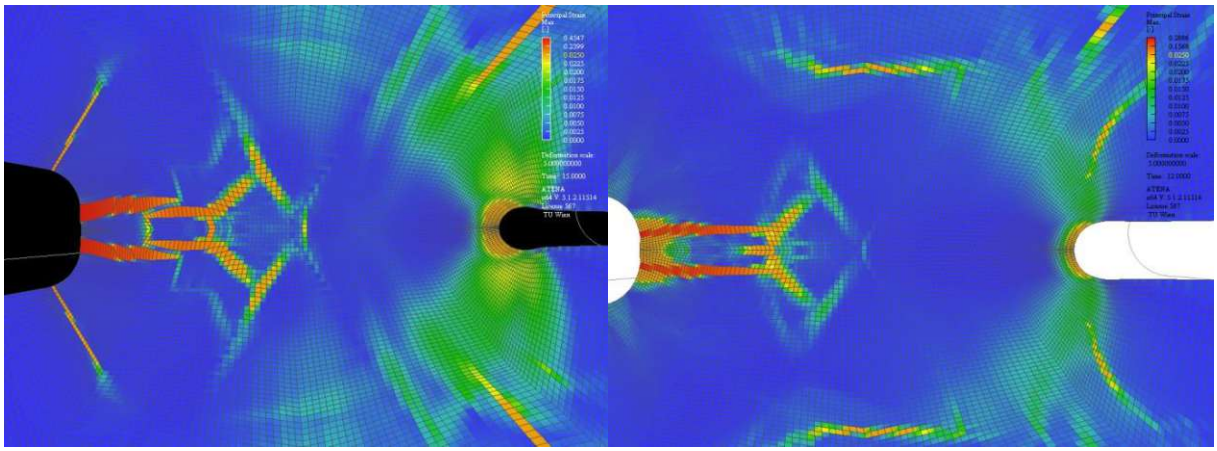

Fig. 11.72: ϵ_I first principal strain for EXC=0.5 (left) and EXC=1 (right)

[34] "Acceptable range: <0.5; 1>" according to [GiD 12.0,2015] with [ATENA, 2015] Out of obvious reasons it is unlikely that a concave failure surface can exist, therefore values between 0.5 and 2 (including border values) will be best representative, for real experiments.

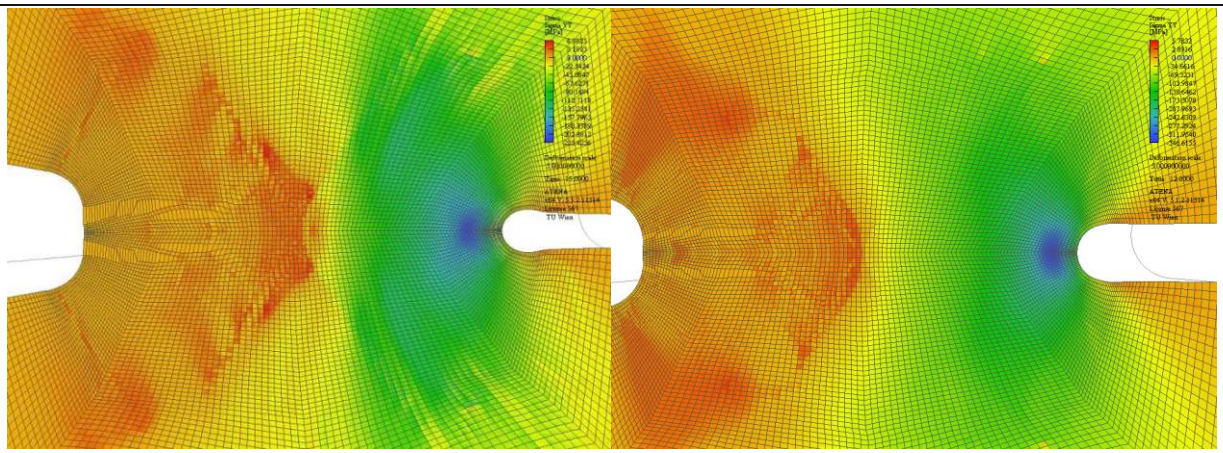

Fig. 11.73: σ_{LL} stresses in Load-Direction for EXC=0.5 (left) and EXC=1 (right)

11.3.7 Plastic Strain-EPS CP

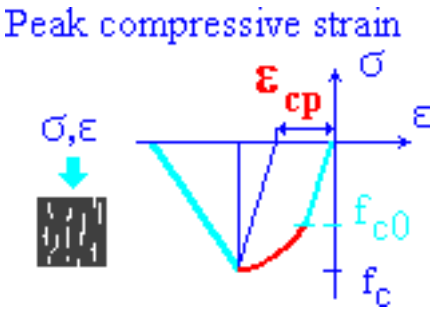

Fig. 11.74: (≙**Fig. 8.11a**) grafical explantation of ϵ_{cp} [GiD 12.0,2015][ATENA, 2015][Červenka, 2014]

ϵ_{cp} is the *plastic compressive strain-capacity*[35], which is for uniaxial loading the plastic strain at the compressive strength f_c. The plastic strain for uniaxial loading is defined as the strain at f_c after removing the linear-elastic strains.

[35]In [GiD 12.0,2015] called "Plastic Strain-EPS CP" and in in [ATENA, 2015]: "EPS_CP". Those names can be irritating, because plastic strains are depending on the loading not on the material, so strain-capacity would be more correct

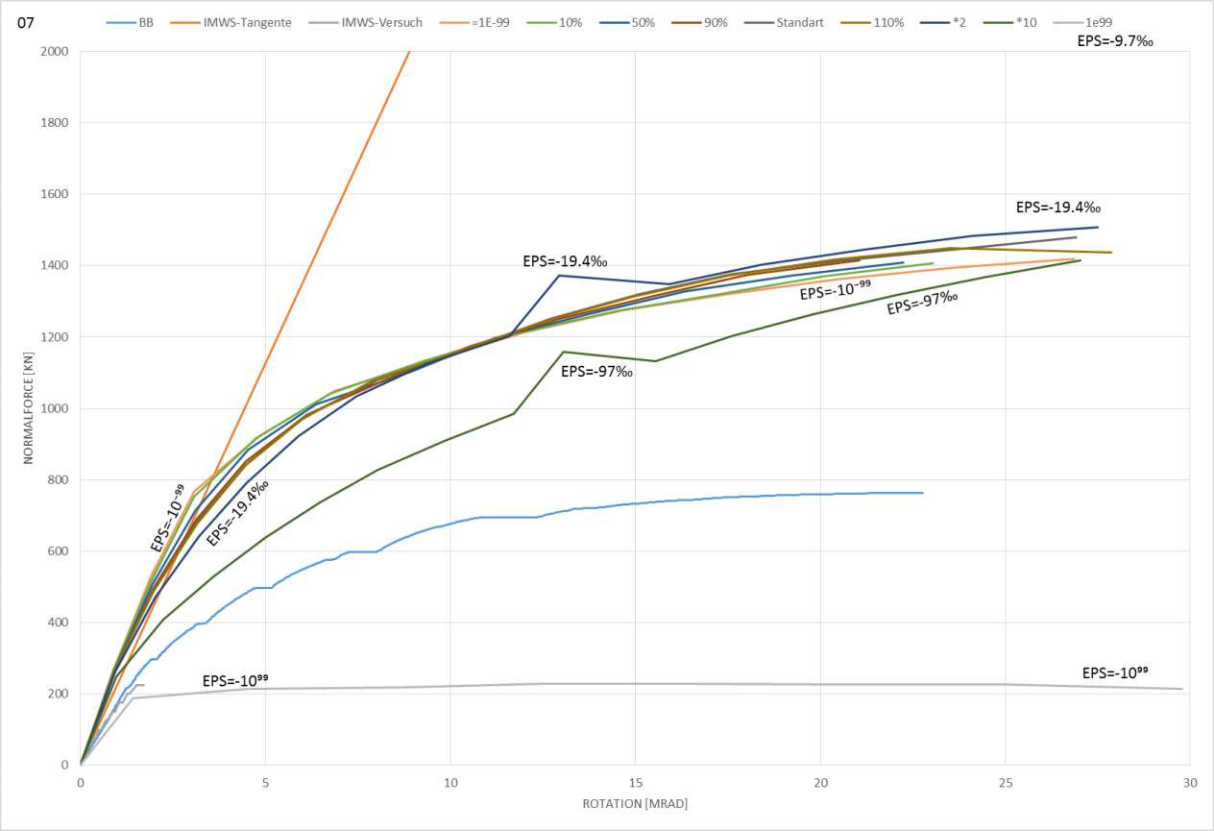

Fig. 11.75: Effect of the different plastic compressiv straincapacity in the Rotation-Load-Curve

Small plastic compressive stain-capacities lead to more stiffness, but in general to a smaller peak load. Big compressive strain-capacities lead to less stiffness and a higher peak-load. Unrealistic big compressive strain-capacities (f.e. EPS=10^{99}) lead to limiting the stress to FC0, because the it need unrealistic big strains to reach FC. If you compare EPS=10^{99} in **Fig. 11.75** with FC=FC0=6.09MPa in **Fig. 11.43**, you will see almost the same curve.

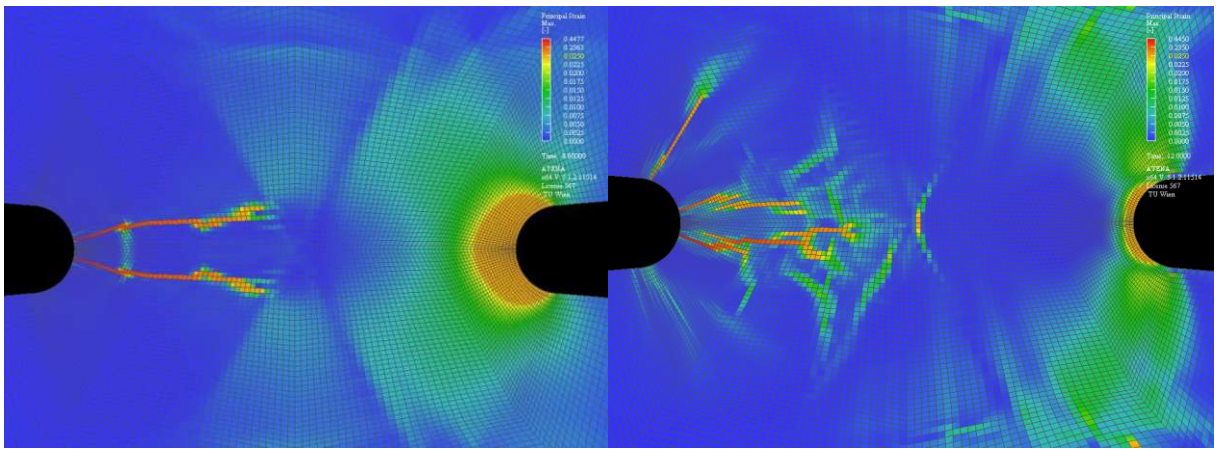

Fig. 11.76: ϵ_1 first principal strain for EPS=-∞ (left) and EPS=0 (right)

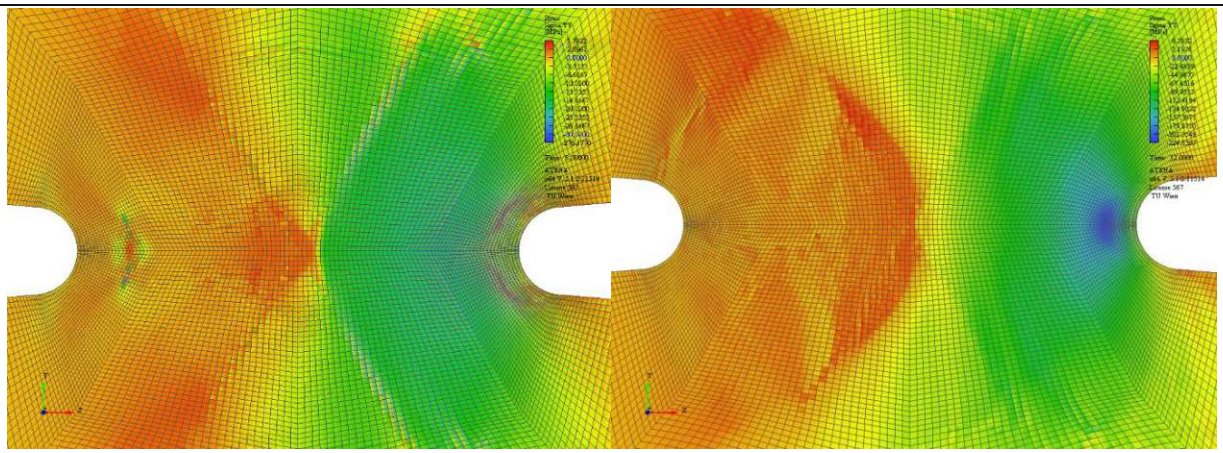

Fig. 11.77: σ_{LL} stresses in Load-Direction for EPS=-∞ (left) and EPS=0 (right)

11.3.8 Onset of Crushing (FC0)

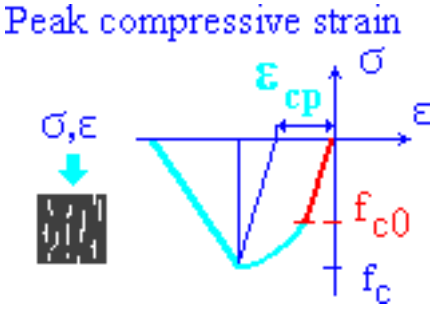

Fig. 11.78: (≙**Fig. 8.11a**) grafical explantation of f_{c0} [GiD 12.0,2015][ATENA, 2015][Červenka, 2014]

The *"linear-elastic-strength"* f_{c0} is the maximal stress, where the material is assumed only to behave only linear-elastic, without plastic deformations or fracturing. So the loading path and unloading path is in the static analysis the same as long as $0 \leq \sigma_{uniaxial} < f_{c0}$.

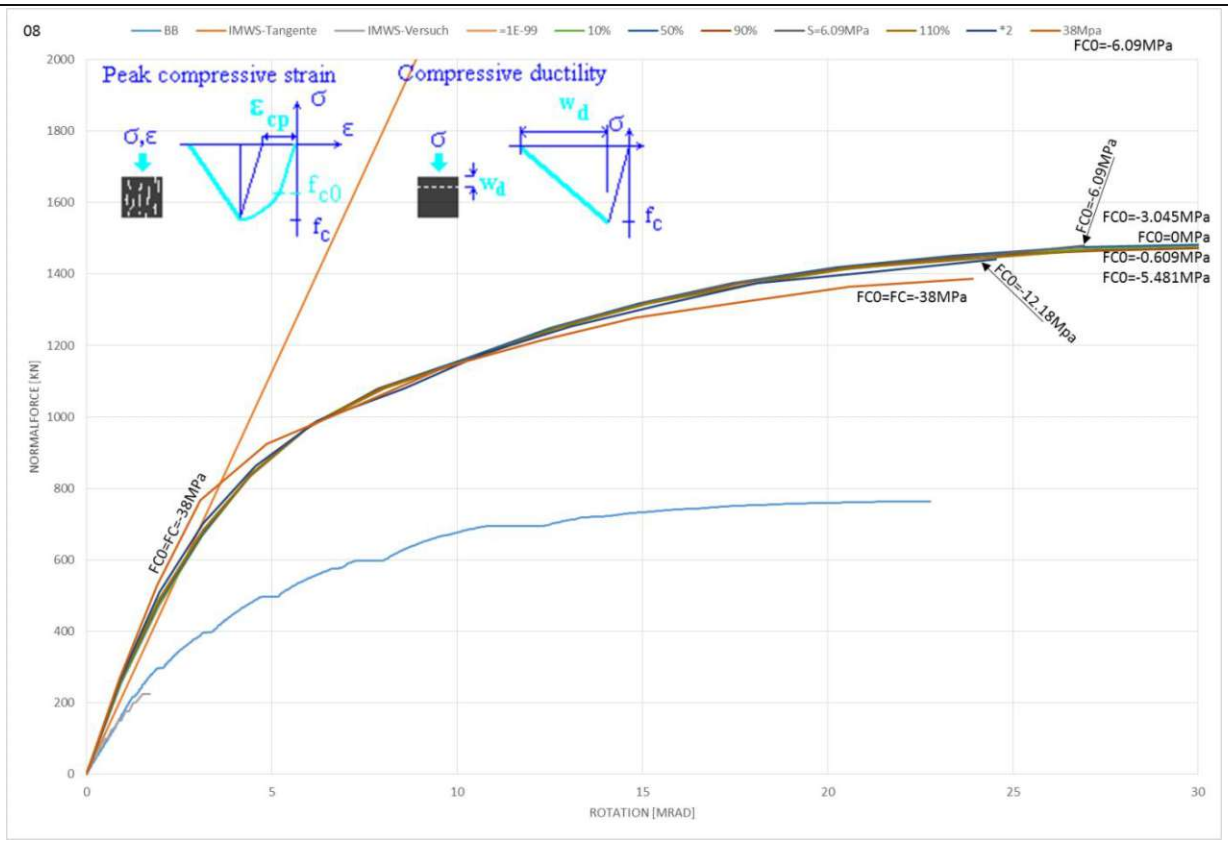

Fig. 11.79: Effect of the different ... in the Rotation-Load-Curve

As you can see in

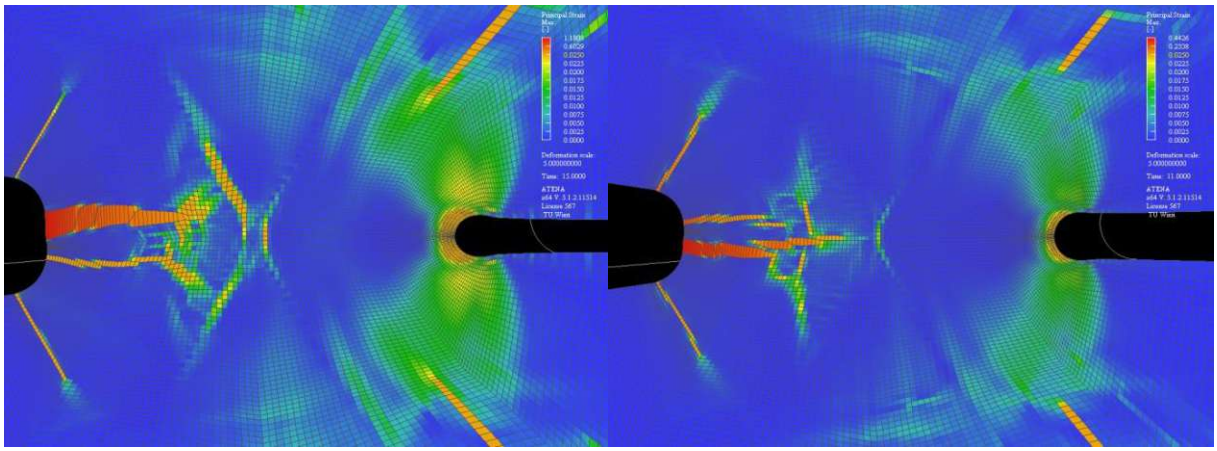

Fig. 11.80: ϵ_I first principal strain for ... (left) and ... (right)

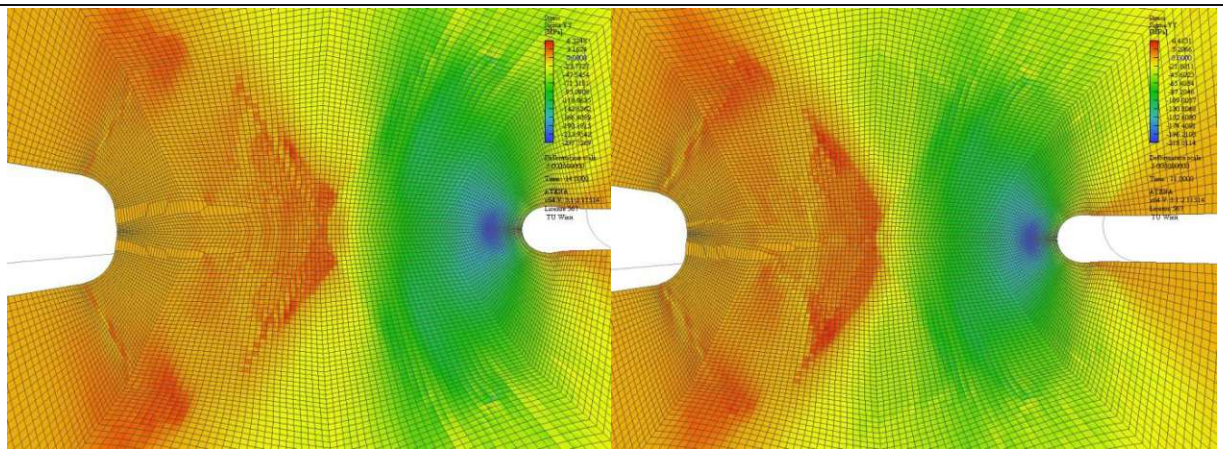

Fig. 11.81: σ_{LL} stresses in Load-Direction for ... (left) and ... (right)

11.3.9 Critical Comp Disp-WD

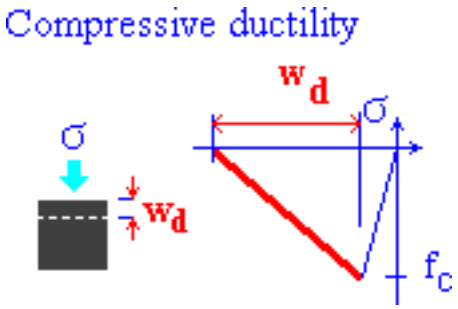

Fig. 11.82: (≙**Fig. 8.11b**) grafical explantation of w_d [GiD 12.0,2015][ATENA, 2015][Červenka, 2014]

The *critical compression displacement* is the critical additional displacement for compressive loading after reaching the compressive strength and further increasing compressive strains. Increasing strains after already reaching the compressive strength lead to a decreasing strength of this element[36]. It can be still be possible to increase the stress loading further, also due to bigger strains this Element can sustain less stresses, but other Elements might be still on the pre-peak and can still increase the stresses. This compressive ductility is somewhat similar to crack opening, which might be easier to image and understand. (see Chapter 11.3.5 Fracture Energy)

[36] Valid for $f_{c0}<f_c$

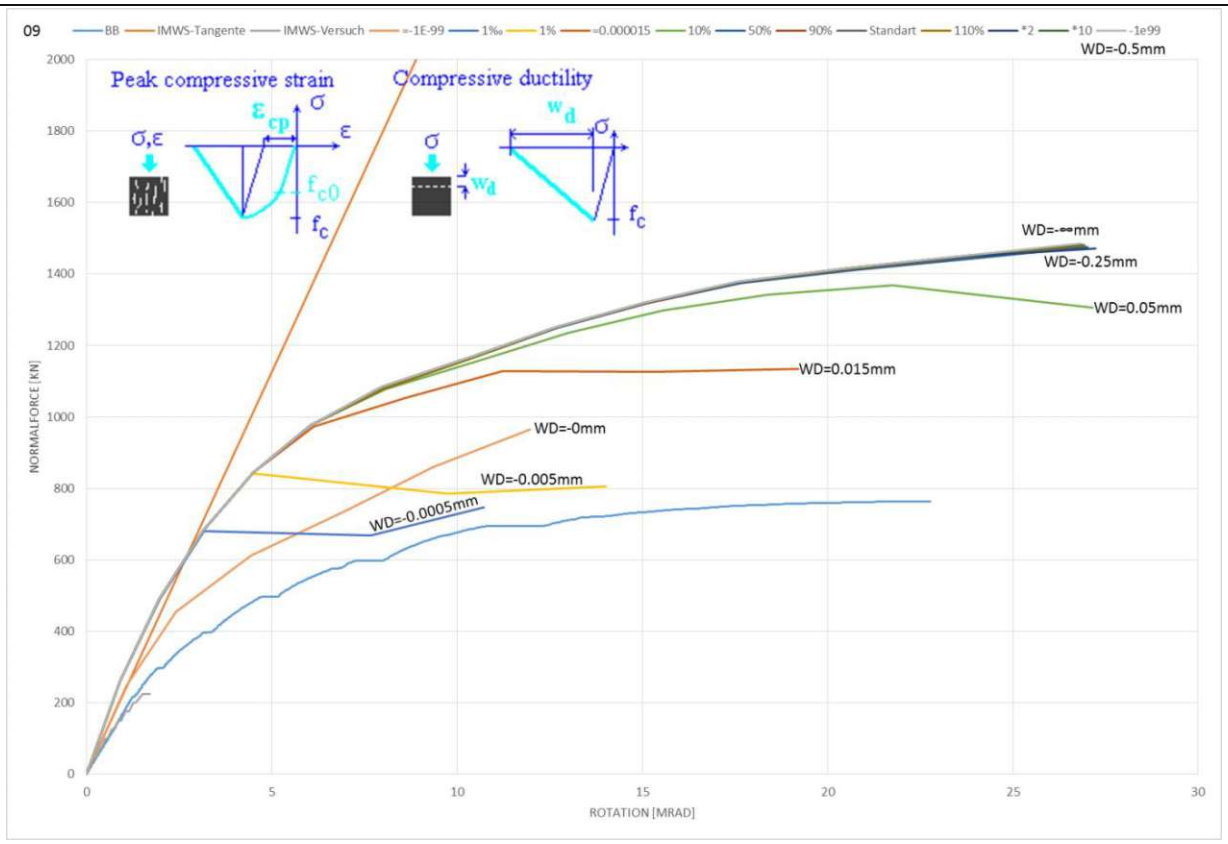

Fig. 11.83: Effect of the different critical compressional distance in the Rotation-Load-Curve

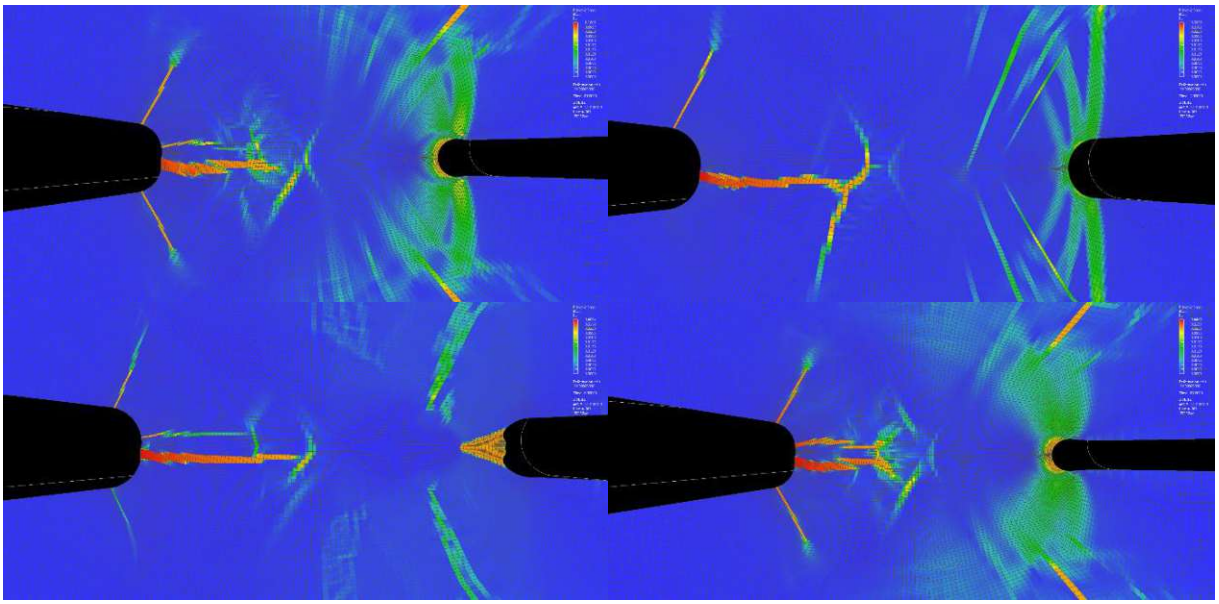

Fig. 11.84: ϵ_1 first principal strain for WD=0 (top left) , WD=-0.0005mm (top right), WD=-0.015mm (bottom left) and WD=-∞(bottom right)

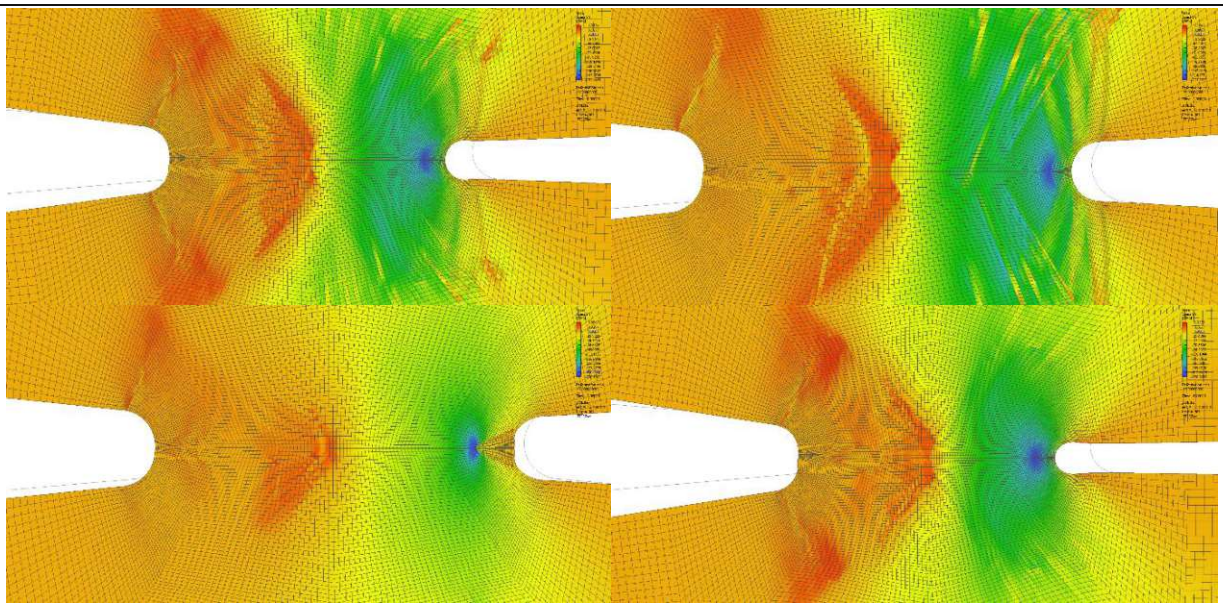

Fig. 11.85: σ_{LL} stresses in Load-Direction for WD=0 (top left) , WD=-0.0005mm (top right), WD=-0.015mm (bottom left) and WD=-∞(bottom right)

11.3.10 β

The "*direction of plastic flow*" can go to hydrostatic compression (β>0) or to hydrostatic tension (β<0), default is that the hydrostatic stresses say the same and the deviatoric strains are reduced to the failure surface. β≥0.7 lead to expansion of the model also it is under compression. So pressing down lead to lifting up, which is obviously wrong. The difference of the behavior is quite big. A much negative β-Value leads to a strange looking failure, which might be a shear-failure. A much positive β-Value leads to a compressive failure only in the first row of elements at the free surface, which could be explained because there cannot be this triaxial stresses, which are expected in the middle of the neck.

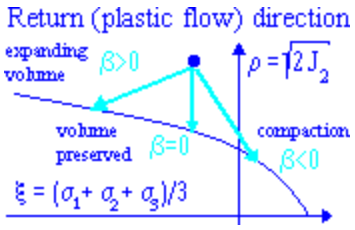

Fig. 11.86: Deviatoric plain in [GiD 12.0,2015][ATENA, 2015] [Červenka, 2014]

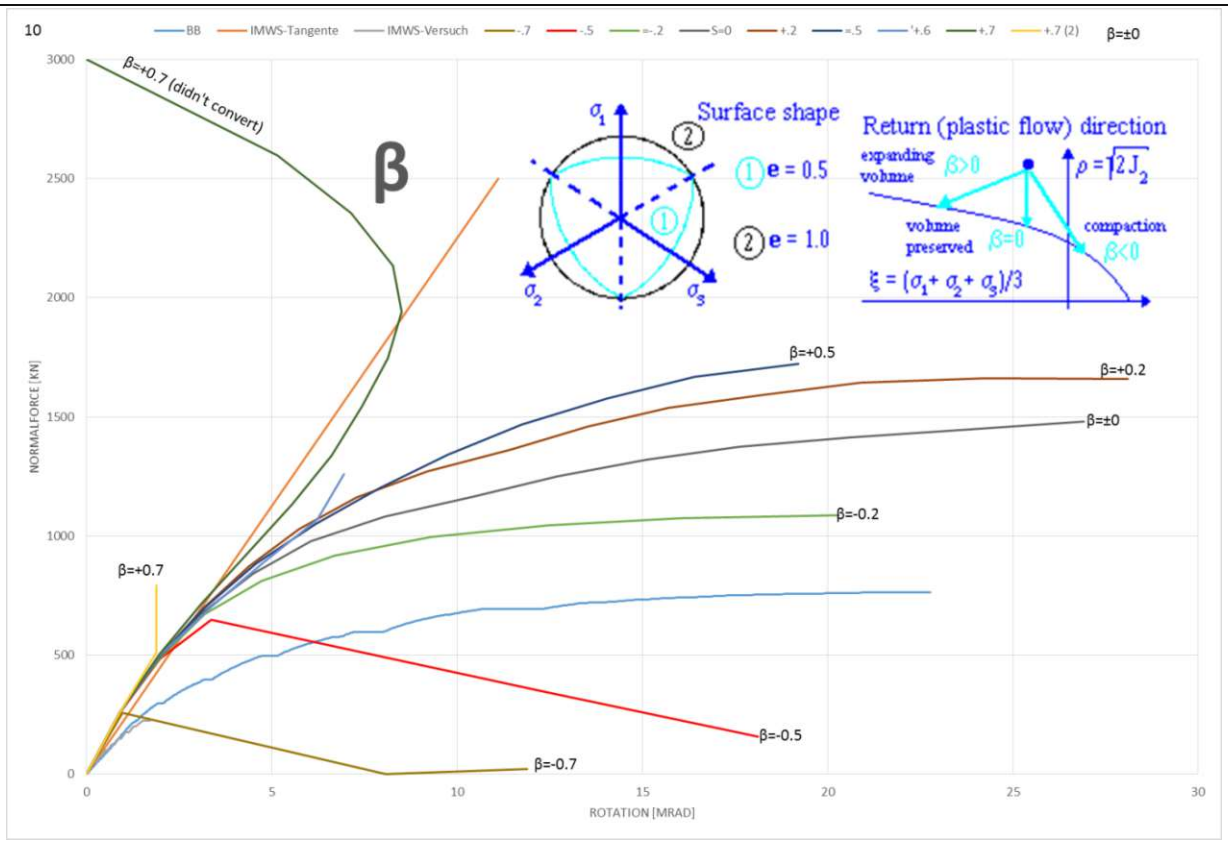

Fig. 11.87: Effect of the different direction of platic flow in the Rotation-Load-Curve[37]

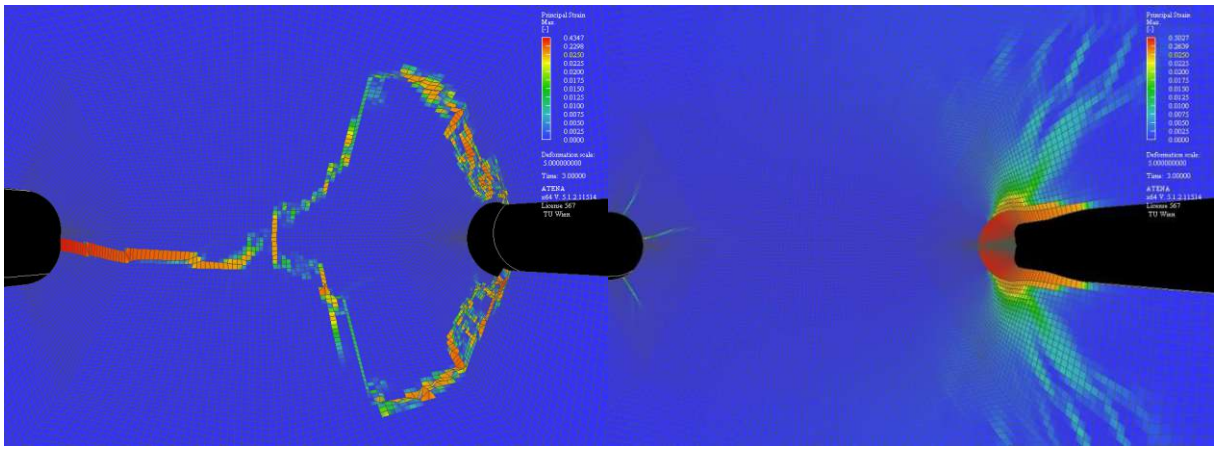

Fig. 11.88: ϵ_1 first principal strain for β=-0.7 (left) and β=+0.7 (right)

[37] The Y-Assis (Normal force) has different values than the other Load-Rotation-Diagrams in this Parameter-Studies

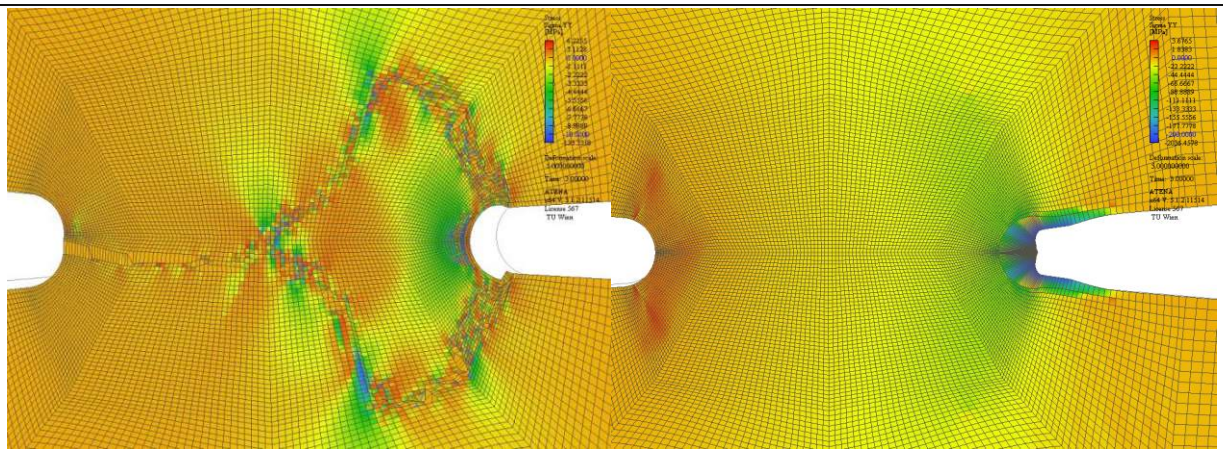

Fig. 11.89: σ_{LL} stresses in Load-Direction for ... (left) and ... (right)

11.3.11 ρ

The Parameter-studies showed that $0 \leq \rho \leq 10^{99}$ does not have any influence on the results.
The influence of the own weight is ignored.

11.3.12 α

The Parameter-studies showed that $-10^{99} \leq \alpha \leq 10^{99}$ does not have any influence on the results.
This parameter would only lead to influence if there is a thermal problem involved.

11.3.13 FIX

Two crack-models are available in Atena. One model considers rotated cracks and one considers fixed cracks. Rotated cracks mean, that the cracks are parallel and orthogonal to the principal stresses, which might sound obvious, but if some micro-cracks are already developed, they will not change their direction to the current principal stresses; also they might extend into a different direction and connect together. To consider that the crack cannot change their direction the fixed crack-model is developed. The fixed-crack-model considers that the cracks keep their direction; therefore the anisotropic crack-model is not parallel any more with the principal strains. The rotated crack model is usually the lower bound limit and the fixed-crack-model is the upper bound limit. Atena supports to make a compromise between both assumptions. In this compromise the User decides until which tensile-strength-reduction due to the crack-opening Atena assumes rotated cracks for each element and afterwards it switches to the fixed-orientated-cracks (only for those elements), which has a bigger tensile-strength-reduction. (See **Fig. 11.90**) The standard-value for "FIX" is one, which means; that as soon as the tensile strength of the element is one times the tensile strength of the uncracked model it assumes the fixed-cracks, which is now from the beginning on. If the value is reduced to zero it means, until the end it assumes that the cracks can rotate. Atena "only" supports smeared-crack-models not like some other FE-solver discrete-crack-models. The advantage of smeared cracks models is that, if there are several cracks in a material the solver is still able to solve it in a reasonable time. Especially in an inhomoge-

neous material, like concrete, which creates many micro-cracks, a discrete crack-model can "explode" the calculation time, until it converts.

The influence of crack-development is in general negligible for the concrete hinge; only at some load-steps the rotated-crack-model got lower values. In the principal-strains (see **Fig. 11.92**) you can see that the two tension-crack develops in the rotated-crack-model slightly to the reinforcement and in the fixed-crack-model the two tension-cracks almost connect together and before the reinforcement the line of biggest principal strains spread out orthogonal to the reinforcement and along the reinforcement the principal strains are higher.

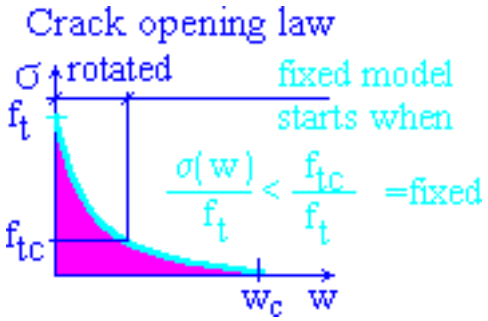

Fig. 11.90: Rotated and fixed-Model in [GiD 12.0,2015][ATENA, 2015] [Červenka, 2014]

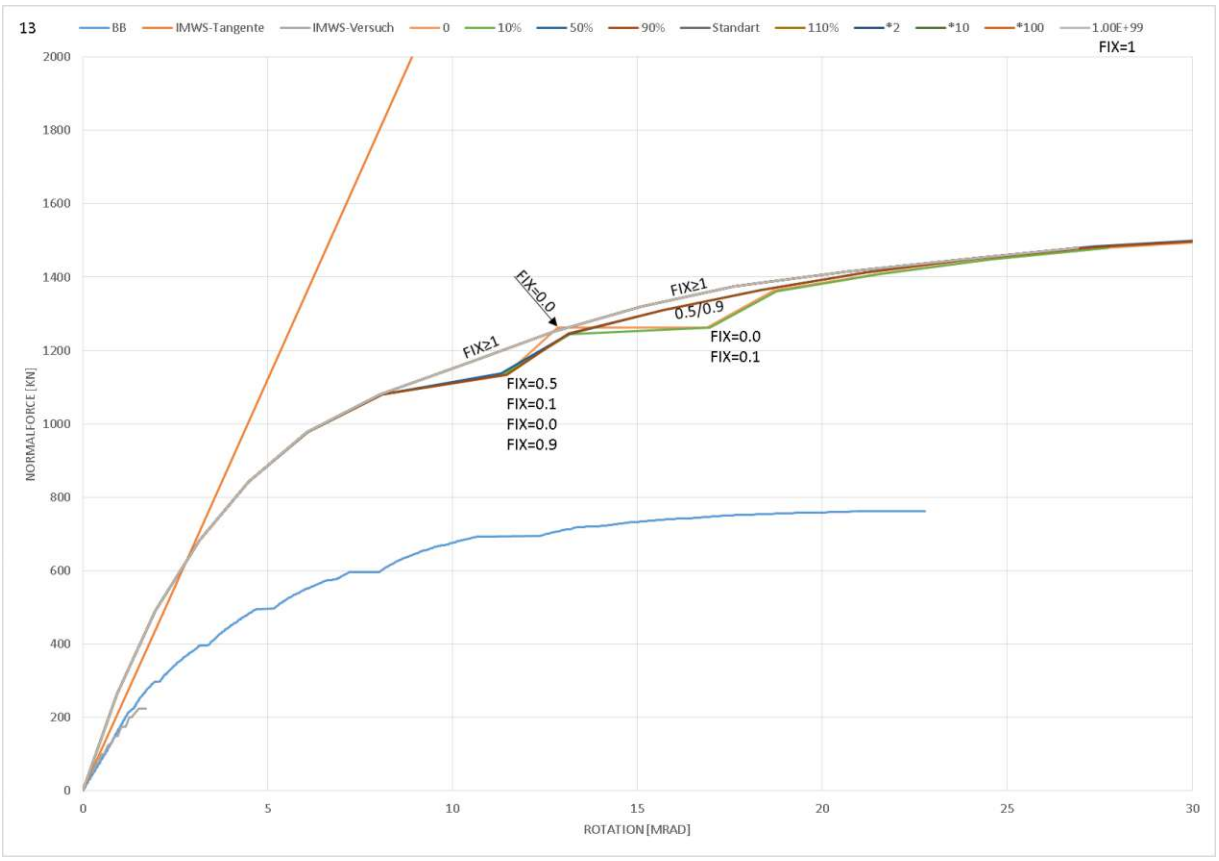

Fig. 11.91: Effect of the different Crack-models in the Rotation-Load-Curve

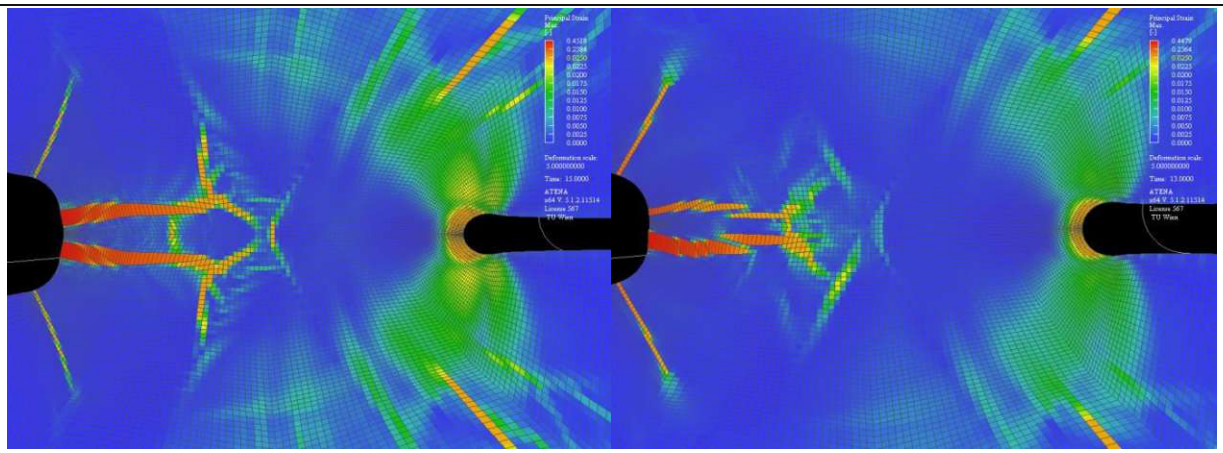

Fig. 11.92: ϵ I first principal strain for FIX=0 (left) and FIX≥1 (right)

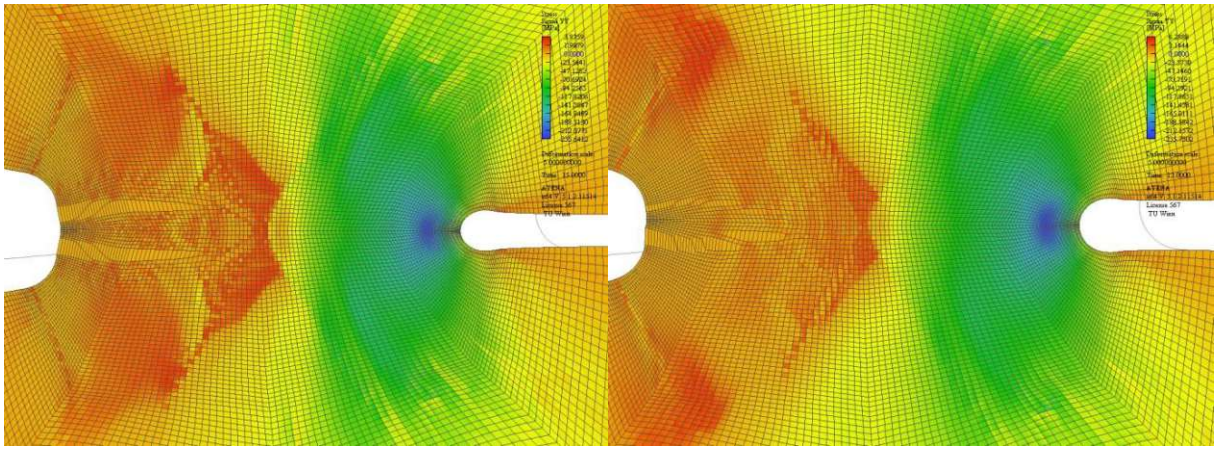

Fig. 11.93: σ_{LL} stresses in Load-Direction for FIX=0 (left) and FIX≥1 (right)

11.3.14 FC_R

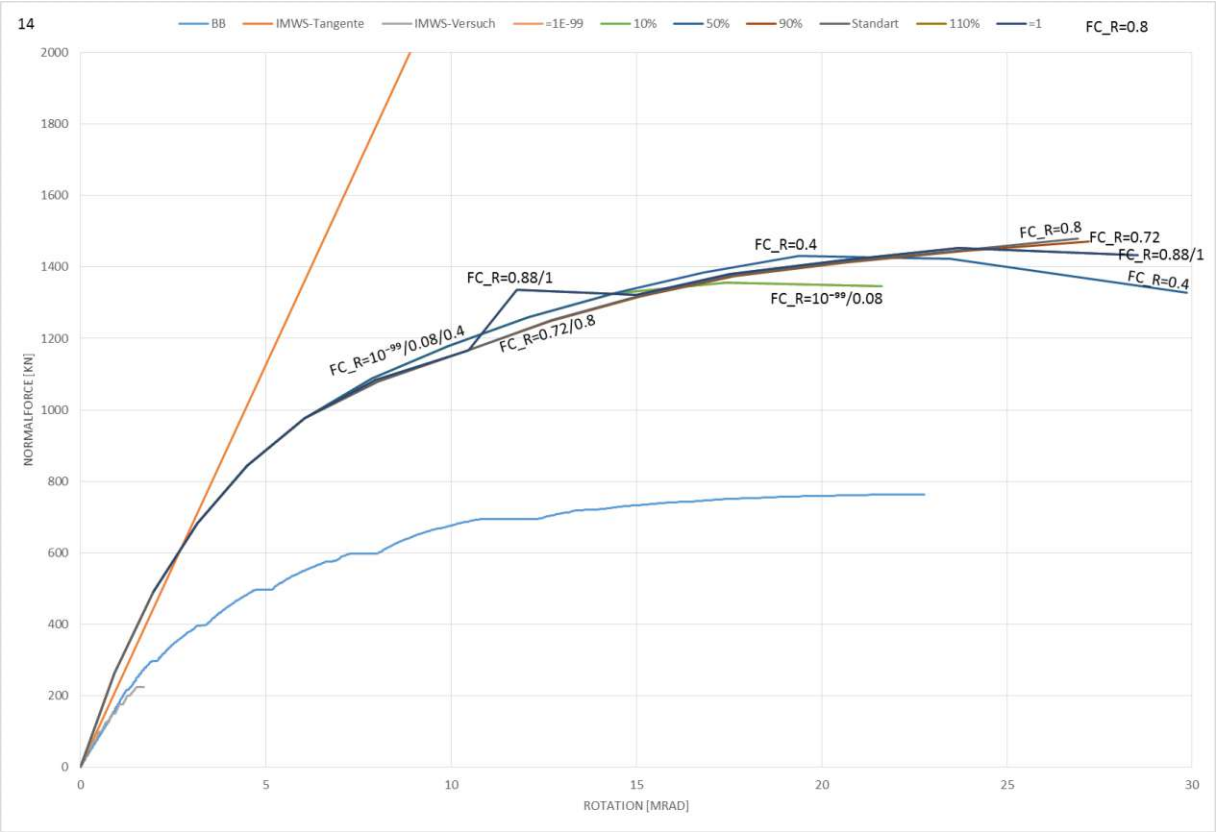

Fig. 11.94: Effect of the different FC_R in the Rotation-Load-Curve

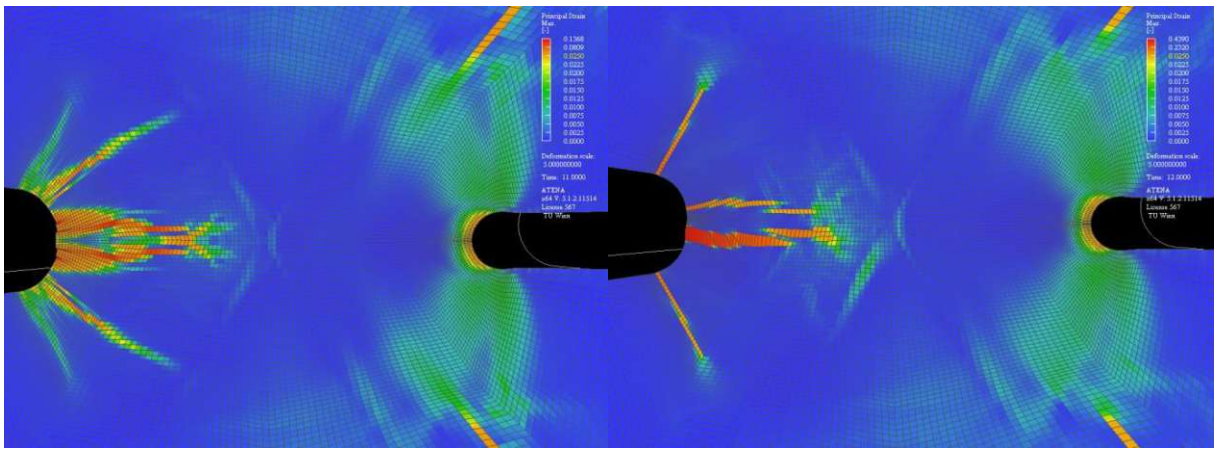

Fig. 11.95: ϵ_1 first principal strain for FC_R=0 (left) and FC_R=1 (right)

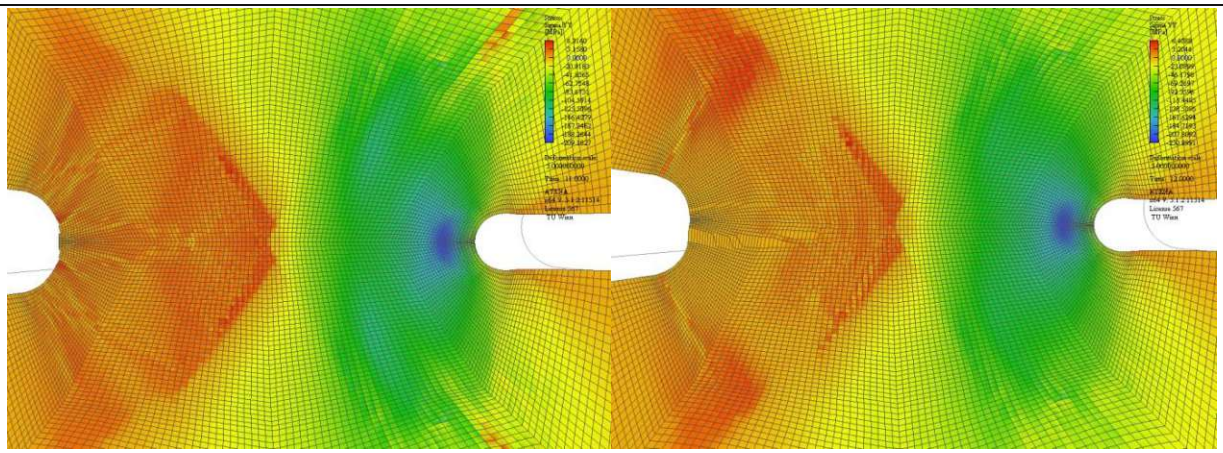

Fig. 11.96: σ_{LL} stresses in Load-Direction for FCR=0 (left) and FCR=1 (right)

11.3.15 AGG

The Aggregate-size has a negligible influence, because in Atena has only an influence on the shear-strength.

$$\sigma_{ij} \leq \frac{0.18 \cdot \sqrt{MPa} \cdot \sqrt{f'_c}}{0.31 + \frac{24 \cdot w}{a_g + 16mm}} \tag{5}$$

— ATENA Theory [Červenka, 2014] equation 2.48 referring on the *"Modified Compression Field Theory of VECHIO and COLLINS (1986)"*[Červenka, 2014]

The influence is in a magnitude of about 1‰ of the peak-load, strange is that they are ordered except Agg=10^{99} is not in order, it might be cause of numerical problems, so for comparing principal strains and principals stresses the results of 10^{99} are not taken into account. The difference in the plot of principal strains and in the principal stresses are almost impossible to determine.

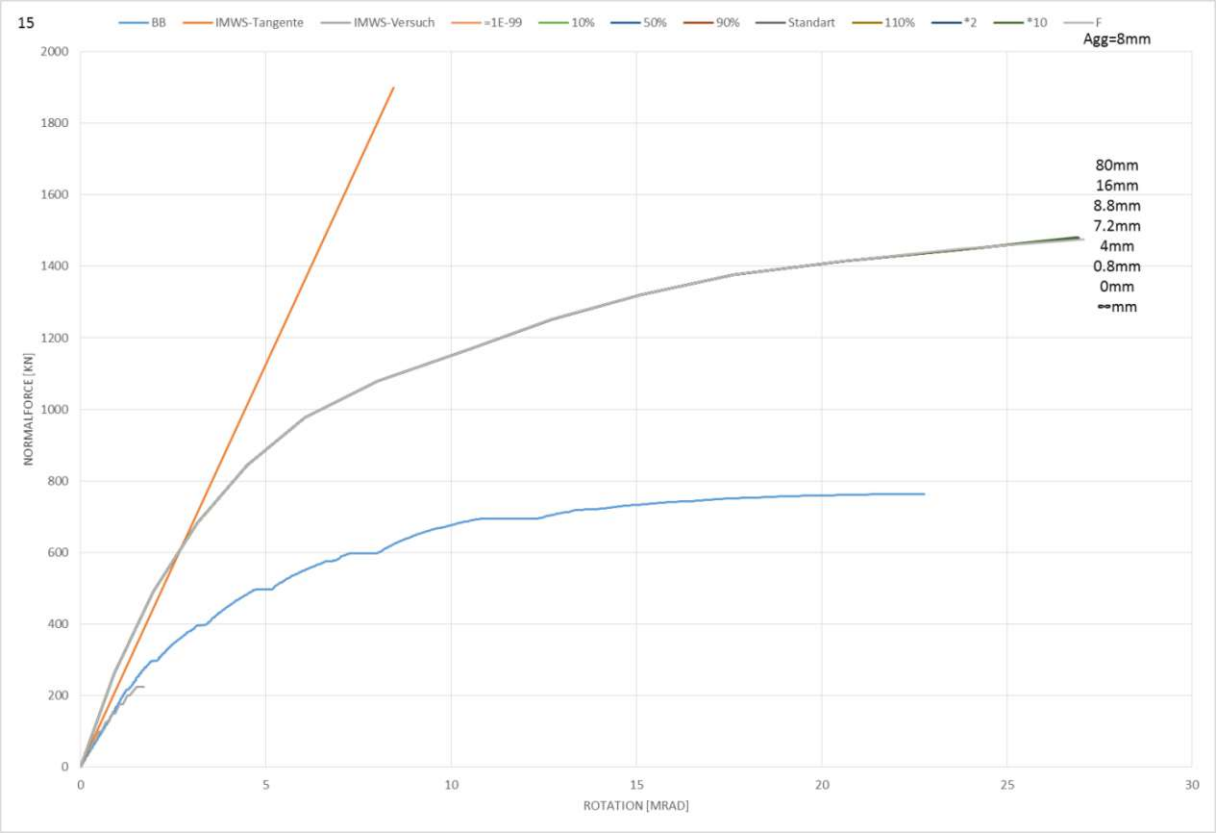

Fig. 11.97: Effect of the different Aggregate Size in the Rotation-Load-Curve.

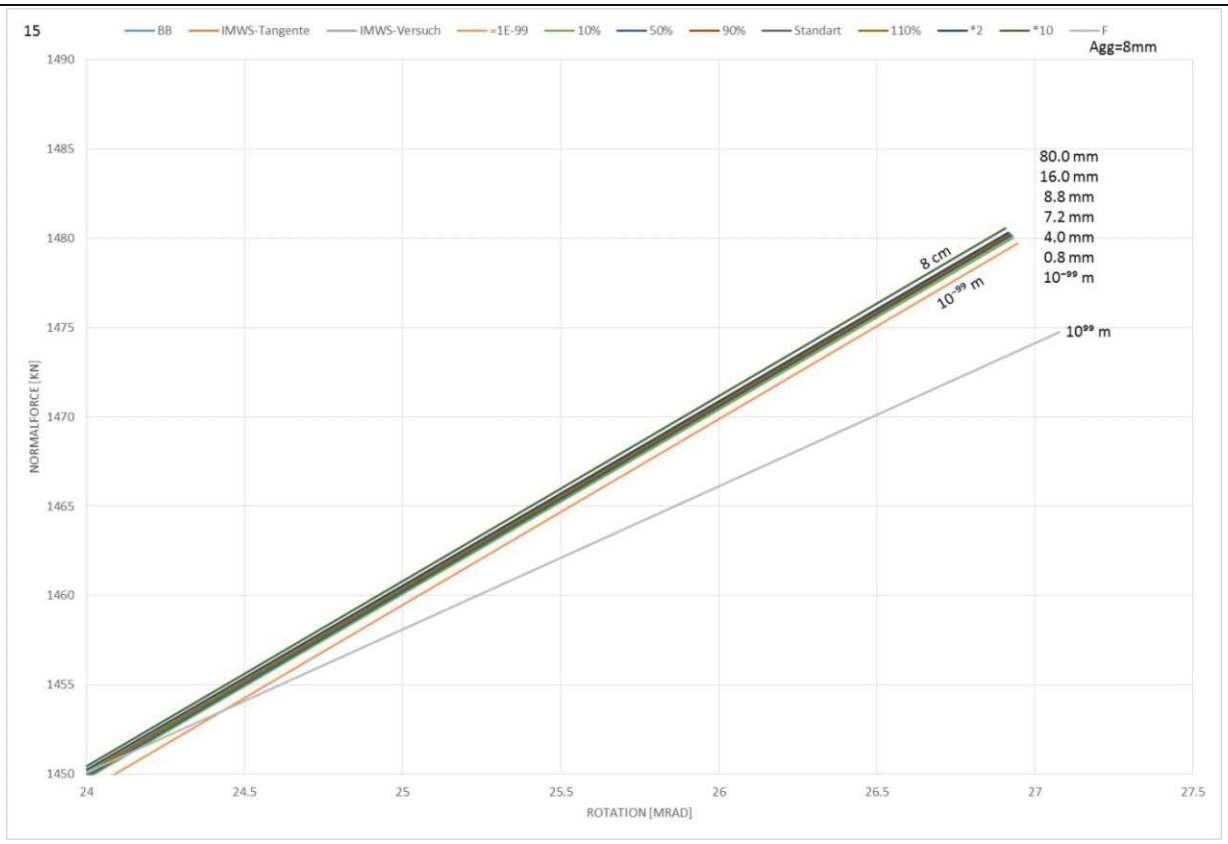

Fig. 11.98: Detail of the different Aggregate Size in the Rotation-Load-Curve.

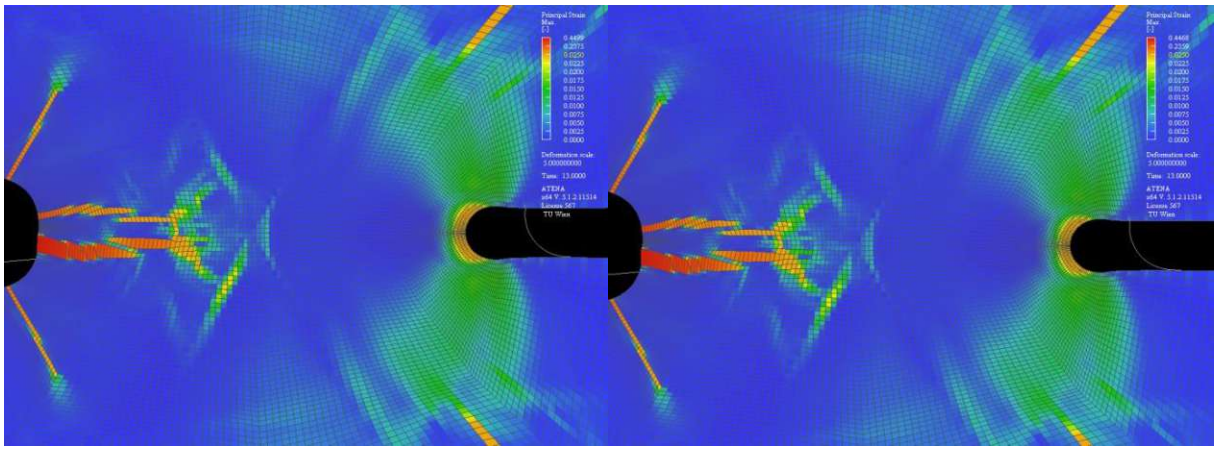

Fig. 11.99: ϵ_I first principal strain for AGG=0 (left) and AGG=80mm (right)

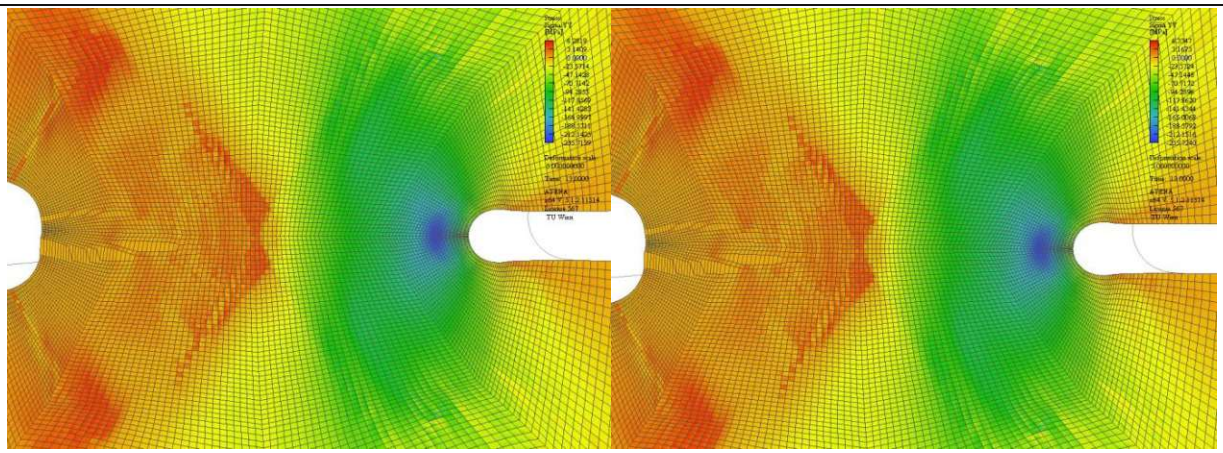

Fig. 11.100: σ_{LL} stresses in Load-Direction for AGG=0 (left) and AGG=80mm (right)

11.4 Boundary Conditions

The impression due to the loading plate on the steel-plate was mostly in the middle of the hinge, at the front and at the back it was not loaded at all, and it was even possible to look through the loading plate and the hinge-steel-plate. There were two main reasons for it, firstly on the top and on the bottom the steel-plate was curved, maybe because of the heat-Eigen-strains from welding the steel-bars onto the steel-plate and maybe some shrinkage effects at the surface, and secondly especially at high loads the loading-plate might not be stiff enough and due to big shear-forces[38] and due to bending the ends of the loading plate take off. In the experiments it was able to look through between the loading plate and the hinge, also at load of 200kN.
To see the effect of this loading, FE-Simulations with a line-displacement over 25% and 50% of the thickness (symmetrically in the middle) were tested, with an Excentricity of 24mm.

11.4.1 Load over 0% of the thickness (Point-load)

To see the influence very well the load was also applied on only one mesh-point in the middle (see **Fig. 11.101**). In the picture of the stress-distribution in load-direction (see **Fig. 11.102a**) it is shown that in the middle of the thickness there are only compressive stresses and at the front-surface that the tension-stresses are almost over the whole thickness, and on the tension-side are the stresses already reducing due to fracturing-cracks. The tension stresses are shown in **Fig. 11.102b**, it is very interesting that the highest stresses (red) are in hinge middle very close to the neutral line, but not at the free surface, but at the front and back-surface that the high tensile-stresses do not occur that much and mostly in the middle. The compressive stresses (**Fig. 11.102c**) are also very interesting, that the area of high compressive stresses (green and blue) are local on the compressive side, but in thickness-direction very constant, also the neutral line is partly close (front-surface) and partly not even in the neck (middle).

[38] A FE-Model including the loading plates show that shear-deformations seems to be dominant.

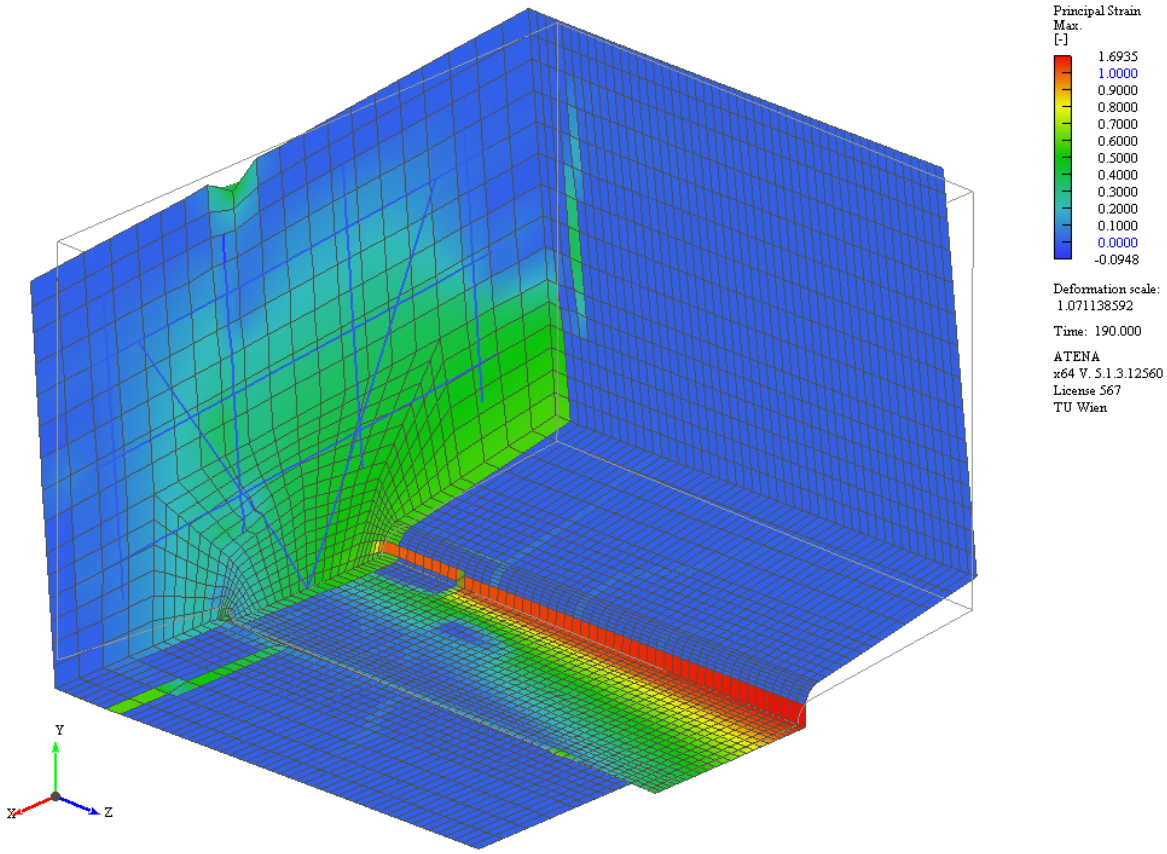

Fig. 11.101: Deformations and Principal Strains of Pointload

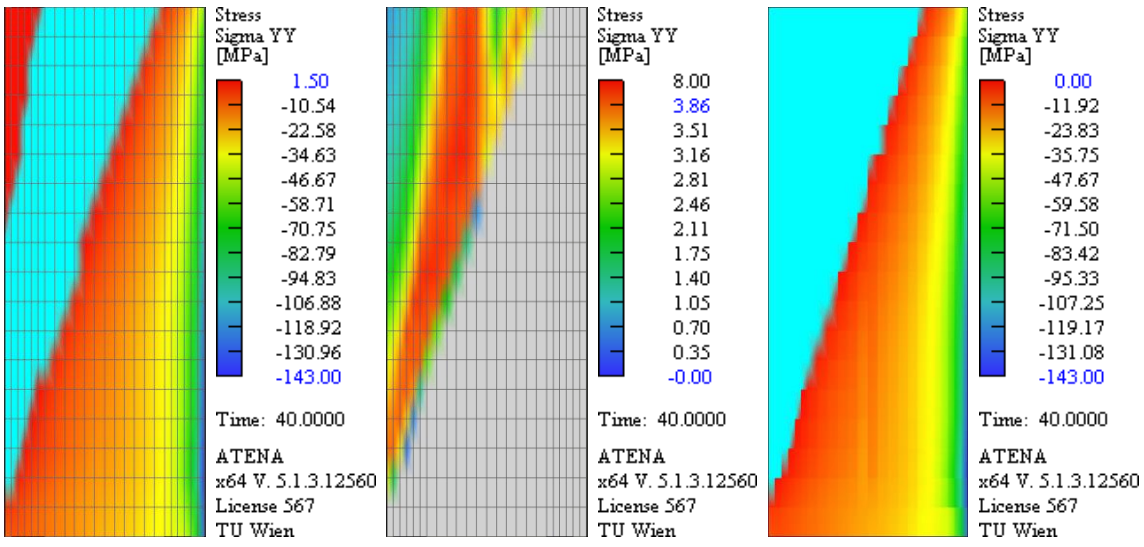

Fig. 11.102: σ_{LL} for a Pointload

11.4.2 Load over 25% of the thickness

In **Fig. 11.103** you can see the maximal principal strains of the quarter-model. At the free surface and over mostly of the thickness a crack in the hinge-neck is the most relevant crack, but in the Middle (3.1cm in this quarter-model so 6.2cm in the full model) the relevant crack is in the 3-Element-Row (≈ 4mm from the hinge-neck) (see **Fig. 11.104**).

In **Fig. 11.103** are some crack-surfaces orthogonal to the thickness-direction (see also **Fig. 11.106** and **Fig. 11.107**). Some of them correlate with the rebar-planes.

In **Fig. 11.108** are the steel stresses, they are almost at the level of the mean-yield-stress (605MPa for BST550). One of the reinforcing bars already seems to buckle; next to this a horizontal rebar has almost reached the yield-tension-strength. Very interesting is that also the horizontal steels in the thickness-direction have high stresses at the symmetry-surface.

Fig. 11.105 shows the stresses in load-direction in the hinge-neck. Red and orange are tension-stresses, yellow are zero-stresses, green, cyan and blue are compressive stresses. So in this Graph you can see the "neutral line" (the line of zero "normal-stresses"), which is between the green and the orange surface. In the orange surface some green spots accrue, which shows that due tension-cracks stress-jumps accrue, and due to extrapolation local compressive stresses accrue in the FE-Model. "On the first view" **Fig. 11.103** might look better than **Fig. 11.105** for an assumption of the crack-tip, but in **Fig. 11.104** you can see that the crack is in the middle is "higher" and so you cannot see the deep of crack-tip, so **Fig. 11.105** gives better responses. In **Fig. 11.11** you can see in more detail how the "neutral-line" corresponds with the stress-distribution in the case of plane strain.

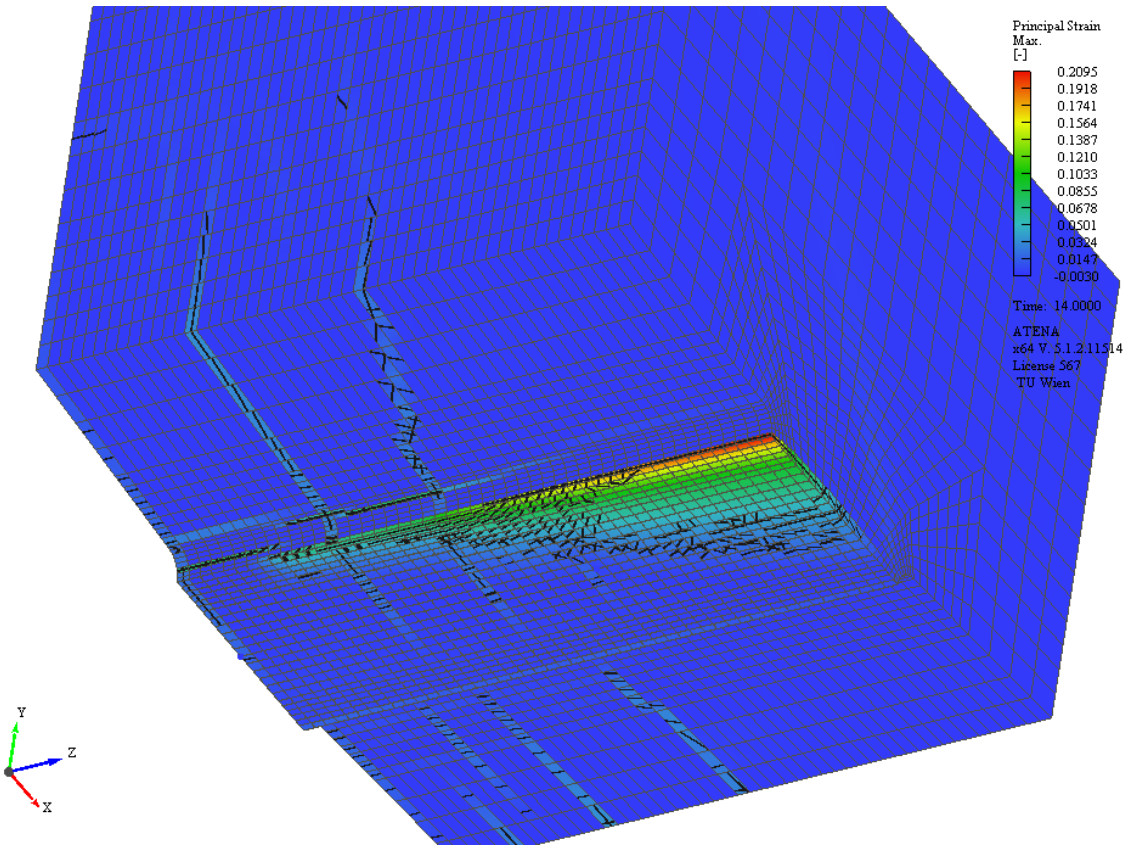

Fig. 11.103: max principal strain, view from the Tension-side, below, front

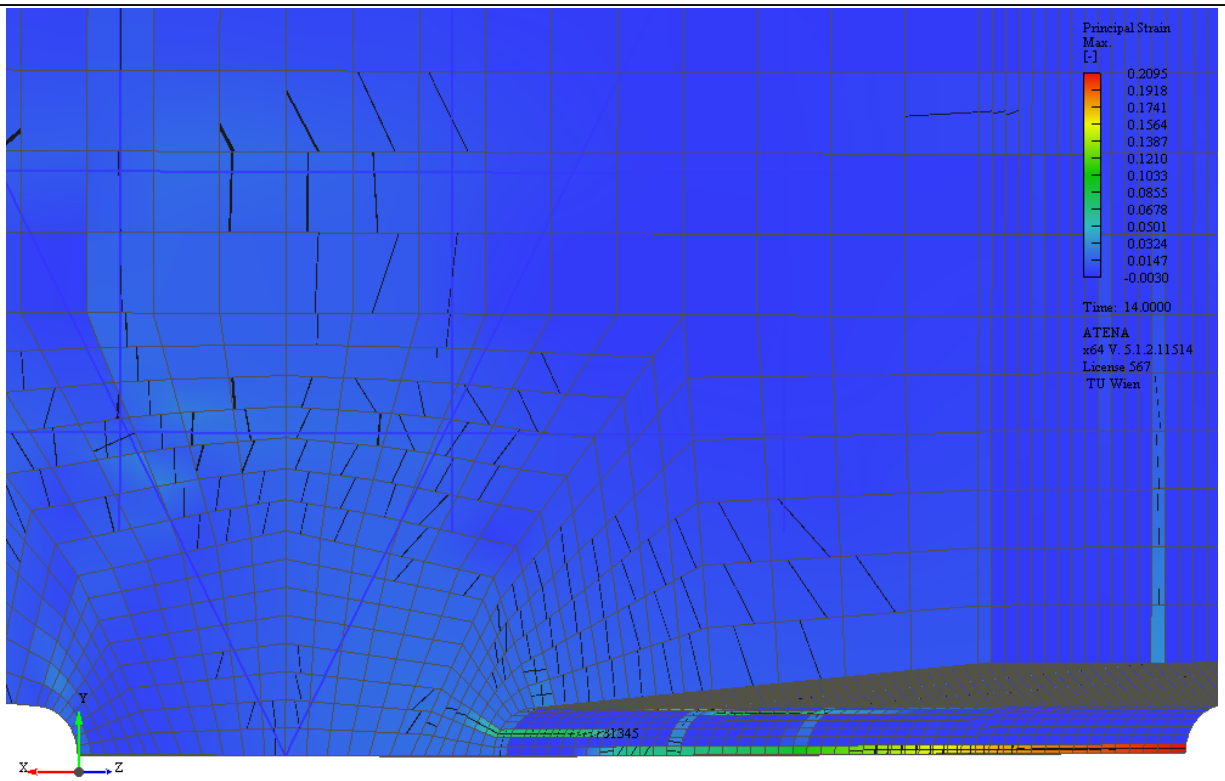

Fig. 11.104: max principal strain, view from the Tension-side, middle

The neutral line in **Fig. 11.105** moves from +24 mm (from the centerline to the direction of the compressive side) at the free surface to -15mm in the symmetry-plane, so the crack-length changes quite much compared to the neck-with of 75mm, so approximately the half of the neck-with.

The loading over a shorter length leads to crack patterns, which are parallel to the front/back-surface (see **Fig. 11.105**, **Fig. 11.106** and **Fig. 11.107**), also the steel-stresses are almost in the middle at the yield-stress of ±605MPa[39] and seems to buckle, but to the front/back-surface of hinge the steel-stresses are quite low (see **Fig. 11.108**).

[39] Mean-value for Rebar with a characteristic-yield-stress of 550 MPa (B550A)

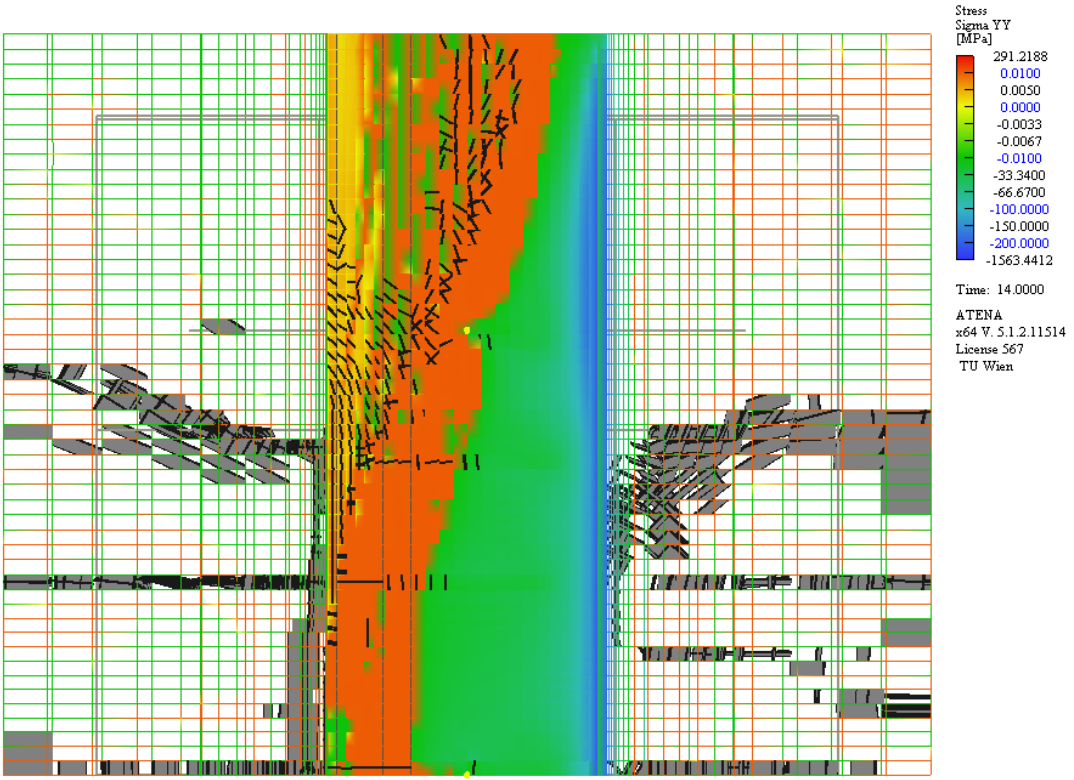

Fig. 11.105: σ_{LL} at the hinge-neck (look from below)

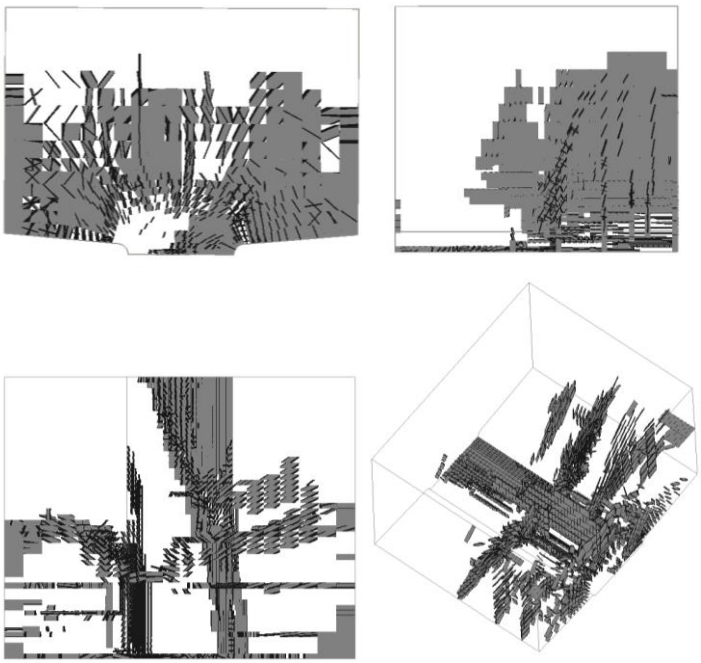

Fig. 11.106: Cracks bigger than 0.03mm

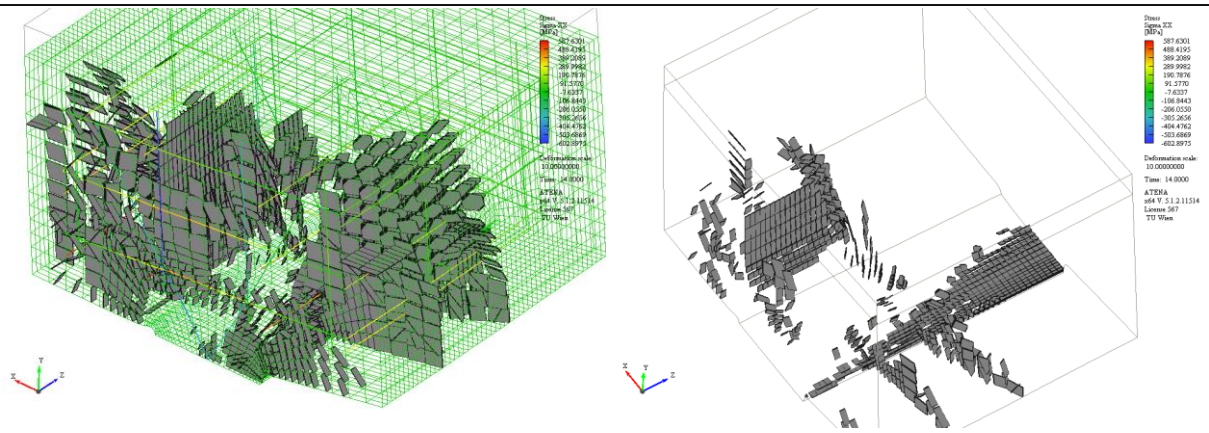

Fig. 11.107: tension splitting Cracks (left:≥0.03mm; right ≥0.1mm)

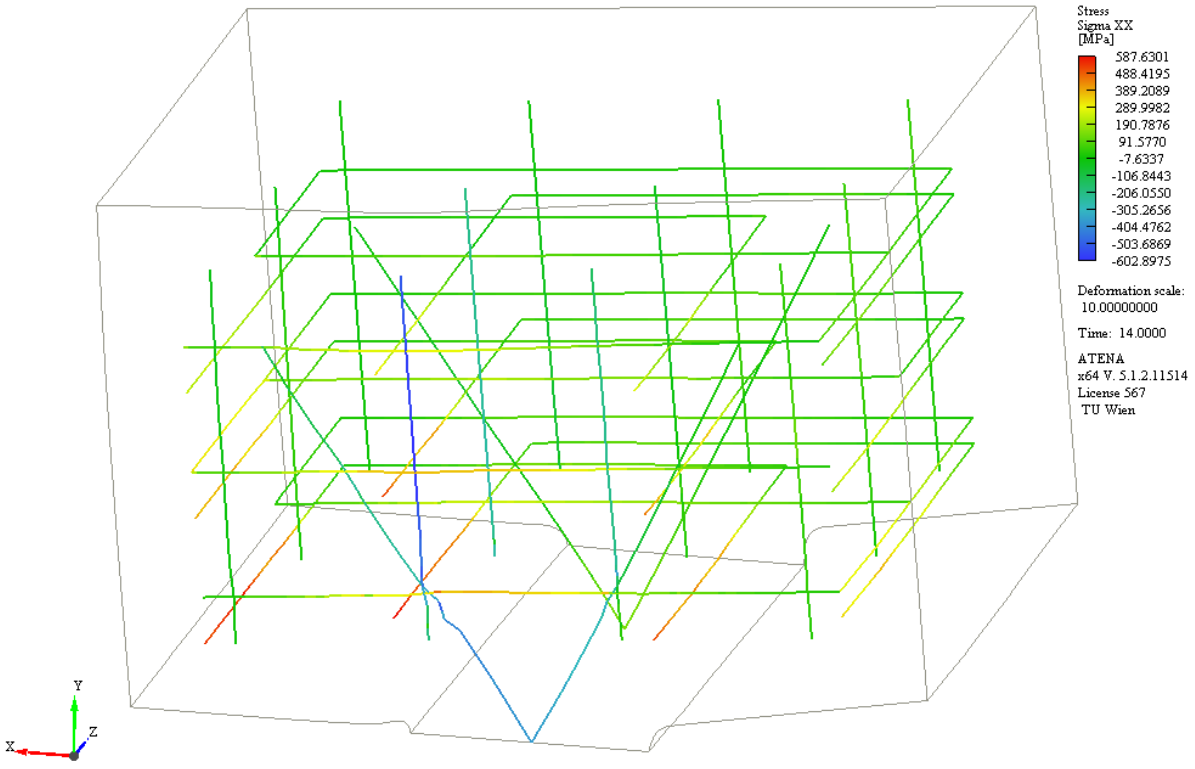

Fig. 11.108: Steel-stresses

11.4.3 Displacement-Load over 50% of the thickness

50% of the length might be more realistic then the previous one.

In **Fig. 11.109** it shows the stresses in load-direction in the "hinge-neck". The neutral line moves from +15mm (from the middle to the direction of the compressive part) at the free surface to --4mm in the middle, so here the neutral line is almost parallel to the hinge.

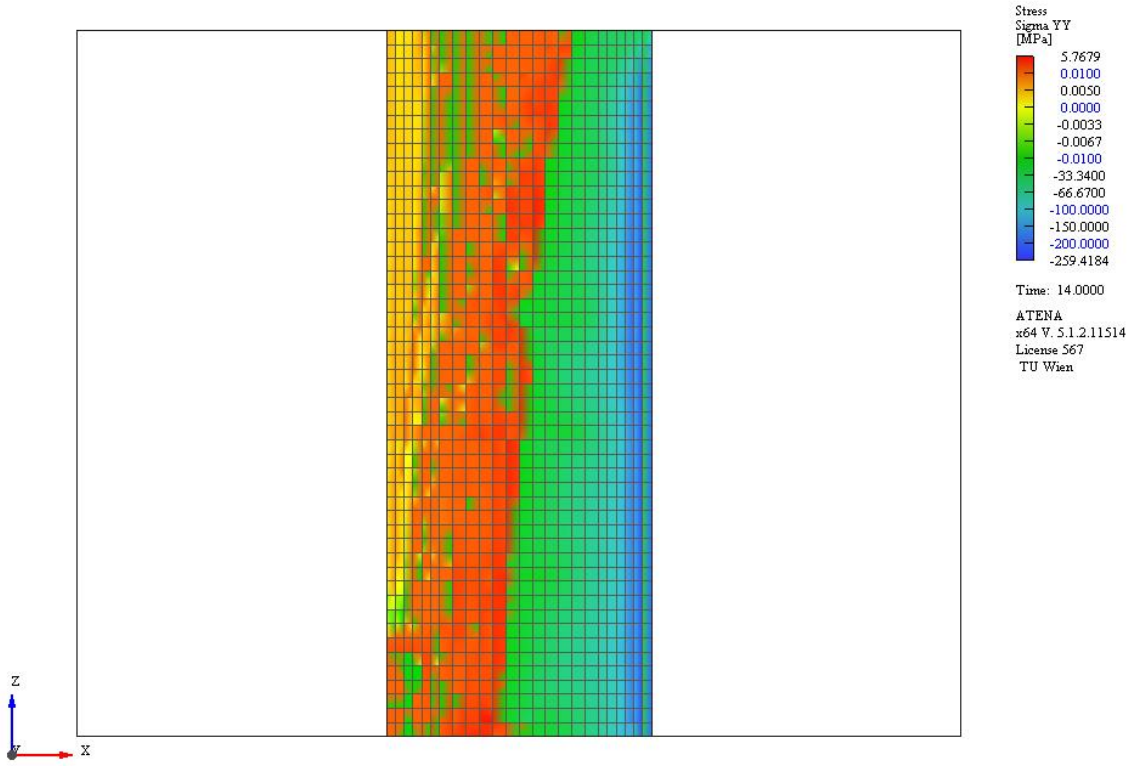

Fig. 11.109: σ_{LL} at the hinge-neck (look from below)

11.4.4 Loadingplate

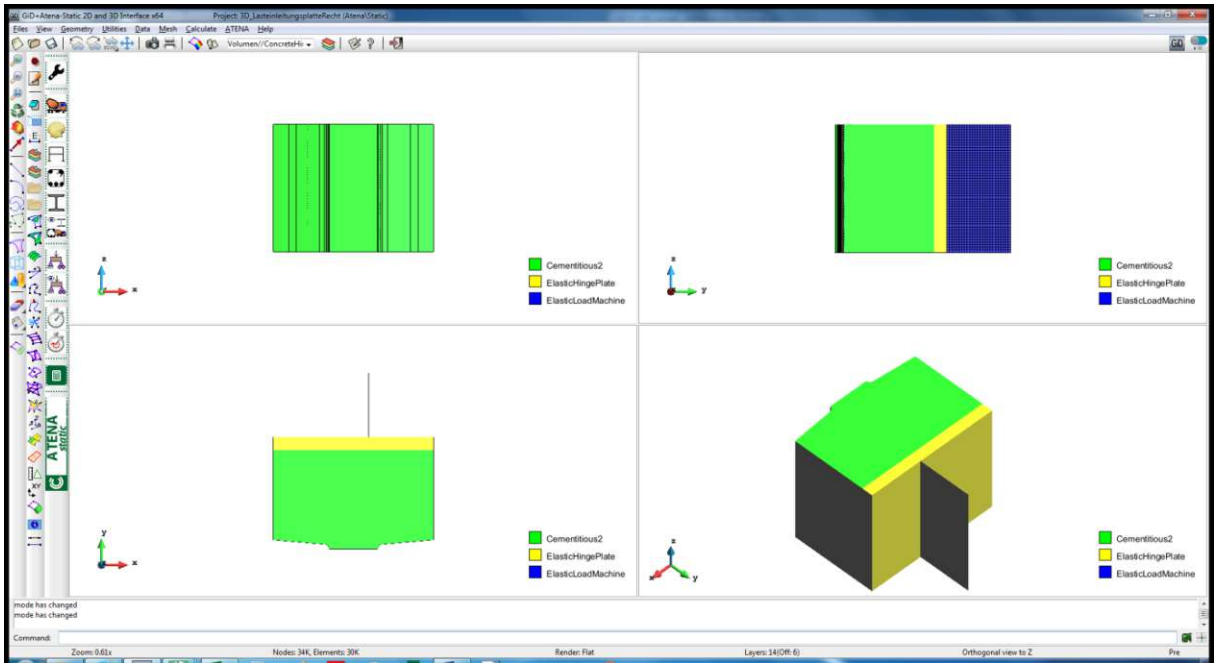

Fig. 11.110: GiD Graphical Tangible User Interface

Some FE-models where done with including the loading plate[40], which is loaded in the middle, but these models show that the stiffness does not change that much but the peak-load is reducing (see **Fig. 11.113**). Also a curved loading plate was tested, but in the peak-load did not change much and even increased slightly, so they were not added into this report. Loading-plates over a part of the length were also tested, but they had the same problem as the displacement-controlled model, which have big peak-stresses at the loading-length-end, and had more numerical problems, so they are also not added to the report.

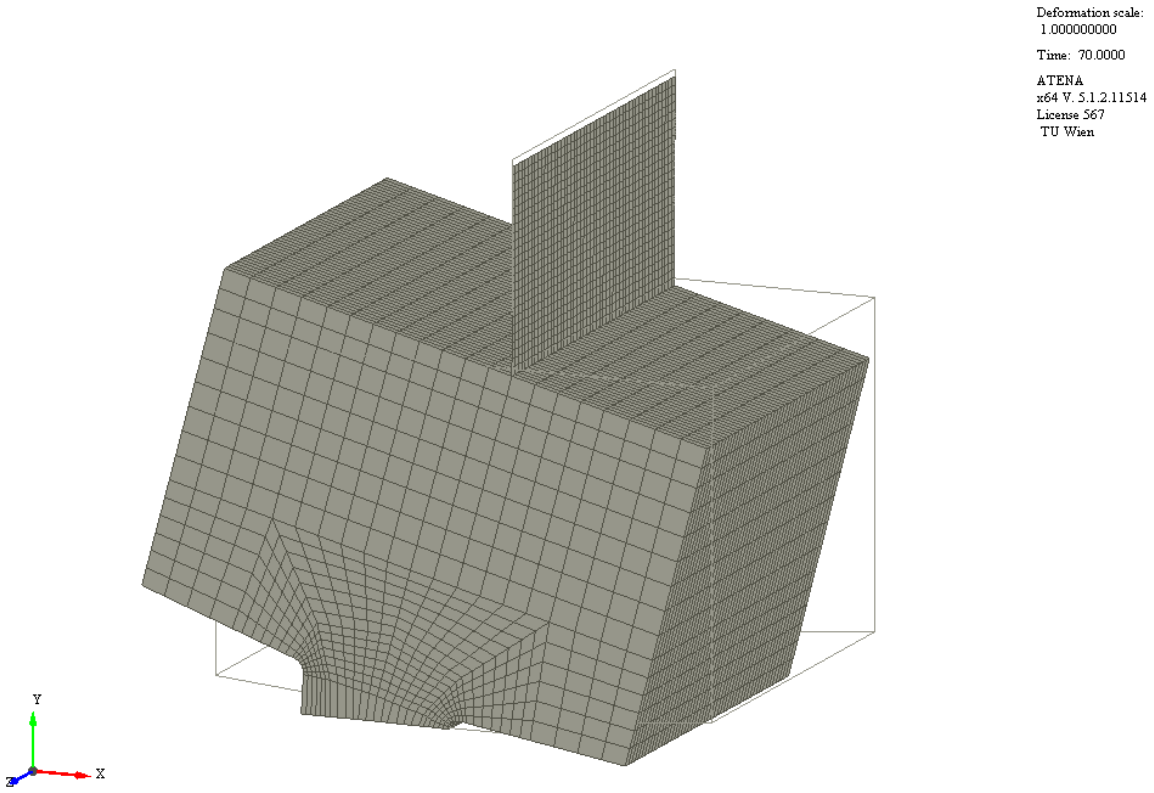

Fig. 11.111: Deformation of concrete-hinge in the post-peak

11.4.5 Comparison

The peak load of the model loaded over the 25% of the length is reducing to 55% of the original FE-Model, as you can see in the Load-Displacement-curve (**Fig. 11.112**), so this parameter is very sensitive for calculating the peak-load.

[40] in a 3D-model using both symmetry-conditions, which means that the loading plates are assumed on both sides, which might not be realistic

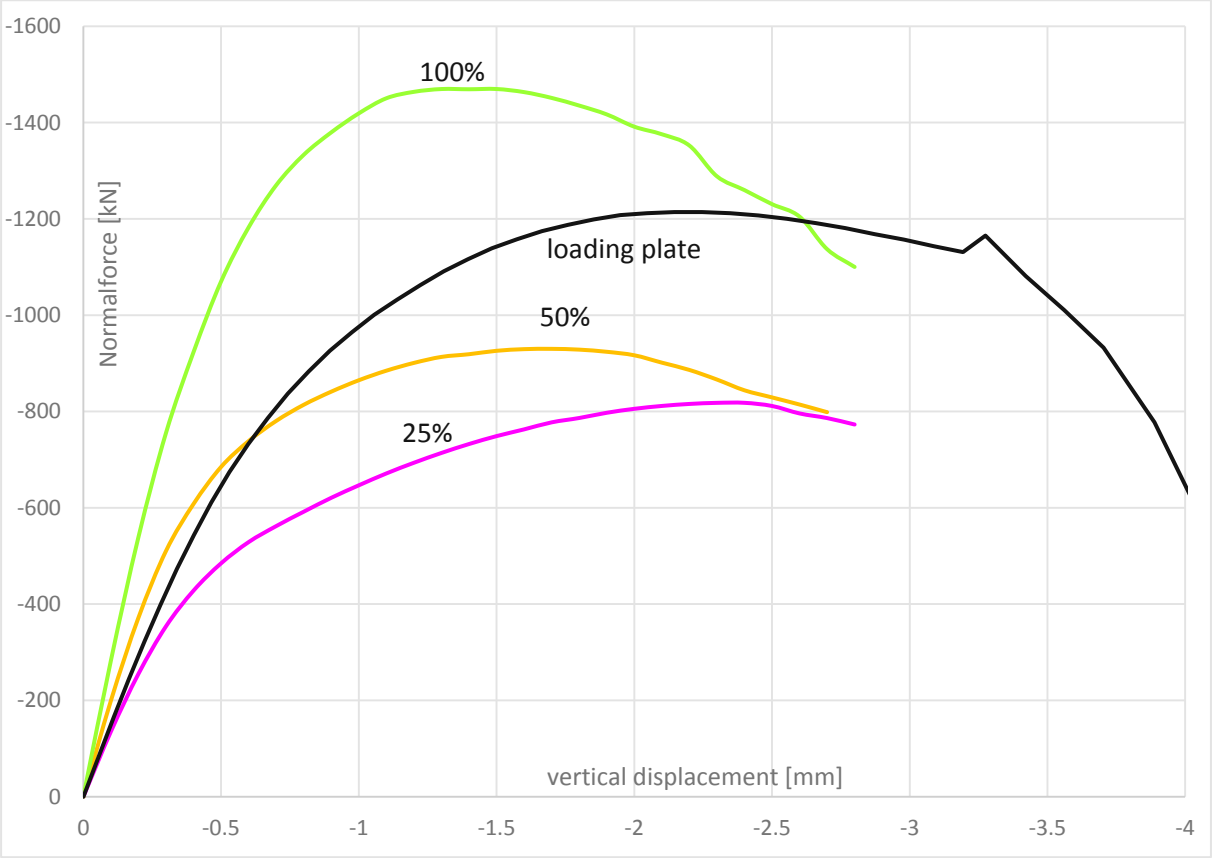

Fig. 11.112: Load-Displacement-curve of different loading-length

The "Normal force"-Rotation-Curve of the finite-Element-Models are compared with the experiments. In the first Diagram (**Fig. 11.114**) you can see that the stiffness of "full length", "50% length" and even "25% length" are quite the same, but the experiments are less stiff. The 1h-creep-plateaus are smaller than the differences, so it might be unlikely that the changes are due to creep in the first few seconds. Reducing to a point load really decreases the rotation-stiffness much more than the experiments, but this might not be meaningful any more. In the second Diagram (see **Fig. 11.113**) you see different peak-behaviors. The reason, why all FE-Models have two lines, is that the rotation is measured at the front-surface and in the middle. Those models, which are loaded mostly in the middle, the Rotation in the middle is a little bit bigger than at the front.

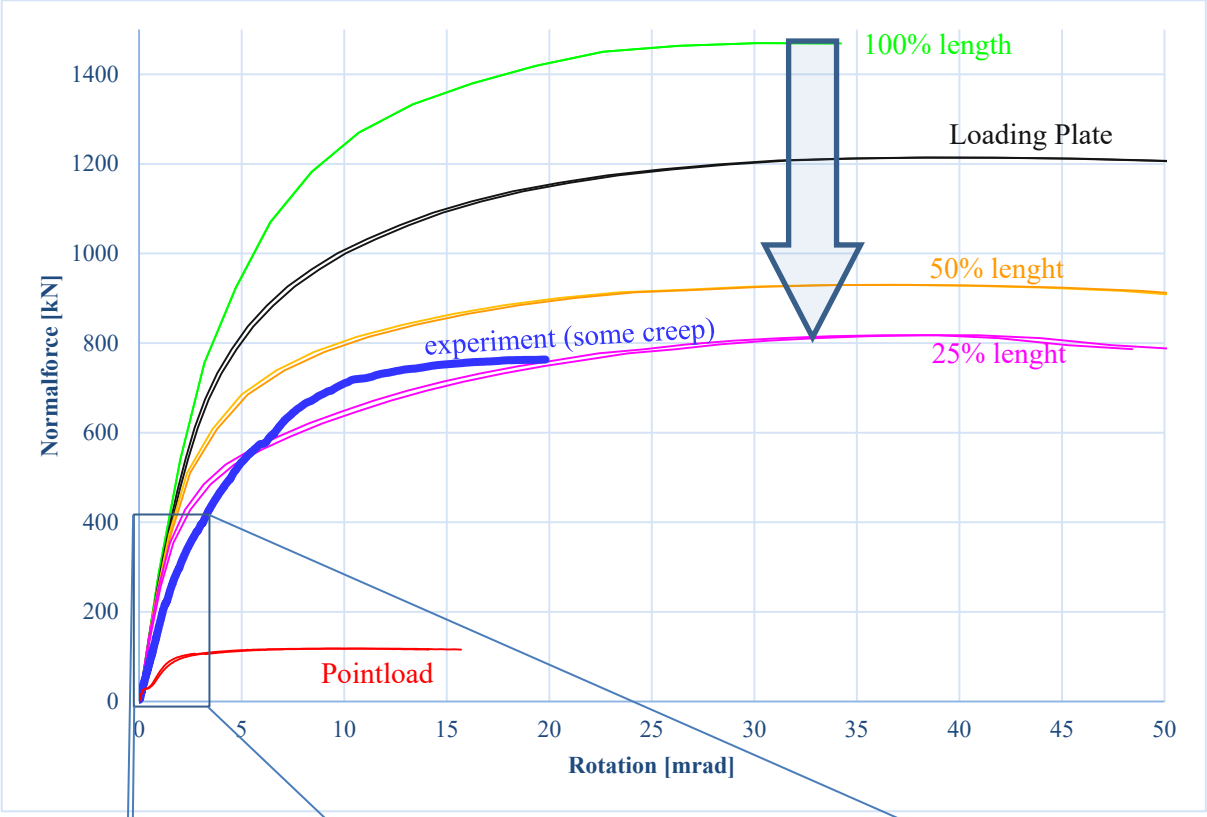

Fig. 11.113: Rotation of different load-length (peak-behaviour)

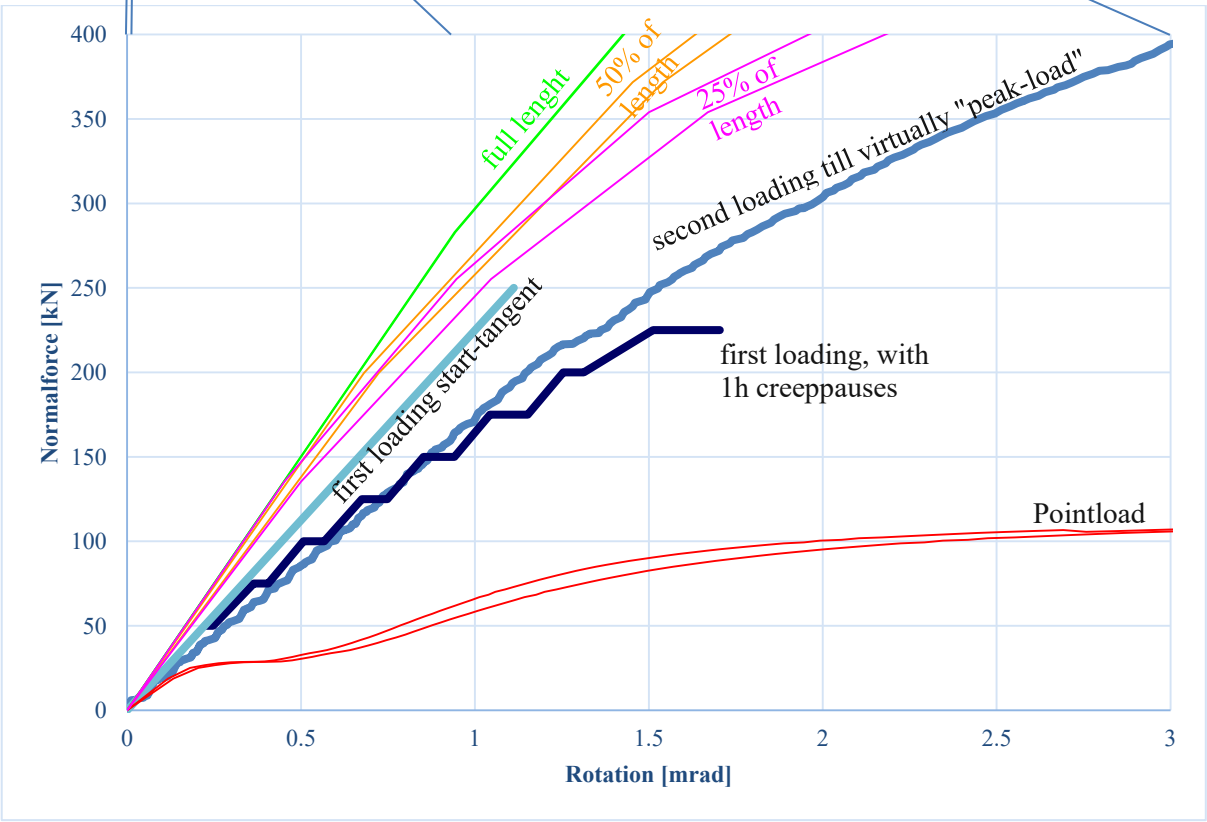

Fig. 11.114: Rotation of different load-length (low-load-level)

The following picture show for different length of loading how the neutral line differs. For experiments it is important to have an applied load over the whole length, that the crack-tip and strains at the front surface is representative of the crack-tip and strains of the hinge.

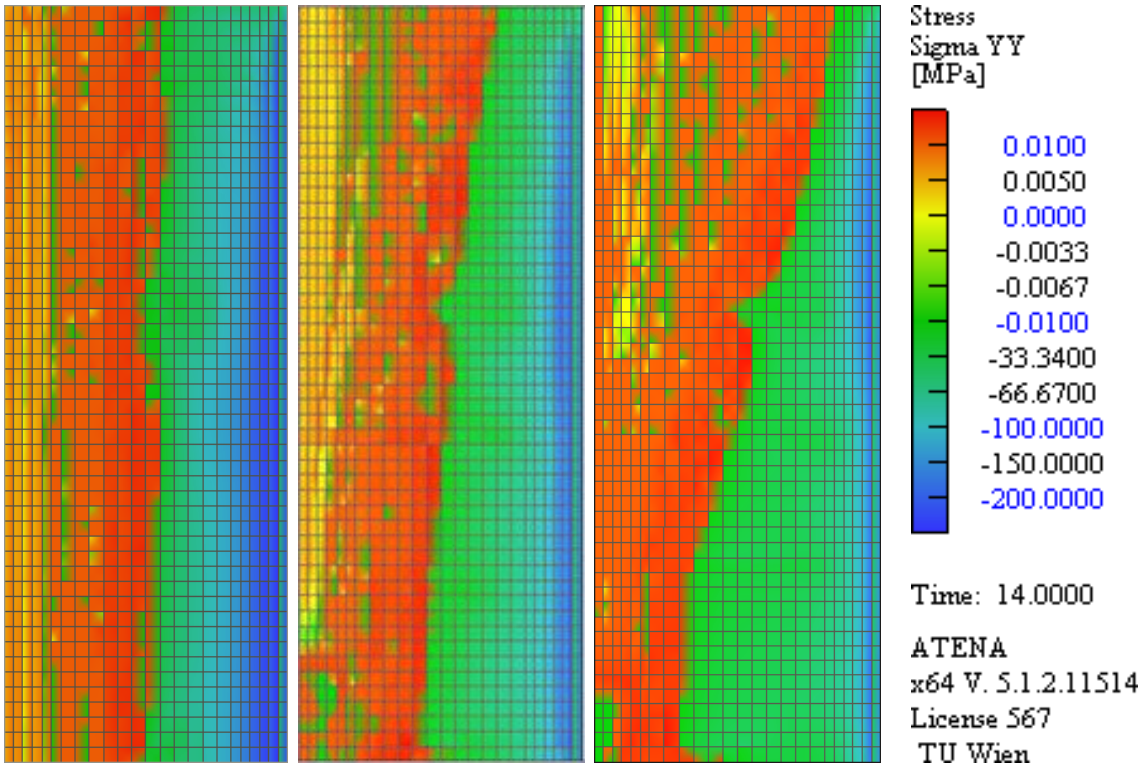

Fig. 11.115: σ_{LL} at the hinge-neck; left 100%, middle: 50%, right 25%

12 Stochastic Sensitivity Analyses carried out with SARA, involving ATENA Eng. and FREET

In this chapter SARA Studio [SARA, 2002] involving ATENA Engineering[41] and FREET[42] are used.

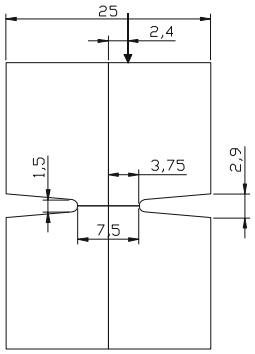

Fig. 12.1: The Geometry of the Concrete Hinge VV3

[41] www.cervenka.cz/products/atena/
[42] www.freet.cz

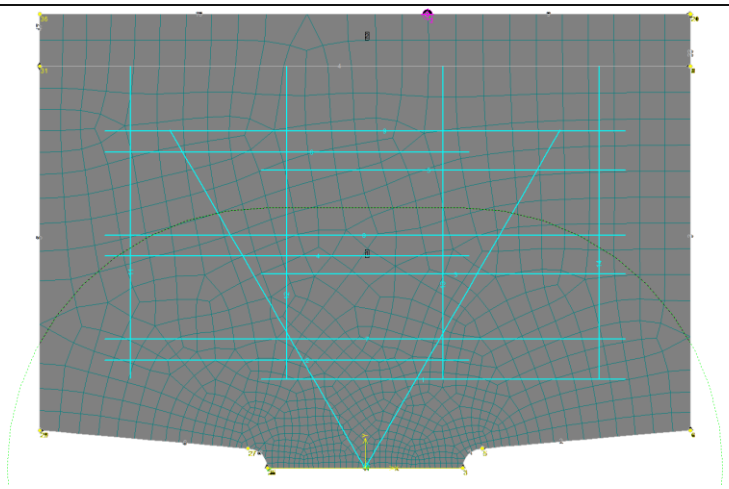

Fig. 12.2: Model with Reinforcement Bars – 2D

The deterministic peak-value in this model of the load is 1711kN, which is the similar to the mean value of the results of the stochastic calculations with correlated values (see 12.1.1: 1710,5 kN and 12.1.2: 1711,9 kN).

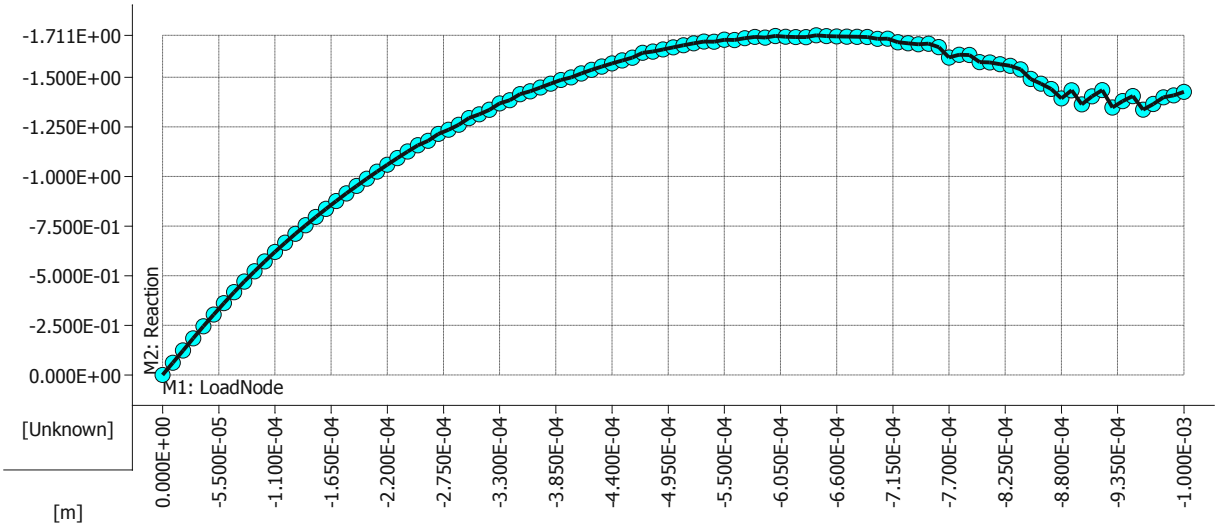

Fig. 12.3: Load-Dispacement-Curve with a peak-value of 1711kN

12.1 Correlated sensitivity analyses using spatially uniform properties

12.1.1 Simulation1 of two identical correlated Random Values simulations

#	Name	Distribution	Descriptors	Mean	Std
1	E	Normal	Moments	35000	700
2	Ft	Lognormal (2 par)	Moments & params	3.533	1.09
3	Fc	Lognormal (2 par)	Moments & params	-48	4.8
4	Gf	Lognormal (2 par)	Moments & params	8.831e-005	2.7245e-005

Fig. 12.4: Mean Value and Standart deviation of Input-Random-Values

	E	Ft	Fc	Gf
E	1	0.5	-0.6	0.4
Ft	0.5	1	-0.8	0.9
Fc	-0.6	-0.8	1	-0.7
Gf	0.4	0.9	-0.7	1

Fig. 12.5: Correlation Matrix[43]

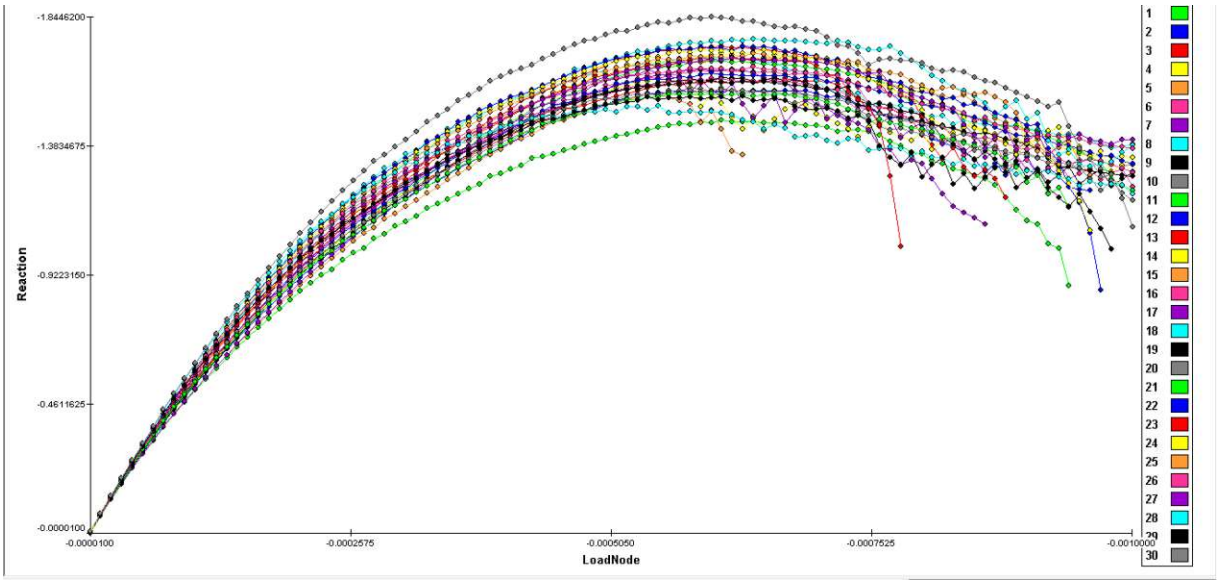

Fig. 12.6: Load-Dispacement-Curve of Correlated sensitivity analyses using spatially uniform properties

[43] This correlation Matrix provide a quite strong correlation. The numbers might be an unrealistic guess of the author, but it might be better than no correlation. The correlation matrix is "positive definite", which is necessary to be logical consistence.

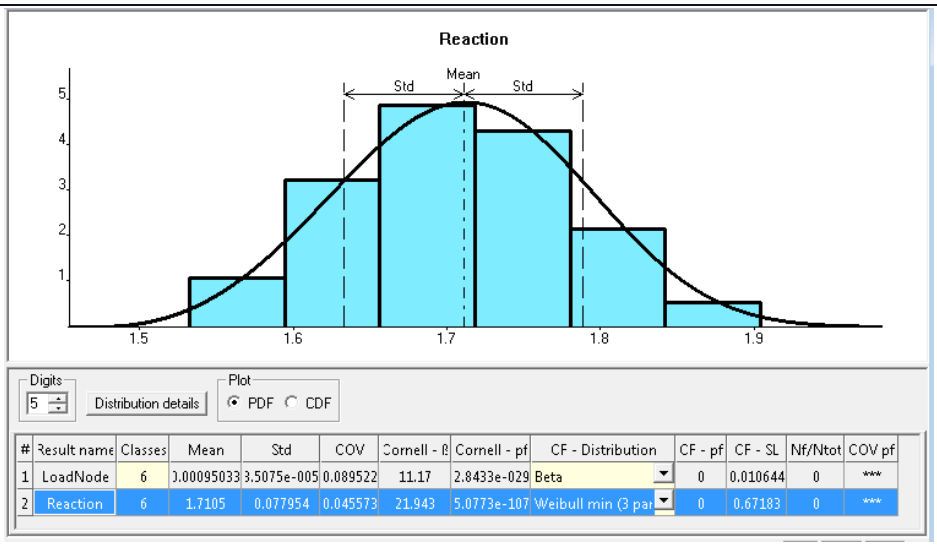

#	Result name	Classes	Mean	Std	COV	Cornell - β	Cornell - pf	CF - Distribution	CF - pf	CF - SL	Nf/Ntot	COV pf
1	LoadNode	6	0.00095033	3.5075e-005	0.089522	11.17	2.8433e-029	Beta	0	0.010644	0	***
2	Reaction	6	1.7105	0.077954	0.045573	21.943	5.0773e-107	Weibull min (3 par	0	0.67183	0	***

Fig. 12.7: Relibility and variance in Freet

#	Name	+ sensi	— sensi	x -1
3	ConcHinge_Cem2_Materialwerte.Fc		-0.68409	
4	ConcHinge_Cem2_Materialwerte.Gf	0.3584		
1	ConcHinge_Cem2_Materialwerte.E	0.31346		
2	ConcHinge_Cem2_Materialwerte.Ft	0.31301		

Fig. 12.8: Influence of Input Values on Peak-Reaction-Load

12.1.2 Simulation2 of two identical correlated Random Values simulations

#	Name	Distribution	Descriptors	Mean	Std
1	E	Normal	Moments	35000	700
2	Ft	Lognormal (2 p	Moments & para	3.533	1.09
3	Fc	Lognormal (2 p	Moments & para	-48	4.8
4	Gf	Lognormal (2 p	Moments & para	3.831e-005	1.7245e-005

Fig. 12.9: Mean Value and Standart deviation of Input-Random-Values

	E	Ft	Fc	Gf
E	1	0.5	-0.6	0.4
Ft	0.5	1	-0.8	0.9
Fc	-0.6	-0.8	1	-0.7
Gf	0.4	0.9	-0.7	1

Fig. 12.10: Correlation Matrix

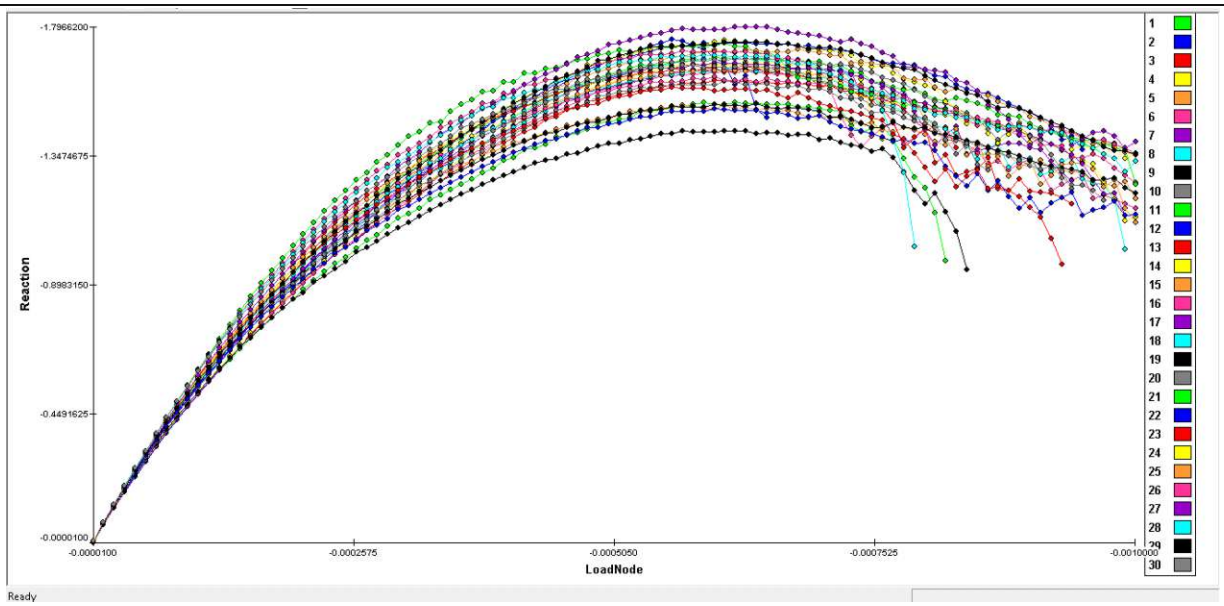

Fig. 12.11: Load-Dispacement-Curve of Correlated sensitivity analyses using spatially uniform properties

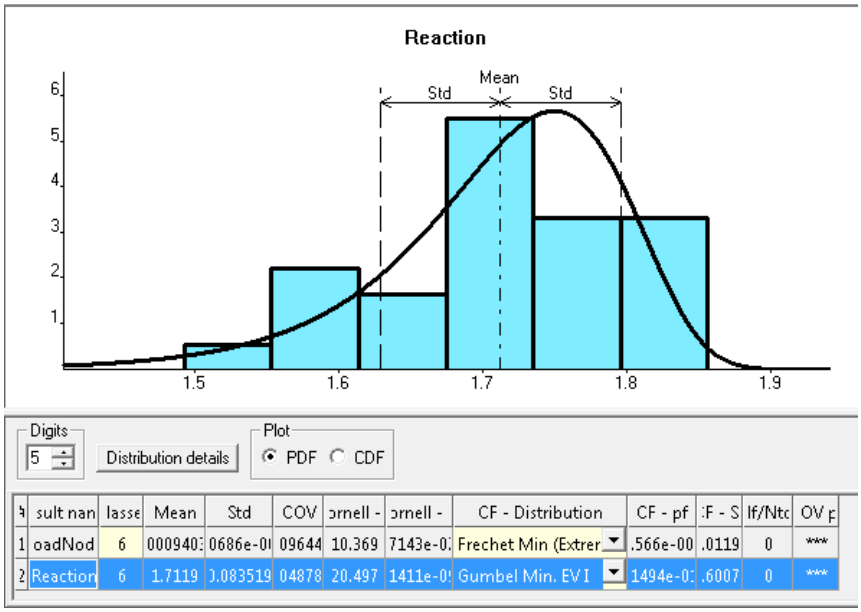

Fig. 12.12 Relibility and variance in Freet

#	Name	+ sensi	— sensi	x -1
3	ConcHinge_Cem2_Materialwerte.Fc		-0.64761	☐
1	ConcHinge_Cem2_Materialwerte.E	0.402		☐
4	ConcHinge_Cem2_Materialwerte.Gf	0.081201		☐
2	ConcHinge_Cem2_Materialwerte.Ft	0.05406		☐

Fig. 12.13: Influence of Input Values on Peak-Reaction-Load

12.2 Uncorrelated sensitivity analyses using spatially uniform properties

12.2.1 simulation of all variables

#	Name	Distribution	Descriptor	Mean	Std	COV
1	E	Normal	Mome	35000	700	0.02
2	Mu	Normal	Mome	0.2	0.02	0.1
3	Ft	Normal	Mome	3.533	1.09	1.3085
4	Fc	Normal	Mome	-48	4.8	0.1
5	Gf	Normal	Mome	.831e-00	.7245e-00	1.3085
6	Wd	Normal	Mome	-0.0005	5e-005	0.1
7	Exc	Normal	Mome	0.52	0.052	0.1
8	Beta	Rectangu	Mome	0	0.1	***
9	Rho	Normal	Mome	0.023	0.0023	0.1
10	Alpha	Normal	Mome	1.2e-005	1.2e-006	0.1
11	Fixed	Rectangu	Mome	0.5	0.25	0.5
12	EPS_CP	Normal	Mome	0.001246	0.0001246	0.1
13	C_REDUCTIO	Normal	Mome	0.8	0.08	0.1
14	HEAR_FACTC	Normal	Mome	20	2	0.1
15	AGG_SIZE	Normal	Mome	0.008	0.0008	0.1

Fig. 12.14: Mean Value and Standart deviation of Input-Random-Values

	E	Mu	Ft	Fc	Gf	Wd	Exc	Beta	Rho	Alpha	Fixed	EPS_CP	FC_REDUCTION	SHEAR_FACTOR	AGG_SIZE
E	1	0	0	0	0	0	0	0	0	0	0	0	0	0	0
Mu	-0.00012708	1	0	0	0	0	0	0	0	0	0	0	0	0	0
Ft	-8.2707e-005	-0.00030889	1	0	0	0	0	0	0	0	0	0	0	0	0
Fc	-0.00012097	-0.00034139	1.3494e-005	1	0	0	0	0	0	0	0	0	0	0	0
Gf	9.7337e-005	-3.7734e-005	-0.00045302	7.7784e-005	1	0	0	0	0	0	0	0	0	0	0
Wd	0.0010227	-0.00041736	-0.00024691	0.00107	0.00069063	1	0	0	0	0	0	0	0	0	0
Exc	-0.00019733	-0.00054058	0.00023062	0.00045641	-0.00065839	5.3726e-005	1	0	0	0	0	0	0	0	0
Beta	-0.00035208	-0.00026406	0.00023488	-0.00022089	-0.00011856	-0.00036292	-0.00070693	1	0	0	0	0	0	0	0
Rho	3.319e-005	-0.00031078	-0.00044675	-0.00075038	-0.00012941	0.00084938	-0.0010902	-0.00073751	1	0	0	0	0	0	0
Alpha	0.00031353	0.00086472	-0.0003199	-0.00011046	0.00030257	-0.00034541	0.00047048	0.00010596	-0.00019793	1	0	0	0	0	0
Fixed	-0.0002797	-0.00033253	0.00017814	0.00060418	-0.00013665	0.0001747	0.0010698	6.0006e-005	0.00045957	4.5952e-005	1	0	0	0	0
EPS_CP	0.00044385	0.00032946	0.0004704	0.00032538	0.00042738	-0.00010627	-0.00024208	0.00035062	0.00038769	-5.4132e-005	-5.1713e-005	1	0	0	0
FC_REDUCTION	0.00080599	-0.00070863	-0.0005203	0.00052855	-0.00026857	3.8353e-005	0.00029579	0.00036571	-0.00015159	0.00012083	0.00011624	-0.00093246	1	0	0
SHEAR_FACTOR	0.0007429	-0.0001324	-0.00073329	0.0001248	-1.1681e-005	0.00029127	0.0011201	0.00033125	0.00022626	-0.00031544	6.023e-005	-0.00056897	0.00054789	1	0
AGG_SIZE	-0.00041731	0.00020441	0.00032911	-0.00024333	-4.7935e-005	5.3361e-005	-0.00016047	-0.00030313	-0.00025546	0.00020668	-0.00012646	-0.0005692	0.00029091	0.0005513	1

Fig. 12.15: Uncorrelated values, the biggest correlation is smaler than 1.2‰

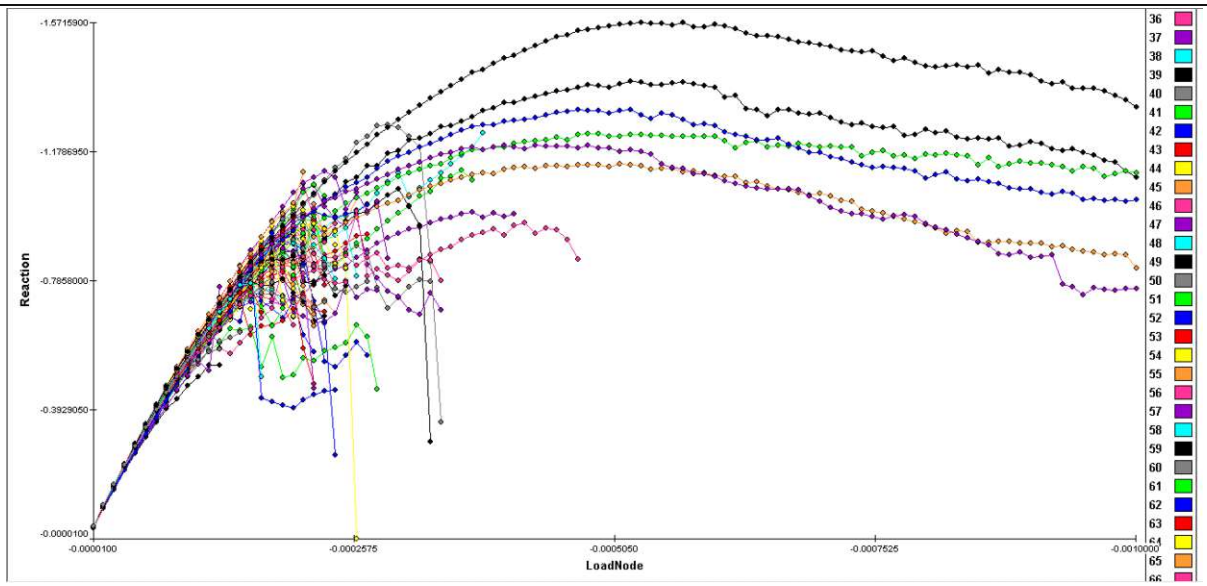

Fig. 12.16: Load-Dispacement-Curve of Uncorrelated sensitivity analyses using spatially uniform properties[44]

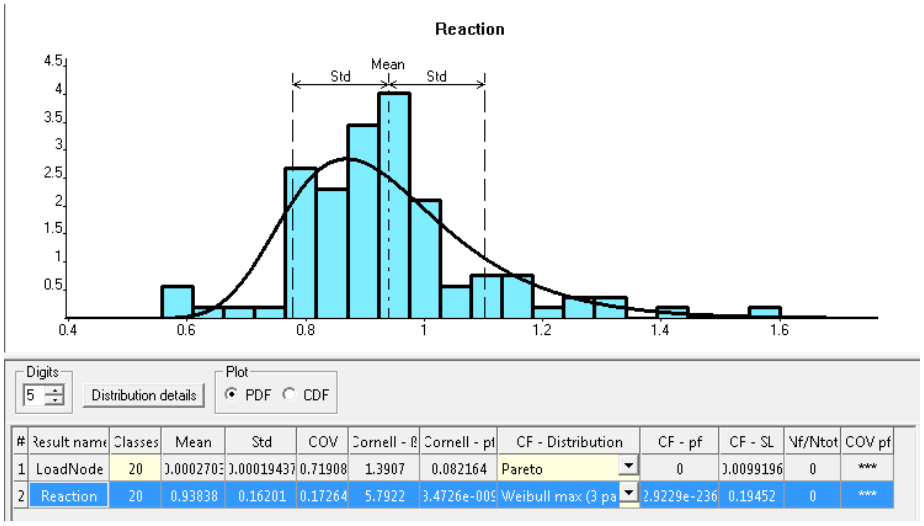

Fig. 12.17: Relibility and variance in Freet[45]

[44] 6% of the models finished, but some did not even reach the peak-load, they might should be deleted, because they falsify the mean-value of the peak-load, but that would in General lead to not completely uncorrelated values, which would lead to other "problems". In this work this problem is not considered any further, and all model-calculations were kept as they are.

[45] The mean-value of about 0.94MN, isn't very meaningful. It might be due to many calculations that broke up too early, even before they reached the peak-load-value.

#	Name	+ sensi	— sensi	x -1
3	ConcHinge_Cem2_Materialwerte.Ft	0.50507		
1	ConcHinge_Cem2_Materialwerte.E		-0.25383	
11	ConcHinge_Cem2_Materialwerte.Fixed	0.22209		
2	ConcHinge_Cem2_Materialwerte.Mu		-0.16995	
10	ConcHinge_Cem2_Materialwerte.Alpha	0.13953		
8	ConcHinge_Cem2_Materialwerte.Beta	0.099766		
13	ConcHinge_Cem2_Materialwerte.FC_REDUCTION	0.086901		
12	ConcHinge_Cem2_Materialwerte.EPS_CP		-0.078104	
14	ConcHinge_Cem2_Materialwerte.SHEAR_FACTOR	0.077228		
7	ConcHinge_Cem2_Materialwerte.Exc		-0.076028	
6	ConcHinge_Cem2_Materialwerte.Wd		-0.064782	
4	ConcHinge_Cem2_Materialwerte.Fc		-0.063054	
9	ConcHinge_Cem2_Materialwerte.Rho		-0.027603	
15	ConcHinge_Cem2_Materialwerte.AGG_SIZE		-0.025371	
5	ConcHinge_Cem2_Materialwerte.Gf	0.020462		

Fig. 12.18: Influence of Input Values on Peak-Reaction-Load

The influence of Alpha (Thermal coefficient) and Rho (density) does not influence the static calculation in ATENA at all, so this sensitivity-values have to be zero. They were added to the calculation, to see the precision of this values. Rho has a small influence according to Freet, but Alpha has a quite big value of about 0.14 according to Freet, only the

12.2.2 simulation of 4 important Values

#	Name	Distribution	Descriptors	Mean	Std
1	E	Normal	Moments	35000	700
2	Ft	Lognormal (2 par)	Moments & params	3.533	1.09
3	Fc	Lognormal (2 par)	Moments & params	-48	4.8
4	Gf	Lognormal (2 par)	Moments & params	8.831e-005	2.7245e-005

Fig. 12.19: Mean Value and Standart deviation of Input-Random-Values

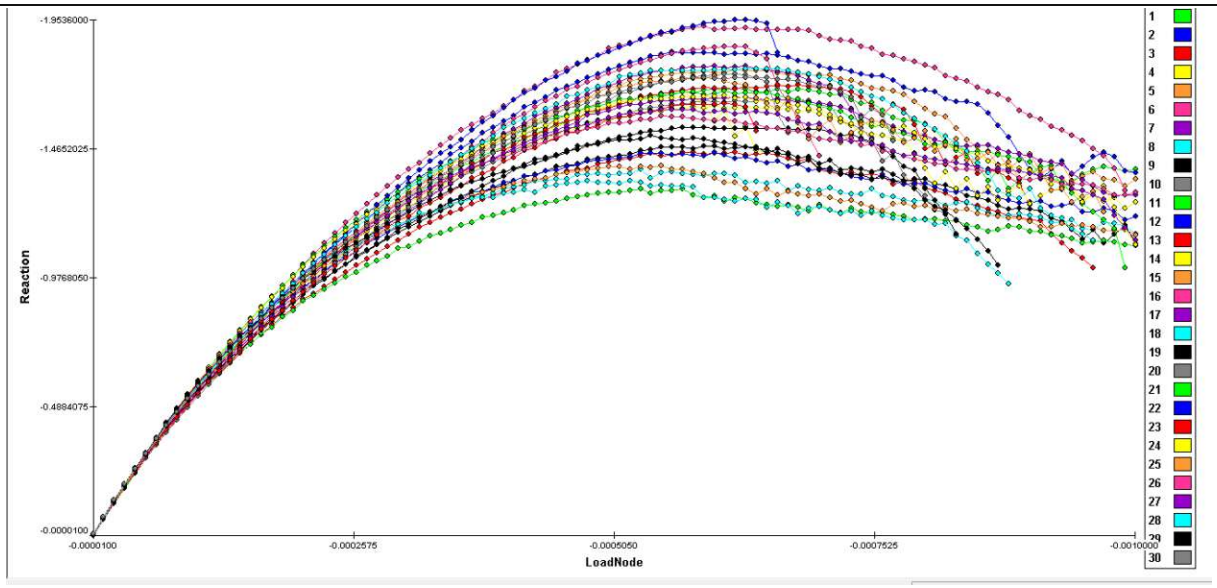

Fig. 12.20: Load-Dispacement-Curve of Uncorrelated sensitivity analyses using spatially uniform properties

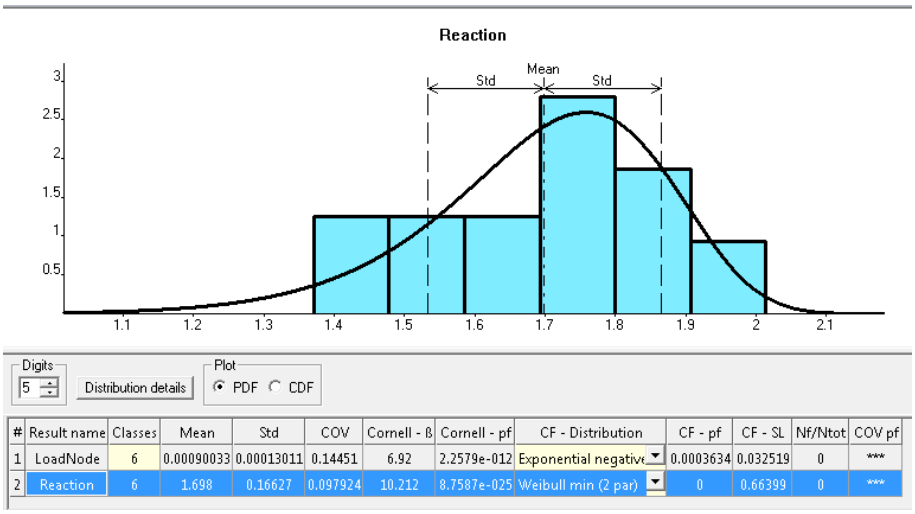

#	Result name	Classes	Mean	Std	COV	Cornell - ß	Cornell - pf	CF - Distribution	CF - pf	CF - SL	Nf/Ntot	COV pf
1	LoadNode	6	0.00090033	0.00013011	0.14451	6.92	2.2579e-012	Exponential negative	0.0003634	0.032519	0	***
2	Reaction	6	1.698	0.16627	0.097924	10.212	8.7587e-025	Weibull min (2 par)	0	0.66399	0	***

Fig. 12.21: Relibility and variance in Freet

#	Name	+ sensi	— sensi	x -1
3	ConcHinge_Cem2_Materialwerte.Fc		-0.76107	☐
2	ConcHinge_Cem2_Materialwerte.Ft		-0.58176	☐
4	ConcHinge_Cem2_Materialwerte.Gf	0.24405		☐
1	ConcHinge_Cem2_Materialwerte.E		-0.0073415	☐

#	Name
1	LoadNode
2	Reaction

Fig. 12.22: Influence of Input Values on Peak-Load

12.3 Uncorrelated sensitivity analyses using spatially fluctuating material properties (“random fields”)

Also in this simulations symmetry is assumed, also for the random field. If you consider unsymmetrical random fields, which will be more likely, the hinge will very unlikely behave symmetrically. Especially the crack development of unsymmetrical random fields might only happen only on one (the weak) side, instead of on both sides symmetrically.

12.3.1 correlation length of 10cm

#	Name	Mean	Std	COV	dx	dy
1	E	35000	700	0.02	0.1	0.1
2	Ft	3.533	1.09	0.30852	0.1	0.1
3	Fc	-48	-4.8	0.1	0.1	0.1
4	Gf	8.831e-005	2.7245e-005	0.30852	0.1	0.1

Fig. 12.23: Mean Value and Standart deviation of Random Fields

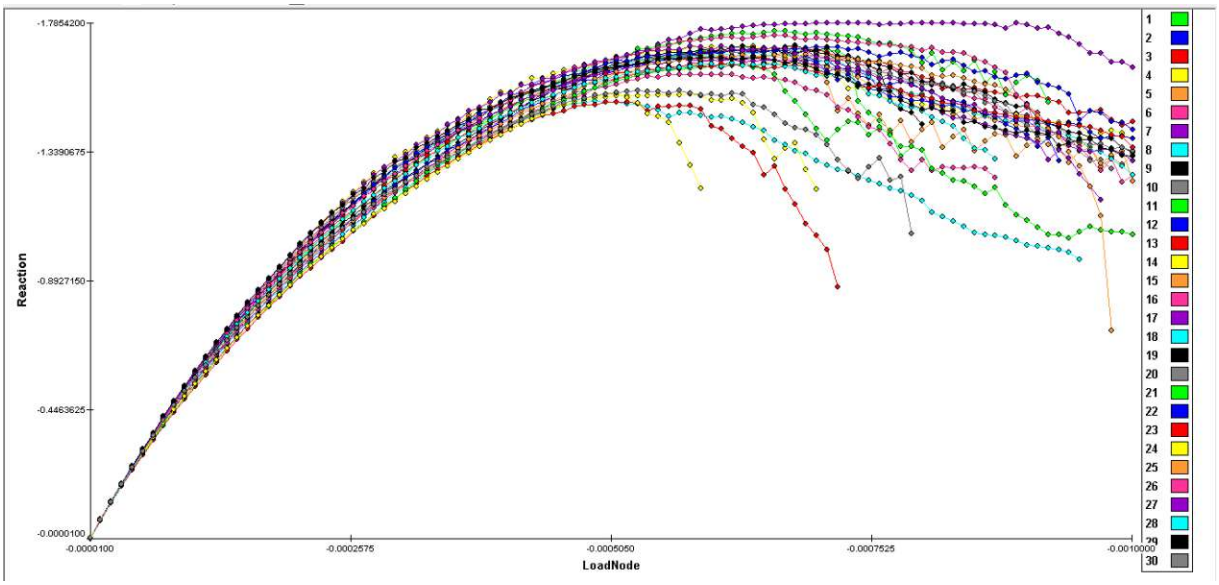

Fig. 12.24: Load-Dispacement-Curve of Uncorrelated sensitivity analyses using spatially fluctuating material properties (“random fields”)

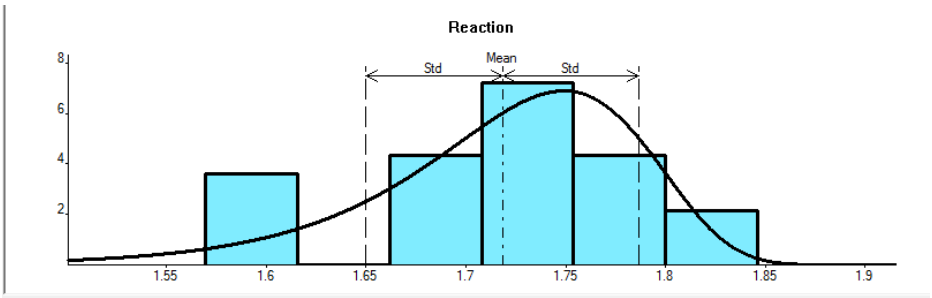

#	Result name	Classes	Mean	Std	COV	Cornell - β	Cornell - pf	CF - Distribution	CF - pf	CF - SL	Nf/Ntot	COV pf
1	LoadNode	6	0.00092567	0.00011085	0.11975	8.3507	3.3927e-017	TwoBounded Normal	3.3927e-017	0.016316	0	***
2	Reaction	6	1.718	0.068555	0.039903	25.061	6.698e-139	Gumbel Min. EV I	6.2172e-015	0.2255	0	***

Fig. 12.25: Relibility and variance of Reactions in Freet

12.3.2 correlation length of 1cm

Because of the quite big fluctuation distance the fluctuation over the neck-size is very small; therefore the amount of fluctuation is increased from 1dm to 1cm for Young’s-Modulus and Compressive strength. The fluctuation distance for tensile strength and Fracture-Energy is

kept the same, because in random fields (in contrast to random variables) only Gaussian Distribution is possible and the Covariance is about 31% and that might could lead to a higher possibility of negative values, which aren't physically meaningful, and might lead to errors. This high Covariance is according to Freet from JCSS[46] for Concrete C35 with three in situ sample-tests for pre cast concrete. The Covariance from JCSS only change between 30% and 32% between different concrete strengths, for "ready mixed" or "pre cast elements" and for three to infinite number of test-Samples. All 30 Samples reached the load-peak-values.[47]

#	Name	Mean	Std	COV	dx	dy
1	E	35000	700	0.02	0.01	0.01
2	Ft	3.533	1.09	0.30852	0.1	0.1
3	Fc	-48	-4.8	0.1	0.01	0.01
4	Gf	3.831e-005	2.7245e-005	0.30852	0.1	0.1

Fig. 12.26: Mean Value and Standart deviation of Random Fields with increased flutuation

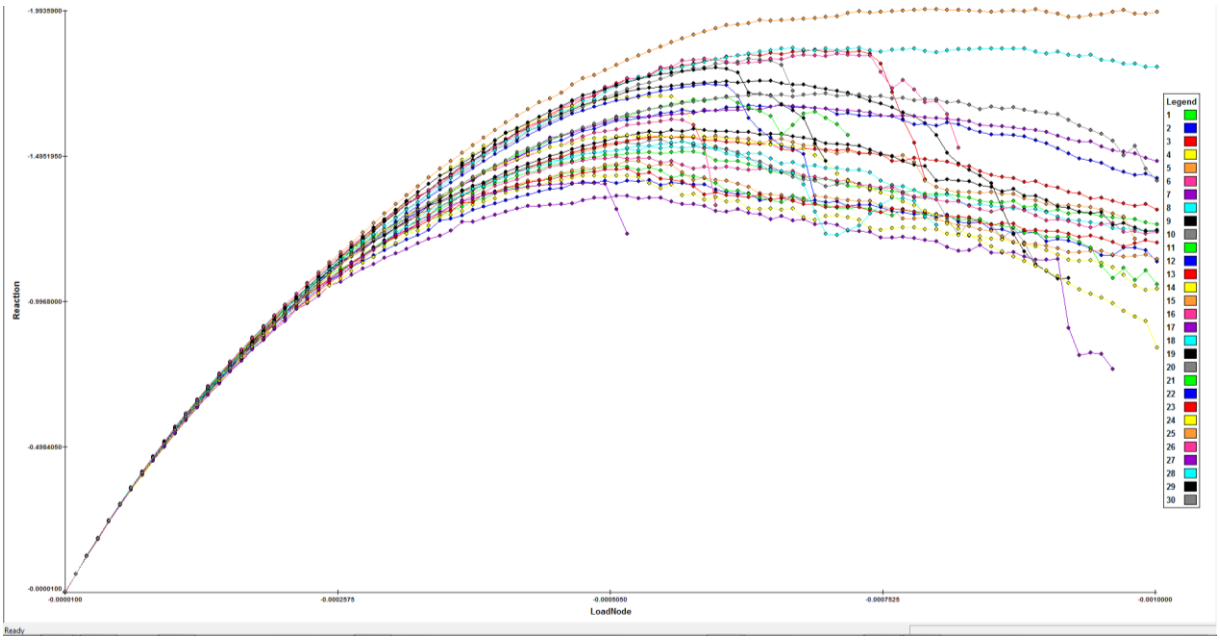

Fig. 12.27: Load-Dispacement-Curve of Uncorrelated sensitivity analyses using spatially fluctuating material properties ("random fields")

[46] Joint Committee on Structural Safety 12 th draft, Part 3 Material Properties (-*-) Kersken-Brandley, M.,Rackwitz, R., Stochastic Modeling of Materials Properties and Quality Control, JCSS Working Document, IABSE-publication, March 1991 (-*-) Rackwitz, R., Predictive Distribution of Strength under Control, Materials& Structures, 16, 94, 1983,pp.259-167

[47] Sometimes it could occur that the calculation cannot start, due to meaningless input values, or that the model cannot convert anymore and stops calculating even bevor the peak-load is reached.

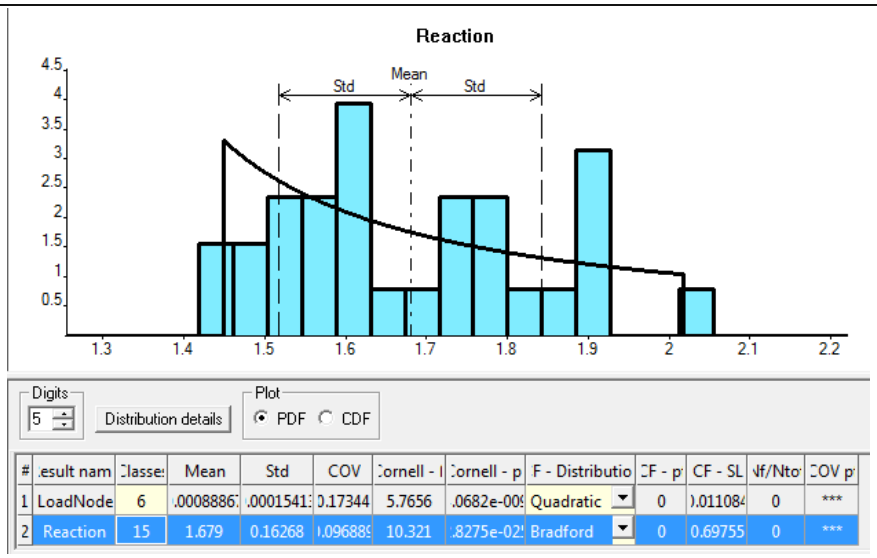

#	esult nam	lasse:	Mean	Std	COV	ornell - l	ornell - p	F - Distributio	F - p	CF - SL	Nf/Nto	OV p
1	LoadNode	6	.0008886	.0001541	0.17344	5.7656	.0682e-00	Quadratic	0	0.011084	0	***
2	Reaction	15	1.679	0.16268	0.096889	10.321	.8275e-02	Bradford	0	0.69755	0	***

Fig. 12.28: Relibility and variance of Reactions in Freet

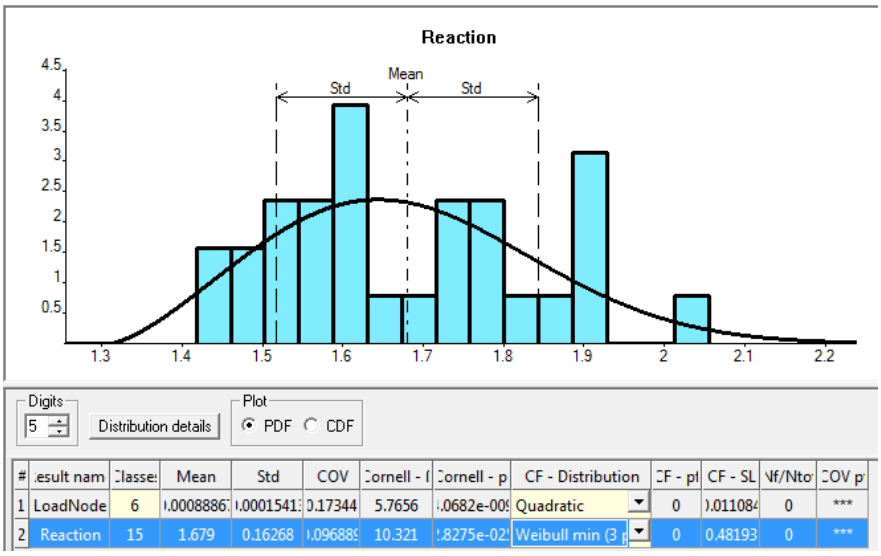

#	esult nam	lasse:	Mean	Std	COV	ornell - l	ornell - p	CF - Distribution	F - pl	CF - SL	Nf/Nto	OV p
1	LoadNode	6	.0008886	.0001541	0.17344	5.7656	.0682e-00	Quadratic	0	0.011084	0	***
2	Reaction	15	1.679	0.16268	0.096889	10.321	.8275e-02	Weibull min (3 p	0	0.48193	0	***

Fig. 12.29: Relibility and variance of Reactions in Freet with Weibull-Distribution

12.3.3 Differences of the input tensile strength of Simulations of 12.3.1

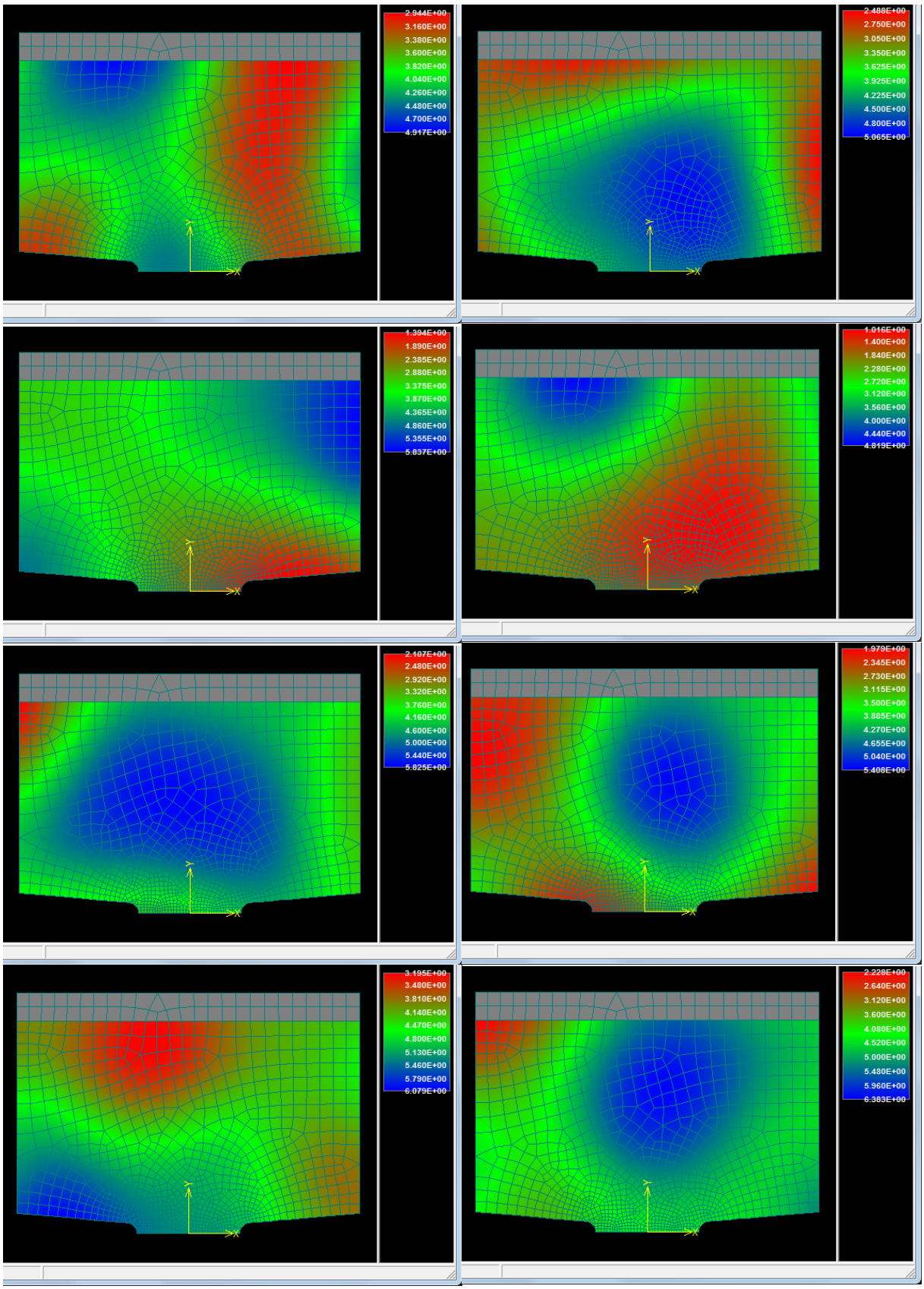

Fig. 12.30: Tensile-Strength-Distribution with a fluctuating distsance over 10cm unsing Atena

To see the influence on the tensile Strength on the peak-reaction-load-value, this works also compares the tensile strength field of the smallest peak-load with the one with the highest peak-load.

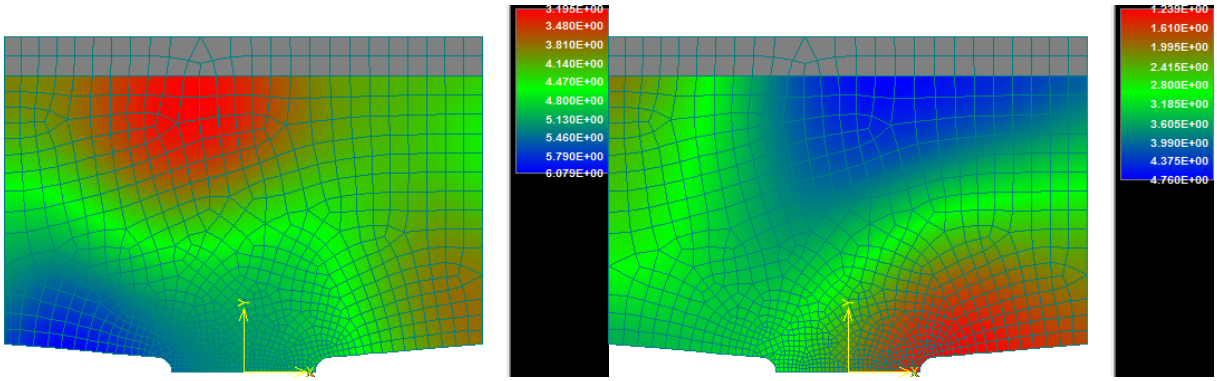

Fig. 12.31: Tensile-Strength-Distribution of the weakest (left) and the strongest(right) simulation in Atena

The differences in the tensile strength of the weakest and strongest simulation are quite big. The weak model has higher tensile strength in the neck then in the head and a mean value over the whole model of 4.7MPa and the strong model has a low tension in the neck compared the hinge-head and the mean value over the whole model of 2.8MPa.

The weak model has 5.6MPa tensile strength on the tension-side and 5.0MPa on the compressive side. The tensile strength of strong model has 3.0MPa on the tension-side and 1.4MPa on the compressive side. Therefore the tension strength is up to 3.6 times bigger in the weak model. There are two reasons why a high tensile strength decreases the peak-load: First a high tensile strength leads to a bigger tension neck-crack that leads to a smaller eccentricity in the hinge-neck, so there is a smaller moment, which leads to a more constant compressive-strength distribution. Second a high-tension-strength, and keeping the compressive strength the same leads to smaller triaxial compressive strength considering the failure surface of the Cementitious2-Model.

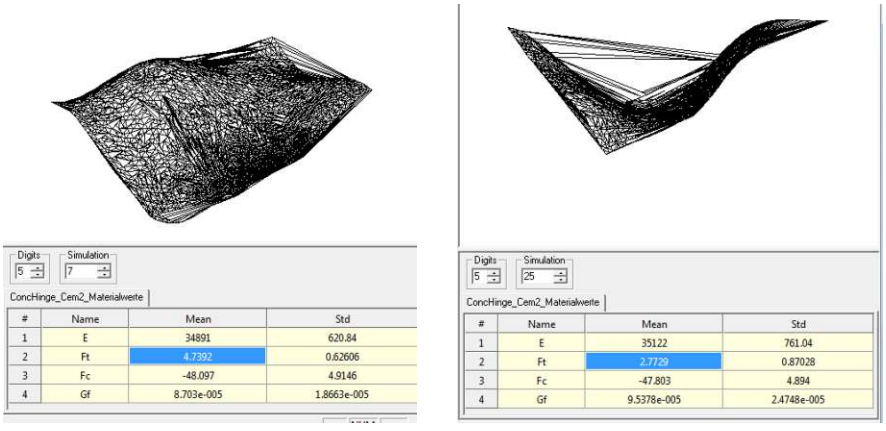

Fig. 12.32: Tensile-Strength-Distribution of the weakest (left) and the strongest(right) simulation in Freet

It seems that Atena Engineering can only display the field of the tensile strength[48], therefore no further input parameters are included in this work.

[48] In Atena, the tensile strength decreases during calculation, because of cracks, which might be the reason to view it in the post processing.

12.3.4 Differences in crack-development of Simulation of Subsection 12.3.2

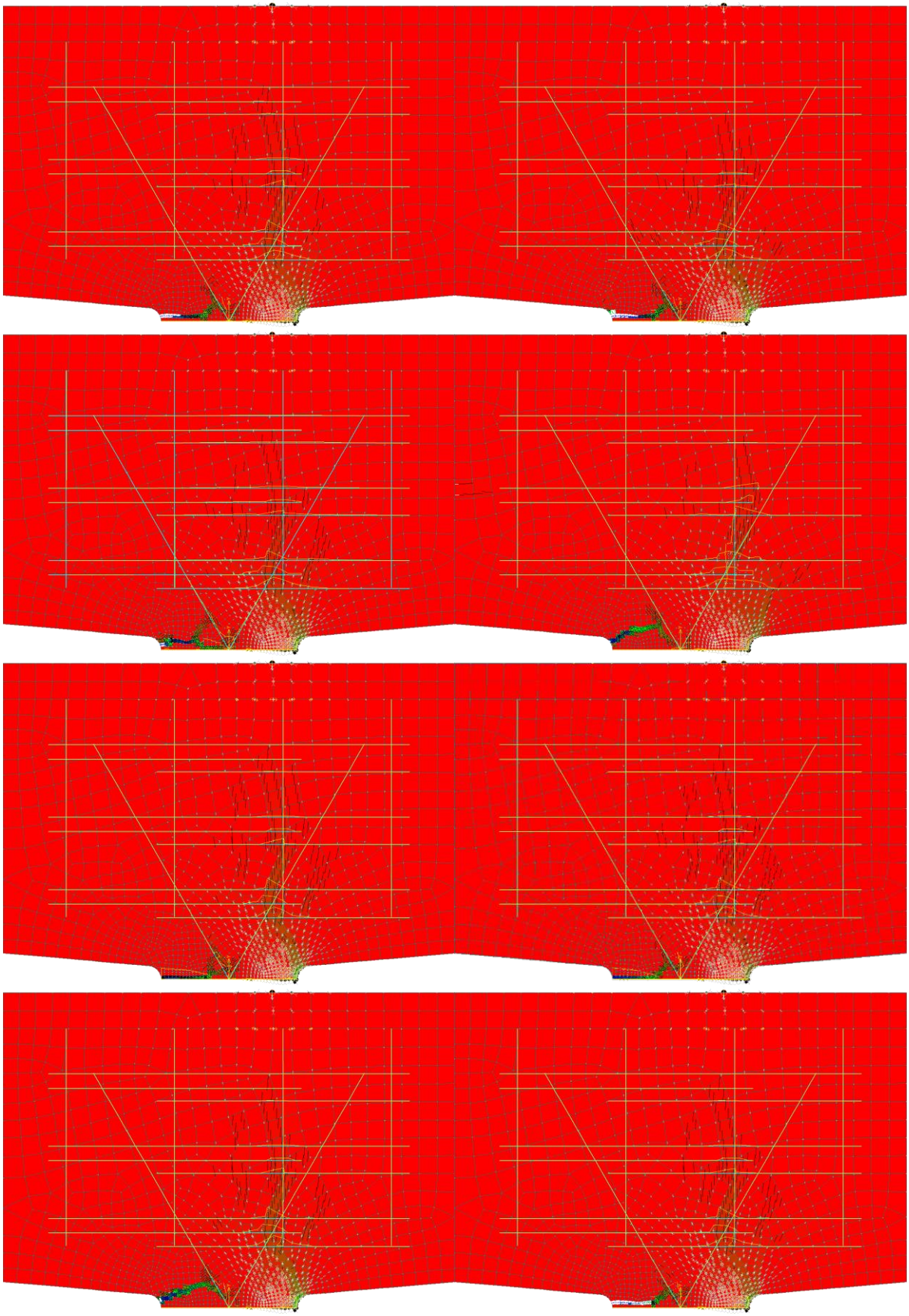

Fig. 12.33: Deviaton of stochasitc fields with weeker and stronger distribution

There are some differences in the crack development (**Fig. 12.33**). Some tension cracks appear horizontal in the middle and some are up to about $\pi/6$ ($\triangleq 30°$) from the horizontal. The tensile splitting cracks are almost identical, and they are very much following the erratic mesh. The cracks in every integration point, which are above 0.03 mm, are shown in the picture. Cracks smaller than 0.03 differ much more between the samples, but in general those micro-cracks might be negligible. To be focused on the "main cracks", those micro-cracks are not shown. The max principal strains are in color and are biggest in the tension-cracked-elements. The principal stresses are shown in the nodes (Yellow arrows for tension and gray arrows for compression). The reaction of the external force at the free surface is shown at the nodes with a white arrow. And in Yellow along the reinforcement bars are the plastic strain of the reinforcement. In the pictures you see that the steel is yielding above the compressive zone along the tensile-spliting-cracks and sometimes also yielding of the neck-reinforcement next to tension cracks.

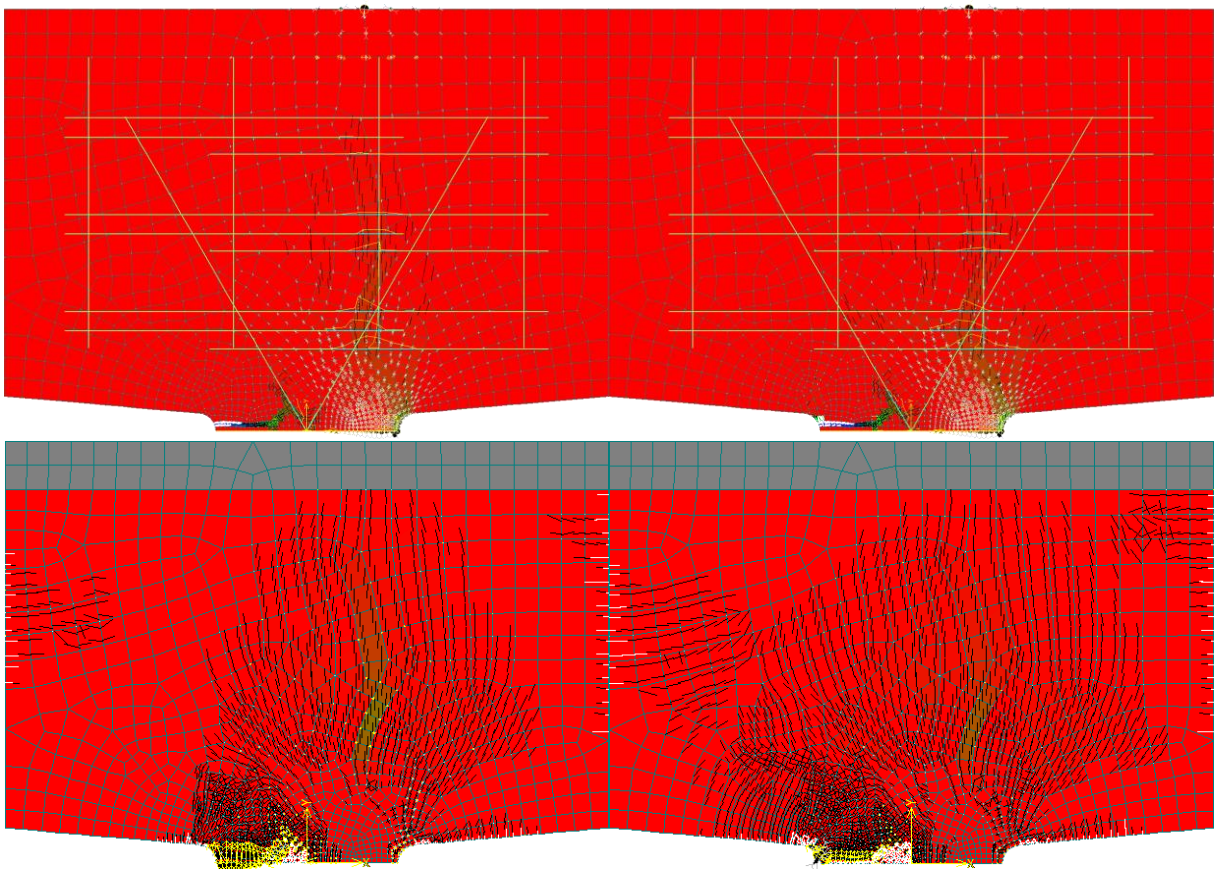

Fig. 12.34: Differeces on the cracks

Also two simulations look quite similar in **Fig. 12.33** in **Fig. 12.34** you can see that there are some differences. The differ

- in the amount of cracks (black lines)
- in the size and direction of the fracturing strain (yellow and gray arrows)
- in the size of the crack-width (color in the lower pictures of **Fig. 12.34**)

Interesting is that the right one has more elements with cracks, but the crack-width and the fracturing strain in the tension crack is in general smaller, but the biggest crack-with and the biggest fracturing strain are in both almost equal.

12.4 Comparison

12.4.1 Reliability

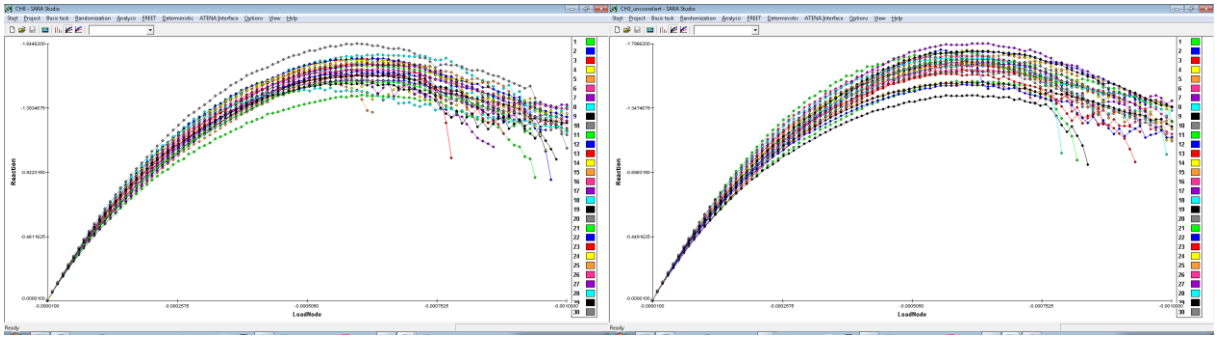

Fig. 12.35: Comparison of two equivalent statistic calculations

There is almost no difference in the Reliability of Peak-Load, but some differences in the "Senility analysis" for the Peak-Load of this two identical randomized analysis of correlated values. Therefore 30 Examples are enough for the Reliability-Analysis, but the results of the sensitivity analysis should be questioned.
The mean-value and standard deviation of this two calculations are almost identical. The results are very similar also one is fitted with a Weibull- and one with a Gumbel-Deviation.

Table 6: Reliability of peak load in two equivalent stochastic simulations

	Subchapter 12.1.1	Subchapter 12.1.2	Relative difference[49]
Mean	1,7105	1,7119	0,08%
Standard deviation	0,078	0,084	6,89%

12.4.2 Sensitivity analysis

The correlation of the compressive strength on the peak-load is very obvious, and in both calculations the correlation coefficient are similar. Also the correlation coefficient for the Young modulus is also quite similar. Fracture Energy and Tensile Strength have smaller correlation coefficient Values and they scatter very much. One of the reasons is that a "bigger" negative compressive strength leads to a higher tensile strength. Deterministic evaluation show that a higher tensile strength lead to smaller peak-values, so it should have negative correlation coefficient, but because it is related to the compressive strength, which has a higher influence on the peak-Value, in the correlated calculations it has a positive correlation coefficient. So the correlation matrix leads to a correlation of the correlation coefficients, which is not very meaningful, and which seems to be ignored in SARA and Freet. Useful would be if the stochastic software would be able to calculate a multidimensional plane for all correlation coefficients. Then you have correlation coefficient, which is now independent

[49] $2 \cdot |\#_1 - \#_2| / |\#_1 + \#_2|$

on the correlation matrix. Sara is a useful software for Atena Engineering, but compared to other stochastic software like optiSLang®[50], it is still in its infancy.

The big differences between both stochastic calculations are really high for 30 Examples, maybe more Examples are required to get reproducible results for correlation coefficient, but anyway the results have to be scrutinized or even revised, because of reasons[51] written above, which is not further done in this work.

Table 7: Correlation coefficients of two identical sensitivity analysis. (ordered in importance)

	Subchapter 12.1.1	Subchapter 12.1.2	Factor of difference[52]
$\lvert F_c \rvert$[53]	0,68	0,65	1,06
E	0,31	0,40	1,28
G_f	0,36	0,08	4,41
F_t	0,31	0,05	5,79

12.4.3 comparison of correlated and uncorrelated values

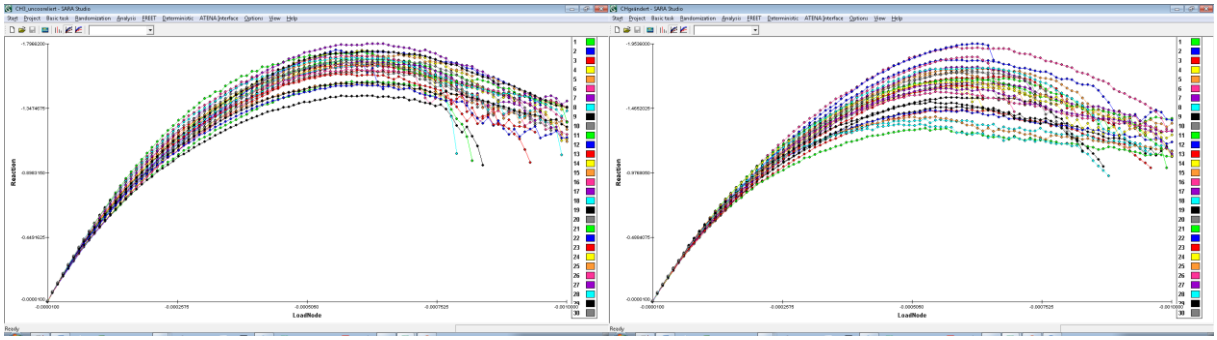

Fig. 12.36: Comparison of Load-Dispacement-Curve between correlated and uncorrelated random values

Table 8: Reliability-of-peak-load-comparison of correlated an uncorrelated Values

	12.2 Correlated Random Values	12.3 uncorrelated Random Values	Relative difference[54]
Mean	1,711	1,698	0,77%
Standard deviation	0,081	0,166	69,3%

Table 9: Correlation coefficients of two identical sensitivity analysis.

	12.1.1 correlated Random Values	12.1.2 correlated Random Values	Absolute difference[55]
$\lvert F_c \rvert$[56]	0,67	0,76	0,10
E	0,36	- 0,01	0,37

[50] optiSLang® is a Software for sensitivity analysis, reliability, robustness and more by dynardo
[51] The Sensitivity analysis seems to be dependent on the correlation matrix
[52] Bigger Value over smaller Value
[53] F_c<0, so a high performance concrete has a "low" compressive strength, because it has a high negative value.
[54] $2 \cdot |\#_1 - \#_2| / |\#_1 + \#_2|$
[55] Bigger Value minus smaller Value
[56] F_c<0, so a high performance concrete has a "low" compressive strength, because it has a high negative value.

G_f	0,22	0,24	0,02
F_t	0,18	- 0,58	0,77

The Young's Modulus has a negligible influence in the uncorrelated case. With the correlation-Matrix it has a positive correlation value, which is only caused, because of the correlation with the compressive strength. The tensile strength is very interesting, because a higher tensile strength lead to a smaller tension-crack, which leads to a smaller eccentricity, which leads to a better compressive distribution over the remaining cross section, which leads to less stress concentration at the free surface on the compressive side, which leads to higher peak-loads. It is explained in the deviatoric sensitivity-analysis more in detail (not included here). In the correlated case it has a positive correlation, which might look like a big tensile strength is good, but actually a high tensile strength leads to a smaller peak-value. Sara pushes back the correlation coefficient, with ignoring that the increase and decreased is caused by the compressive strength, which is correlated with the tensile strength over the correlation matrix. The influence of the compressive strength is reduced in the correlated case, because it is correlated with the tensile strength. That indicates that improving all the concrete strengths does not help as much as only improving the compressive strength. More important would be to know the slop of the dependence, which will be in general in the case with the higher standard deviation of the peak-load higher. For such calculations it means in general, that the uncorrelated case has higher slopes, because it has a higher standard deviation. This difference in the standard deviation can be explained, because the effect of the compressive and the tensile strength are reversing each other's influence.

12.4.4 Comparison of uncorrelated values and uncorrelated fields

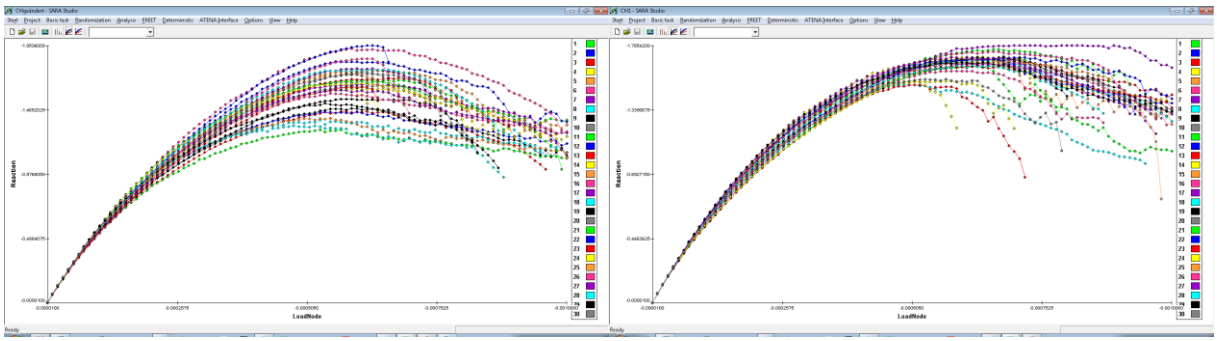

Fig. 12.37: Comparison of Load-Dispacement-Curve between uncorrelated values and uncorrelated fields

Table 10: Reliability-of-peak-load-comparison of stochastic values and stochastic fields

	12.2.2 uncorrelated Random Values	12.3.1 random Fields (uncorrelated)	Relative difference[57]
Mean	1,698	1,718	1,17%
Standard deviation	0,166	0,069	83,2%

[57] $2 \cdot |\#_1 - \#_2| / |\#_1 + \#_2|$

That the mean value of random Fields is higher is a little bit stange and unexpected and might be because of to less samples. The Standard deviation is 2.4 times smaller. That the standard deviation is smaler could be explained because every concrete-hinge model now has somewhere week points and somewhere strong points, so somehow every model equal. Often the cross-section with week areas reduce the peak-load, but in this case it seems to be able to distribute stresses to stronger areas, but the increasing of the mean load might only occur because of to less samples to be representativ.

A representativ length of 10cm was chossen for all parameters, if you consider that the hinge has a 7cm neck and has radiuses of 1,5cm the parameters are very similar in the important region within one sample. This is now a little bit in contrast to the behavior of the standard deviation, explained before.

12.5 Comparison between two stochastic fields, with different fluctuation-distances

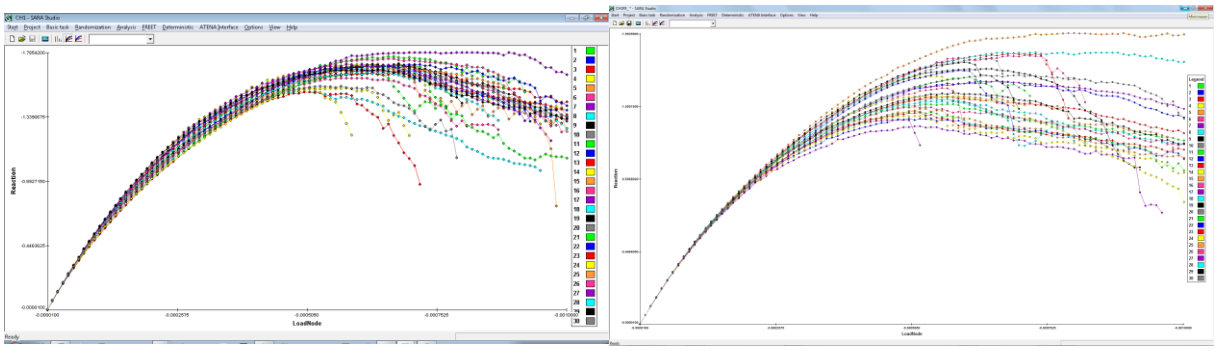

Fig. 12.38: Comparison of Load-Dispacement-Curve between two uncorrelated fields, with different fluctuation-distances

Table 11: Reliability-of-peak-load-comparison of stochastic fields with different fluctuation-distances

	Subchapter 12.1.1	Subchapter 12.1.2	Relative difference[58]
Mean	1,718	1,679	2,30%
Standard deviation	0,069	0,163	81,4%

The Mean-value of the one with higher fluctuation gradient (smaller fluctuation-distance) is, as expected, smaller. The reason is that , there is more likely to have a flaw-area in the neck-area, but compared to the one with the calculation of uncorrelated stochastic values the Mean-value and the standard deviation is quite similar. Which could mean that there might be an input-error in the calculation of Subsection 12.1.1, but the Atena-File and the stochastic input-variance seems to be identical, except the values mentioned earlier in this report. This (small) differences might could occur because it is calculated on two different computers with different Processors and different Atena-Versions[59], which might lead to different rounding errors. The stochastic simulation with a higher fluctuation gradient shows almost no differences in the early behavior (low load-level), compared to all other stochastic simulations in this work. In this early behavior the young's modulus is important and it is fluctuating so much, that for the stiffness of the whole model you could assume the mean modulus of

[58] $2 \cdot |\#_1 - \#_2| / |\#_1 + \#_2|$
[59] ATENA 5.1.2c.11461 and ATENA 5.1.3b.12325

the model[60] and stiff areas are "attracting" the stresses. But for the compressive strength this assumption would not make sense, because in a weak-compressive-strength-area the concrete would fail, and for the compressive strength the weakest link is most important for the behavior. Therefor the compressive strength cannot (easily) be (meaningful) averaged over the whole model.

12.6 Further notes

SARA is a very useful tool, which can help a lot, and puts back quite fast a stochastic analysis, and a quick reliability analysis, but for a convincing stochastic analysis, you may have to use other software, but for this work this Software is more than sufficient.

To get a reliability analysis, with a probability of failure like postulated in Eurocode, it is necessary to know also the standard deviation of the loading, which is not done in this work. The standard deviation of the reaction very much scatter[61], between the different stochastic analysis, so to find the Eurocode target failure probabilities for ultimate limit state of about 10^{-6} will differ very much, so that it might won't be possible to find a ultimate limit state with a reproducible magnitude of loading maybe even with the same type of derivation (Gaussian, Weibull, Lognormal,..).

13 Discussion and Conclusions

In the current Project Work, several simulation studies were carried out in order to assess different sources for deviations between Finite Element simulation results and observations from testing of concrete hinges. The following conclusions are drawn:

- Numerical errors play an important role in Finite Element analysis. They stem (i) from the discretization of the structure of interest and (ii) from the incremental-iterative solution strategy used to solve a non-linear simulation challenge. Optimal trade-offs have to be found between simulation efforts and reliability of the simulation results, because both aspects increase with increasing mesh fineness and with increasing the requested accuracy which needs to be reached before an iteratively found solution is accepted.
- Support and loading conditions play an important role for the behavior of reinforced concrete hinges. Therefore, it is desirable to reduce uncertainties regarding support and loading conditions in practical testing of concrete hinges. This calls not only for a proper design of the test setup, but also for the use of measurement instrumentation which allows for quantifying the quality with which desired support and loading conditions are actually realized.

[60] The mean young's modulus between the models have (a much) smaller standard derivation, because of the small fluctuation distance, which averages over the whole model. That means that the standard derivation is mainly within every model, and not between two models.

[61] The big scatter might be explained, because of the less samples.

- Material models for concrete exhibit many input parameters, and many of them have a strong influence on the simulated structural behavior of reinforced concrete structures. Therefore, one can expect that it shall be possible to obtain almost any desired simulation result by fitting of the input parameters.

In the context of the latter point, it is recommended to check the predictive capabilities of any developed Finite Element model in comparison with independent experimental data, whereby "independent" means that the considered experimental data were not used to develop the model. If such an assessment is impossible, for instance because no additional experimental data are available, parameter fitting should be handled with care. It is recommended to accept only as few fitting parameters as possible, to chose fitting parameters which exhibit a clear mechanical interpretation, and to check the plausibility of the finally obtained values of the fitting parameters. This is setting the scene for the follow-up Master Thesis. Therein, it will be shown that highly non-linear behavior of concrete hinges (loaded up to their load carrying capacity) can be explained by considering (i) default input values which depend of the actual stiffness and the actual cube compressive strength of the used concrete, (ii) damage resulting from hindered shrinkage of concrete, and (iii) a realistic approach to modeling strength of the material under triaxial compression.

14 Acknowledgment

Very helpful and friendly support regarding the use of the Finite Element software ATENA 5.1 from Mr. Dr.-Ing. Dobromil Pryl (Main Support), Mr. Ing. Radomír Pukl CSc. (lecturer) and Mr. Ing. Jan Červenka Ph.D. (for scientific questions), Červenka Consulting, Prague, Czech Republic, is gratefully acknowledged.

15 Table of Figures

16 Bibliography

[Franz, 1959] Franz, G.: *„Betonkalender"* Hallen: Wilhelm Ernst & Sohn - (1959)

[Tourasse, 1961] Tourasse, M.M.: *„Essais sur articulation Freyssinet"* Annales de l'Institut Technique du Bâtiment et des Travaux Publics 40 (57) (1961) P62-87

[Dix, 1962] Dix, Johannes.: *"Betongelenke"– „unter oftmals wiederholter Druck- und Biegebeanspruchung"* Konstanz: Wilhelm Ernst & Sohn - (1962) P.: Preamble, 1, 2-3, 18-19, 34-35

[Leonhardt, 1965] Leonhardt, Fritz. Reimann, Horst.:*„Betongelenke"– "Versuchsbericht, Vorschläge zur Bemessung und konstruktiven Ausbildung" // "Kritische Spannungszustände des Betons bei mehrachsiger, ruhender Kurzzeitbelastung"*, Berlin: Wilhelm Ernst & Sohn - (1965) P25, 26-27

[Menétrey, 1995] Menétrey, Philippe. Willam K. J.:*"Triaxial failure criterion for concrete and its generalization"*, in: *"ACI structural journal"* "May-June 1995" Volume: 93 Issue:3 (1995-05-01) ISSN=0889-3241 P 312-313
URL:
http://www.ingphi.ch/images/web/ingphi/publication/philippe.menetrey/Triaxial%20Failure%20Criterion%20for%20Concrete%20and%20Its%20Generalization.pdf

[SARA, 2002] Červenka Consulting.: “SARA-Studio”
URL.: http://www.cervenka.cz/products/sara

[Bernhardt, 2003] Bernhardt, Klaus. Mohr, Burkhard Seifried, Gerhard. Angelmaier, Volkhard.: *„Stahlbau Volume 32, Issue 2 (pages 61-70)“ – „Talbrücke Korntal-Münchingen - innovativer Brückenentwurf als Rohrfachwerk-Verbundbrücke, Teil 1- Entwurf“*. Berlin: Ernst & Sohn Verlag für Architektur und technische Wissenschaften GmbH & Co. KG - (2003) Chapter: 3.2.1 (P67-68)
URL: http://onlinelibrary.wiley.com/doi/10.1002/stab.200300240/abstract

[Červenka, 2008] Červenka, Jan. Papanikolaou, Vassilis K.: *“Three dimensional combined fracture–plastic material model for concrete”*. International Journal of Plasticity Volume 24, Issue 12 - (2008-12) P2195, P2202-2206
URL: https://www.researchgate.net/publication/223405193
URL: http://www.sciencedirect.com/science/article/pii/S0749641908000259

[Tue, 2009] Tue, Nguyen Viet. Jankowiak, Holger.: „Betongelenke aus selbstverdichtendem und hochfestem Beton bei der neuen Elbebrücke Mühlberg“ Bautechnik 86 (10) (2009) 637–646.
URL http://onlinelibrary.wiley.com/doi/10.1002/bate.200910064/abstract

[Marx, 2009] Marx, Steffen. Schacht, Gregor.: „*Gelenke im Massivbau*“ - „Beton- und Stahlbetonbau Volume 105, Issue 1 (pages 27-35)“. Ernst & Sohn Verlag für Architektur und technische Wissenschaften GmbH & Co. KG - (2009-12-23) Chapter: 1 (P27); Chapter 4 (P33)
URL: http://onlinelibrary.wiley.com/doi/10.1002/best.200900061/abstract

[Marx, 2010] Marx, Steffen. Schacht, Gregor.: *„Betongelenke im Brückenbau“* Berlin Deutscher Beton- und Bautechnik Verein 18 in German
URL https://www.researchgate.net/publication/265597571_Betongelenke_im_Bruckenbau

[Schacht, 2010] Schacht, Gregor. Marx, Steffen.: „Unbewehrte Betongelenke – 100 Jahre Erfahrung im Brückenbau“ „Beton- und Stahlbetonbau Volume 105, Issue 9 (pages 599-607)“ – .
Berlin: Ernst & Sohn Verlag für Architektur und technische Wissenschaften GmbH & Co. KG - (2010-09-01) Chapter: 1 (P599)
URL: http://onlinelibrary.wiley.com/doi/10.1002/best.201000030/abstract

[EN1992, 2011] EN 1992-1-1:2011-01, *„Eurocode2: Bemessung und Konstruktion von Stahlbeton- und Spannbetontragwerken – Teil 1-1: Allgemeine Bemessungsregeln und Regeln für den Hochbau; Deutsche Fassung EN 1992-1-1:2004 +AC:2010“* CEN Europäisches Komitee für Normung, (2010) Chapter 6.7 „Teilflächenpressung“

[IMWS, 2011] Institut für Mechanik der Werkstoffe und Strukturen.: *„Skriptum zur Festigkeitslehre Übung 2011/2012“*. Vienna: Vienna University of Technology - (2011) Chapter 4

[Wiktionary, 2012] Equinox. (https://en.wiktionary.org/wiki/User:Equinox).: *“excentricity”* Wiktionary - (30.01.2012)
URL: https://en.wiktionary.org/w/index.php?title=excentricity&oldid=16182436
Access-Date: 20.10.2015

[Hellmich, 2012] Hellmich, Christian., (et al.): *“Skriptum zur Vorlesung aus Festigkeitslehre”* Vienna: IMWS - (20.02.2012) P 2, 59

[Červenka, 2014] Červenka, Vladimír. Jendele, Libor. Červenka, Jan.: *“ATENA Program Documentation Part 1” - “Theory”,* Prague: Červenka Consulting s.r.o. - (19.09.2014) Chapter: 2.2.12, 2.4
URL: http://www.cervenka.cz/assets/files/atena-pdf/ATENA_Theory.pdf
Access-Date: 27.08.2015

[Grassl, 2014] Grassl, Peter.: *“Structural Concrete” - “Lecture notes 2014”*, Glasgow: The University of Glasgow - (22.09.2014) P 48-52, P57-61

[Morgenthal, 2015] Morgenthal, Guido. Olney, Peter.: *“Concrete hinges and integral bridge piers”* - Journal of Bridge Engineering 21 (1) (2015) 06015005
URL: http://ascelibrary.org/doi/10.1061/(ASCE)BE.1943-5592.0000783

[GiD 12.0,2015] ATENA-Add-On for GiD: *"The personal pre and postprocessor GiD Version 12.0."*, Barcelona: CIMNE, International Center for Numerical Methods in Engineering. - (14.05.2015)
URL: http://www.cervenka.cz/download/
Atena-Version: Build "12562 & Atena 5.1.3"

[ATENA, 2015] ATENA: *"Software for non-linear analysis of reinforced concrete and concrete structures."*, Prague: Červenka Consulting s.r.o. - (© 2013-2015)
URL: http://www.cervenka.cz/download/
Version: 5.1.2.11514 (5.1.2 Build 11419)

[Thomson, 2015] Thomson, Ron.: *„Computational Solid Mechanics"* Glasgow: University of Glasgow - (2013-2015) Chapter: 23 P14,26; Chapter: 25 P1-8; Chapter: 26; Chapter 28 P1; Chapter: 31

[Trouble, 2015] Pryl, Dobromil. Červenka, Jan.: *"Troubleshooting Manual"* Prague: Červenka Consulting s.r.o. - (28.05.2015) Question: 2.1.3, 2.1.10.1
URL: http://www.cervenka.cz/assets/files/atena-pdf/ATENA-Troubleshooting.pdf
Access-Date: 06.08.2015

[Support, 2015] Pryl, Dobromil.: Mail: *"Re: Betongelenk – TU-Wien" & "Re: Betongelenk – TU-Wien"* Prague: Červenka Consulting s.r.o. (Support) - (NLCem3: 07.08.2015) & (Convergenz:17.08.2015)

[Hlobil, 2016] Hlobil, Michal. Göstl, Maximilian. Burrus, Jacques. Hellmich, Christian. Pichler, Bernhard: "*Molecular-to-macro upscaling of concrete fracture: theory and experiments"*, Nanocem steering committee (Draft 11.02.2016)

[Schlappal, 2016] Schlappal, Thomas. Schweigler, Michael. Reihsner Roland. Gmainer, Susanne. Peyerl, Martin. Pichler, Bernhard: *„Creep and cracking of concrete hinges"* Experimental Mechanics (Draft of March 2016)